

2019 NSF/REU

RESEARCH EXPERIENCE
FOR UNDERGRADUATES
IN PHYSICS



STUDENT RESEARCH PAPERS

VOLUME 30



UNIVERSITY OF
NOTRE DAME
College of Science

REU DIRECTOR
UMESH GARG, PH.D.

REU Student Research Papers – Summer 2019
University of Notre Dame – Department of Physics

Student	Research Title	Page No.
Winter Allen Arkansas Technical University	Exploring the Optical Region of Stellar Spectra for Metallicity Dependence	1
Samantha Berek Yale University	Project AMIGA: Circumgalactic Gas about Andromeda and its Dwarf Satellites	11
Hannah Blue University of Hawaii at Hilo	Adaptive Optics: Phase Unwrapping	21
Alyssa Davis Swarthmore College	Determining the astrophysical $^{20}\text{Ne}(\alpha, p)^{23}\text{Na}$ reaction rate from measurements with the Notre Dame 5U accelerator	31
Jack Enright University College Cork	Characterization of CeBr_3 Scintillation Detectors for use in Coincidence Measurements	41
Yadira Gaibor Missouri State University	Reducing the uncertainty of the white dwarf spin-down rate in AR Scorpii	51
Arianna García Caffaro University of Notre Dame	Implementation of Tilted Module Bend Corrections in the CMS Detector Track Trigger	59
Curtis Goss Indiana Univeristy Bloomington	Radial Velocity Measurements of Stellar Bodies Observed by the Automated Planet Finder and Their Implications on Exoplanet Exploration	69
Kathleen Halloran Saint Mary's College	The First Extended Look at an Eclipsing Polar: V1309 Orionis	79
Isabella Ianora University of San Diego	Teaching Through the Chart of Nuclides	89
Sean Kelly University of Notre Dame	The High Efficiency Total Absorption Spectrometer (HECTOR) and Correcting for Inconsistencies in $^{27}\text{Al}(p, \gamma)^{28}\text{Si}$	99
Kinsey Lee Scripps College	Dependence of Helium Atmospheric-Pressure Plasma Jet (APPJ)-Induced DNA Damage on Voltage Pulse Duty Cycle and Irradiation Time	109
Emily McGill Dublin City University	Detecting PFAS in Water Samples Using PIGE	119
Austin Mitchell University of Southern Indiana	$^{20}\text{Ne}(\alpha, p)^{23}\text{Na}$	129
Adil Mubarak University of Minnesota at Duluth	Development of the Electrical Feedthroughs for the ND-cube Active-Target Detector	137
Yohan Musle Florida Atlantic University	Synthesis of $(\text{BiSb})_2\text{Te}_3$ Thin Films on Mica Through Chemical Vapor Deposition	147

Ha Cong Nguyen Hanoi National Univ.of Education	A model for marine species distribution in advective-diffusive ecosystems	157
Mary-Ellen Phillips Fort Lewis College	Investigating CMS Binary Chip Data Losses in the Phase II High Luminosity Upgrade to the CMS	167
Jason Prochaska Drake University	Improving the Notre Dame MR-TOF and using Photodiode Detectors for Beam Analysis	179
Rachel Procter-Murphy Arizona State University	Energy Reconstruction of Low Energy Supernova Neutrinos	189
Bingcheng Qing Xi'an Jiaotong University	Measurements on Magnetic Properties and Transport Properties of Spintronic Materials	199
Melissa Quevedo University of Atlántico	Low-energy electron interactions with triatomic molecules: CO ₂ and H ₂ O	209
Zariff Rahman University of Wisconsin-La Crosse	Characterization of Clover Detectors for use in FIREBall Detectors	219
Austin Smith Point Loma Nazarene University	Extraction of Optical Model Parameters for ⁹⁰ Zr(⁶ Li, ⁶ Li) at 60 MEV / U Using a Markov Chain Monte Carlo Algorithm	229
Nicholas Tusay The College of New Jersey	Adaptive Optics Instrumentation: Building a Better Wave Front Sensor	239
Tianyi Wang University of Notre Dame	Study of Stub Momentum Resolution and Hardware Benchmarking for CMS Track Trigger	249
Hiroka Warren University of Southern Mississippi	The Effect of Finite Organism Size and Contact Forces in Population Dynamics	259
Lexanne Weghorn University of Wisconsin-La Crosse	Implanted ¹⁴ N Target Preparation and Evaluation	269
Sierra Weyhmiller University of Notre Dame	A Method to Account for Hydroxide Contamination in Characterizing the Giant Monopole Resonance to Determine an Accurate K _τ	279
Jingxu Xie Xi'an Jiaotong University	Mean Filter Method to Find and Identify Peaks for PIGE and PIXE and Signal Sensitivity Analysis for 2.4-5.1 MeV Protons	289
Haobo Yan Xi'an Jiaotong University	Simulation of the elastic scattering in the HIPPO gas-jet target of the St. George recoil separator	299
Yihao Zhou Xi'an Jiaotong University	Influence of Carbon Abundance on Stellar Photometric Temperature Estimates	309

Exploring the Optical Region of Stellar Spectra for Metallicity Dependence

Winter Allen

2019 NSF/REU Program

Physics Department, University of Notre Dame

Advisors:

Prof. Timothy C. Beers

Prof. Vinicius M. Placco

Abstract

Metal-poor stars are fossil records of the chemical evolution of the Galaxy and the Universe. They are rare and therefore hard to find. The goal of this work is to facilitate the identification of such objects by using photometric filter response curves, designed to be sensitive to metallicity changes. This can make the process of finding the metal-poor stars faster and easier. Using several mathematical methods, a filter response curve has been designed to measure theoretical metallicity sensitivity over the optical region of the electromagnetic spectrum of stars in the Milky Way.

Introduction

In the early universe, the first stars were composed primarily of hydrogen. Elements heavier than lithium were formed in stellar nucleosynthesis. Over time, a portion of these stars ended as supernova explosions, which enriched the surrounding environment with the heavier elements. The subsequent stars to form were composed of those heavier elements. As generations of stars formed, the stars became enriched with heavier and heavier elements. (Welsh, et al., 2019)

In the search for old stars, metal-poor stars are of great interest. The abundance of one metal compared to another in a star relative to solar abundance ratio is defined by Equation 1.

$$[A/B] \equiv \log_{10}(N_A/N_B)_* - \log_{10}(N_A/N_B)_{\odot} \quad (1)$$

The variables N_A and N_B represent the numbers of atoms in the elements A and B, respectively. The * symbol refers to star of interest, while the \odot symbol refers to the sun. (Beers & Christlieb, 2005) For the purposes of this project, the metallicity of a star is referred to by the iron to hydrogen ratio, [Fe/H]. The classifications defined by Beers & Christlieb (2005) for metal-poor stars are shown in Table 1.

[Fe/H]	Term	Acronym
>+0.5	Super metal-rich	SMR
~0.0	Solar	-
<-1.0	Metal-poor	MP
<-2.0	Very metal-poor	VMP
<-3.0	Extremely metal-poor	EMP
<-4.0	Ultra metal-poor	UMP
<-5.0	Hyper metal-poor	HMP
<-6.0	Mega metal-poor	MMP

Table 1. Classifications for metal-poor stars (Beers&Christlieb, 2005).

When stars have low metallicities, they tend to have increased levels of carbon abundances. These are referred to as Carbon-Enhanced Metal-Poor (CEMP) stars. (Yoon, et al., 2016) The abundance of carbon can affect the optical spectrum, so it is important to keep the absolute carbon abundance constant. The carbon abundance is measured in the outer atmosphere of the star where the absorption lines under study are collected. (Beers & Christlieb, 2005) For this project we held the absolute carbon abundance constant and varied the metallicities. The absolute carbon is determined by the relation shown in Equation 2.

$$A(C) = [C/Fe] + [Fe/H] + A(C)_{\odot} \quad (2)$$

Where $A(C)_{\odot}$ is the solar absolute carbon abundance, which has a value of 8.43 . (Yoon, et al., 2016)

The focus of this project is to determine regions in the optical spectrum that are sensitive to metallicity. Currently, when observing the sky, observers must either scan a large portion of the sky for less detailed information of stars, or they can focus on individual stars and collect more information. Developing a filter response curve may aid in the determination for which stars are

metal-poor using the less detailed information. Old stars could hold the important insights into the early universe. Metal-poor stars are rare, which is why a photometric filter response curve developed specifically for metal-poor stars is needed to aid in the search.

Data

The methods for this project were developed using synthetic spectroscopic stellar data from the library developed by Whitten, et al.(2018). The library was developed using model atmospheres computed with the MARCS code. From the model atmospheres, they generated the synthetic spectra using the Turbospectrum routine. The library consists of wavelengths from 3000 to 10,000 Angstroms (\AA). Also, the parameters in the library consist of $3500\text{K} \leq T_{\text{eff}} \leq 8000\text{K}$ in 250K increments, $0.0 \leq \log g \leq 5.0$ in increments of 0.5 dex, $-4.5 \leq [Fe/H] \leq +0.5$ in increments of 0.025 dex, and $-1.5 \leq [C/Fe] \leq +4.5$ in increments of 0.25 dex. (Whitten, et al., 2018)

The synthetic data from this library used on this project consisted of thirty-two files for four different temperatures. The temperatures were $5000\text{K} \leq T_{\text{eff}} \leq 6500\text{K}$ in 500K increments. For each temperature, the absolute carbon abundance was held constant at 6.93. Since the surface gravity and temperature are dependent, its value changed with temperature. The metallicity values ranged from $-4.0 \leq [Fe/H] \leq -0.5$ in increments of 0.5 dex. The data consisted of the wavelengths from 3000 \AA to 10,000 \AA and the corresponding normalized flux and the actual flux. All computation was performed using the actual flux. As a result of the synthetic data used to develop the filter, it is only applicable to the Sloan Extension for Galactic Understanding and Exploration (SEGUE) spectra and Large Sky Area Multi-Object Fiber Spectroscopic Telescope (LAMOST) spectra.

Methods

The computational work performed in this project was done using Spyder 3.2.8. The first step was to compute the variance of the eight different metallicities for each temperature using the NumPy package. The formula for variance is shown by Equation 3.

$$\sigma^2 = \frac{\sum(X-\bar{X})^2}{N-1} \quad (3)$$

The variables X and \bar{X} represent the actual flux values and the average of the actual flux values for each corresponding row. The variable N represents the eight values. This resulted in four different sets of data of the actual flux variance. These sets were plotted versus the wavelength using Matplotlib. This was done to determine and visualize where the actual flux varies most with metallicity. The y-axis values were all divided by the maximum value at each respective temperature, so the scaling would be proportional. The results are shown in Figure 1.

Next, the four sets of data were each smoothed to show a more general trend. The first method of smoothing was done using a Gaussian convolution. This was performed using `convolve` and `Gaussian1DKernel` from Astropy.

$$G(x) = \frac{1}{\sqrt{2\pi\sigma^2}} e^{-\frac{x^2}{2\sigma^2}} \quad (4)$$

The variable σ represents standard deviation, and the variable x is the distance from the origin. Once again, these results were plotted using Matplotlib, which is shown in Figure 2. The purpose of the smoothing was to get a general idea of where the areas of interest are at.

The second method of smoothing was a basic integration of summing in 100 Å intervals. Each 100 Å integration was plotted against the median wavelength of each interval. The result is shown in Figure 3.

The final step was to average the four smoothed lines and compute the standard deviation. This was done using the average function from NumPy package. Finally, the standard deviation was found using the NumPy package. The result was the photometric filter response curve shown in Figure 4.

Results and Discussion

The first step was computing the variance of the metallicity at four different temperatures, which is shown in Figure 1. Part of the goal of plotting the variance was to determine any regions of metallicity sensitivity that were previously unknown. Four portions of the spectrum that were known were the K and H lines, the Magnesium Triplet, the CaII lines, and the CH G-band absorption feature. The K and H lines are represented in the first large peak just before 4000 Angstroms. This peak represents the K line at 3934 Å and the H line at 3969 Å. The Mg Triplet absorption lines are between 5150 and 5200 Å. These only appear to be visible at 5000K. Also, the CaII lines are the last three peaks on the spectrum. They are at 8500, 8544, and 8664 Å. The final peak is around 4300 Å, which is likely the G-band at 4305 Å. All these absorption lines were confirmed by a table of spectral lines from the Sloan Digital Sky Survey (SDSS) website. In addition to these established absorption lines, there seems to be a region of interest between 4500 and 5000 Å. This could indicate a new region of metallicity sensitivity.

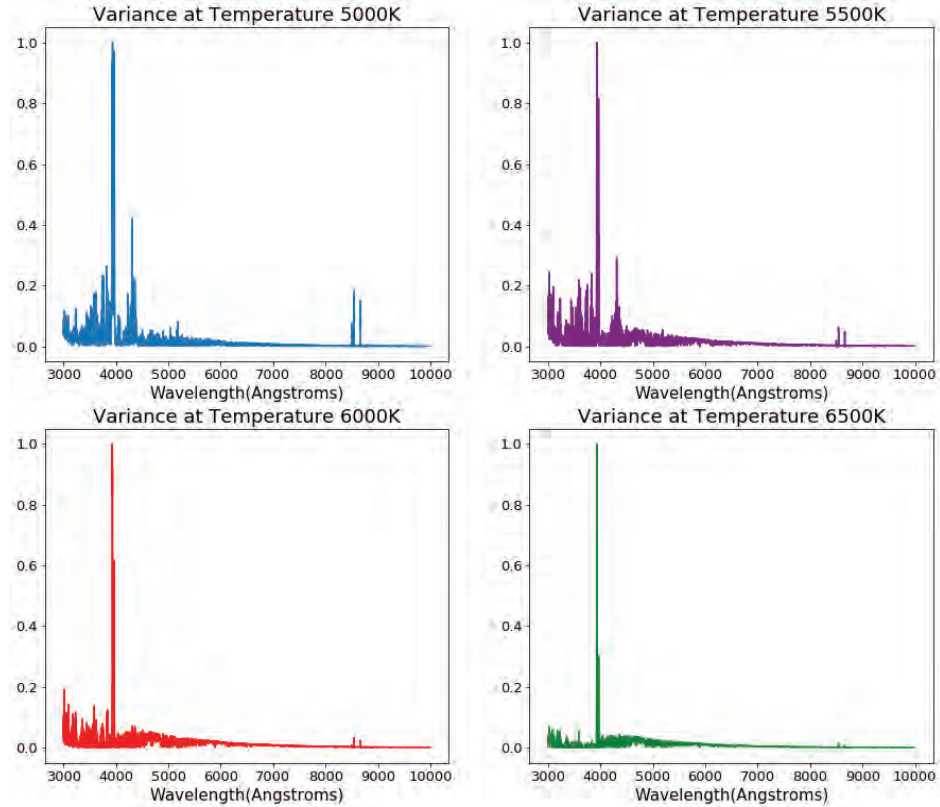


Figure 1. Variance of the Metallicity at Four Temperatures.

After the variance was computed, a Gaussian convolution was performed, which is shown in Figure 2. The image to the left is a general shape of the curve, which may be useful as a more general photometric filter response curve. The image on the right holds more information than the one on the left. For instance, a little before 4000 Å all the curves peak in the same spot, which are the K and H lines. In addition, there are a few peaks around 4500 Å to 5000 Å, which supports the idea that there may metallicity sensitivity in this region.

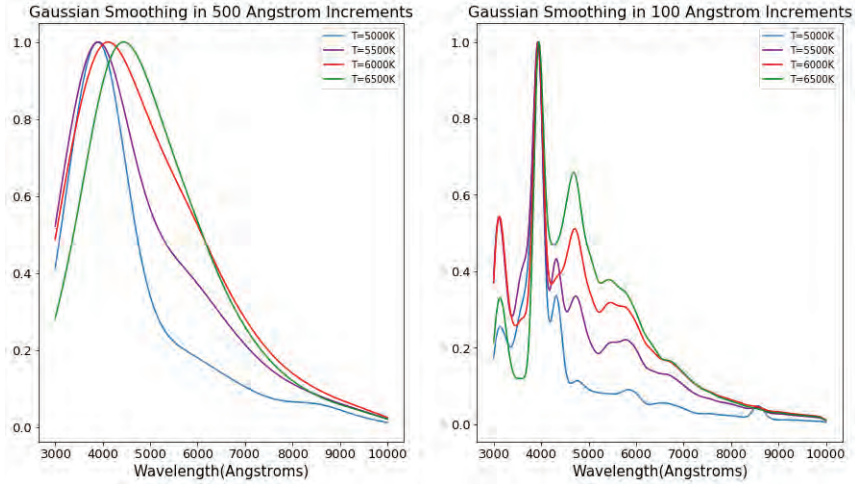


Figure 2. Gaussian Smoothing of the Variances

The second method of smoothing was integration. The result is in Figure 3. All the peaks are the same as in Figure 2. Due to the nature of Gaussian convolution, it seemed to be a better method for developing the filter response curve.

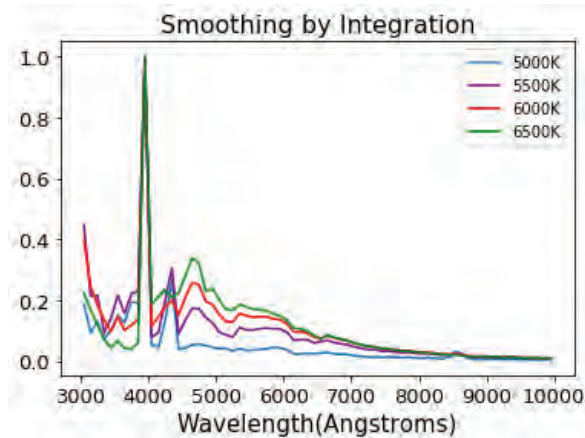


Figure 3. Smoothing by Integration

The four Gaussian convolution curves were averaged together to form one photometric response curve in Figure 4. The image on the left is a result of averaging the 500 Å increments, and the image on the right is a result of averaging the 100 Å increments. These are broad-band filters, which can be used for measure stars with low luminosities. They both are in general agreement with the previous plots. They both show a peak around the K and H lines; however, any

peaks that are missing indicates that the variance was not as great as the K and H absorption lines. These two plots may be used as photometric filter response curves for SEGUE and LAMOST.

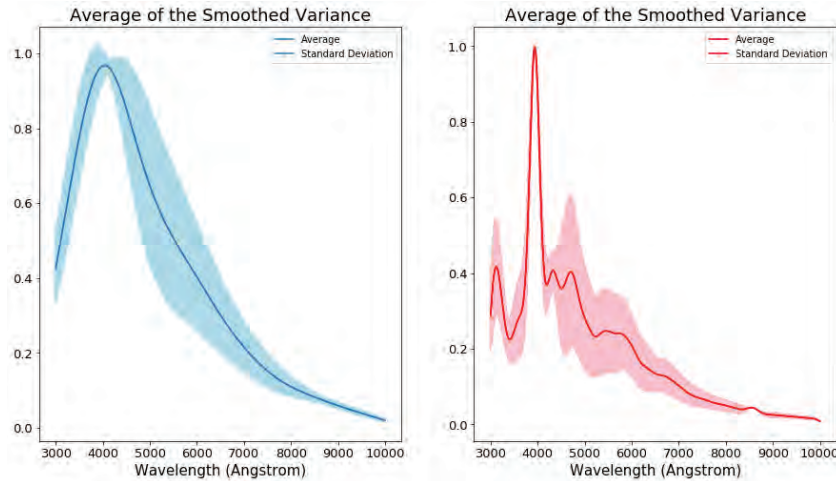


Figure 4. Average

Conclusions

In conclusion, a photometric filter response curve was developed to determine theoretical metallicity sensitivity over the optical region of the electromagnetic spectrum of stars. Eventually, this curve will be used for observed metallicity values and aid in mapping the chemical evolution of the Galaxy. In the future, these techniques could be used to determine general metallicity values of certain data.

Acknowledgements

I would like to thank the Research Experience for Undergraduates (REU) program at Notre Dame for hosting this opportunity and the National Science Foundation (NSF) for funding this program. In addition, thank you to Professor Timothy Beers for allowing me to work with his lab, and thank you to Professor Vinicius Placco and Devin Whitten for the guidance on this project.

References

1. Welsh, L., Cooke, R., & Fumagalli, M. (2019). Modelling the chemical enrichment of Population III supernovae: The origin of the metals in near-pristine gas clouds. *Monthly Notices of the Royal Astronomical Society*. doi:10.1093/mnras/stz1526
2. Yoon, J., Beers, T. C., Placco, V. M., Rasmussen, K. C., Carollo, D., He, S., Hansen, T., Roederer, I., Zeanah, J. (2016). Observational Constraints On First-Star Nucleosynthesis. I. Evidence For Multiple Progenitors Of Cemp-No Stars. *The Astrophysical Journal*, 833(1), 20. doi:10.3847/0004-637x/833/1/20
3. Beers, T. C., & Christlieb, N. (2005). The Discovery and Analysis of Very Metal-Poor Stars in the Galaxy. *Annual Review of Astronomy and Astrophysics*, 43(1), 531-580. doi:10.1146/annurev.astro.42.053102.134057
4. Whitten, D. D., Placco, V. M., Beers, T. C., Chies-Santos, A. L., Bonatto, C., Varela, J., . . . Vázquez Ramió, H. (2018). J-PLUS: Identification of low-metallicity stars with artificial neural networks using SPHINX. *Astrophysics & Astronomy*.
5. Table of Spectral Lines Used in SDSS. (n.d.). Retrieved from <http://classic.sdss.org/dr6/algorithms/linestable.html>

**Project AMIGA: Circumgalactic Gas about
Andromeda and its Dwarf Satellites**

Samantha Berek

2019 NSF/REU Program

Physics Department, University of Notre Dame

Advisors: Dr. Chris Howk, Dr. Nicolas Lehner

Abstract

Project AMIGA (Absorption Maps in the Gas of Andromeda) is the first program to characterize absorption from gas in the circumgalactic medium (CGM) of a single galaxy, in this case M31/Andromeda, against a large number of sightlines (43). We use Hubble Space Telescope spectroscopy of 43 QSOs projected within 2 virial radii of M31 collected by Project AMIGA to limit the amount of gas associated with M31's dwarf satellite galaxies. We examine absorption in SiII, SiIII, and SiIV along sightlines near 32 M31 dwarf galaxies. As part of this assessment, we develop a new methodology to identify and remove contamination from the foreground Magellanic Stream (MS), an extended, diffuse band of gas covering a large fraction of the sky, including the M31 region. The cleaned absorption line measurements reveal clear trends between the column densities of SiII, SiIII, and SiIV and projected distances from M31. Additionally, the spectra of 19 quasar sightlines at distances less than one virial radius from M31 dwarf galaxies were examined. Very little gas seen in absorption was within the escape velocity range of the nearby dwarf. Therefore, most of the absorption in Project AMIGA is not bound to dwarf satellites, but arises in the CGM of Andromeda itself.

1 Introduction

The circumgalactic medium (CGM) is the diffuse, multiphase gas surrounding galaxies within at least 1-2 virial radii. The gas making up the CGM comes from various sources, including inflows from the intergalactic medium (IGM) and outflows from the galactic disk driven by supernovae [1]. The CGM may contain a large portion of the metals present in

star-forming galaxies, and it could be the answer to the "missing baryon" problem, in which the mass of baryons observed in stars are far lower than predictions [2]. Much of the fuel for star formation is accreted from the CGM. Thus the CGM is an important driver for galaxy evolution as both the source of fuel and waste for a galaxy [2].

As its emission is exceedingly faint, the CGM is best studied in absorption. Typically, QSO sightlines that pass through the CGM of a foreground galaxy are rare, and only one or occasionally a few can be found for a single galaxy. However, the position of the Andromeda Galaxy (M31) means that there are numerous observable sightlines passing through its CGM. This allows for an unparalleled study of the CGM of an L^* galaxy that could have implications for our understanding of the role a galaxy's CGM plays in its evolution.

Project AMIGA (Absorption Maps in the Gas of Andromeda) undertook this study of the CGM of M31. So far, the study has found evidence of an extended CGM around M31 consisting of bound, multiphase gas that becomes more highly ionized at larger impact parameters [3]. This study extends the initial Project AMIGA work by characterizing the contamination of M31 absorption by the Magellanic Stream (MS), a tidal feature originating in the Magellanic Clouds and extending to this region of the sky. We used the MS-corrected data to characterize the CGM of Andromeda as well as its dwarf satellites.

2 Data

AMIGA sample: The QSO sample used in this analysis contains 43 background QSOs at projected distances up to $2R_{vir}$ and observed by the Cosmic Origins Spectrograph (COS)

on board the Hubble Space Telescope (HST). The data were collected using COS’s G130M and/or G160M gratings, and relatively low redshift quasars were chosen to reduce contamination from higher redshift absorbers. However, some of the spectra include absorption from the foreground MS. Figure 1 shows a map of the complete set of QSOs.

M31 Dwarf Galaxy Sample: The dataset of M31 dwarf galaxies is drawn from the McConnachie et al (2012) [4] study of local group dwarfs, in which the properties of 29 M31 dwarf satellites were summarized. Four additional dwarfs were added from recent discoveries [5] [6] [7] [8] [9] [10] [11]. The large galaxies M33, M32, and NGC 205 were excluded from consideration, as their large masses are not characteristic and/or their proximity to M31 is a confusing effect. Figure 1 shows positions and velocities of the dwarfs relative to M31.

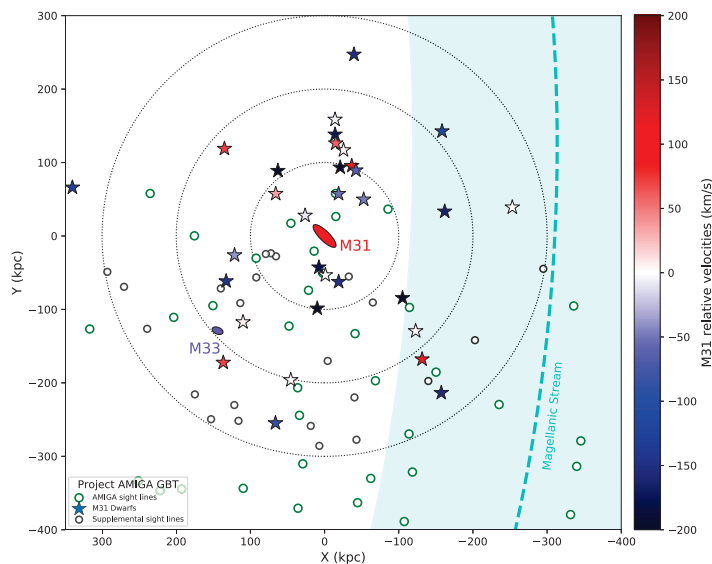


Figure 1: Projected map of the area around Andromeda with data used for this study. M31 dwarf galaxies are color coded according to their relative velocity to M31. QSO sightlines appear both from the first AMIGA study and more recent archival additions. The MS overlays almost half of the M31 area, and possible contamination exists in the area in which they overlap.

3 Removing MS Contamination

The MS is a gaseous tidal stream originating from the Magellanic Clouds and extending at least 200 degrees across the sky [12]. It cuts across the M31 system, overlapping with slightly less than half of the CGM of M31 (Figure 1 illustrates the placement of the MS with relation to M31). The extent and velocities of the MS gas are not well determined, making contamination difficult to remove. In the first AMIGA study, all sightline velocities $-430 \text{ km/s} \leq v_{LSR} \leq -300 \text{ km/s}$ were considered potential MS contamination and discarded.

Although velocities of the MS are generally similar to those expected for M31 absorption, its velocity distribution is not random. MS velocities are more negative with decreasing MS longitude (l_{MS}) [13] until $l_{MS} \approx -130$, when the trend reverses [12]. We constrained the range of possible MS velocities as a function of l_{MS} [12] using observations from Nidever et al. All velocity components that fell between the range of fits were discarded from our sample. Any remaining outliers, as seen on column density graphs, were individually examined. Those that were found to be close to the MS range of velocity and positions were flagged as possible contamination. Figure 2 shows a comparison of original and cleaned column density data for SiII.

4 Column Density of Silicon Ions

We examined column density in SiII, SiIII, and SiIV, looking for patterns in absorption throughout M31's CGM. The first AMIGA study found that, as theoretically expected, column density falls off relatively quickly with increasing impact parameter in SiII and SiIV,

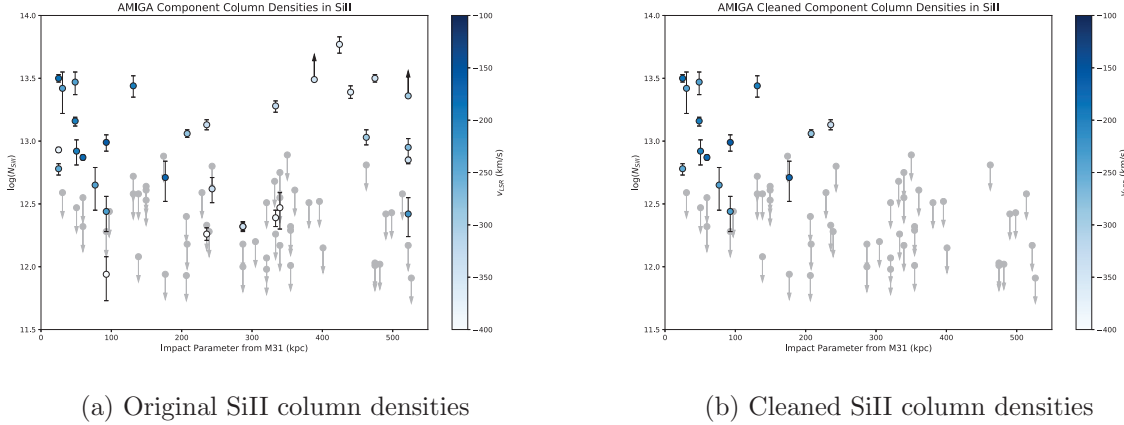


Figure 2: SiII column densities plotted as a function of impact parameter from M31 before and after being cleaned of MS contamination. Much of the noise present in the original plot is filtered out by the data cleaning process, creating a plot that was expected, with high column densities at low impact parameters and mostly non-detections at high impact parameters.

but extends to further distances in SiIII. With contamination removed, our more extensive survey confirms these previous findings to higher levels of certainty, and the presence of data between $0.2 \leq R_{vir} \leq 0.8$ allows us to understand how column densities drop off with impact parameter. Downward trends are present in both component and total column density as a function of impact parameter. As can be seen in Figure 3, SiII is found to ≈ 200 kpc from the center of M31, with all sightlines at higher impact parameters being non-detections. The total column densities of detections are as high as $\log N_{SiII} \approx 13.5$ at the lowest impact parameters, and steadily decrease to $\log N_{SiII} \approx 12.5$ near 200 kpc. SiIV can be seen out to higher impact parameters, although at lower levels, and column density doesn't decrease as steeply as it does in SiII. SiIII is detected to 500 kpc, although column densities decrease and non-detections increase at these large distances. Strong, saturated absorption is only seen at low impact parameters where gas is most dense.

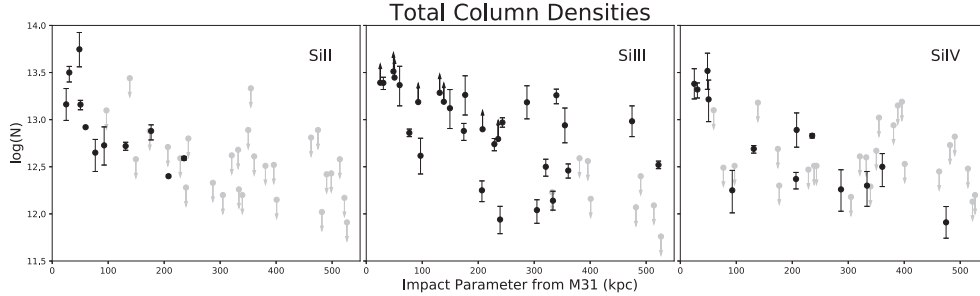


Figure 3: Total column densities of SiII, SiIII, and SiIV as a function of impact parameter from M31. Upward facing arrows indicate saturations (lower limits on the column density) for that sightline, while downward facing arrows indicate only non-detections (upper limits) for a sightline. Downward trends are obvious for all ions, although SiII cuts off fastest and SiIII slowest.

5 Searching for Absorption from Dwarf Satellites

Any gas associated with the M31 dwarf galaxies would be found nearby and with a similar M31-centric velocity as the dwarf. Our sample contains 19 sightlines-dwarf pairs that are at $\leq R_{vir}$ projection. We find 32 individual velocity components within R_{vir} and 89 within $2R_{vir}$ of satellites. As seen in Figure 4, a good number of these components fall within the escape velocity of their nearby dwarf, suggesting that some of the gas could still be bound to dwarfs. Even gas with larger relative velocities, though, could have been recently stripped from a dwarf and so no longer bound to it.

To ensure that no absorption was overlooked, we analyzed spectra projected within R_{vir} of satellites for the SiIII line at 1206.495 \AA and SiII lines at 1193.290 \AA and 1526.707 \AA . The spectra were transformed into the velocity space of the nearby dwarf so that any absorption within the escape velocity of the dwarfs could be easily seen. Figure 5 shows a representative sightline. Many of the sightlines have no observable absorption in these three lines within or near the escape velocity of the dwarf. Some absorption is further

complicated by contamination both from MC high velocity clouds (HVC's) and the MS. We characterized MW absorption as being between $-150 \text{ km/s} \leq v_{LSR} \leq 100 \text{ km/s}$ and used our MS fits to define the range of MS contamination for the position and velocity of each dwarf. Disregarding areas of contamination removed some absorption from consideration, leaving only some of the absorption that could possibly be associated with dwarfs.

A few of the sightlines did show absorption within the escape velocity of their nearby dwarf that was not contaminated by HVC's or the MS. This gas could be gravitationally bound to the dwarf or be in the process of being stripped. For dwarfs with velocities similar to M31, the absorption may be from M31's CGM instead.

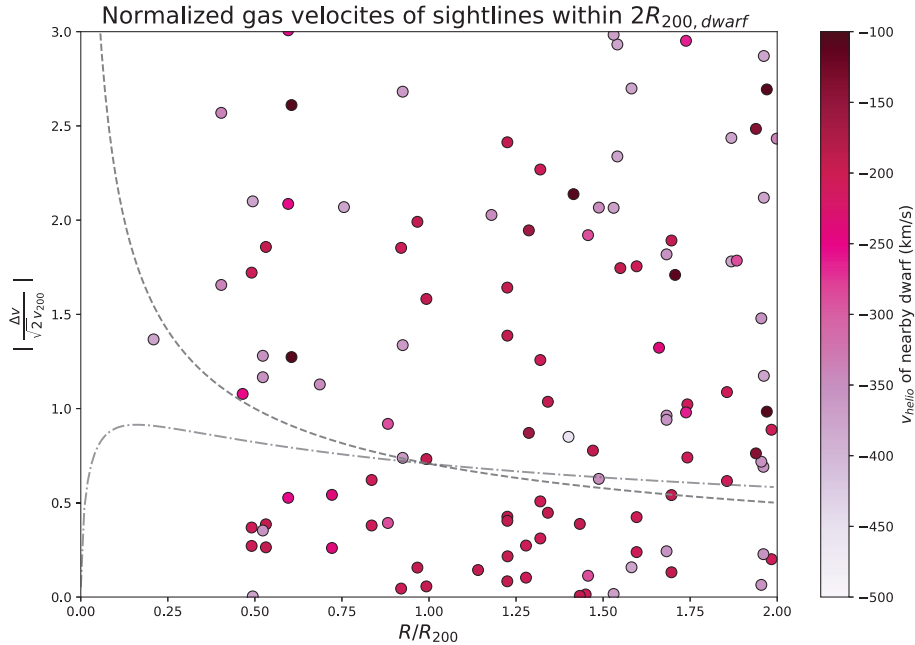


Figure 4: Sightline components within $2 R_{vir}$ of a dwarf galaxy. Velocities are normalized and plotted relative to the nearby dwarf. The dashed curve shows the normalized dwarf escape velocity as a point mass calculation, while the dotted/dashed line shows the NFW dark matter halo escape velocity curve. Sightlines are color coded based on the heliocentric velocity of their nearby dwarf.

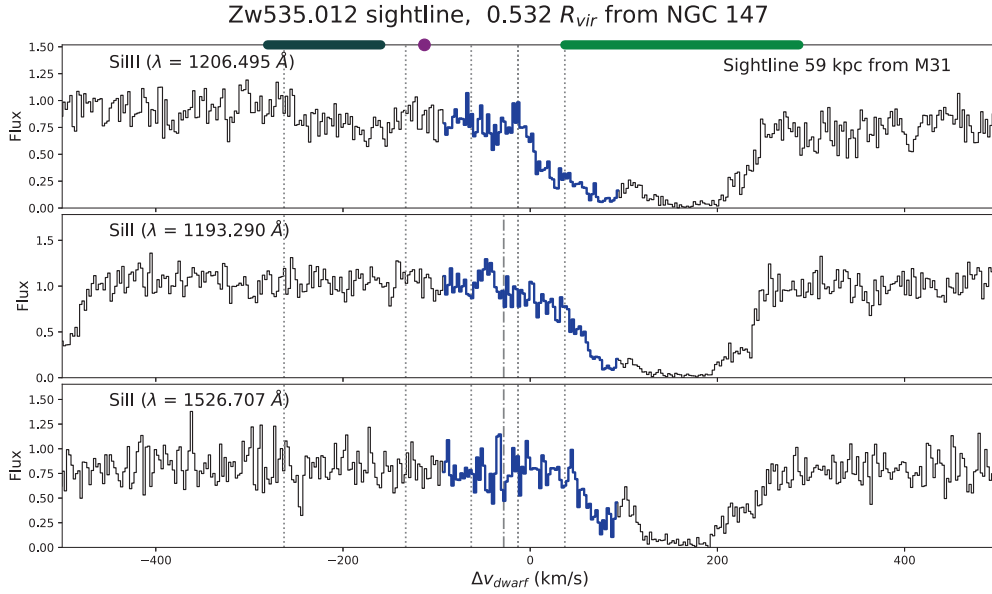


Figure 5: An example spectra showing the Zw535.012 sightline, which is $0.532 R_{vir}$ from dwarf galaxy NGC 147. The blue area of the spectra shows what is within the escape velocity of NGC 147. Colored bars along the top of the spectra show, from left to right, the area of MS contamination, the central velocity of M31, and the area of MW HVC contamination. Dotted lines show areas of flux integration, and dashed lines show central velocities of absorption components (found at the 3σ level).

Conclusions and Further Work

We have constrained the absorption of the MS to effectively remove contamination from our samples without sacrificing large percentages of the Project AMIGA data. We observe strong trends of decreasing column density with impact parameter in SiII, SiIII, and SiIV. Fits can be applied to these trends, which will allow for the estimation of the mass of the CGM. We will also use this large sample of MS contamination-free measurements to study the azimuthal structure of M31’s CGM as well. It is predicted that inflow occurs mostly along the disk plane while outflow is mostly present in vertical cones extending from the halo, but we don’t know what to expect in between these regions or if these predictions

hold up to observations.

Additionally, our MS fit can be applied to produce a clean sample of M31 dwarf galaxies. Understanding gas in these satellites will require additional limits to the sample, such as using dwarfs at large distances from M31 and with velocities dissimilar from M31 and/or the MS. This will remove some of the ambiguity of absorption seen in sightlines near dwarfs, allowing stronger conclusions to be made about any gas present within the escape velocity parameters of a dwarf.

References

- [1] M.E. Putman, J.E.G. Peek, and M.R. Joung. Gaseous Galaxy Halos. *Annual Review of Astronomy and Astrophysics*, 50:491–529, 2012.
- [2] Jason Tumlinson, Molly S. Peeples, and Jessica K. Werk. The Circumgalactic Medium. *Annual Review of Astronomy and Astrophysics*, 55:389–432, 2017.
- [3] Nicolas Lehner, J. Christopher Howk, and Bart P. Wakker. Evidence for a Massive, Extended Circumgalactic Medium around the Andromeda Galaxy. *The Astrophysical Journal*, 804(2), May 2015.
- [4] Alan W. McConnachie. The Observed Properties of Galaxies in and Around the Local Group. *The Astrophysical Journal*, 144(1), 2012.
- [5] Nicolas F. Martin, Daniel R. Weisz, Saundra M. Albers, et al. A Rogues’ Gallery of Andromeda’s Dwarf Galaxies. I. A Predominance of Red Horizontal Branches. *The Astrophysical Journal*, 850(1), 2017.
- [6] Nicolas F. Martin, Colin T. Slater, Edward F. Schlafly, et al. Lacerta I AND Cassiopeia III. Two Luminous and Distant Andromeda Satellite Dwarf Galaxies Found in the 3 PAN-STARRS1 Survey. *The Astrophysical Journal*, 772(1), 2013.
- [7] Nicolas F. Martin¹, Rodrigo A. Ibata, Geraint F. Lewis, et al. The PAndAS View of the Andromeda Satellite System. II. Detailed Properties of 23 M31 Dwarf Spheroidal Galaxies. *The Astrophysical Journal*, 833(2), 2016.
- [8] Nicolas F. Martin, Kenneth C. Chambers, Michelle L. M. Collins, et al. Spectroscopy of the Three Distant Andromedan Satellites Cassiopeia III, Lacerta I, AND Perseus I. *The Astrophysical Journal Letters*, 793(1), 2014.
- [9] Nicolas F. Martin, Edward F. Schlafly, Colin T. Slater, et al. Perseus I: A Distant Satellite Dwarf Galaxy of Andromeda. *The Astrophysical Journal Letters*, 779(1), 2013.
- [10] A. R. Conn, R. A. Ibata, G. F. Lewis, et al. A Bayesian Approach to Locating the Red Giant Branch Tip Magnitude. II. Distances to the Satellites of M31. *The Astrophysical Journal*, 758(1), 2012.
- [11] Michelle L. M. Collins, Scott C. Chapman, R. Michael Rich, et al. A Kinematic Study of the Andromeda Dwarf Spheroidal System. *The Astrophysical Journal*, 768(2), 2013.
- [12] David L. Nidever, Steven R. Majewski, W. Butler Burton, and Lou Nigra. The 200° long Magellanic Stream System. *The Astrophysical Journal*, 723(2), 2010.
- [13] David L. Nidever, Steven R. Majewski, and W. Butler Burton. The Origin of the Magellanic Stream and its Leading Arm. *The Astrophysical Journal*, 679(1), 2008.

ADAPTIVE OPTICS: PHASE UNWRAPPING

HANNAH BLUE

2019 NSF/REU Program
Physics Department, University of Notre Dame

ADVISOR: Justin Crepp

Abstract

In an effort to increase the resolution of astronomical images taken at visible wavelengths, new technologies are being developed such as the nonlinear curvature wavefront sensor (nlCWFS) which recovers phase values from recorded intensity information. However, these phase values are mathematically wrapped over each other which poses a significant problem as Adaptive Optics (AO) systems expect a continuous phase input to account for the light distortions. This paper discusses a technique that can be applied to AO systems to recover the unwrapped phase information.

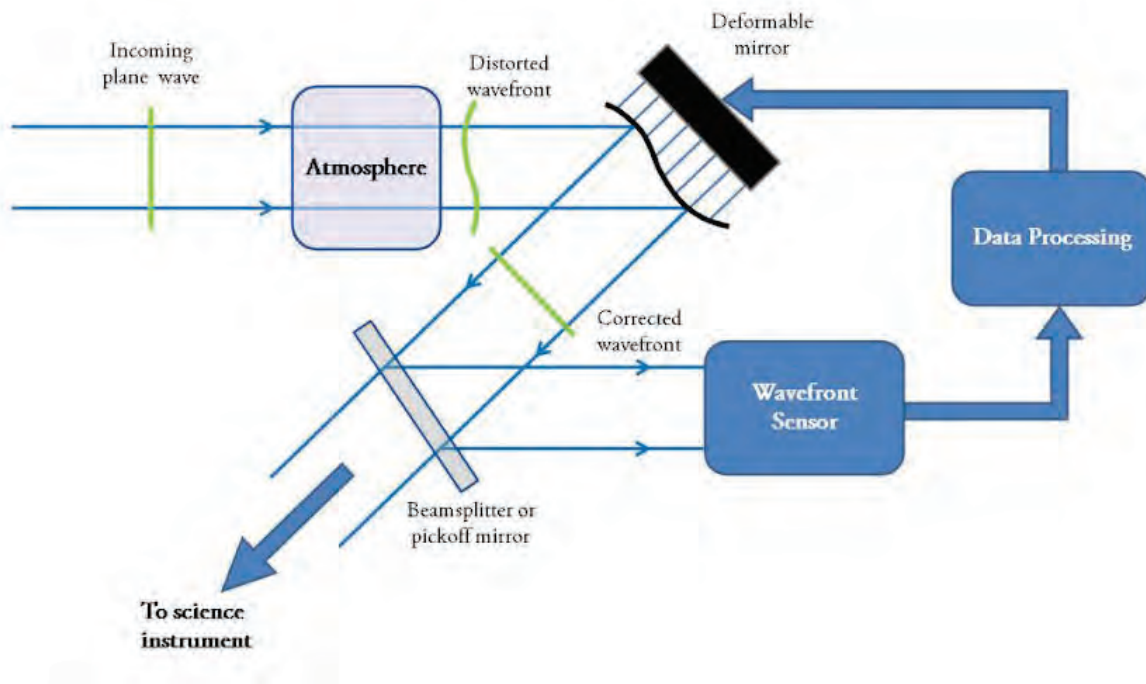
Introduction

The predominant limiting factors on the resolution of land based optical instruments are the optical elements themselves, and the atmosphere. There are always strides being made towards higher resolution and better sensitivity of observations. The current step in this ongoing development is the construction of telescopes of significantly larger size relative to current telescopes. These include the Giant Magellan Telescope, the European Extremely Large Telescope, and the Thirty Meter Telescope. All of these will provide large collecting areas and thus higher potential to provide high resolution imaging. This new wave of telescopes will have the power to revolutionize observational astronomy, but to achieve their full potential, they have to have effective atmospheric correction.

Since the 1600s, it has been known that optical waves passing through Earth's atmosphere are subjected to disturbances due to the turbulent nature of the atmosphere. Newton even predicted that the effects of these disturbances would ultimately be the limitation to optical systems for astronomy. We have many working observatories such as the Large Binocular

Telescope, Gemini, Subaru, and Keck to name a few. These are some of the most scientifically productive optical and infrared telescopes. However, the key word here is infrared. These telescopes can deliver images at infrared and near-infrared wavelengths but as the wavelengths get closer to visible light, the images get blurrier. Thus, for several science applications the required wavefront quality is still well beyond what current systems deliver [1]. Due to this, there is increasing interest in the development of new technology for effective imaging at visible wavelengths, since crisp, clear images cannot currently be produced. This comes back to the random motions of the Earth's atmosphere which essentially create an upper bound on the resolution of all large ground based telescopes. Astronomers have found two possible ways to overcome this. One way is by sending telescopes above the atmosphere as seen by the Hubble Space Telescope and the plans for its successor the James Webb Space Telescope. The second way is to correct for the effects of the atmosphere on the ground. This is where AO systems come in, which use real time correction to measure and counter the effects of the atmosphere.

AO systems rapidly counteract the effects of turbulence by measuring the phase distortions on the incoming wavefront and applying inverse phase shifts to the wave. This effectively compensates for the distortions, correcting the distorted light reaching the science detector, and thus increasing the resolution of the obtained image.



The figure above depicts a standard AO system in which distorted light with an uncorrected wavefront enters from the telescope. The light is then reflected off a deformable mirror and passed to a wavefront sensor which reconstructs the wavefront allowing the real time control system to calculate the phase distortions. The control system then instructs the deformable mirror surface to change to the appropriate shape to apply counter distortions to offset the effects of atmospheric turbulence on wavefronts [2]. At a surface level, this seems like a fairly intuitive process. However, before the phase distortions of the reconstructed wavefront can be calculated, the phenomena of phase wrapping needs to be accounted for.

The nonlinear curvature wavefront sensor (nCWFs) uses an iterative reconstruction algorithm to recover phase values from recorded intensity information. By propagating light waves between imaging planes and applying these intensity measurements, an estimate of the wavefront will converge to the actual value. When we consider the propagation of light in terms

of ‘wavefronts’ we define these wavefronts as lines of constant phase in the complex field to which the propagation of light is perpendicular. When the nCWFS is used to reconstruct the wavefront, due to their complex nature, they are represented by trig functions which mathematically limits the phase values to an interval of $-\pi$ to π . It is expected that phase values would increase linearly as the wave is propagated however, the phases end up wrapping over themselves on an interval of 2π . The wrapping of these phase values poses an obstacle in using the nCWFS as an input for wavefront correction as deformable mirrors require continuous phase values and as such, strategies must be employed to unwrap the recovered phase [3].

Methods

In order to account for the phase wrapping, an algorithm derived by Marvin A. Schofield and Yimei Zhu in their paper “Fast phase unwrapping algorithm for interferometric applications,” was tested. This algorithm was originally applied to electron holography data and is believed to be similarly stable with respect to noise when applied to other techniques that extract information from waves through interferometry, such is the case with the nCWFS. The wavefront reconstruction technique of the nCWFS must output the recovered wavefront on a similar timescale to the coherence time of the atmosphere. In order to propagate the wavefronts between planes, the nCWFS employs the use of Fourier transforms which have reasonable computational demands. The most attractive aspect of the Schofield and Zhu equations are that they can be represented in terms of Fourier Transforms and thus will not increase the reconstruction time as drastically as other methods.

In order to test the effectiveness of the phase unwrapping formula in an adaptive optics system, a simulation was created to generate a wavefront with arbitrary aberrations. This

represents the true phase that is trying to be reconstructed and in practice, this original wavefront would be unknown. The phase is then put through a function that wraps it over an interval of 2π , and then through the phase unwrapping algorithm. As mentioned before, the recovered phase numbers are limited to the interval of $-\pi$ to π which creates artificial discontinuities since the true phase can range over a larger interval. Unwrapping these discontinuities can be done by adding an appropriate integer multiple of 2π to each pixel of the wrapped phase map. First, the true, unwrapped phase $\Phi(r)$ is defined in terms of the wrapped phase $\Phi_w(r)$ such that $\Phi(r) = \Phi_w(r) + 2\pi n(r)$ where r represents the pixel position and $n(r)$ is an integer. Then, $n(r)$ can be determined by calculating the two-dimensional Laplacian of $\Phi(r) = \Phi_w(r) + 2\pi n(r)$ and solving for $n(r)$. This produces

$$n(r) = \frac{1}{2\pi} \nabla_{\perp}^{-2} [\nabla_{\perp}^2 \Phi(r) - \nabla_{\perp}^2 \Phi_w(r)], \quad (1)$$

where ∇_{\perp}^2 and ∇_{\perp}^{-2} are the forward and inverse Laplacian operators. Representing this formula in terms of these operators offers the distinct advantage of being able to solve Equation (1) with fast Fourier techniques relating to the Laplacian operators given by

$$\nabla_{\perp}^2 f(x, y) = -\frac{4\pi^2}{N^2} FFT^{-1} \{ (p^2 + q^2) FFT[f(x, y)] \} \quad (2)$$

$$\nabla_{\perp}^{-2} g(x, y) = -\frac{N^2}{4\pi^2} FFT^{-1} \left\{ \frac{FFT[g(x, y)]}{(p^2 + q^2)} \right\} \quad (3)$$

where (x, y) and (p, q) are the real-space and Fourier-space pixel coordinates, respectively, N is the number of pixels in the input image, and $FFT[...]$ is the fast Fourier transform operation.

With Eqs (2) and (3) the iterative solution for the unwrapped phase is

$$\Phi_{j+1}(x, y) = \Phi_j(x, y) + 2\pi \text{round} \left[\frac{\Phi'_j(x, y) - \Phi_j(x, y)}{2\pi} \right] \quad (4)$$

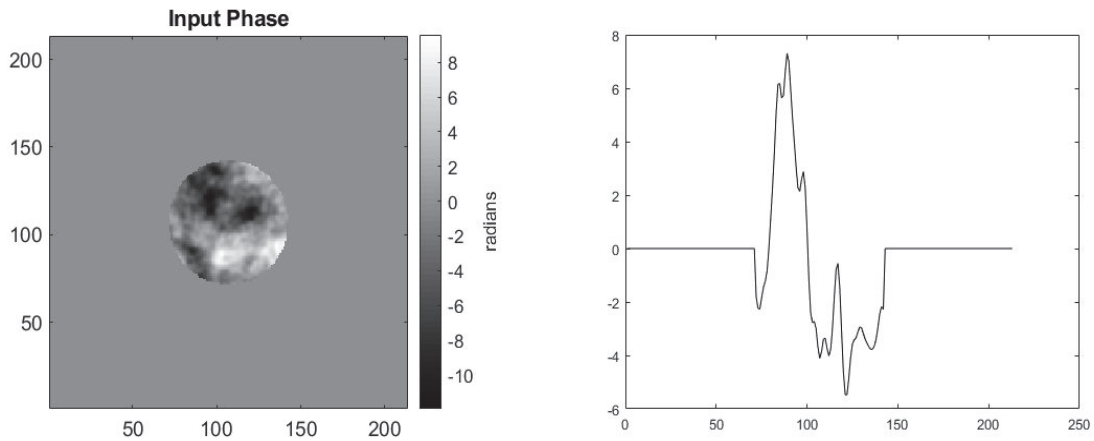
where j represents the iteration step with $j = 0$ being the original wrapped phase, $round [\dots]$ is the rounding operator, and

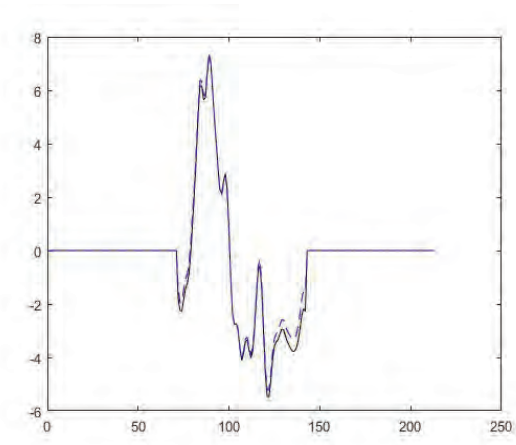
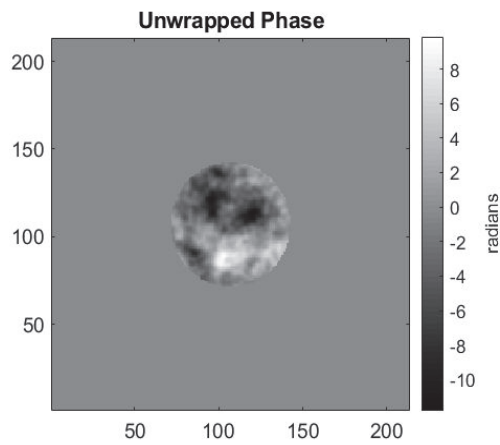
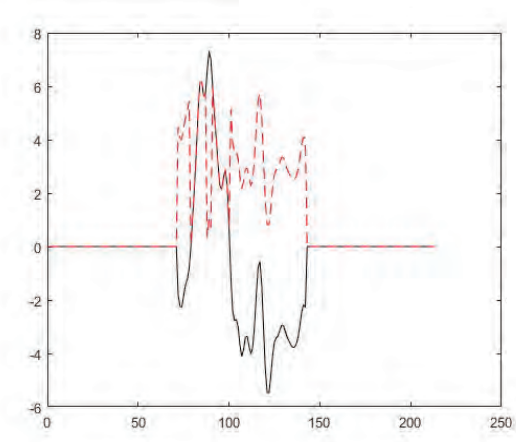
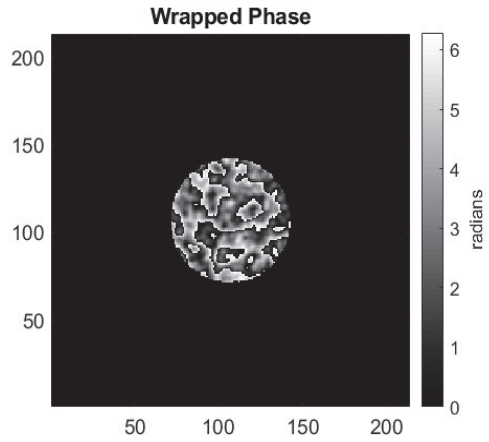
$$\Phi'(x, y) = FFT^{-1} \left(\frac{FFT\{\cos \Phi_w FFT^{-1}[(p^2+q^2)FFT(\sin \Phi_w)]\}}{(p^2+q^2)} \right) - FFT^{-1} \left(\frac{FFT\{\sin \Phi_w FFT^{-1}[(p^2+q^2)FFT(\cos \Phi_w)]\}}{(p^2+q^2)} \right)$$

The expression for $\Phi'(x, y)$ is derived from the term in Eq.(1) involving the Laplacian of the true phase and is an estimate of the true unwrapped phase. The iterations of Eq.(4) are meant to converge to $\Phi'(x, y)$ as closely as can be done by the addition of integer multiples of 2π [4].

Results

The figures below show the phase maps (left) and their corresponding phase graphs (right). The first pair of figures are the simulated true, unwrapped phase values which the Scofield and Zhu algorithm will attempt to recover. The second pair of figures are the phase values after they have been forced to wrap over an interval of 2π with the wrapped phase represented by the dashed line. The last pair of figures are the recovered phase values from the unwrapping algorithm with the recovered phase represented by the dashed line.





Conclusion

The phase unwrapping algorithm performed sufficiently well over many simulations, and only required one iteration due to $\Phi'(x, y)$ being a very close estimate to the true values. However, it is unclear how this algorithm will perform in reality and may fail to fully unwrap the phases if the wrapped data is abnormally noisy or if the wavefront aberrations are more extreme.

References

- [1] Guyon, O. (2009). High sensitivity wavefront sensing with a nonlinear curvature wave-front sensor. *Publications of the Astronomical Society of the Pacific*, 122(887), 49.
- [2] Crass, J. (2014). *The Adaptive Optics Lucky Imager: combining adaptive optics and lucky imaging* (Doctoral dissertation, University of Cambridge).
- [3] Mateen, M. (2015). *Development and verification of the non-linear curvature wavefront sensor*.
- [4] Schofield, M. (2003). *Fast phase unwrapping algorithm for interferometric applications*.

Determining the astrophysical $^{20}\text{Ne}(\alpha,p)^{23}\text{Na}$ reaction rate from measurements
with the Notre Dame 5U accelerator

Alyssa Davis

2019 NSF/REU Program

Physics Department, University of Notre Dame

Advisor: Dr. Dan Bardayan, Ph.D.

Abstract

In binary star systems including at least one white dwarf, the companion star may accrete mass onto the white dwarf until electron degeneracy pressure can no longer support the additional mass. A threshold is surpassed at high accretion rates, causing a stellar explosion categorized as a type Ia supernova. The system undergoes nucleosynthesis throughout the mass transfer and supernova process, producing heavier elements. Uncertainties in the $^{20}\text{Ne}(\alpha,p)^{23}\text{Na}$ reaction rate have been shown to significantly affect the final abundances of a number of nuclei produced in type Ia supernovae. Although previous inverse kinematic measurements have been conducted to model this reaction rate, the explored beam energies were not of astrophysical significance. Utilizing the 5U vertical pelletron accelerator and the Rhinoceros extended gas target at the University of Notre Dame, new direct kinematic cross section measurements were conducted using beam energies as low as 3.5 MeV. Theory, experimental methods, preliminary results, and future analysis plans will be discussed.

This work is supported by the US National Science Foundation PHY-1713857.

1 Introduction

This summer, we conducted a cross section study of the $^{20}\text{Ne}(\alpha,p)^{23}\text{Na}$ reaction using forward kinematic techniques. We used the 5U vertical pelletron accelerator to focus an alpha beam onto a differentially pumped, recirculating, windowless gas target named Rhino containing ^{20}Ne . Ruggedized silicon detectors were placed on Rhino at discrete angles in order to measure the ground and excited state energies of the protons ejected from collision.

2 Astrophysical Theory

A white dwarf is a collapsed core of a low mass star. It is kept in equilibrium through the balancing of gravitational and electron degeneracy pressure. When a white dwarf is a part of a binary system, the companion star may accrete mass onto the white dwarf. This added mass changes the original equilibrium state of the white dwarf, and the added gravitational pressure increases the internal temperature of the star. Normally, stars expand and contract in response to temperature changes. However, white dwarfs cannot expand to compensate for temperature increases, so instead the surface temperature allows for the facilitation of exothermic nuclear reactions. This presents the problem of a runaway temperature increase, resulting in a stellar explosion characterized by a Type Ia supernova.

3 Nuclear Theory

3.1 Cross Section and Reaction Rate Calculations

The cross section is defined as the probability of a given reaction occurring. In order to correctly estimate a cross section, it is important to take both classical and quantum effects into account. From the classical perspective, the cross section model is more geometric in nature. It is defined by calculating the probability of two nuclei colliding with each other,

$$\sigma = \pi(R_A + R_a)^2. \tag{1}$$

We can see clear dependence on R_A and R_a , which are the nucleus radii of the target and projectile particles, respectively. An added complexity is introduced once we account for the wavelike nature of the particles involved in collision by including the deBroglie wavelength λ . The modified cross section equation becomes

$$\sigma = \pi\lambda^2 = \pi \frac{m_a + m_A}{m_A} \frac{\hbar^2}{(2m_a E)^{1/2}}. \quad (2)$$

It is important to note the new cross section's dependence on the lab energy, E . If we integrate the cross section across a certain energy range and include necessary proportionality constants, we are able to model the reaction rate,

$$r = \sqrt{\frac{8}{\pi\mu}} (kT)^{-\frac{3}{2}} \int_0^\infty \sigma E e^{-\frac{E}{kT}} dE, \quad (3)$$

where

$$E = \frac{1}{2}\mu v^2, \quad (4)$$

in which μ is the reduced mass and v is the relative velocity due to the stellar environment being described [1].

4 Previous Experiments

Many reactions take place during the mass transfer and supernova process. A sensitivity study was previously performed by Parikh et. al. to monitor the reactions that have a heavy influence on the final abundances of nuclei after type Ia supernovae. It was found that the reaction rates of the $^{12}\text{C}(\alpha, \gamma)$, $^{12}\text{C} + ^{12}\text{C}$, $^{20}\text{Ne}(\alpha, p)$, $^{20}\text{Ne}(\alpha, \gamma)$, and $^{30}\text{Si}(p, \gamma)$ reactions have the greatest effect on element production [2].

There is uncertainty regarding the $^{20}\text{Ne}(\alpha, p)$ reaction rate at astrophysically relevant energies, despite the reaction being notably modeled twice with varying experimental setups. In 1968, the experiment was first conducted using a tandem accelerator at the Australian National University. A forward kinematic technique was used; a beam comprised of alpha particles was accelerated and directed toward a ^{20}Ne target. The explored beam energies ranged between 3.96 MeV and 5.25 MeV, but the cross section was not measured in the experiment. Instead, the research group measured the number of reactions occurring as a function of incident beam particles. This was done by detecting the gamma rays emitted from the excited state of ^{23}Na . Because of this, they only recorded information about the first excited state proton energy, p1, but nothing about the ground state proton energy, p0 [3]. The second experiment was conducted at Argonne National Lab using the Helical Orbit Spectrometer (HELIOS). An inverse kinematic technique was used, in which a ^{20}Ne beam was accelerated toward a helium target. The explored beam energies were within the range of 30 MeV to 100 MeV, which is much higher than any astrophysically significant energy range [4].

5 Experimental Apparatus and Methods

5.1 Notre Dame's 5U Accelerator

Figure 1 displays a schematic of the 5U vertical pelletron accelerator used to accelerate our alpha beam. This accelerator used an electron cyclotron resonance (ECR) source to produce ions that accelerate the beam. A series of magnets and analyzing devices were used

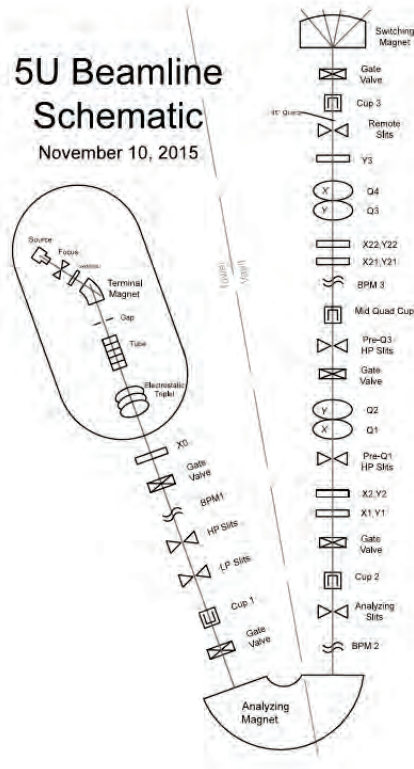


Figure 1: Schematic of 5U vertical pelletron accelerator used in the $^{20}\text{Ne}(\alpha, p)^{23}\text{Na}$ experiment.

to focus, shape, and purify the helium beam created. Several Faraday cups were utilized to record the current at multiple locations in the beamline [1].

5.2 Rhino Gas Target and Silicon Detectors

Figure 2 displays the Rhino gas target with silicon detectors mounted at discrete angles. This gas target has two special characteristics: it is recirculating and differentially pumped. Recirculation of gas through the multiple-aperture system allows us to use less gas for the experiment and constantly have fresh ^{20}Ne gas in our target. Differential pumping prevents the high pressure in the target chamber from leaking up the near vacuum beamline.

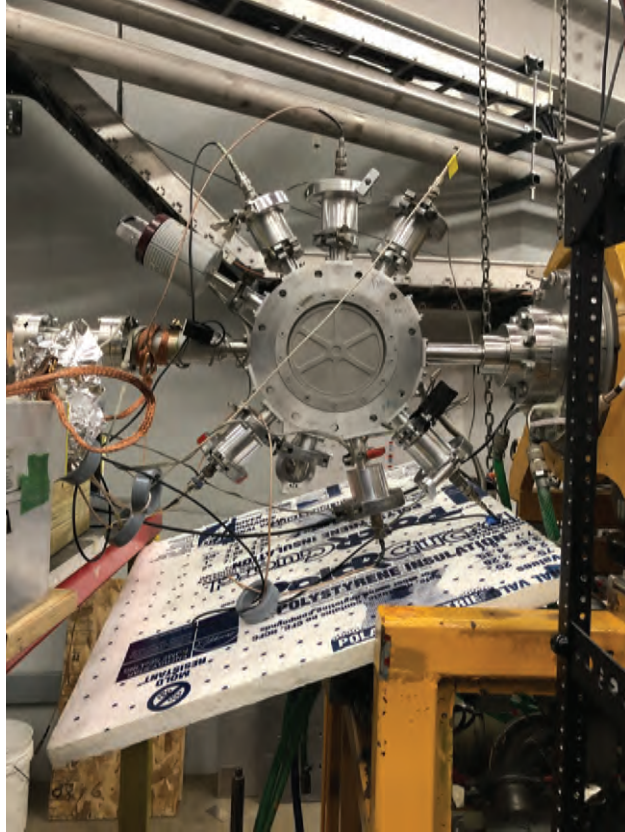


Figure 2: Rhino: the recirculating, differentially pumped, windowless gas target. Ruggedized silicon detectors are mounted at discrete angles to detect ejected protons.

In order to reduce the contamination in our gas target, we utilized a cold trap full of liquid nitrogen to freeze out any contaminants. We also used Rutherford scattering cross section estimations to find the ideal detector collimation arrangement, optimizing the count rate and effective target length seen by each detector angle. As for the silicon detectors, both light isolation and ambient light tests were previously conducted to ensure that background noise, such as fluorescence of the neon gas, would not overwhelm the count rate.

5.3 Data Acquisition System/Run Plan

An adaptive step size plan was utilized to determine the energy steps in between runs. If there was no detectable resonance, the energy would be stepped down by 20 keV. If a resonance was detected, the operator would decrease the energy step size to 10 keV. In order to normalize our data, two minute charge integration runs were measured before and after each data acquisition run by a Faraday cup at the end of the beamline.

6 Preliminary Results

Figure 3 displays two energy spectra as seen from the 90 and 120 degree silicon detectors. We can clearly see 4 peaks. From left to right in each image, the peaks represent p1 and p0 proton energies, and ^{20}Ne and ^{22}Ne alpha scattering.

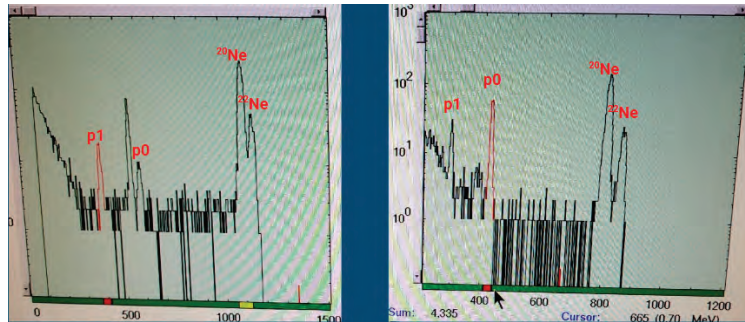


Figure 3: Two energy spectra from the silicon detectors during a data acquisition run. The left spectrum is from a detector oriented at 90 degrees, and the right spectrum is from a detector oriented at 120 degrees. We are able to see clear peaks representing the p0 and p1 proton energies and alpha scattering off of ^{20}Ne and ^{22}Ne .

Figure 4 displays preliminary yield calculations for the ground and first excited proton

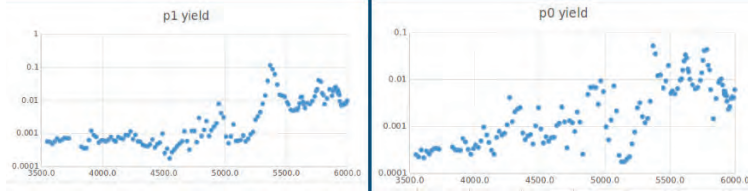


Figure 4: Preliminary yield calculations for both p1 and p0 proton energies. Expected resonances are visible.

energies detected. The peaks seen are classified as resonances; they denote an energy at which the reaction is more likely to occur.

7 Future Analysis Techniques

In the coming months, the charge integration runs conducted before and after each data acquisition run will be used to normalize our detector data and extract a more exact cross section measurement. Finally, R-matrix analysis will be conducted to further characterize the cross section.

8 Conclusion

We successfully conducted the experimental component of the $^{20}\text{Ne}(\alpha,p)^{23}\text{Na}$ cross section study. In the future, the cross section will be further characterized through normalization and R-matrix analysis.

References

- [1] Lyons, “ $^{20}\text{Ne}(p,)^{21}\text{Na}$ cross section study with the 5u accelerator,” 2016.
- [2] Parikh, “The effects of variations in nuclear interactions on nucleosynthesis in thermonuclear supernovae,” 2013.
- [3] Spear, “Gamma radiation from the reactions $^{20}\text{Ne}(\alpha, \alpha \text{ g}1.63)^{20}\text{Ne}$ and $^{20}\text{Ne}(\alpha, \text{p g}0.44)^{23}\text{Na}$,”
- [4] J. Lai, “A direct study of $^{20}\text{Ne}(\alpha, \text{p})^{23}\text{Na}$ with the helical orbit spectrometer (helios),” 2016.

**Characterization of CeBr₃ Scintillation Detectors for
use in Coincidence Measurements.**

Jack D. Enright

2019 REU Program

Department of Physics

University of Notre Dame

Supervisors: Wanpeng Tan and Ani Aprahamian

Abstract

Coincidence measurements play an important role in nuclear experiments. The advantages of CeBr_3 scintillation detectors over the more commonly used LaBr_3 and HPGe detectors in the detection of gamma-rays such as in $^{12}\text{C}+^{12}\text{C}$ measurements is shown. The coincidence technique is required for the carbon fusion reaction in order to measure its cross section at energies well below the Coulomb barrier. The usefulness of CeBr_3 scintillation detectors for the most important energies of astrophysical $^{12}\text{C}+^{12}\text{C}$ fusion processes ($1 - 3 \text{ MeV}$ in the center of mass) is discussed. The results of a gamma-gamma coincidence set-up for ^{60}Co including two CeBr_3 scintillation detectors from Berkeley Nucleonics are reported. The results of a gamma-neutron coincidence experiment for ^{252}Cf using the aforementioned CeBr_3 detectors alongside lithium glass and liquid scintillators are shown also.

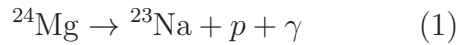
1 Introduction

Low intensity gamma-ray spectroscopy has been a focus of late due to the ever advancing research into the area of $^{12}\text{C}+^{12}\text{C}$ reactions. It is due to these advancements that new scintillation materials have become commercially available such as CeBr_3 which rival commonly used materials such as LaBr_3 and HPGe . The remarkably reduced intrinsic ac-

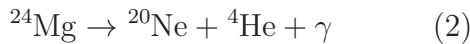
tivity of CeBr_3 relative to LaBr_3 results in gamma-ray detection sensitivity about 1 order of magnitude greater in the energy range of $1.461 \text{ MeV} - 2.615 \text{ MeV}$.^[1]

Carbon-burning is an astrophysical nuclear reaction which occurs in stars with mass $\geq 8M_{\odot}$. At this critical mass and at a certain depth below the surface (carbon-burning layer), the gravitational force, temperature and density becomes strong enough to over-

come the large repulsive Coulomb forces inflicted on the $^{12}_6\text{C}$ nuclei by each other. The reactions of most relevance with respect to coincidence measurements are the p_1 reaction (emission of a proton to the first excited state in ^{23}Na which is then followed by the 440 keV γ transition to the ground state):



and the α_1 transition (emission of alpha particles to the first excited state in ^{20}Ne which is then followed by the 1634 keV γ transition to the ground state):



However, it should be noted that this range has proven difficult to measure in the past due to the reduction of the cross section from the Coulomb barrier. Early efforts that were experimentally made following the observation of resonances in carbon fusion are direct, one time measurements for detection of gamma-rays or charged particles. This

method suffers background issues at the astrophysically relevant energies due to rapidly declining cross section.

The two radioactive samples used in this experiment were ^{60}Co and ^{252}Cf . The decay scheme of ^{60}Co is shown in figure 1.

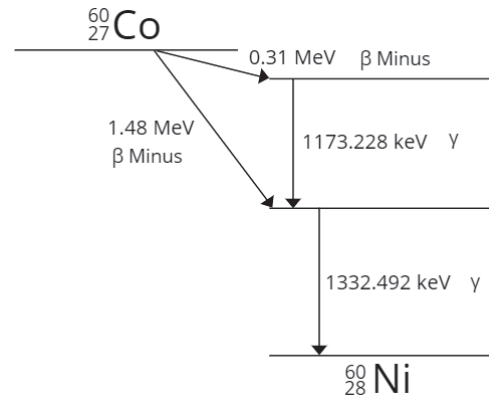


Figure 1: Decay Scheme of ^{60}Co

The most important decay is the 0.31 MeV β^- decay followed by the cascade of gamma-ray emissions with energies shown in the diagram. This allows coincidence measurements to be done in the gamma-gamma set-up in part one. The decay scheme of ^{252}Cf is shown in figure 2.

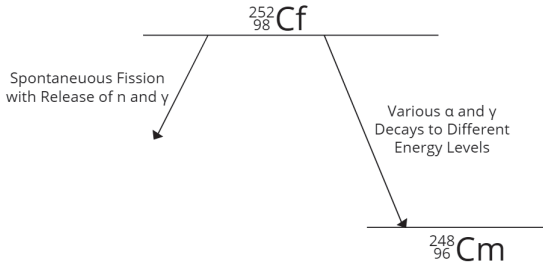


Figure 2: Decay Scheme of ^{252}Cf

Due to the nature of this experiment, the most important decay process is spontaneous fission as it emits the neutron and gamma-ray necessary to perform the coincidence measurements for part two. However, only $\sim 3\%$ of decays happen in this fashion.

2 Equipment

The CeBr_3 detectors used in this study were designed by Berkeley Nucleonics and is the 51B51/2M-CEBR-LB-E2-X-NEG model. A schematic of this model can be seen in figure 3. One detector required a bias voltage of -670V and the other required a bias voltage of -750V as stated by Berkeley Nucleonics.

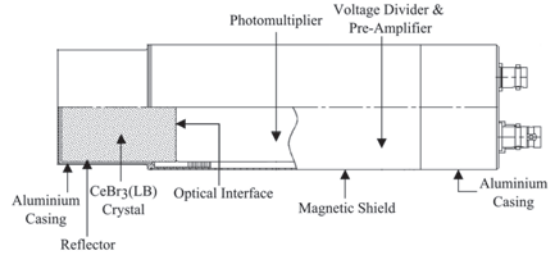


Figure 3: Schematic of the CeBr_3 Scintillator^[2]

This model contains a photomultiplier (PMT) from Hamamatsu. It is the model R6231-100-01. The data acquisition system used was designed by Mesytec. It is the MDPP-16. It is a fast, high resolution time and amplitude digitizer. It is internally realized as a 16 channel adjustable low noise amplifier and a variable differentiation stage, followed by filters and 80 MHz sampling ADCs. The digitized data are analyzed in an FPGA and reconstructed.

The liquid and lithium glass neutron scintillators were both designed and constructed by Bicron.

3 Method

Part 1: γ - γ Coincidence Measurements

The apparatus was set up as shown in figure 4.

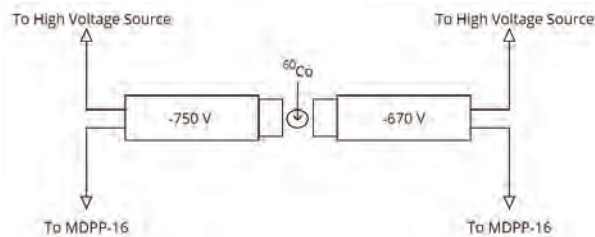


Figure 4: Diagram of Apparatus for γ - γ

The data acquisition system was set running for 10 minutes. The corresponding file was converted to a ROOT file and analyzed through ROOT. The timing difference was then plotted in ROOT which resulted in a plot as seen in figure 5. Channel width was then converted to time. Note: Each channel number increment is equivalent to 24 ps. This remains constant throughout the paper.

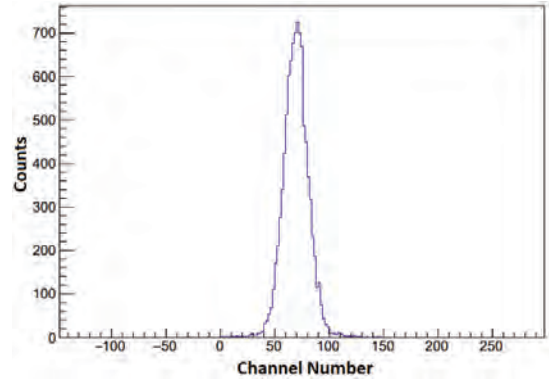


Figure 5: Timing Difference Between CeBr₃ Detectors

Part 2: γ - n Coincidence Measurements

CeBr₃ scintillators are not efficient when it comes to neutron detection. For this reason lithium glass and liquid scintillators were added to the set up above. Also, the ⁶⁰Co sample was replaced by a sample of ²⁵²Cf as it is a commonly used gamma-neutron source.

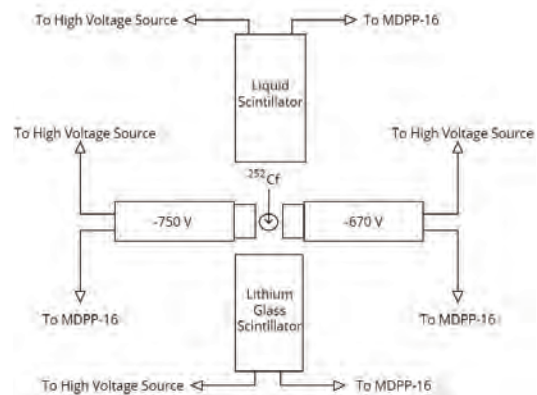


Figure 6: Diagram of Apparatus for γ - n

The data acquisition system was set running for 10 minutes. The corresponding file was converted to a ROOT file and analyzed through ROOT. The timing difference for both the CeBr₃ detectors against each of neutron detectors was then plotted in ROOT which resulted in a plot as seen in figures 7 and 8. Channel width was then converted to time.

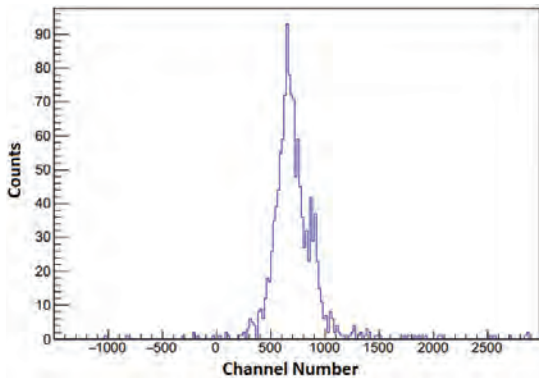


Figure 7: Timing Difference between CeBr₃ and Liquid Scintillators

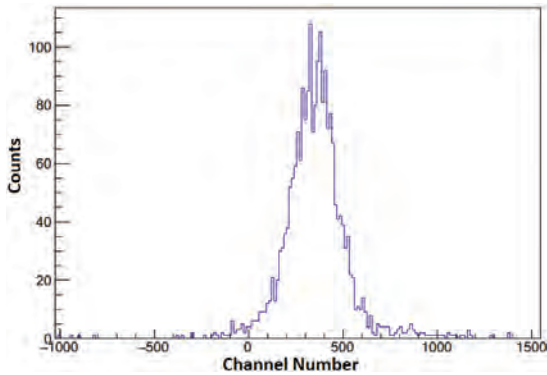


Figure 8: Timing Difference between CeBr₃ and Lithium Glass Scintillators

4 Analysis & Results

Part 1: γ - γ Coincidence Measurements

The energy resolution for each of the gamma peaks from ⁶⁰Co was found and the results for each individual CeBr₃ detector can be seen in tables 1 and 2.

⁶⁰ Co Energy	Energy Resolution
1173.228keV	$33.2 \pm 0.1keV$
1332.492keV	$32.5 \pm 0.1keV$

Table 1: -750 V CeBr₃ Scintillator Results

⁶⁰ Co Energy	Energy Resolution
1173.228 keV	$32.4 \pm 0.1 keV$
1332.492 keV	$33.6 \pm 0.1 keV$

Table 2: -670 V CeBr₃ Scintillator Results

The 10 minute data acquisition period with a sample of ⁶⁰Co resulted in spectra which could be analyzed in order to see the timing and efficiency of the CeBr₃ set-up for γ - γ coincidence. Due to the cascading nature of gamma-rays emitted in the decay of ⁶⁰Co to ⁶⁰Ni (see figure 1), gates had to be placed on opposite gamma-ray energies for each detector. From this it is possible to analyze whether two gamma-rays are emitted from the same decay. Gating refers to program-

ming in ROOT to tell the software to only consider values between certain ranges. This can be seen in figure 9. This is a visual representation of what is meant by gating. The data in the clear section of the plot is kept in the analysis. However, the shaded data is removed.

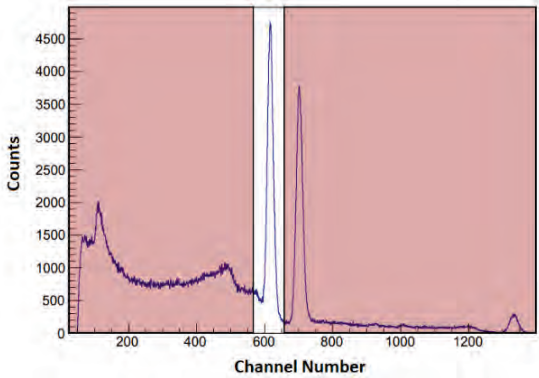


Figure 9: Gating of a ^{60}Co Peak

One detector was gated on one peak and the other was gated on the other peak. From this the timing resolution was found to be 0.616 ± 0.005 ns.

Part 2: γ -n Coincidence Measurements

The 10 minute data acquisition period for the sample of ^{252}Cf resulted in various boundary conditions which could be imposed on data via ROOT in order to see the effect of these boundary conditions on the measured

$FWHM$.

First, the liquid detector was analyzed with the CeBr_3 scintillators. The time difference between -750 V CeBr_3 and the liquid scintillator was calculated using ROOT and the resulting implications of the various data gates on the $FWHM$ can be seen in table 3.

For some visual representation of what these gates represent:

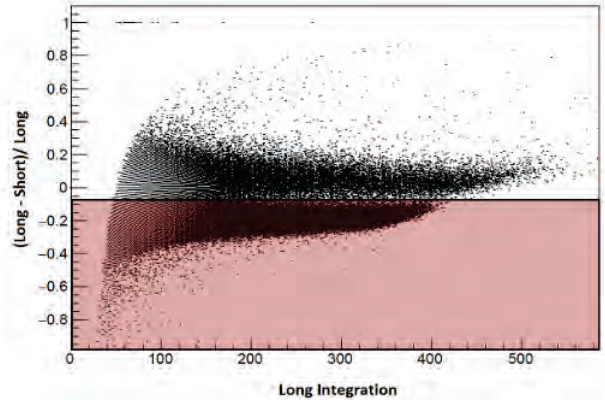


Figure 10: PSD Gate 1

Due to the receptivity of the liquid scintillator to both neutrons and gamma-rays, a pulse shape discrimination diagram (PSD) is used in order to differentiate which pulse is caused by which particle. Due to neutrons having a larger decay time in detectors than

photons, it thus becomes possible to differentiate them when it comes to a PSD diagram. The white-area in figure 10 represents all the neutrons which caused reactions in the detector.

Gate Condition	σ	
	Channel Width	Time (<i>ns</i>)
PSD 1 Gated	40.66 ± 0.34	2.30 ± 0.02
PSD 2 Gated	31.15 ± 0.56	1.77 ± 0.03
PSD 2 & Gamma Gated	Counts too low	

Table 3: -750 V CeBr₃ Scintillator Results

Gate Condition	σ	
	Channel Width	Time (<i>ns</i>)
PSD 1 Gated	39.97 ± 0.27	2.26 ± 0.02
PSD 2 Gated	31.15 ± 0.56	1.76 ± 0.03
PSD 2 & Gamma Gated	Counts too low	

Table 4: -670 V CeBr₃ Scintillator Results

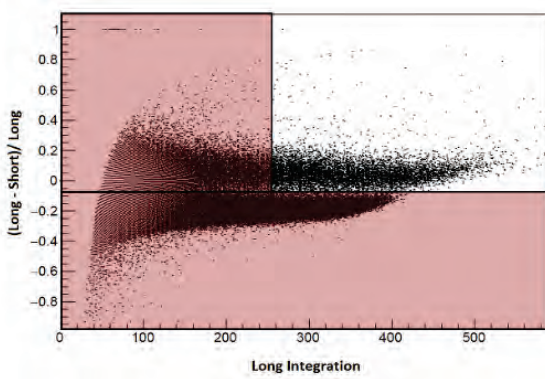


Figure 11: PSD Gate 2

The neutrons towards the start of long integration axis are caused by background noise. Therefore another gate is applied to removed them from the data as seen in figure 11.

This process was repeated for the -670 V CeBr₃ scintillator and the results are shown in table 4.

For the next section of the analysis, the liquid scintillator was replaced by a lithium glass scintillator and more gates were placed on the data in order to analyze the efficiency of this scintillator along side the CeBr₃ scintillators with respect to a coincidence set-up. A different gate was placed on this set-up due to the fact that lithium glass scintillators are not as perceptive to gamma-rays as liquid scintillators. The results of this gate can be seen in tables 5 and 6 for both CeBr₃ scintillators. For some visual representation of the gate see figure 12:

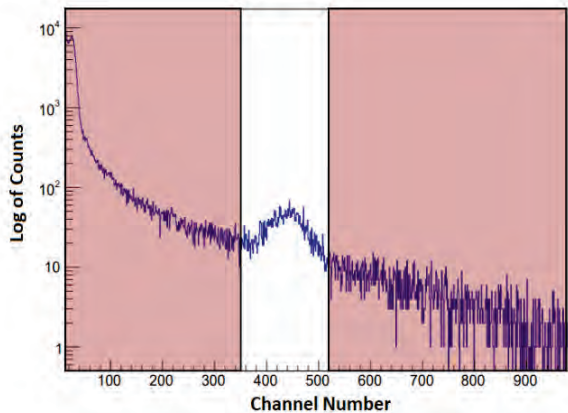
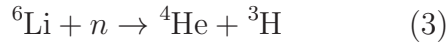


Figure 12: Neutron Bump Gate

Figure 12 represents the gate that was used to eliminate all background noise and other neutron pulses besides the neutrons caused by the reaction below:



Gate Condition	σ	<i>FWHM</i>
	Channel Width	Time (<i>ns</i>)
Neutron Bump Gate	148 ± 18.9	8 ± 1

Table 5: -750 V CeBr₃ Scintillator Results

Gate Condition	σ	<i>FWHM</i>
	Channel Width	Time (<i>ns</i>)
Neutron Bump Gate	158.9 ± 14.3	9.0 ± 0.8

Table 6: -670 V CeBr₃ Scintillator Results

5 Conclusion

With regards to energy resolution, LaBr and CeBr₃ prove to be similar and quite larger

than HPGe. However, this is expected as HPGe crystals are more commonly used if the goal of an experiment relies on the energy resolution of the detector to be small.

The timing of the CeBr₃ detectors are significantly smaller at 0.616 ± 0.005 ns compared to HPGe which can range from tens of nanoseconds to 100 nanoseconds for larger crystals. It is thus shown that CeBr₃ is the best possible compromise between HPGe and LaBr when it comes to ${}^{12}\text{C}+{}^{12}\text{C}$ fusion processes due to the increased sensitivity of CeBr₃ detectors at astrophysically important energies over LaBr detectors, alongside its largely increased timing ability over HPGe detectors.

The liquid scintillator is intended to measure fast neutrons and the lithium glass scintillator is intended to measure slow neutrons. As a result the variation in the speeds of the neutrons can vary the timing peak significantly. The general performance of the lithium glass scintillator in the gamma-neutron coincidence set-up is poor relative

to the performance of the liquid scintillator. This is due to the broadening caused by the variation in neutron speeds as mentioned above. The results for the gamma-neutron set-up with the liquid scintillator tend to be in the range of around $1 - 2 \text{ ns}$ as the liquid scintillator is more perceptive to fast neutrons. However, the results are in the range of $8 - 9 \text{ ns}$ for the lithium glass scintillator which is more perceptive to slow neutrons.

Future work would include testing a charged particle-gamma coincidence set-up. This set-

up would include a silicon detector alongside the CeBr_3 detectors. Timing efficiency with regards to the use of silicon detectors is usually within the range of a few nanoseconds.

6 Acknowledgements

I would like to thank Dr. Wanpeng Tan for his consistent support through-out my REU experience. I would also like to acknowledge Professor Ani Aprahamian and Bryce Frenz for their help as well as The Naughton Foundation for funding my REU experience.

7 References

1. F.G.A Quarati - Nuclear Instruments and Methods in Physics Research, 2013.
2. Berkeley Nucleonics Corporation

Reducing the uncertainty of the white dwarf spin-down rate in AR Scorpii

Yadira S. Gaibor

2019 NSF/REU Program
Physics Department, University of Notre Dame

ADVISORS:

Peter Garnavich

Colin Littlefield

Abstract

AR Scorpii is a binary system consisting of a low-mass star and a white dwarf. From previous observations, we know that the system has a 3.56-hour orbital period, and a brightness beat pulse period of 1.97 minutes related to the spin of the magnetized white dwarf. We analyze photometry data of AR Scorpii from the South African Astronomical Observatory (SAAO) and the Sarah L. Krizmanich Telescope (SLKT) over the span of 5 years. Our main goal was to obtain an improved estimate of the white dwarf spin-down rate, and compare it to that of Stiller et al. (2018). We found the beat frequency derivative of SAAO to be $-5.137(25) \times 10^{-17} \text{ Hz s}^{-1}$. A re-analysis of the SLKT data with additional observations from the 2019 season provides a value of $-4.98(17) \times 10^{-17} \text{ Hz s}^{-1}$.

Introduction

AR Sco is an asynchronous binary system that can be recognized by its periodic bursts in brightness every 1.97 minutes, and orbital period of 3.56 hours. The system emits light over a broad range, from radio to soft X-rays. In the absence of accretion signs, it has been suggested that this variation in luminosity is due to the spin of the magnetic WD in the system (Marsh et al., 2016). Previous studies have termed AR Sco a white dwarf pulsar, due to the strong linearly polarized pulses that are consistent with synchrotron radiation. (Buckley et al. 2016).

The spin-down rate has been measured and contested before. The latest study by Stiller et al. (2018) suggests that such a term should be considered when calculating the beat ephemeris and further confirms that the WD spin can power the observed emission. The purpose of our study is to use a broader baseline of observations and calculate a spin-down ephemeris. We individually

process and analyze SAAO data ranging from 2015 to 2019, and SLKT data from 2016 to 2019. We can then compare it with previous findings and attempt to reduce uncertainties in the value of this rate of change.

Method

The first step for processing data is running a 5 point median filter, then sigma clipping bad points. In particular, the SAAO data had a large number of deviant points that needed to be identified and removed using this method. To find the brightness peaks, we iteratively create a window of ~ 55.3 seconds around the predicted peaks, based on the Stiller et.al 2018 ephemeris (Fig.1). Then we fit a gaussian function to the points and find the mean time of the peak. We find the corresponding phase by using the Marsh et al (2016) orbital ephemeris.

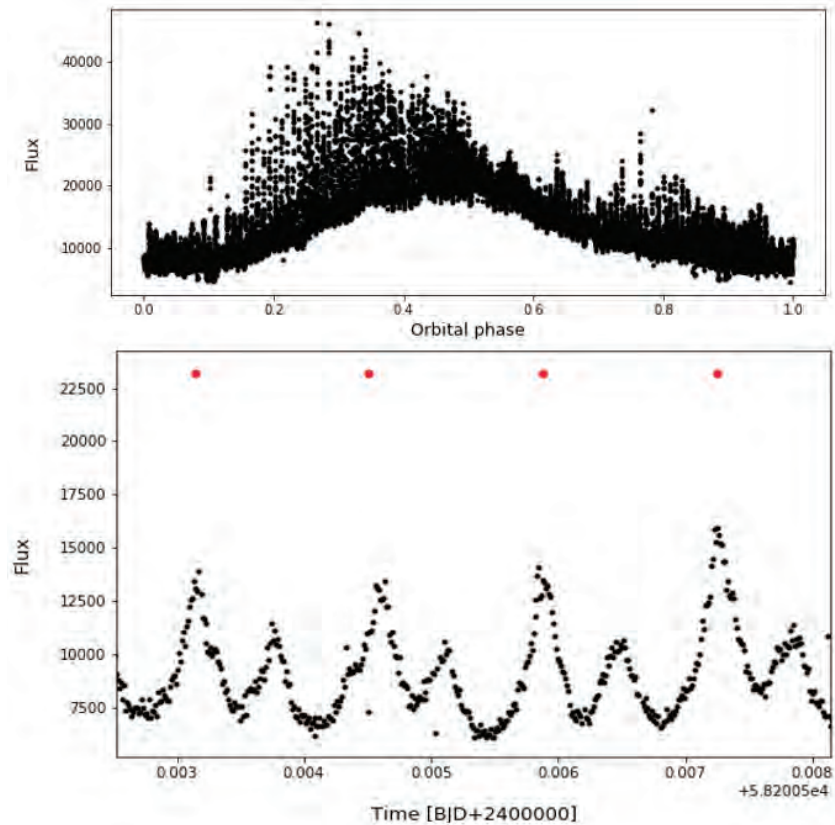


Figure 1. Top: SAAO 2018 lightcurve over one orbit. Bottom: Section of lightcurve showing predicted beat peaks (red markers). Note that there are secondary beat pulses between the main pulses.

Once we have all the beat timings, we plot an O-C diagram where orbital modulation can be seen. In order to correct for this effect, we fit a Fourier Series to this data as seen in Figure 2. Then, we subtract the fit from the original timings, and the O-C diagram should oscillate around zero (Fig.3).

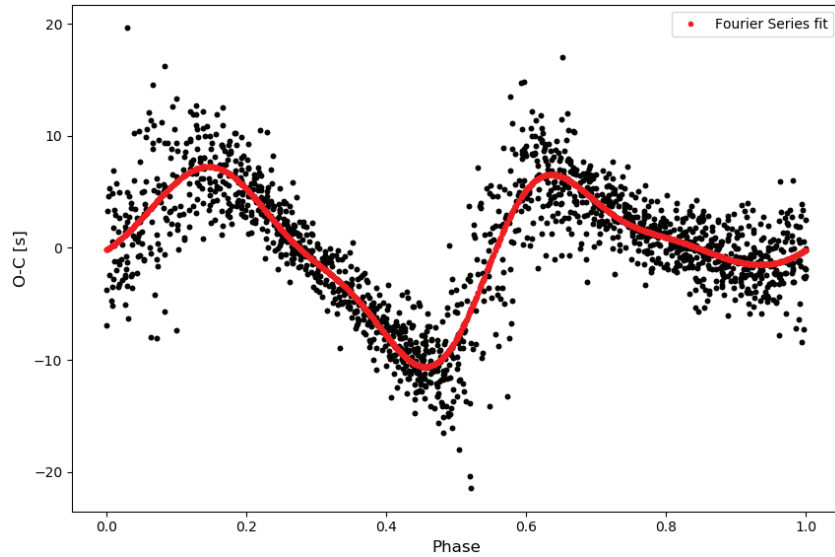


Figure 2. Fourier series fit used to correct for timings for orbital-phase dependence

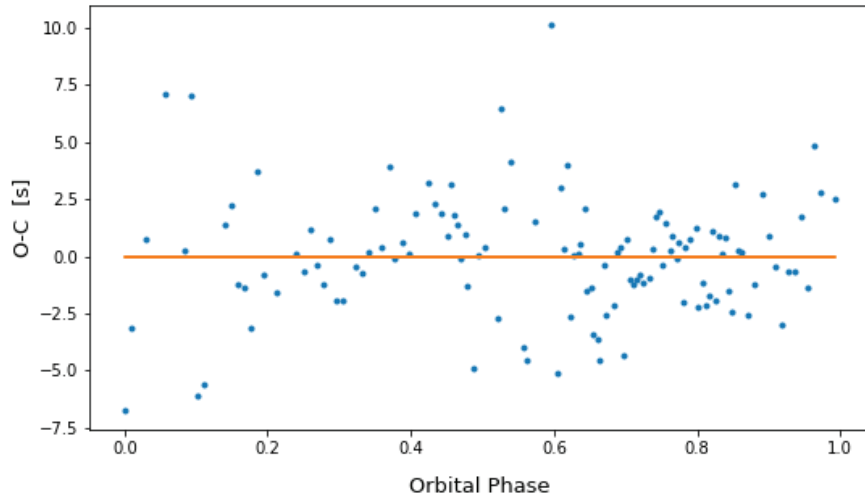


Figure 3. Residuals after corrections, the mean is close to zero.

Results

After applying corrections, we fit individual lines to the timings of each observing run (Figure 4). Then, we will take the first point of this linear fit as an average of the entire night.

Next, we fit first and second order polynomials to the beat timings. We can compare their residuals to determine which fit better describes our data (Figure 5). The plot of the residuals clearly show that a quadratic fit is better suited.

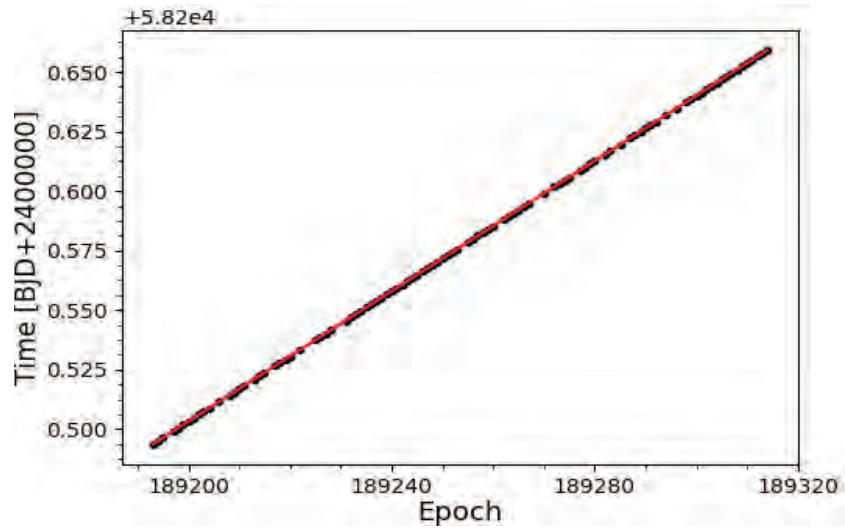


Figure 4. Beat pulse timings linear fit of a single observing run to extrapolate the data

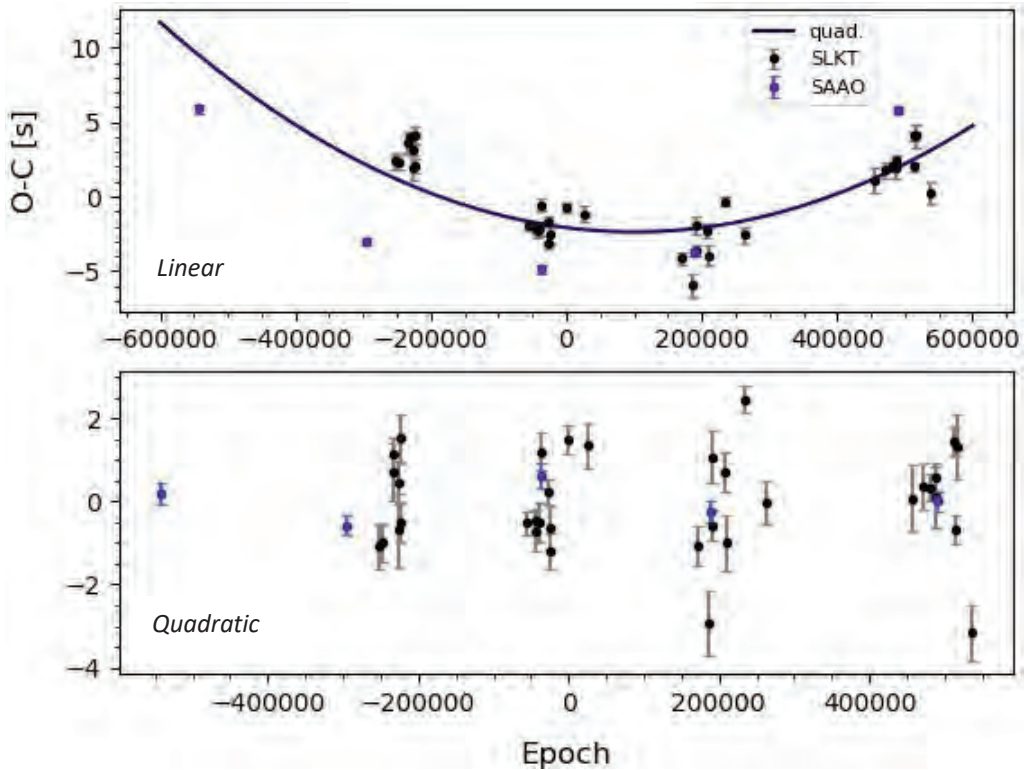


Figure 5. O-C diagram showing the residuals after each fit. It is clear that a quadratic ephemeris would better describe our data.

To better understand the behavior of the system, we can calculate an ephemeris. As mentioned before, adding a quadratic term produces a better fit: $T_{max} = \alpha E^2 + PE + T_0$. Where T_{max} is the beat pulse time at maximum, E is the epoch number, P is the period, and T_0 is the time at epoch zero, defined here as 2457941.6688507 BJD, from Stiller et al. (2018) ephemeris. Alpha is equivalent to $\frac{1}{2}\bar{P}_{beat}\dot{P}_{beat}$, where \bar{P}_{beat} is the average beat period and \dot{P}_{beat} is the period derivative. We perform a Markov Chain Monte Carlo algorithm on the datasets to find the ephemeris and corresponding uncertainties in the last two digits:

$$T_{max}BJD_{SAAO} = 4.91(12) \times 10^{-16}E^2 + 0.0013680458306(35)E + 2457941.6688734(21)$$

$$T_{max}BJD_{SLKT} = 4.76(16) \times 10^{-16}E^2 + 0.0013680458239(61)E + 2457941.6688656(12)$$

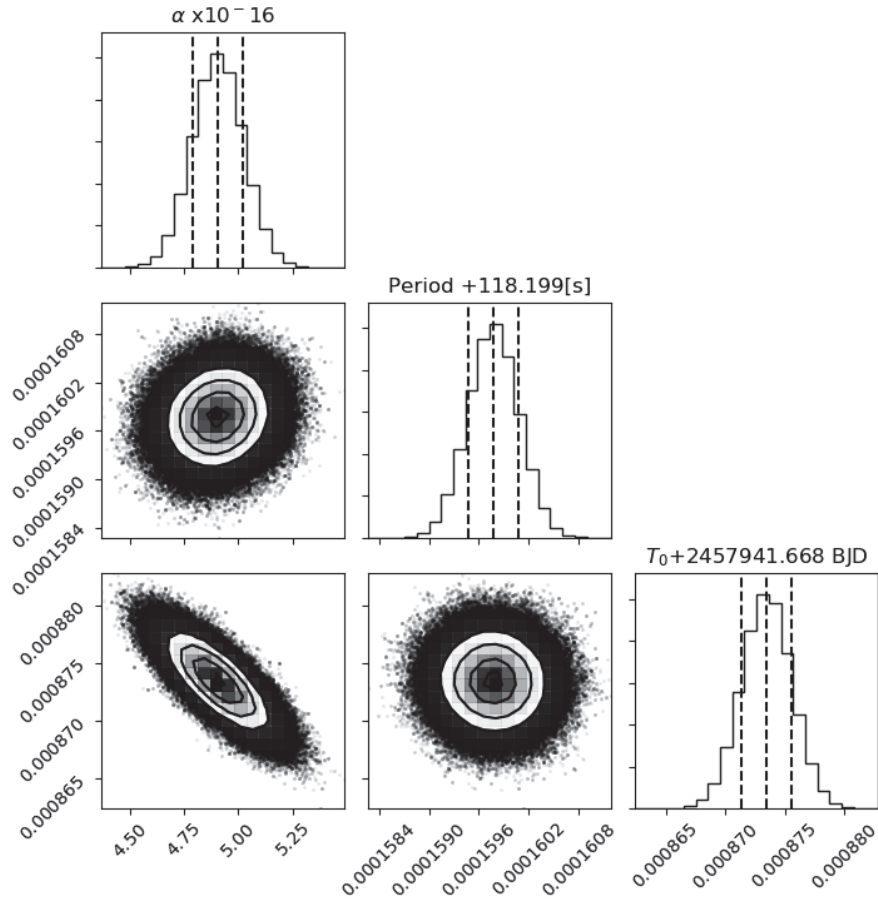


Figure 6. Corner plot of MCMC results for finding SAAO ephemeris.

From the quadratic coefficient, we can calculate $\dot{P}_{beat\ SAAO} = 7.1781(54) \times 10^{-13}$. By definition, we can calculate the beat frequency $\nu = P^{-1}$, then the beat frequency derivative

$\dot{\nu} = -\frac{\dot{P}}{P^2}$. Therefore, $\dot{\nu}_{beat\ SAAO} = -5.137(25) \times 10^{-17}\ Hz\ s^{-1}$. The same procedure applies

to the SLKT data. The ephemerides and values are compared in Table 1 below.

Value	SAAO	SLKT	$ \Delta $
$\dot{\nu}\ [Hz\ s^{-1}]$	$-5.137(25) \times 10^{-17}$	$-4.98(17) \times 10^{-17}$	1.57×10^{-18}
$P\ [s]$	118.19915976 (30)	118.19915918(53)	5.8×10^{-7}
$T_0\ [s]$ +212366160000	190.66(18)	189.99(10)	0.67

Table 1. Comparison of measured values (beat frequency, period, and time zero). Last column is the absolute difference.

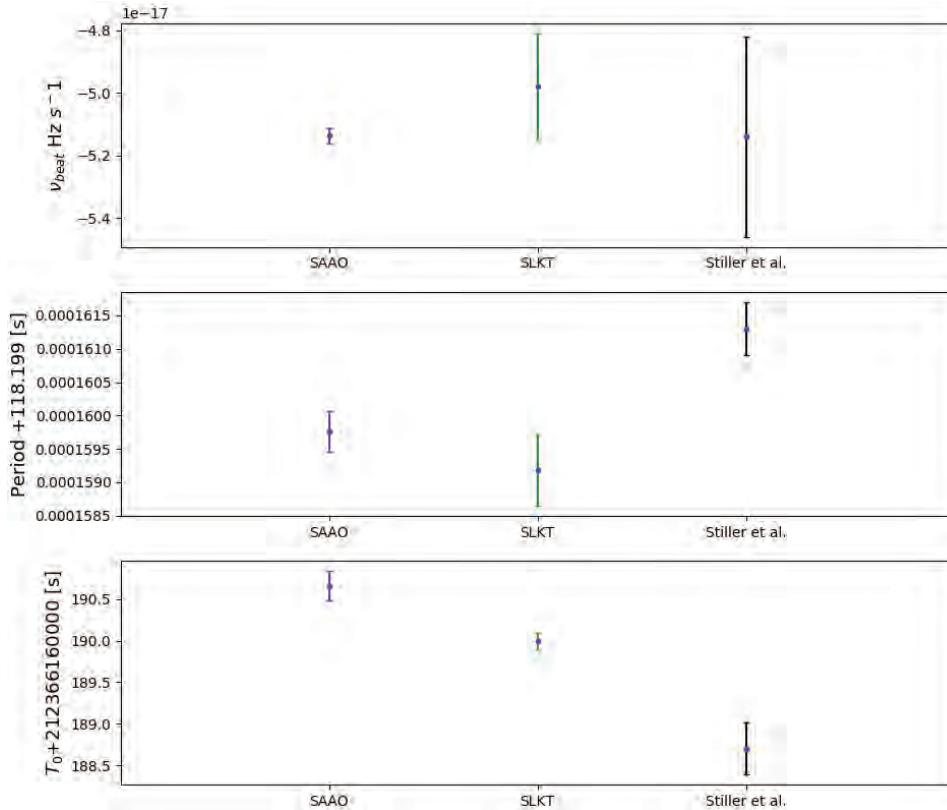


Figure 7. Visual comparison of values in Table 1.

Conclusion

We have found a mean beat frequency derivative (between SAAO & SLKT) of $-5.134(28) \times 10^{-17} \text{Hz s}^{-1}$, which is close to the value found $-5.14(32) \times 10^{-17} \text{Hz s}^{-1}$ in Stiller et.al (2018). This is promising, because it further supports the belief that the WD is spinning down and potentially powering the system of AR Sco. Furthermore, the ephemerides values are in close agreement, and we have managed to improve the number for the SLKT data. Further studies on different datasets could be performed, as to have a broader baseline for comparison.

References

- Buckley, D. A., Meintjes, P. J., Potter, S. B., Marsh, T. R., & Gänsicke, B. T. (2017). Polarimetric evidence of a white dwarf pulsar in the binary system AR Scorpii. *Nature Astronomy*, 1(2).
- Marsh, T., Gänsicke, B., Hümmerich, S., Hamsch, F., Bernhard, K., & Lloyd, C. et al. (2016). A radio-pulsing white dwarf binary star. *Nature*, 537(7620), 374-377.
- Stiller, R., Littlefield, C., Garnavich, P., Wood, C., Hamsch, F., & Myers, G. (2018). High-time-resolution Photometry of AR Scorpii: Confirmation of the White Dwarf's Spin-down. *The Astronomical Journal*. 156(4), 150.

Implementation of Tilted Module Bend Corrections
in the CMS Detector Track Trigger

Arianna Gemma García Caffaro

2019 NSF REU Program

Physics Department, University of Notre Dame

Advisors: Kevin Lannon, Michael Hildreth

Abstract

In response to the High-Luminosity Large Hadron Collider (HL-LHC) upgrade, the Compact Muon Solenoid (CMS) Collaboration has developed a new trigger system, called the Track Trigger. The Track Trigger reconstructs particle tracks by connecting small fragments of the particle's trajectory, known as stubs, together to determine the full particle trajectory. Written for an FPGA implementation, the algorithm builds look up tables (LUT) to determine which stubs belong together to form a single consistent particle trajectory. This stub consistency test is performed calculating a quantity called bend, which gives a rough approximation of the particle's trajectory when passing through a set of closely spaced detectors. It is possible to perform a basic assessment of the stubs' consistency without considering the detector's geometry in detail. However, by providing the algorithm with greater detail of the detector's geometry during the consistency check stages, a higher performance can be achieved. For this reason, the LUT were expanded to include further geometrical information relevant to the bend calculation and thus, to the reconstruction of the particle's trajectory. The goal of these changes is to make the window between the calculated and the observed bend tighter, up to a reasonable range, which would allow us to get rid of stubs that are not relevant without losing stub information needed to find the desired tracks. A successful implementation would result in a decrease of data left unprocessed (decreased truncation) and a slight, if any, decrease in efficiency; thus, lowering the fake rate without significantly hampering the efficiency.

Background

The HL-LHC upgrade seeks to increase its luminosity by a factor of 10 from the initial maximum by 2026.¹ This increased luminosity will translate into a higher collision rate, generating a need for a trigger system capable of handling the increased occupancy. Hence, the

CMS Collaboration is working on augmenting the current trigger system, L1 Trigger, with an additional component, called the Track Trigger. The Track Trigger is built to have access to the tracking detector, allowing it to read out its reduced data in the 25ns between collisions and thus, incorporating the reconstruction of high momentum tracks into the L1 Trigger.

The CMS tracker measures the positions of the particles as they pass through the different layers of the detector. Each layer consists of a pair of closely spaced tracking sensors, which record the particle's hits. The tracker then selects pairs of hits in a layer consistent with a high transverse momentum (p_T) track, called stubs (Fig. 1). Numerous

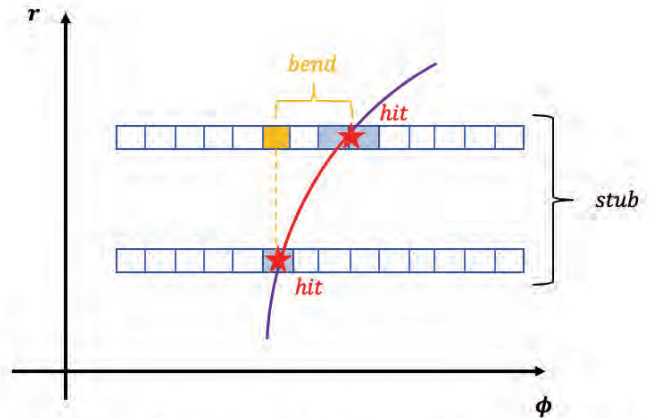


Fig 1. Several closely spaced sets of sensors, like the one pictured above, build the different layers and disks in the detector. Two hits, one in each sensor, consistent with a high p_T track form a stub. The horizontal distance between the first and second hit describes the particle's bend.

stubs are built in this process, some of them belong to a particle's track we want to reconstruct while others come from tracks we are not interested in due to their low p_T , or are a consequence of random sensor noise. The job of the Track Trigger is to decide which stubs go together to reconstruct real particle tracks. To achieve this, it follows three main steps: seeding, projecting, and fitting. In the seeding stage, pairs of consistent stubs in adjacent layers are selected to build a tracklet. This tracklet is later used to extrapolate a consistent particle track and match it to further consistent stubs. Finally, the fitting stage analyzes all the hits matched to the tracklet to calculate the single most consistent trajectory. This study is concerned with the seeding and projecting stages.

In order to build the tracklet and match its projection to further stubs, several stub consistency checks are performed. These rely on the matching of the stub's expected and

observed bends. A bend is defined as the horizontal distance (in units of strips) between the inner and outer hits that make up a stub. It is a measurement of how much the trajectory of a given charged particle bends in the 3.8T magnetic field¹; also described by the particle's radius of curvature which is proportional to its p_T . Given that stubs are built from hits in two rows of

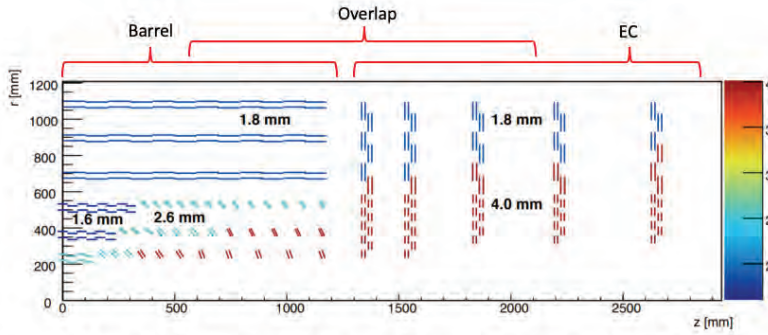


Fig 2. The new geometry layout is divided into three main regions. The barrel, the end cap, and the overlap (figure created by CERN¹).

strips with varied spacing and tilt angles (with respect to the z axis), an accurate bend calculation must consider the detector's geometry.

The upgraded CMS tracker geometry will divide the detector

into three main regions: the barrel, overlap, and endcap (EC). The barrel consists of tilted and un-tilted modules with spacings ranging from 1.60 - 4.00mm, while the EC is built out of modules with 90° tilts with a sensor spacings of either 1.80 or 4.00mm¹. The overlap region is defined as that for which the inner and outer stub are in the barrel and EC, respectively (Fig.2).

Methods

This study was performed on an emulation of the detector; that is, on a computer simulation that strives to faithfully reproduce not only the signals measured by the detector, but the logic FPGAs would implement for the trigger. In it, the bend is calculated from the particle's p_T such that

$$\tan\left(\frac{\beta}{2}\right) = \frac{(pitch)*SW}{\Delta r} \quad [1] \quad \text{and} \quad \sin\left(\frac{\beta}{2}\right) = \frac{r}{2\rho} \quad [2]$$

Where SW is the bend (also known as stub width), pitch is the width of the detector strips, and the other variables are set as shown in Fig. 3. The particle's p_T is given by

$$p_T = 0.3 Bq\rho = 1.14q\rho$$

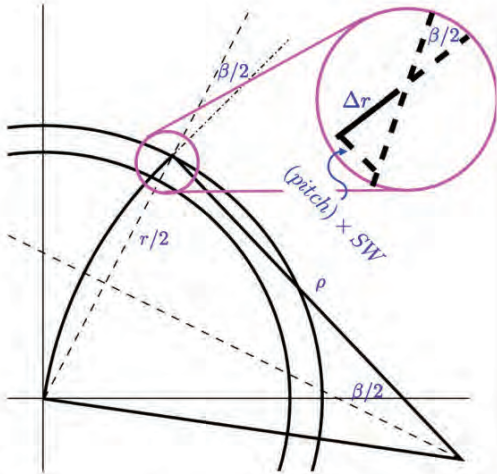


Fig 3. Geometry for calculating the stub's bend from the p_T . The semi-circles indicate the position of stubs (as they go around the detector), which need to be matched².

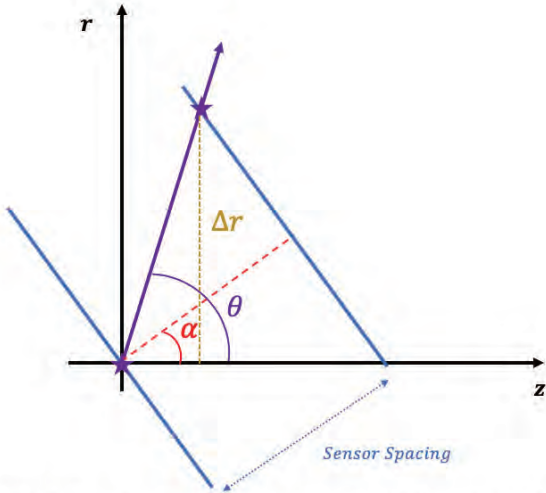


Fig 4. Tilted module geometry. Where α defines the module tilt, with $\alpha = 90^\circ$ for a flat module, and $\alpha = 0^\circ$ for a disk.

solving for ρ , plugging it back into Eq. 2 and using trig identities to solve for SW in Eq. 1 we get the exact

$$\text{solution: } SW = \frac{\Delta r}{(\text{pitch}) * \sqrt{\left(\frac{p_T}{0.57qr}\right)^2 - 1}}$$

Using the small angle approximation,

$$SW = \frac{\Delta r}{(\text{pitch})} * \frac{0.57qr}{p_T}$$

However, for tilted modules Δr does not equal the sensor spacing (Fig. 4), instead it is given by:

$$\Delta r = (\text{sensor spacing}) * \frac{\sin \theta}{\cos(\theta - \alpha)} \quad [3]$$

Where θ is the angle of the stub with respect to the z axis, and α is the tilt angle of the module (with $\alpha = 90^\circ$ for a flat module). Setting the trigonometric term multiplying the sensor spacing in Eq. 3 equal to

$\frac{1}{\text{Correction Factor (CF)}}$, expanding and simplifying the cosine term we get

$$CF = \cos \alpha * \frac{z}{r} + \sin \alpha \quad [4]$$

Given that the detector's algorithm is to be implemented in firmware, the code was written to use only the processing power available to Field Programmable Gate Arrays (FPGAs), thus imposing limitations on the types of calculations that can be implemented and on the precision that these can achieve. For this reason, the calculations for the CF were approximated, by another CERN researcher, to

$$CF = 0.886454 * \frac{|z|}{r} + 0.504148 \quad [5]$$

and

$$CF = \frac{|z|}{r} \quad [6]$$

Where Eq. 5 is the approximation for the tilted barrel and Eq. 6 for the EC, since all sensors in the EC (disks) are simply modules tilted by 0° .

To decrease the amount of mathematical operations performed by the firmware, the stub consistency checks are used to build look up tables (LUTs). These allow the program to simply take in a set of inputs from the inner and outer stubs and map them to an output value from the table. Stub consistency checks, and thus LUTs, were implemented in the Tracklet and Match Engine which perform the seeding and projection stages respectively³.

Tracklet Engine

The Tracklet Engine has three main LUTs, one for each region of the detector, which match pairs of consistent stubs to build a tracklet. For each region, the stub analysis is performed using two tables, the Phi and the p_T Table, which are later joined into one final LUT. Before any improvements to the bend calculation were made, the barrel Phi Table used in inner phi, and outer phi from the inner and outer stubs, respectively, as inputs. From these it calculated their corresponding expected inner and outer bend. However, because we only use a given number of bits to encode phi, the phi values are not precise. In general, more bits are allocated to the outer phi values than to the inner ones. In the case of the barrel LUT, inner phi is represented with 2 bits, while outer phi is represented with 3. Thus, for a given pair of stubs there is not a single consistent bend value; instead, a whole range of possibly consistent values must be considered. Consequently, the Phi Table finds the upper and lower limits of the possibly consistent bend range and sets a maximum and minimum bend value for both the inner and outer bend.

Following the Phi Table, the p_T Table takes in the observed bend values as inputs and checks that the observed bend is in the range between the maximum and minimum bend values calculated before, up to a window which we call the bend cut. If the observed bend is outside

this window, then the table is filled with a *false* for those given parameters. Alternatively, if the observed bend is inside the range set by the bend cut then the table is filled with a *true*. The algorithm can then check if any given pair of stubs is consistent by looking up their respective phi and bend values. Those which are not consistent, do not form part of a particle's track and are tossed away, avoiding wasting time and resources on further fruitless calculations. In this manner, the consistency check helps save space by efficiently deciding which stubs may contain valuable track information and getting rid of those that do not, which is essential when working with high volumes of data and limited time to process it.

Before improvements to the bend estimation were implemented, the overlap LUT worked just like the barrel's, taking in inner and outer phi, and observed bend as inputs to perform the same stub consistency check. Likewise, the EC LUT took in all the same parameters, plus outer r, as inputs to implement the consistency check. In order to account for all the geometric

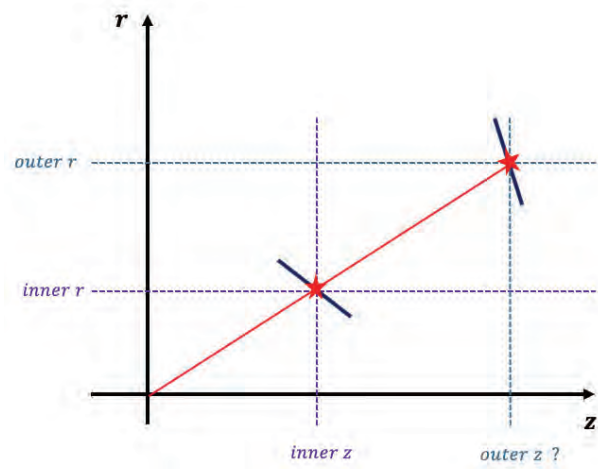


Fig 5. Similar triangles were used to calculate outer z from inner z, inner r, and outer r.

subtleties that come with tilted barrels and varied sensor spacings, the LUTs had to be expanded and the bend calculations modified. The barrel LUT was expanded to include 3 bits of inner z information (z position of the inner stub), which was needed to calculate the corrected inner bend Eq. 5. Inner z was later used along with inner r and outer r (which are given by the layer of the inner and outer stubs) to project back to the barrel, using similar triangles, to find outer z (Fig. 5). The new bend function for the barrel takes in the z position of the stub, its layer number (which

gives its r position), and its inverse radius of curvature, r_{inv} , to calculate the bend using the CF in Eq. 5.

In the EC there was no need to expand the LUT, since it already contained all the information relevant to the bend calculation. Values for inner z and outer z were accessed through the inner and outer stubs disk's number, respectively, and used with outer r to get inner r . The new bend function for the EC takes in the stub's position in r , its disk number, and its associated r_{inv} to calculate the corrected bend using the CF shown in Eq. 6.

Finally, the overlap's LUT was expanded to include 3 bits of inner z information and used along with inner r from the inner stubs' layer, and outer z from the outer stub's disk, to calculate outer r (Fig. 6). It was decided to expand the table in inner z instead of in outer r because using inner z to project onto outer r gave a better resolution than using outer r to project onto inner z . Lastly, the inner bend was changed to match the corrected bend function for the barrel, while the outer bend was changed to match the corrected bend function for the EC. This LUT was built so that the first bin in inner z was always set to *false*, given that there should be no stubs in the barrel with z values in the 0-150 mm range that are matched to a stub in the EC.

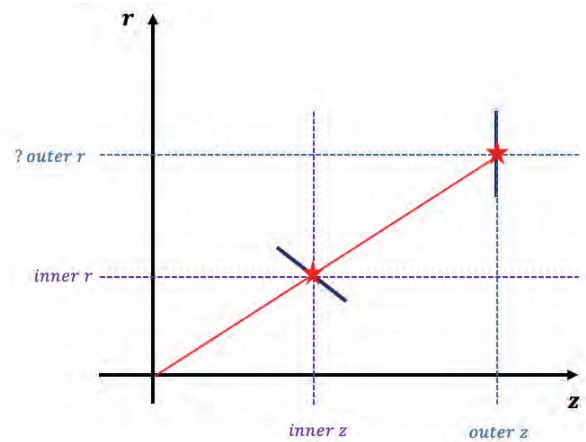


Fig 6. Inner z , inner r , and outer z were used to project out from the barrel to the EC in order to get outer r .

Match Engine

The Match Engine builds one LUT for the barrel and one for the EC, which perform a bend projection, using the tracklet built in the Tracklet Engine, to match further stubs to the track. Before any corrections were made, the barrel's LUT took r_{inv} and observed bend as inputs. It used r_{inv} to calculate the projected bend, and checked if it matched the observed bend,

up to a bend cut window. The barrel LUT was expanded to include 3 bits of the stub's z information and, as done in the Tracklet Engine, the bend function was changed to take in z , layer, and r_{inv} as arguments and reflect the correction outlined by Eq. 5. Furthermore, the bendcut was turned into a tunable parameter, to make its access easier for further studies.

The EC's LUT only takes in the observed bend as input and uses it to perform the stub bend consistency check. The EC's projected bend is calculated in the Projection Router, inside a function called `bendTable()`. Before any bend corrections were implemented, `bendTable()` took in the disk index and `bendindex` as arguments. It built a LUT that took in disk number, sign of the track (indicates if it is forward or backward), r position, and phi derivative to get the projected r and r_{inv} . These last two were used as the inputs to calculate the projected bend inside the table. This projected bend was later sent into the Match Engine's stub consistency check. To account for the tilt and diverse spacing of the sensors, `bendTable()` was changed to take in disk number and `bendindex` as values. The new bend function replaced the old one in the Projection Router's LUT, taking as arguments projected r , disk, and r_{inv} and calculating the corrected bend for the EC using the correction factor shown in Eq. 6.

Results and Discussion

Every collision generates a high volume of data which must be processed to reconstruct the desired particle's track. Given that the time and resources available to analyze the information are limited, there is often too much data that requires processing and not enough time, so we are forced to truncate it, leaving behind some unprocessed data. This generates a considerable loss of valuable information, for we may not have processed the data we needed to find the desired particle's track. Thus, we wish to reduce how often these truncations happen and cleverly choose the data we process in order to decrease the amount of valuable lost

information. The Track and Match Engines are tasked with finding consistent stubs and assembling them into a real particle's track. Given that assembling stubs into a track is a long and expensive task, one of the best ways of increasing this process' efficiency is to cut down on the number of tracks we try to assemble. This study achieves that by improving the resolution of the bend calculation. A more precise bend calculation in the Match and Tracklet Engines, allows for the trigger to get rid of more stubs that are unlikely to build a real track, giving it more time to study other stubs, and reconstruct more real tracks. Following the implementation of the tilted module bend corrections, the efficiency of track reconstruction has not decreased noticeably. Further studies are underway to characterize the precise improvements these corrections bring to the truncation, and the loss in efficiency, if any, that must be tolerated to benefit from those gains.

Further Studies

This study could further improve the stub consistency checks' performance by tuning the bend consistency cuts in the different regions of the Tracklet and Match Engines. Other researchers at CERN have done this for the emulation before the tilted module bend corrections, but it remains to be done after their implementation. Studies should also be done on the bend and phi representations. The number of bits in which these values are encoded also vary by regions and should be optimized to improve the Track Tigger's efficiency.

References

- [1] CERN. (n.d.). *High-Luminosity LHC*. Retrieved from CERN Accelerating Science: <https://home.cern/science/accelerators/high-luminosity-lhc>
- [2] Figure created by Kevin Lannon
- [3] Original code for the Tracklet Engine, and Match Engine written by Anders Ryd

Radial Velocity Measurements of Stellar Bodies Observed by the Automated Planet Finder and Their Implications on Exoplanet Exploration

Curtis Goss

2019 NSF/REU Program
Physics Department, University of Notre Dame

Advisor: Dr. Jeffrey Chilcote

Abstract

We present a number of radial velocity (RV) calculations obtained by performing Doppler spectroscopy on stellar observations made by the Automated Planet Finder (APF). The observed celestial bodies are in binary or multi- star systems in well-documented orbital moving groups (OMGs). RVs provide tremendous insight into exoplanet exploration and astrophysical understanding. Because RV computation has such vast implications, we've created a calculational pipeline to produce RVs for the APF to utilize these values as parameters in more profound explorations. Our team's underlying motivation is to advance our understanding of direct and indirect exoplanet detection, thereby advancing our execution of these techniques. Further, such a tool would aid the entire community of those studying multi-star systems in OMGs.

1. Introduction

1.1 Exoplanet Exploration

For millennia, mankind has clung to an innate curiosity which has propelled us into and through the most exciting voyages of our astronomically brief history. We've consistently yearned to push the forefront of the reality we've come to understand into domains once thought beyond feasibility. Such exploration brought about wondrous discoveries, but naively birthed the notion that "the sky is the limit." Factually speaking, the mirage of a boundary we blanket by the term "the sky" isn't a limit at all. It is truly nothing more than the transition into a frontier that will require humanity's greatest minds to understand: space.

Such transcendent curiosity is what drives astronomers, cosmologists, physicists, and the like to expend countless resources into fields we were once simply too ignorant to even acknowledge existed. In this paper, we delve into such a field, namely, exoplanet exploration. This particular search was conceived the minute man grew capable of pondering the most fundamental of existential questions regarding whether we were the sole conscious beings of this universe. The

1995 discovery of the first definitive planet outside of our own solar system, known as an extrasolar planet, or exoplanet, metaphorically fanned the fire to such profound questions (Mayor & Queloz). Scientists across the board grew fascinated in the idea of finding other planets, and hopefully, eventually, other life forms.

Exoplanet discoveries may come from a number of varying techniques. Modern technological capabilities confine these discoveries to be mostly made through indirect detection, where the exoplanet is discovered from electromagnetic signals implicating the physical influence it has on its host system. The foremost indirect approaches are gravitational micro-lensing, transit intensity fluctuations, and spectroscopic radial velocity, the latter of which is the focus of this paper (Strojnjk & Bravo-Medina 2018). The converse to these methodologies, direct detection, is conducted through actually observing the planet itself. Although direct detection is a promising technique with growing potential, present technological capabilities are hindered by the population of exoplanets that can be discovered by it. At the moment, direct imaging is best suited for giant exoplanets, which, indirect methods have proven are far rarer than super-Earths and terrestrial planets (Bowler 2016).

1.2 Doppler Spectroscopy

Spectroscopic radial velocity detection, or Doppler spectroscopy, is a useful and accurate tool for measuring the speed at which a celestial body moves parallel to an observer's line of sight, also known as its radial velocity (RV). The underlying principle behind this technique is explained by the Doppler-Fizeau effect which states that light produced by an approaching source is shifted towards shorter wavelengths (redshift), while light from a receding source is shifted towards longer wavelengths (blueshift). By quantifying this shift, we obtain the Doppler formula,

$$z = \frac{\lambda - \lambda_0}{\lambda_0} = \frac{1 + \frac{V_r}{c}}{\sqrt{1 - \frac{V^2}{c^2}}} - 1, \quad (1)$$

where z is the red- or blue- shift, λ is the observed wavelength, λ_0 is the wavelength from the rest frame, V_r is the RV, and V is the velocity from the lab frame (Eggenberger & Udry 2010). Often when observing the radial velocity of stellar targets, $c \gg V$, thus we can utilize this limit to approximate the Doppler formula (Eq. 1) to

$$\frac{\lambda - \lambda_0}{\lambda_0} \approx \frac{V_r}{c} \quad (2)$$

while preserving significant accuracy.

1.3 Radial Velocity Implications

Establishing RVs gifts astronomers the ability to study and understand a vast array of characteristics depicting moving bodies. In the context of exoplanet exploration, the integral tool unlocked by the determination of a body's radial velocity is its orbit. Evidently, if we have the ability to observe a target, we can determine its location. Therefore, understanding how it moves around this location over time, as observed from a relative inertial frame, provides sufficient archival points of data to create a precise map of the body's orbit (Nielsen et al. 2016). In the context of a star system, understanding its orbit and meticulously monitoring its RV over time allows astronomers to account for gravitational abnormalities. Referred to as the system's wobble, these fluctuations indicate another body must be present. The amplitude of such wobble is directly proportional to the system's companion's mass thereby indicating to observers whether the abnormality is indeed an exoplanet, or another massive celestial body, such as a brown dwarf (Mayor, Lovis, & Santos 2014).

Aside from leveraging RVs to indirectly detect exoplanets, furthering our understanding of stellar RVs advances the field of astronomy as a whole. Albeit a bold claim, RVs are a versatile tool which provide astronomers valuable insight into distant systems. A specific focus which is most pertinent to our research is that of RV's ability to deduce stellar age. In binary and multi- star systems, observers can conveniently derive masses of the involved stellar bodies by understanding

the gravitational influence that these bodies impose upon one another and their orbits. Once we establish the mass of a star, we can utilize stellar models in conjunction with aging techniques, such as lithium depletion estimates, to predict the age of the star (Carlos, Nissen, & Meléndez 2015). We capitalize upon this computation by observing bodies conceived in stellar nurseries, which have now conglomerated into comoving star clusters, hereafter referred to as orbital moving groups (OMGs). In young OMGs, the age of an arbitrary star is roughly the same for the rest of the group, as they were all born together (Nielsen et al. 2016). With the high frequency of multi-star systems in OMGs throughout the universe, such a notion allows us to determine the age of entire stellar regions. As claimed above, this furthers understanding in a vast array of aspects throughout astronomy.

When factoring back in exoplanet exploration, specifically via direct imaging, the age of stellar bodies is a crucial consideration. As Bowler (2016) explains, young stars are most attractive because their presumably-young planets are vastly more luminous than aged planets; further, the contrast between planets and their host stars is optimized. In a field where even the slightest bit of exploration demands significant resources, it logically follows that observers need to be meticulous when selecting targets to rigorously study. One way to find the best prospective hosts, and ultimately discover new exoplanets, is by leveraging stellar age as a predictive metric to fine-tune the pool of considered star systems.

Beyond utilizing binary and multi- star systems to understand the age of OMGs, it's imperative that astronomers understand these systems for the fact that they themselves are hosts to extrasolar planets. According to Raghavan et al. (2006), 23% of exoplanets detected through Doppler spectroscopy have a binary stellar host system. This fact, along with the aforementioned claims, provide much of the underlying motivation for studying the motion of multi-star systems in OMGs and calculating their RVs.

2. The Automated Planet Finder

The Automated Planet Finder (APF) is an instrument built specifically for the observation of precise Doppler velocimetry. Mounted at the Lick Observatory, atop Mt. Hamilton, the APF is comprised of a 2.4m, f/15 telescope with a throughput of 114,000" and spectral resolution up to 150,000. The instrument has a fixed spectral domain ranging from 3740 to 9700 Å. It contains a Levy spectrometer which is an extremely precise instrument that has helped optimize the APF's radial velocity error to under 1 m/s (Vogt et al. 2014).

3. Radial Velocity Pipeline for FGKM Stars Observed by the Automated Planet Finder

3.1 The APF RV Pipeline

Because RVs are such a powerful tool in the field of astronomy, we deemed the necessity in creating a pipeline which would take in data from the APF and return a radial velocity for the observed target. Our team already configured an algorithm to do so with data taken by the Southern African Large Telescope (SALT), therefore we modified this system to generate radial velocities using Doppler spectroscopy for both instruments.

The algorithm starts by reading in the pre-reduced APF data which consists of numerous variables. In the case of calculating RVs, wavelength and spectral flux are the most important variables of the dataset. After importing the data, we then convert the target's wavelengths from vacuum to air conditions. This is a vital consideration due to the fact that light behaves differently depending on the medium in which travels. The template spectra, which act as λ_0 when we apply Eq. 2, considers atmospheric wavelengths rather than those in a vacuum, therefore consistency must be established.

The APF's Levy spectrometer parses the observed target's spectrum into several orders, or echellograms. Such an effect creates curvature, commonly referred to as the echelle ripple, in the plot of the target's data (Heap and Brown 1997). This distortion hinders our method of performing

Doppler spectroscopy, so we eliminate it by flattening the data through a two-step best-fit. According to Schroeder and Hilliard (1980), Echelle gratings vary by the blaze function,

$$f(x) = \left(\frac{\sin(x)}{x} \right)^2, \quad (3)$$

such that x is the wavelength and $f(x)$ is the intensity distribution within the flux. The algorithm fits the flux to this function through a least-squares approach, then divides the flux data by the resultant best-fit to eliminate this distortion. After our initial analysis, we deemed that the blaze function (Eq. 3) failed to account for the entirety of the curvature in the data, thus we also convolved the data with a Gaussian filter. This is an approach commonly used in astronomy to fix resolution discrepancies and more aptly shape the data. Our application of Doppler spectroscopy utilizes the alignment of telluric lines, or absorption peaks, which are preserved even after applying the blaze function (Eq. 3) and Gaussian convolution. Altogether, this yields relatively flattened spectra, with well-defined peaks, compartmentalized into 65 varying orders. Figure 1 illustrates one of 65 orders of PX Vir, a G5V star in a multi-star system. The plotted order in Figure 1 is pertinent as it corresponds to the spectral wavelength range with which we will eventually be focusing our Doppler shift on for the majority of our targets.

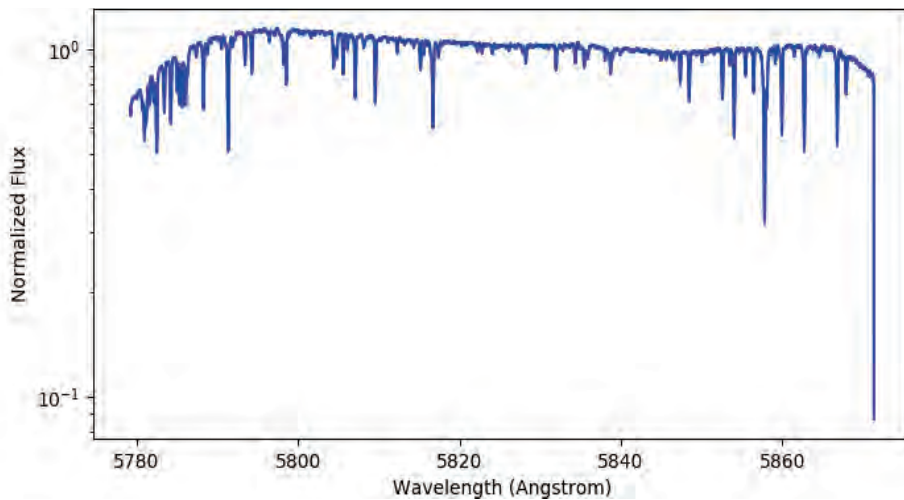


Figure 1. PX Vir’s normalized flux plotted as a function of wavelength in the spectral range of 5750-5875 Å as observed on 6/27/2018 by the APF.

Once the data is optimally-shaped, we're able to execute the spectroscopic shift. To do so, our algorithm reads the target's wavelength and flux into an "Empirical SpecMatch," a tool which selects a referential template by comparing the target to a library of 404 stars observed with the powerful Keck/HIRES instrument (Yee et al. 2017). After finding a similar star, the function returns the template's wavelength and normalized flux. As previously stated, this dataset is what we utilize to ultimately perform the computation of eq. 2, where λ_0 is a wavelength correlating to a telluric peak of the template and λ is a wavelength correlating to the same respective-yet-shifted telluric peak of the target. To quantify this effect, the Empirical SpecMatch tool utilizes a bootstrapping approach to test varying shifts in pixel space. It selects the shift which generates the largest median cross-correlation between the target and template and provides this value back into our algorithm (Yee et al. 2017). Our pipeline then converts the resultant pixel shift into a wavelength shift by averaging the quotient of change in wavelength over change in pixel. It subsequently calculates the product of this conversion and the pixel shift, thereby finding the value of $\lambda - \lambda_0$. Figure 2 demonstrates the shift made by the Empirical SpecMatch. The last value we need to be able to obtain a RV is λ , which is simply the mean of the target's wavelengths.

Once we have a RV, the final factor we must account for is the Earth's velocity imposed by its orbit around its barycenter. Any orbital system has a barycenter, or the center of mass about

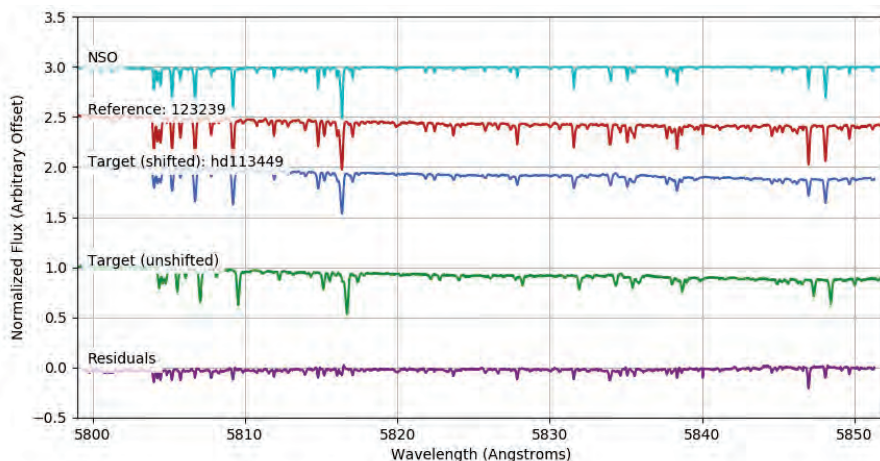


Figure 2. The resultant plot of PX Vir's normalized flux shifted by the Empirical SpecMatch in the spectral range of 5750-5875 Å as observed on 6/27/2018 by the APF. The shift is 15.86 pixels or 0.33 Å.

which the bodies in the system orbit. Because the Earth is not a stationary body, observations made from it are biased by the velocity at which it orbits its barycenter. Our pipeline considers this by utilizing a barycentric correction as outlined by Wright and Eastman (2014). This correction is extremely precise, with an error of at most 1 m/s. We then relativistically detract this value from our previously calculated RV with the relation

$$V_r = RV + V_{BC} + \frac{RV \cdot V_{BC}}{c}, \quad (4)$$

where V_{BC} is the barycentric velocity and V_r is the true radial velocity (after correction).

3.2 Data Analysis

Through the development of our pipeline, our team came across a multitude of errors which led to various underlying considerations not evident in the final product. We initially thought miscalculations were due to resolution discrepancies therefore we tested a number of Gaussian convolutions, most of which had no effect on the resultant RVs. We then looked to Doppler broadening which brought the APF data and template down to the same spectral resolution, which again was futile. Because resolution changes had no effect, we then looked to ensure the wavelengths had been considered in the proper medium. Assuming APF data had been reduced to include wavelengths in air conditions, we converted the wavelengths to those of vacuum, which made our RVs absurd. Ultimately, performing the converse of this is what attributed to the final necessary correction to our pipeline, which wasn't figured out until late in the project's timeline.

4. Results

Prior to building the pipeline, we determined that focusing on the star PX Vir would be most beneficial as we have well-documented archival data on its RVs and orbit. From this data, we hypothesized that we should see RVs within ± 15 km/s to know the pipeline is accurate. After overcoming the numerous obstacles posed in the development of our pipeline, we were finally able to deduce RVs for PX Vir in this theorized range. Figure 3 depicts our calculated RVs for PX Vir

Epoch	RV (km/s)	Standard Error (\pm km/s)
3/29/2018	12.2730	0.0369
4/11/2018	8.7796	
4/21/2018	6.1428	0.0354
5/5/2018	4.1589	
5/8/2018	1.8849	0.1035
5/17/2018	0.1251	
6/5/2018	-4.5304	
6/26/2018	-8.8776	0.0280
6/27/2018	-11.0235	
12/20/2018	2.6867	
1/23/2019	-3.6852	
1/28/2019	-4.3755	0.0612
3/16/2019	-11.4563	0.1118
3/31/2019	-11.0614	
4/8/2019	-8.8014	0.2099
4/15/2019	-5.3965	
4/29/2019	1.7391	0.0242
5/7/2019	6.0401	

Figure 3. Radial velocities of PX Vir from observations made by the APF

on numerous dates. We further confirmed our pipeline’s accuracy by manually computing PX Vir’s Doppler shift with a synthetic star from the BT-Settl grid. This yielded identical results.

In conclusion, we now have a verified pipeline to streamline the computation of RVs for the APF’s data. We will utilize this pipeline to indirectly search for exoplanets via observation of stellar wobbles. Further, this algorithm acts as a convenient tool for the entirety of those studying multi-star systems in OMGs, which also inadvertently aids our ability to directly image exoplanets.

References

- Belikov, R., Barclay, T., Batalha, N. M., et al. 2019, BAAS, 51, 517
Bowler, B. P. 2016, PASP, 128, 102001
Carlos, M., Nissen, P. E., & Meléndez, J. 2016, A&A, 587, A100
Eggenberger, A., & Udry, S. 2010, EAS Publications Series, 27
Heap, S. R., & Brown, T. M. 1997, The 1997 HST Calibration Workshop with a New Generation of Instruments, 114
Mayor, M., & Queloz, D. 1995, Nature, 378, 355
Mayor, M., Lovis, C., & Santos, N. C. 2014, Nature, 513, 328
Nielsen, E. L., De Rosa, R. J., Wang, J., et al. 2016, ApJ, 152, 175
Raghavan, D., Henry, T. J., Mason, B. D., et al. 2006, ApJ, 646, 523
Rich, E. A., Wisniewski, J. P., Currie, T., et al. 2019, ApJ, 875, 38
Schroeder, D. J., & Hilliard, R. L. 1980, Appl. Opt. 19, 2833-2841
Strojnink, M., & Bravo-Medina, B. 2018, Proc. SPIE, 107650Y
Vogt, S. S., Radovan, M., Kibrick, R., et al. 2014, PASP, 126, 359
Wright, J. T., & Eastman, J. D. 2014, PASP, 126, 838
Yee, S. W., Petigura, E. A., & von Braun, K. 2017, ApJ, 836, 77

The First Extended Look at an Eclipsing Polar:

V1309 Orionis

Kathleen M. Halloran

2019 NSF/REU Program

Physics Department, University of Notre Dame

Advisors: Peter Garnavich, Colin Littlefield

ABSTRACT

Over a period of 4 weeks, the V1309 Orionis system was studied by the Transiting Exoplanet Survey Satellite (TESS) Space Telescope. TESS collected data every 2 minutes over a span of 4 weeks, creating a light curve featuring a double hump. We find that the relative amplitudes of the two humps in the orbital waveform varied independently of each other during the TESS observation, and we consider the physical origins of this unexpected behavior. These observations are the first to be recorded and discussed for a time period longer than several hours or days. The span of 4 weeks allows for a more thorough analysis given more consistent data, and sets a foundation for future observation and theory to develop around this system.

1. INTRODUCTION

Cataclysmic variables are binary star systems comprised of a primary white dwarf, or the small dense remnant of what was once a low-to-medium mass main sequence star, and a secondary red dwarf of lower mass [1]. As these two stars orbit each other, as represented in Fig.1, the one-way orbit features the white dwarf gravitationally stripping material from the outermost layers of the companion star, contributing additional brightness to the system. The leftover material forms an accretion disk composed of leftover material and gas surrounding the primary star.

A different category of these systems, magnetic cataclysmic variables, are characterized by the intense magnetic fields surrounding the white dwarf and the behavior of the accretion that follows [1]. This particular category is divided into classifications - intermediate polars and polars. Polars exhibit surface magnetic field strengths of 10-100 Mega Gauss, high enough that it prevents an accretion disk from forming. The force from the magnetic field forces the two stars

to rotate synchronously, such that the same side of one star always faces the same side of the other. These are also referred to as AM Her stars; V1309 Ori falls into this category of magnetic cataclysmic variables, but still proves to be one of the most unique, exhibiting rare qualities not seen in other systems.

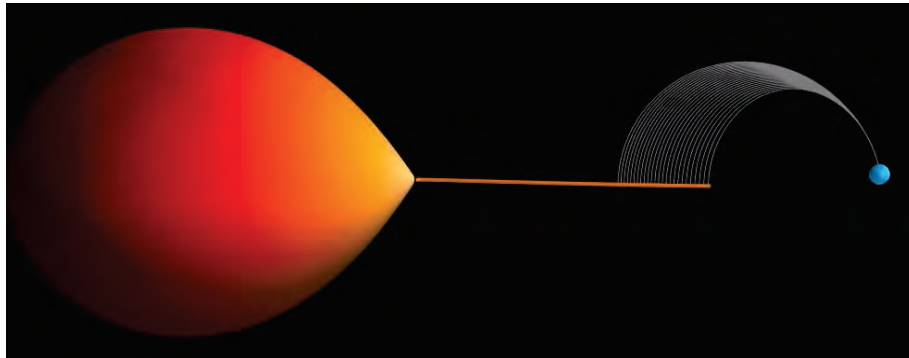


Figure 1. Visualization of the binary star system, comprised of the red dwarf and white dwarf, in orbit. Orange line represents the accretion flow from the companion star; white, curved structure is accretion flow after it has been captured by the white dwarf's magnetic field.

2. OBSERVATIONS

Orbiting the Earth every 13.7 days and dividing the sky into 26 sectors, TESS collects about 200,000 two-minute exposures for 27.4 days per sector. Within the first year of observation, TESS completed studies of the southern hemisphere, and will observe the northern hemisphere in its second year [3]. Along with the data from TESS, previous reports on V1309 were used to provide context and additional background information to compare observations.

2.1 Structure and Time

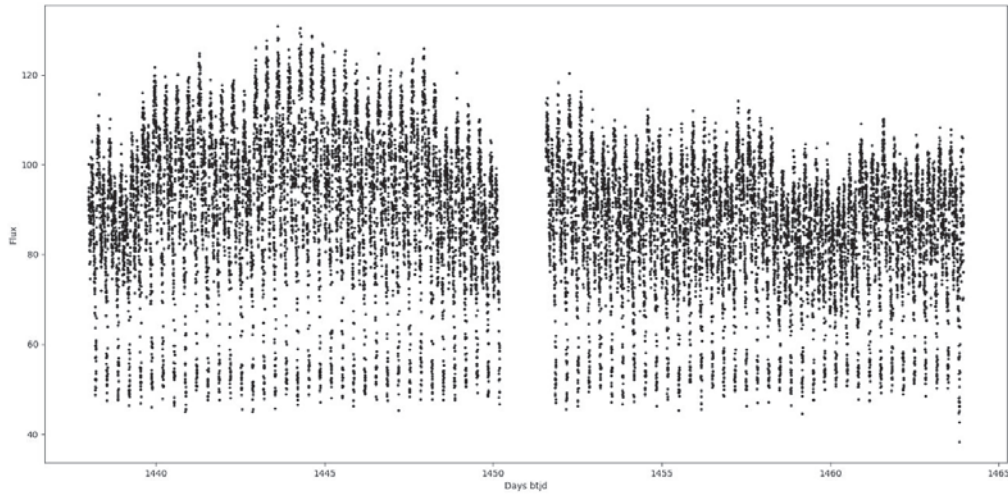


Figure 2. V1309 Ori light curve over 27.4 day span.

The data collected from TESS is the first continuous, nearly uninterrupted light curve over an extended period of time. Prior to the TESS observation, the only light curves of V1309 Ori were ground-based and were very poorly sampled, with large gaps. Fig. 2 shows the light curve modeled by TESS over 27.4 days. The only interruption in the data occurs in the middle of the light curve, where TESS was unable to capture the system due to transmission of data.

With this light curve, we observed both the interval between eclipses as well as the duration of each eclipse. We also noted the consistent structure of the orbital waveform and eclipse. According to Garnavich et al., the eclipse has an orbital period of 7.98 hours; this conclusion allowed us to determine whether or not the system consistently completed a full eclipse [4]. We compared the times of eclipse with an Observed - Calculated graph (O-C), which allowed us to determine whether or not the eclipse occurred early or late compared to what the orbital period predicted. The question of interest is whether there are internal changes in the O-C

graph, specifically whether or not the O-C graph changes in response to the overall brightness calculation.

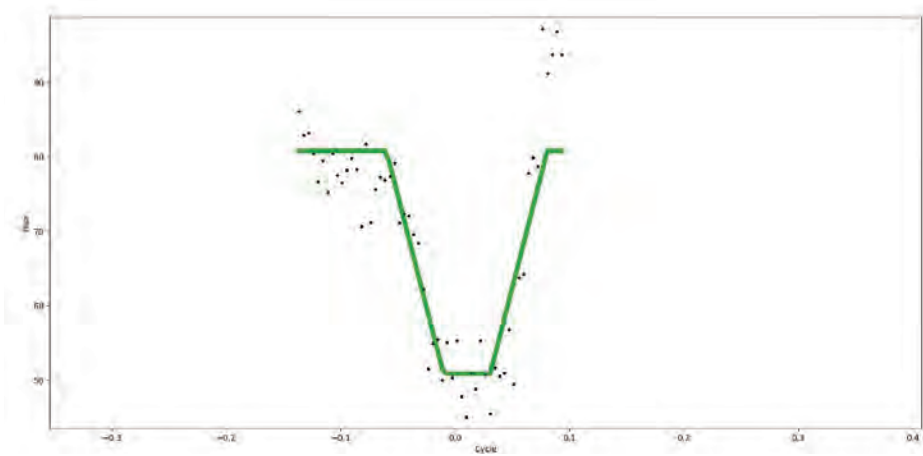


Figure 3: Trapezoidal line of best fit of one eclipse of the system. The trapezoid parameters are used to extract eclipse parameters, especially the time of mid-eclipse.

This light curve also allowed us to gain a better understanding of the structure of the eclipse. After isolating the data to focus on the immediate ingress, egress, and eclipse, we fit each curve with a trapezoidal function. Fig. 3 shows the fit for one eclipse in the light curve. Each data point represents a recorded brightness of the system; the fits show us how the brightness changes entering and exiting the eclipse. This confirmed the flat bottom shape of the eclipse, signifying a total eclipse where light and gas from the primary star are completely prevented from escaping past the secondary star. Any random points are most likely background noise. The trapezoidal fit also allowed us to gain a better measurement of times of eclipse, which helped us more precisely calculate the orbital period.

2.2 Brightness

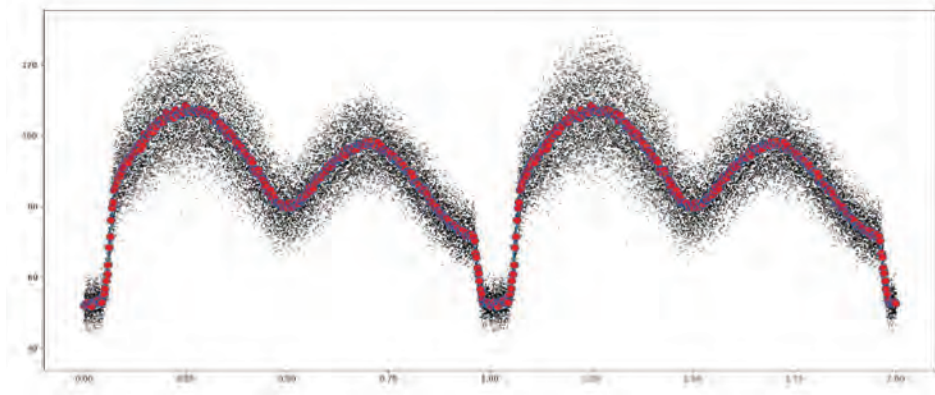


Figure 4. Phased light curve displaying trend of average brightness

Since V1309 is such a unique AM Her system, studying the brightness of the system helps us to draw further conclusions as to the intensity of the magnetic field surrounding each star, and how bright the system truly is as compared to surrounding stars. Fig. 4 displays a phased light curve plotting points over one orbital cycle. The data is duplicated to provide a second set of curves in order to accurately depict the eclipse. Once we constructed the plot, we calculated the average brightnesses and modeled it in a line over the phased light curve. This demonstrated how the brightness fluctuated throughout the cycle.

The images taken by TESS are taken in the Near- Infrared spectrum. When comparing the light curve in Fig. 4 to previous literature, we concluded that the eclipse has changed since last observed. In the Infrared light curve of Figure 1 in Katajainen's observations, a similar light curve is included, but looks more scattered than the data we collected [5]. We concluded that this was due to a change in the system.

From Fig. 4, we also took a deeper look at the double hump structure of the eclipse. This piques interest because the orbital light curve shows a large contribution from the ellipsoidal

shape of the secondary. Knowing this, each of the two humps reflects one “side” of the secondary star; a visual depiction of this is seen in Fig 1. The surface area of the secondary star is the same on either side, so, in theory, the two humps should be the same size peaks. However, the possible reasoning for a varying shape is that one of the peaks is reinforced by light from the accretion region, or the region directly surrounding the white dwarf, and is only visible at one part of the orbit. This still causes question as to why it is only visible after the eclipse and not before. We plan on completing further study as to why the data represents this oddity, and refining our observations and calculations to try and draw conclusions.

The most significant takeaway from this set of data is the overall understanding of the eclipses of other polars and magnetic cataclysmic variables. In Fig 4, we visually see how the light source from the primary star in the system is being blocked; using this information, we can further study where the light from the system is being produced and how the gas moves between the two stars. We also can model longer term variations, looking for correlation between peaks and activity in each orbital cycle. Previously, conclusions were limited by actual observing capability and collection, even as recent as 2012. In Kalomeni’s observations, Figure 6 presents two light variations, one of which is from a phase diagram similar to the one presented in our study [6]. The presentation of this figure displays seemingly scattered and interrupted data. Now, with the ability to access nearly uninterrupted observations, we can create more clear and concise figures that provide optimal results.

4. CONCLUSION

During the course of this study, we accomplished a variety of objectives and answered several questions about this unique system. Using the TESS data, we supported the observation that V1309 has an orbital period of 7.98 hours, and completes a total eclipse every full cycle. We learned how the structure and brightness of the eclipse is affected by the magnetic field surrounding it, as well as how the gas and material flows around the system. Using techniques of trapezoidal fitting and phasing, we provided concrete values of the average brightness of the system over the course of an orbital cycle. The light curve that we developed will assist future studies, and will allow for remaining questions regarding specific details to be answered. After completing our study, we hope to answer the question as to why the system seems to be brighter after the eclipse, and what the shape may have to do with it. We also hope to work further with our phased curve to learn why the peaks of the eclipse vary when the surface area of the secondary star is the same. Overall, we look forward to seeing how this system will vary over the course of further observations, and will be looking for trends that will predict the system's future.

In the future, we plan on conducting further studies on the magnetic fields, accretion, patterns of the eclipse, and the structure of the system. What is truly remarkable about the data we utilized is the newfound ability to observe with a longer span, granting us a better ability to search for orbital derivatives and obtaining the mass transfer rate over the past few decades. This information will allow us to complete a more comprehensive study, and will help future amateur and professional astronomers alike to learn more about magnetic cataclysmic variables and eclipsing polars of this nature.

REFERENCES

- [1] "AM Herculis." *American Association of Variable Star Observers*, 4 Apr. 2010, www.aavso.org/vsots_amher.
- [2] "TESS." *TESS*, Isaac Partnership, tess.mit.edu/.
- [3] Garnavich, Peter M., et al. "RJ 051542+0104.7: A New Magnetic, Eclipsing, Cataclysmic Variable." *Astrophysical Journal Letters*, vol. 435, Nov. 1994, pp. L141-L144. *Astrophysics Data System*, doi:10.1086/187614.
- [4] Katajainen, S., et al. "UBVRI Photopolarimetry of the Long-Period Eclipsing AM Herculis Binary V1309 Ori." *Monthly Notices of the Royal Astronomical Society*, vol. 340, no. 1, Mar. 2003, pp. 1-11. *Astrophysics Data System*, doi:10.1046/j.1365-8711.2003.06280.x.
- [5] Kalomeni, Belinda. "Short and Long Time-Scale Variability in Magnetic Cataclysmic Variables: Long-term Monitoring of Polars." *Monthly Notices of the Royal Astronomical Society*, vol. 422, no. 2, May 2012, pp. 1601-08. *Oxford University Press*, doi:10.1111/j.1365-2966.2012.20736.x.

TEACHING THROUGH THE CHART OF NUCLIDES

ISABELLA IANORA
2019 NSF/REU Program
Physics Department, University of Notre Dame

ADVISOR: Dr. Kilburn

Abstract

The Chart of Nuclides is an expanded version of the Periodic Table of Elements with over 3,000 different known isotopes of the existing elements. Due to the sheer size of this chart, it is difficult to present this information to audiences outside of nuclear physics. Therefore, this summer, our goal was to determine a simpler way of presenting the chart. In addition to this I also spent time teaching the skills I developed over the summer to younger students. In this paper, I will discuss the Chart of Nuclides and my experiences teaching coding and 3D design.

Introduction

The Chart of Nuclides was designed to help organize all the information scientists knew about isotopes and their behavior patterns. It is similar to the Periodic Table in the sense that you can use both to observe trends and predict behaviors of new elements or isotopes, but the Chart of Nuclides is much more detailed. The periodic table includes general information about the elements- atomic number, proton number, and mass (usually a weighted average of all stable isotopes)- whereas the Chart of Nuclides contains information about all isotopes of a given element. The Chart of Nuclides displays the proton number (Z) on the y-axis and the neutron number (N) on the x-axis. Each row across represents one element and its isotopes. The isotopes are chemically identical, but will have very different nuclear properties because of the difference in neutrons in the nucleus.

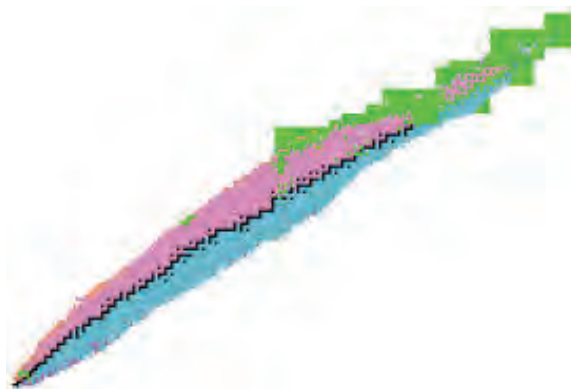
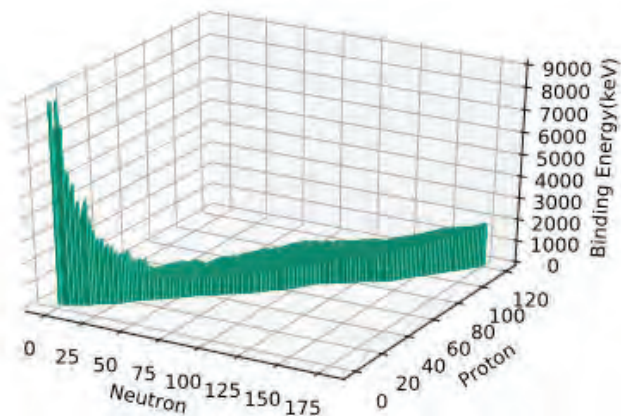


Figure 1: This is an overall view of the Chart of Nuclides. The black boxes represent the most stable isotopes and the pink, blue, and green boxes represent beta-plus decay, beta-minus, and alpha decay respectively [1].

Chart of Nuclides

The first couple weeks of the summer I spent getting to know the 3D printer, Cura software, and the Chart of Nuclides. The Cura software that is connected to the 3D printer can only read a specific type of file called stereolithography (STL). STL files are the only type of files that can save a 3D image in regards to its surface shape. To create the three dimensional Chart of Nuclides, I found and modified a python script to create a 3D histogram of my data which included proton number, neutron number, and binding energy. The data used to create the chart was taken from reference [2]. Binding energy was used for the z-axis to physically display the trend of stable to unstable isotopes. The most stable isotopes have the highest binding energies which would mean that the isotopes in the middle of the chart would have the tallest peaks. However, I inverted the z-axis because the chart is more commonly depicted showing the valley of stability. The valley shows the most stable elements as having the lowest energies and is imagined as a valley because if you were to put a marble on the edge of the chart, it will roll towards the center with the most stable isotopes.



This was a great start, but Python can only save images in formats that are not compatible with the 3D printer software Cura. The plan was to save the figure above as an SVG (Scalable Vector Graphics) file and use a program called Tinkercad to convert it into an STL file. Tinkercad is a site used to create 3D designs for the purpose of 3D printing them. Tinkercad has the ability to import SVG files and can then export them as STL files; however, when this method of conversion was attempted, it was unsuccessful due to the size of the SVG file. A couple other file converting sites were used, but none of them maintained the three dimensional shape of the chart. One solution was to use codeblocks on Tinkercad to create a smaller version of the Chart of Nuclides. Codeblocks allows the user to use drag-and-drop coding to create their design. While this method works extremely well for creating the chart, it also takes a significant amount of time due to the number of isotopes in the Chart of Nuclides. Due to time constraints, the project was reduced to the first eight elements to complement the marble nuclei lessons and activities. The needed isotopes were created using boxes that had the same length and width, but varied by height depending on their respective binding energies. The height of the boxes in centimeters (cm) corresponds to the binding energy in mega electron-volts(MeV)- one cm is equivalent to one MeV.

The interest in creating a Chart of the Nuclides in this way is for teaching purposes. Having a chart that students can observe and touch in real life can help with teaching some of the concepts used in nuclear physics. The Joint Institute for Nuclear Astrophysics- Center for the Evolution of the Elements (JINA-CEE) is a National Science Foundation (NSF) supported group that aims to bring together physicists from different fields to better understand the origin of the elements that make up our universe. In addition to its collaboration, JINA hosts various outreach events at the University of Notre Dame and Michigan State University dedicated to teaching

science to different age groups. This summer I was an activity leader for the Arts 2 Science day camp for 8-12 year-olds and a counselor for the Physics of Atomic Nuclei (PAN) program for high school students. Participating in both of these summer camps gave me the opportunity to observe different teaching styles as well as learn how to teach- at a basic level- the skills I had been using and developing throughout the summer.

Physics of Atomic Nuclei

The PAN program is a week long summer camp for high school students who are interested in learning about nuclear astrophysics. Throughout the week they get to perform experiments in the Notre Dame advanced physics lab, listen to lectures from multiple Notre Dame professors, and at the end of the week they present on what they have learned. During this camp I was entrusted to teach the X-ray Fluorescence experiment in which the campers were tasked with determining the chemical composition of five unknown metals by shooting X-rays at them and seeing what X-ray energy levels were picked up by the detector. When the metals are hit by the X-rays it causes some of the atoms in the metal to ionize which means they will emit an electron from one of the inner electron shells. Another electron from one of the outer shells will then fall into the inner shell in place of the emitted electrons and lose energy in the process. The excess energy the electron lost is emitted as a photon in the X-ray range that can be detected by the detector. Each element has specific electron orbital transitions that emit specific energies of photons. The students used a program called Hephrestus to match up the energies picked up with energies the element would emit due to different electron transitions. Before they were able to get to the unknown metals they had to calibrate the computer so it was in sync with the detector. This turned out to be one of the hardest parts of the experiment because if the

calibration was off then their data in regards to the unknown elements would be completely off and it would be difficult to determine what the unknowns were.

This experience taught me to communicate science using basic language. In my daily life at my university I don't think twice about using the word calibrate; however, most of the PAN students didn't know what I meant when I told them to calibrate the computer. I had to find a different way to explain what calibration means and why it is important. *Include more about how as the week went on explaining the experiment got easier and I got accustomed to talking about physics at a lower level

Arts 2 Science

Arts 2 Science is a week long day camp for kids ages eight through twelve (second through seventh grade) to inspire their creativity and foster enthusiasm for science. Campers are split into groups based on age and spend the week going through twenty-four different activities related to STEM and art. I was an activity leader during the two weeks of this camp in the computer room. I taught two different softwares to the kids: Tinkercad and Scratch. Tinkercad, as I mentioned earlier, is mostly used for 3D design and is typically used in conjunction with a 3D printer. For the purposes of this camp we wanted each kid to be able to design something that could easily be 3D printed in a short amount of time so each child would have something to take home at the end of the week. Scratch is a free website created by the Massachusetts Institute of Technology that teaches students basic levels of coding using a drag-and-drop coding style. Using Scratch students can create games, animate characters to make a story, and even make music using existing sounds Scratch has downloaded or by recording their own.

For the first week of Arts 2 Science the goal for teaching Tinkercad was to show the kids some of the basic skills of Tinkercad and then task them with designing a spirograph that I would

be able to 3D print for them. This turned out to be a very difficult task for most of the kids because it was too hard for them to try to figure out the software while also creating a complex design. By the second day of teaching Tinkercad I decided to have the kids create small designs that would be easy for me to print by the end of the week. The issue with this activity was I didn't give the kids enough constraints to ensure that their designs would be something I would be able to print. The 3D printer works by laying down layers of plastic that are melted at the nozzle right before it is extruded onto the bed of the printer. Designs that have solid bases are the easiest to print layer by layer whereas objects with overhang or holes are harder for the printer to manage and usually don't come out the way it appears on the computer. Many of the kids in the Arts 2 Science camp didn't quite understand all the instructions I gave and made designs I couldn't print.

For the second week of Tinkercad in the Arts 2 Science summer camp I decided that the best way for everyone to learn basic skills of Tinkercad and get something 3D printed by the end of the week was to have them make name tags for themselves. This activity was a lot easier for the kids to do and it was easy for me to do a quick demonstration of a name tag. I also made sure to stress the fact that they needed to pick shapes that were flat so it would be easy for the 3D printer to handle. However there were still some designs that weren't perfectly compatible with my instructions. One way we were able to get around some of the design flaws was to lower the resolution the printer used which allowed some of the design flaws to get smoothed out by the printer.

For the second half of each week I taught Scratch to the campers. Scratch was in some ways easier for the kids to understand because many of them had used Scratch before in their classrooms and were able to help each other figure it out. It was also easier for me because I

didn't need to give specific instructions, I wanted them to spend the hour exploring the different things they could make on Scratch- for some kids that was designing a game and for others it was creating a short story. One of the things I learned very quickly was that most of the kids would end up playing games other people had created unless I specifically asked them not to before I let them go explore Scratch.

Conclusion

Teaching Tinkercad and Scratch was intentionally picked because they both teach skills that I also used this summer. Tinkercad teaches the students how to design a three dimensional object while keeping in mind the limitations of the equipment they are working with (the 3D printer). Scratch was used to teach a basic level of coding which is a skill almost every physicist needs to use at some point in their career. For my project specifically I did not use Scratch, but I did use Tinkercad to create a 3D model of the first eight elements in the Chart of Nuclides.

I think as scientists we are not encouraged to learn how to share our knowledge to audiences outside of physics when that should be an important part of what we do. New discoveries are of no use to people unless it can be explained to the general public. I think my REU experience this summer was extremely important in teaching me the importance of inspiring the next generation of learners. I also learned how to communicate my knowledge and skills I've learned with kids of various age levels and interests in STEM.

References

- [1] "Discovering Frontiers." *JINA*, www.jinaweb.org/.
- [2] "The Ame2016 atomic mass evaluation (I)" by W.J.Huang, G.Audi, M.Wang, F.G.Kondev, S.Naimi and X.Xu *Chinese Physics C* 41 030002, March 2017.

The High Efficiency Total Absorption Spectrometer (HECTOR) and
Correcting for Inconsistencies in $^{27}\text{Al}(p,\gamma)^{28}\text{Si}$

Sean Kelly

2019 NSF/REU Program

Physics Department, University of Notre Dame

Anna Simon

Abstract

The processes responsible for producing heavy nuclei in stellar environments, such as the p-process and s-process, are studied by measuring radiative capture reaction cross sections. The High Efficiency Total Absorption Spectrometer (HECTOR) is a tool for measuring these small cross sections using the γ -summing technique. In order to study the efficiency of HECTOR, resonance strengths of the $^{27}\text{Al}(p,\gamma)^{28}\text{Si}$ reaction measured with HECTOR were compared to results from previous literature. HECTOR's results yield higher resonance strengths than previous works indicate, which may be due to incomplete cascade and branching information used in their calculations. Using a simulation of HECTOR in Geant4, it is possible to quickly calculate and edit cascades for ^{28}Si at different resonances. By editing the cascade inputs of the simulation to agree with HECTOR's experimental data, it may become clear where previous literature underestimates $^{27}\text{Al}(p,\gamma)^{28}\text{Si}$ resonance strengths.

Introduction

In order to improve understanding of the processes of stellar nucleosynthesis, measurements of various nuclear reaction cross sections must be performed. The High Efficiency Total Absorption Spectrometer (HECTOR) was designed for the Notre Dame Nuclear Science Lab to experimentally measure these reactions' cross sections, which are very small. Experimental work done with HECTOR is particularly concerned with the capture reactions that impact the p-process, which is responsible for the creation of proton-rich nuclei in type-Ia and -II supernovae. These reactions are studied using the principle of detailed balance for kinetic

systems. Experiments with HECTOR provide data to calculate cross section for (p,γ) , or (α,γ) reactions, which can be multiplied by a constant to find cross sections for the (γ,p) or (γ,α) reactions that are occurring in stellar environments. For HECTOR to be maximally effective in defining these astrophysical processes, its efficiency and the ways its efficiency depends on other factors must be studied. As a γ -summing detector, HECTOR can handle a wide-range of dynamic events, and should remain efficient at low energies and be able to contribute to measurements of tiny cross sections. The $^{27}\text{Al}(p,\gamma)^{28}\text{Si}$ reaction is a well-studied nuclear reaction with many prior calculations of different resonance strengths. Previous work on the reaction gives the perfect point of comparison for HECTOR. By comparing resonance strengths measured with HECTOR to this literature, it becomes clear that HECTOR generally returns a higher resonance strength for $^{27}\text{Al}(p,\gamma)^{28}\text{Si}$ than previous methods. A previous experiment done with the Summing NaI(Tl) (SuN) detector at the National Superconducting Cyclotron Laboratory at Michigan State University provided the data that aligned the most closely with HECTOR in a previous study [1] [2]. As SuN is a γ -summing NaI(Tl) detector, like HECTOR, this may express that the γ -summing technique can handle a more robust range of events than previous experimental efforts. Either way, it is important to understand where the discrepancies in resonance strengths may come from.

The γ -summing Technique

The γ -summing technique, as shown in fig. 1, adds together the energies of each detected γ -ray in a single cascade. If each γ -ray from a cascade is detected, there should be a single

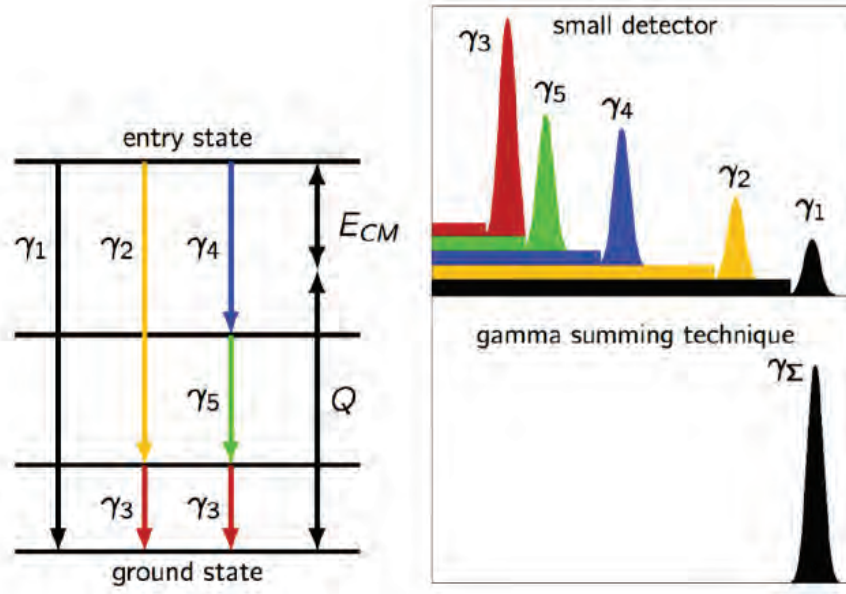


Figure 1: A visual to demonstrate how the γ -summing technique works. HECTOR and its data acquisition system work together to sum the emitted γ -rays, allowing for calculations of reaction cross sections to be made with a clear sum peak.

peak in the data, at the sum of the reaction Q -value and incident particle energy:

$$E_{\Sigma} = Q + E_{cm} \quad (1)$$

An additional advantage to the γ -summing technique is it often creates a clear difference in magnitude between the room background and the desired γ events.

HECTOR

The High Efficiency Total Absorption Spectrometer (fig. 2) consists of 16 4" x 8" x 8" NaI(Tl) crystals arranged in a 16" x 16" x 16" cube. Each crystal is attached to two photomultiplier tubes (PMT's), which turn incident photons into ejected electrons through the photoelectric

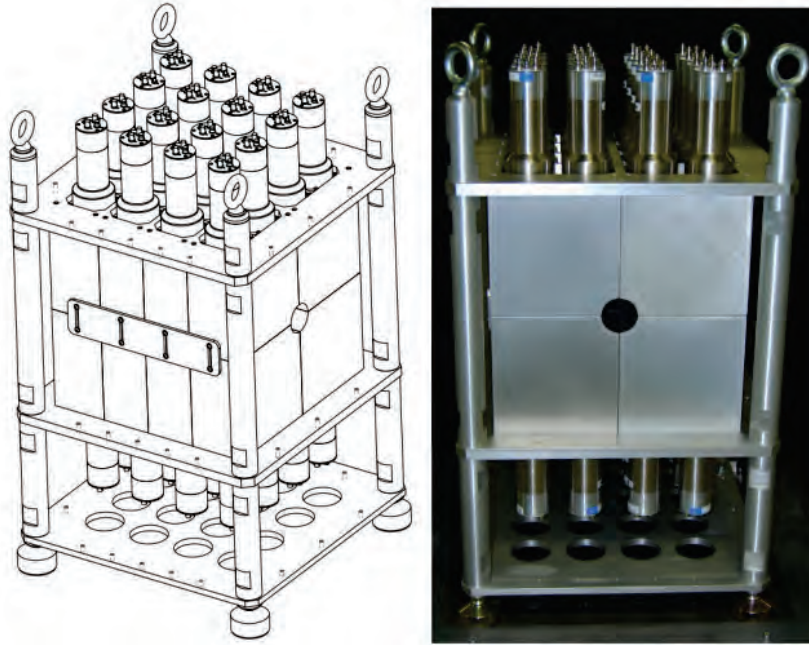


Figure 2: *HECTOR (all 700 lbs. of it!) side-by-side with its schematic, courtesy of St. Gobain Crystals. The PMT's are clearly visible on the upper and bottom halves.*

effect. While the original photon signal is often far too weak to be significant, the effective geometry of a PMT allows for amplification of the electron signal, and the resulting current will be proportional to the original energy of the γ -ray [3]. HECTOR's size and ability to cover the entire 4π angle allows for highly efficient implementation of the γ -summing technique. The Digital Data Acquisition System (DDAS) that is linked to HECTOR uses time signatures to sum the correct γ -rays together.

HECTOR in Geant4

A simulated detector with identical properties to HECTOR was constructed using Geant4 (fig. 3), a program built for the simulation of particles passing through matter. The platform

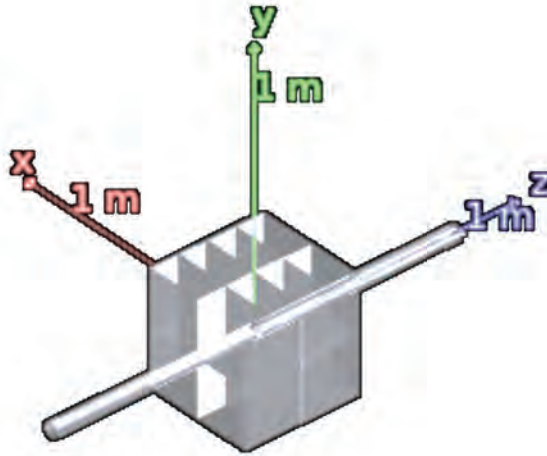


Figure 3: *The rendering of the simulation of HECTOR in Geant4. The crystal compartments are clearly visible, and the software allows for specification of what materials make up the object.*

can be used to study the exact same reactions that have been run with HECTOR, and produces extremely similar data based off of the level scheme of the compound nucleus.

Computational Method

In order to simulate the desired nuclear reaction in Geant4, it is necessary to have a γ -cascade input file for the resonance being measured. Typical γ -cascades are demonstrated on the left side of figure 1. The energy of the incident proton in the $^{27}\text{Al}(p,\gamma)^{28}\text{Si}$ reaction plus the reaction Q-value gives an entry level for the cascade to start at, and from there the compound nucleus can take different paths to decay back to the ground state. This cascade back to the ground state is governed by branching ratios at each energy level, with some

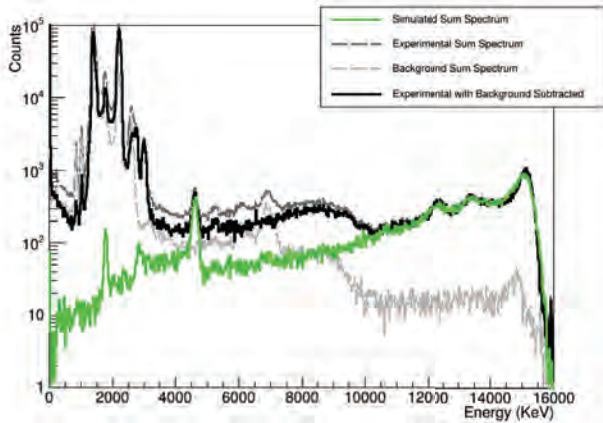


Figure 4: Full γ -summing data from experimentation with HECTOR compared to the Geant4 simulation at $E_{\Sigma} = 15127$ keV.

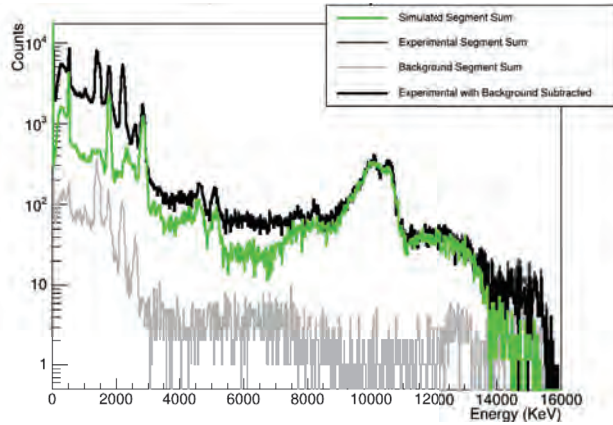


Figure 5: The spectrum of the data from each individual crystal summed, again showing experiment compared to simulation at 15127 keV.

levels having as many as 10 different pathways of γ -decay. Using Python's directed graph class, it is relatively straightforward to calculate all of the different pathways that are possible from an initial energy, including each γ -ray emitted and the total probability for that path. After constructing γ -cascades at a particular resonance with the accepted level scheme for ^{28}Si , the cascade file is used with Geant4 to simulate the data HECTOR would produce at that energy. After simulating data and comparing to real experimental data, the next step is altering branching ratios or incomplete cascade files to discover where discrepancies between experimentation with HECTOR and the aforementioned literature may be occurring.

Comparing Data

Figures 4 and 5 compare real experimental data, taken in June of 2017, to the simulated data at the 3675 keV resonance. In all of the figures that show this data, the thick, dark-colored lines show data from the real experiment, while the lighter-colored lines show the data from the simulation. Figure 5 illustrates the spectrum that is produced by adding the data each separate crystal of HECTOR has taken together, where figure 4 shows a spectrum where events are summed, regardless of which crystal has detected each γ -ray. The sum of separate crystals is very helpful for solving inconsistencies because it shows clearly where simulation may be underestimating individual transitions. It is clear from both of these histograms that the simulated data underestimates the γ -rays that are experimentally detected near 15000 keV—perhaps due to a missing decay from the entry level of 15127 keV. To test this, a decay directly from 15127 keV to the ground state was added to the level scheme, starting with unrealistic probability of 30%. Shown in figure 6, this unrealistic added decay demonstrates the effectiveness of altering the level scheme to change the simulated results.

Altering the Cascades

After testing the method and with an unrealistic decay and proving it effective, it is able to be used for more subtle changes. The simulated decay probability for 15127 KeV directly to the ground state was altered to 5%, and this is shown in figure 7. It is evident after studying the segment sum spectrum with this change that 5% is likely too high an estimate for this decay's probability. In addition to this, it appears that there are two γ -rays near 10000 keV

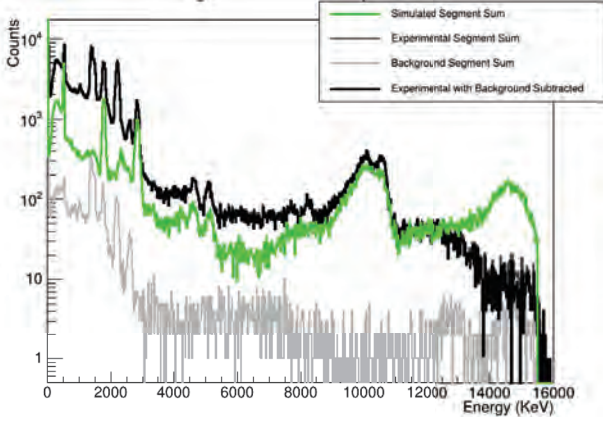


Figure 6: *The same data as figure 5 but with a decay from 15127 keV straight to the ground state added to the simulation at a 30% probability.*

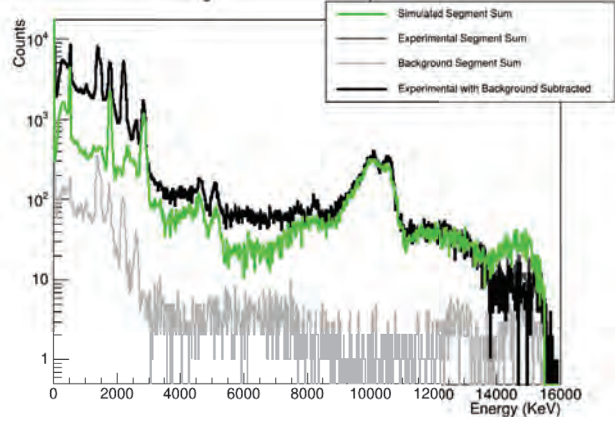


Figure 7: *The same data as figure 5 but with a decay from 15127 keV straight to the ground state added to the simulation at a 5% probability.*

of which the simulation underestimates the intensity. At lower energies, it is assumed that room background causes a majority of the discrepancies between experiment and simulation, although the cascade may still need to be altered to match relative intensities found in the experiment.

Summary

Using the Geant4 version of HECTOR, it is easy to compare experimental data on $^{27}\text{Al}(p,\gamma)^{28}\text{Si}$ taken in the Notre Dame Nuclear Science Lab to simulations based off of level schemes of ^{28}Si . However, it is far more difficult to decipher exactly where the inconsistencies between resonance strength values calculated using HECTOR's results and values calculated in previous literature arise. For the entry energy of 15127 keV, the segment spectrum shows a

consistent double digit value for γ -rays detected at high energies. It appears, then, that the level scheme may be missing a decay straight to the ground state with a small probability, or perhaps several decays to the ground state from close to the entry energy.

Future Plans

The next step for this project is to run through a similar process for other resonances of the $^{27}\text{Al}(p,\gamma)^{28}\text{Si}$ reaction. Measurements with HECTOR and SuN differ significantly from other literature for the 2712, 3792, and 3961 keV resonances [1], so each of these should be tested with the same simulating and altering method that was demonstrated for the 3675 keV resonance in this paper.

References

- [1] A. Simon, C. Reingold, O. Gomez, *et al.*, “High Efficiency Total Absorption Spectrometer (HECTOR) for Capture Reaction Measurements,” *The European Physical Journal A*, 2019.
- [2] A. Simon, S. Quinn, A. Spyrou, A. Battaglia, I. Beskin, A. Best, B. Bucher, M. Couder, P. DeYoung, X. Fang, *et al.*, “SuN: Summing NaI(Tl) γ -ray Detector for Capture Reaction Measurements,” *Nuclear Instruments and Methods in Physics Research Section A*, 2013.
- [3] G. F. Knoll, *Radiation Detection and Measurement*. Wiley and Sons, 1979.

Dependence of Helium Atmospheric-Pressure Plasma Jet (APPJ)-Induced
DNA Damage on Voltage Pulse Duty Cycle and Irradiation Time

Kinsey Lee

2019 NSF/REU Program

Physics Department, University of Notre Dame

ADVISOR: Sylwia Ptasinska

Abstract

Atmospheric pressure plasma (APP) has a wide range of utilities in plasma medicine, particularly because it can create reactive species in an open-air environment. Since plasma is a particularly changeable substance, it is crucial to study the effects of adjusting its variables in relation with its application to biomaterials. DNA was treated with a Helium APPJ for a range of irradiation times and under varying duty cycles in the plasma's voltage pulse. The resulting DNA damage was then analyzed and used to characterize how modifying the above parameters may alter the plasma.

Introduction

Atmospheric-pressure plasmas (APPs) are ionized gases of charged particles, photons, neutral particles, and radicals [1]. One of the most common devices for generating this type of plasma is the dielectric barrier discharge (DBD) APP jet (APPJ), wherein an insulated gas flows through a dielectric capillary tube and transforms into gas discharge while undergoing direct (DC) or alternating current (AC) pulse voltages [2].

APPJs play a pivotal role in plasma medicine—an interdisciplinary field at the intersection of plasma physics, life science, and clinical medicine [3]—for a number of reasons. Since APPs are cold non-equilibrium plasmas, they operate at room temperature and may thus be applied safely to animal and human bodies [3]. Moreover, APPs react with ambient air to form reactive oxygen and nitrogen species (RONS), biologically active substances [4]. As a result, scientists use APPJs in controlled cell adhesion, blood coagulation, wound healing, and induction of apoptosis in cancer cells [5].

Experimental Setup and Method

Figure 1 is a schematic diagram of the APPJ set-up used to conduct this experiment. The jet is a DBD, meaning two 50 mm-brass electrodes—one grounded and the other powered to ensure an electric potential difference—surround a fused silica capillary 30 mm apart. The orifice of the capillary is 5 mm in diameter [1, 5]. The helium gas flow rate through the capillary tube during experiments was 2.04-2.05 standard liters per minute (slm). We ignited the plasma with a range of square pulse widths between 0.2 ms and 0.7 ms at a 1.0 kHz generated by a pulse waveform generator coupled to an HV transformer connected to the powered electrode [5]. The applied voltage was 10 kV. An oscilloscope records the waveforms of the applied voltage, current, and pulse width. In the APPJ, aforementioned, applied voltage pulses accelerate electrons in the helium gas from the powered electrode to the grounded electrode, causing inelastic collisions and creating the charged and excited particles that compose plasma in the 30-mm gap. The plasma then exits through the orifice and reacts with the DNA.

Prior to irradiation, we diluted 0.5- $\mu\text{g}/\mu\text{L}$ puc18 plasmid by a dilution factor of 75 with deionized water for a concentration of 6.67- $\text{ng}/\mu\text{L}$ DNA per 15- μL sample. We irradiated samples for the targeted amount of time, then removed them from the gas flow. The glass well was kept 2.5 cm below the orifice of the system for all treatments to ensure the jet made contact with the sample without saturating possible plasma-induced DNA damage [5]. Irradiated samples were collected via micropipette, and the glass well was washed three times with 5 μL of Phosphate Buffered Solution (PBS) to recover residual DNA.

Samples were then loaded into 0.8% agarose gels and gel electrophoresis was conducted for three hours at 70 V to separate the DNA. Undamaged puc18 plasmid is supercoiled; a single-strand break (SSB) in the plasmid causes it to relax into a circular form; and a double-strand break (DSB) makes the molecule linear. Since each form has a different shape and size, they

separate from each other on the gel (see Appendix A). Gels were then imaged using a UV imager. We used Quantity-One to determine the intensity of the blots on a given agarose gel and related that to the concentration of plasmid found in each blot. We used Python to calculate fractional percentages of DNA damage and subtract the average damage in controls.

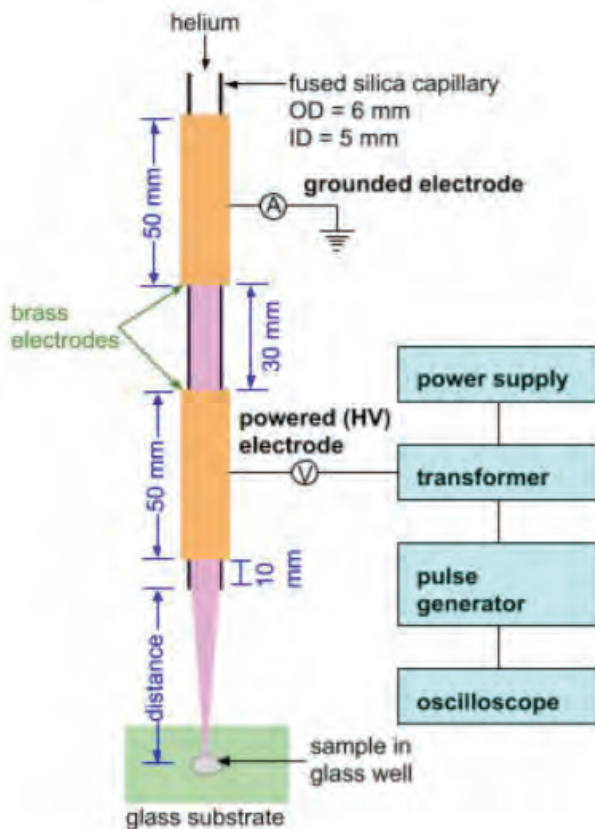


Figure 1. Schematic of the APPJ source.

Results and Discussions

To investigate the DNA damage due to changes in the duty cycle, we wanted to find the optimal irradiation time to observe possible trends. Voltage (10 kV), frequency (1.0 kHz), flow rate (2.04-2.05 slm), distance from the APPJ orifice (2.5 cm) and all other parameters were kept constant for all trials of this experiment. According to Adhikari et al., after 15 s of irradiation, 60% of the DNA is damaged [5]. However, unlike in previous experiments with the APPJ, two

aliquots of DNA per trial were treated to with just the gas flow as control samples. Any damage that appeared in these samples was subtracted from the damage in irradiated samples. Moreover, due to the ambient air conditions, we were concerned that a draft might significantly affect the consistency of the data if the irradiation time was too short. Thusly, all DNA in a given trial was irradiated at a constant time between 15 s and 40 s for duty cycles 0.2 to 0.7. Three trials of samples were irradiated for each time and the error bars represent the standard error between the three trials.

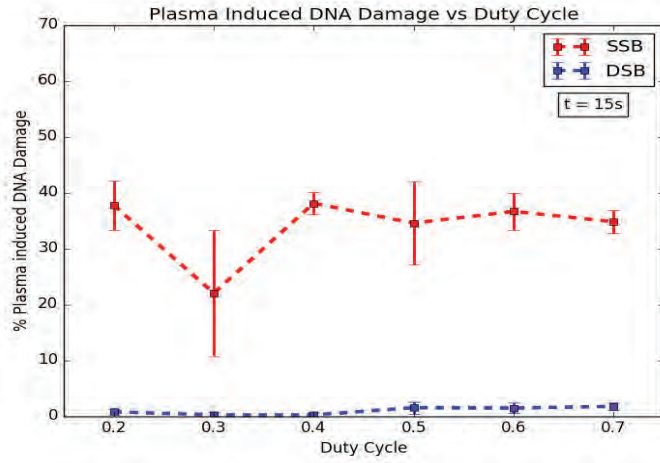
At 15 s (Figure 2a), the average total DNA damage increased from about 35% to 37% from duty cycles 0.2 to 0.7, so the changing this parameter seems nearly irrelevant to plasma-induced DNA damage. However, the standard of deviation at a duty cycle of 0.3 is larger than 10%. Therefore, the data appears relatively inconclusive.

As seen in Figure 2b, the average total DNA damage at 20 s appears to be about 40%, confirming, Adhikari et al., which states that damage increases with irradiation time [5]. In contrast, there is a near zero slope to both the SSB and DSB, implying again, that there is no significant DNA damage induced by changing the duty cycle. Again, the standard of deviation for the samples treated with lower duty-cycle-voltage-pulsed plasma is above 10%, so the data does not appear to be reliable.

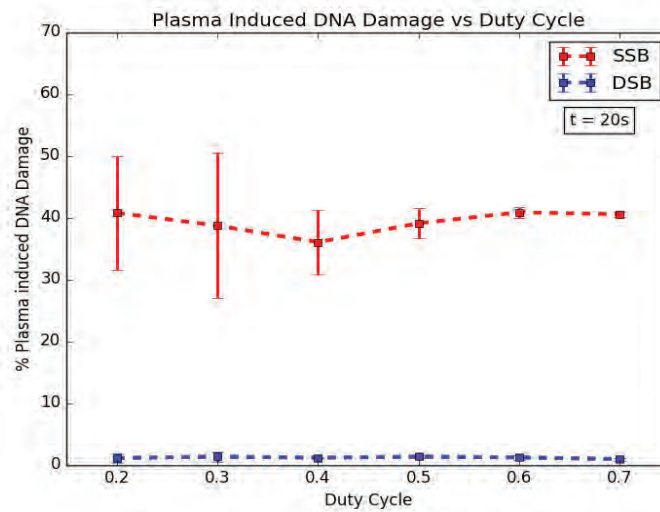
At 30 s (Figure 2c), the average total DNA damage is about 65%; at 40 s (Figure 2d), about 72%. All data over the course of this experiment affirms the importance of irradiation time. In both graphs, all standard of deviation appears at, or below, 10%. Hence, the data was more precise for these irradiation times. While the slopes in Figure 2c are nearly zero, and the slopes in Figure 2d is slightly negative, the change in total DNA damage between 0.2 and 0.7 duty

cycles is no more than 7%. Subsequently, the data suggests there was no change in the plasma-induced DNA damage when the duty cycle what changed.

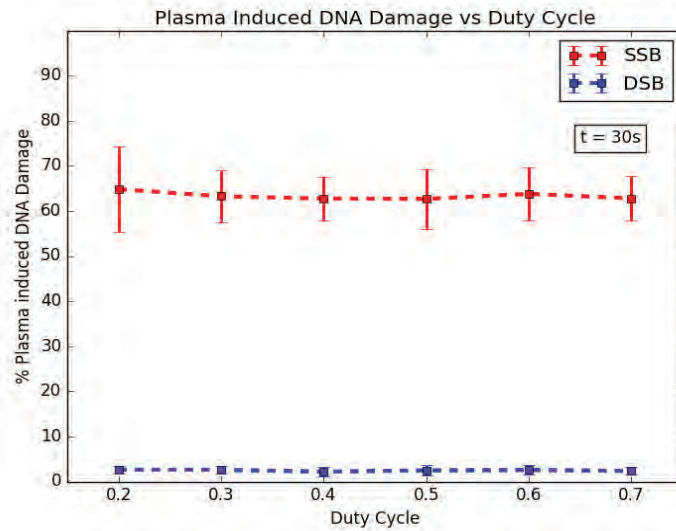
a



b



c



d

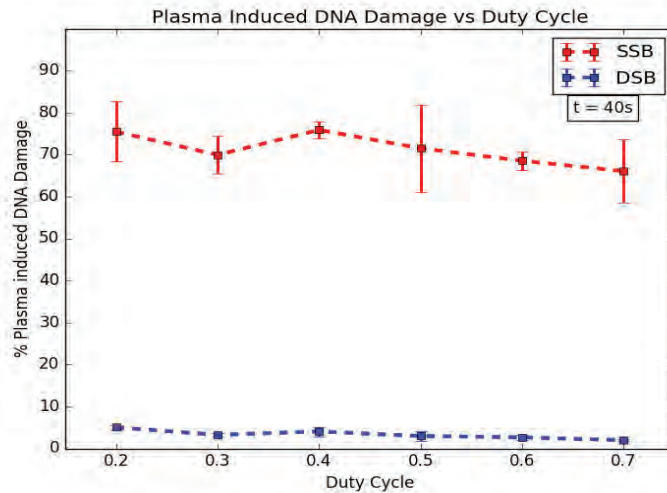


Figure 2. Dependence of APPJ-induced DNA damage on voltage pulse duty cycle for (a) 15 s (b) 20 s (c) 30 s (d) 40 s irradiation times.

Conclusion

The dependence of APPJ-induced damage on the duty cycle of the pulse generator was investigated. In a given trial, DNA samples were irradiated at varying duty cycles while all other parameters for plasma ignition were kept constant. The plasma-induced damage was then quantified via gel electrophoresis and Quantity One. As there was no ostensible change in the damage from the first trials at 15 s, the same experiment was then repeated at longer irradiation

times to confirm that there appears to be no correlation between the duty cycle of the voltage pulse of plasma and the DNA damage it induces. Overall, irradiation time, distance from the orifice, frequency, and gas flow appear to have a larger impact on Helium APP's interaction with biomaterials than the duty cycle, as there seem to be little to no effects in plasma-induced DNA damage regarding changes in the duty cycle [5].

There are several aspects of this experiment that remain inconclusive. The standard of deviation for each of these experiments was quite high. We made several attempts to lower the variance in the data over the course of the experiment: standardizing the placement of the glass well under the APPJ, replacing the gel electrophoresis buffer, and extending the irradiation time. The graphs support the hypothesis that a draft could be affecting these results because the error bars generally decreased as irradiation time increased. In other words, a draft over the course of a longer period of time might flow in the opposite direction and eventually counteract itself. Other hypotheses that might explain the high standard of deviation include the addition of a new buffer tank for gel electrophoresis to this experiment. The older equipment may not function at full capacity due to repeated use. In future experiments, we might pursue a different method of measuring plasma-induced DNA damage aside from gel electrophoresis. It is important to understand where and why DNA breaks occur. Also, to eventually predict how plasma responds to environments in their totality we would need to determine how plasma parameters compound on each other with relative accuracy. Furthermore, if we were to make the sample more complex, if we were to treat cell membrane vesicles instead of plasmid DNA, a precise form of measurement could be useful. We are currently trying to analyze irradiated nucleotides with Fourier Transform Infrared Spectroscopy (FTIR) to address some of these challenges.

References

- [1] K.P. Arjunan, V.K. Sharma, and S. Ptasinska, “Effects of Atmospheric Pressure Plasmas on Isolated and Cellular DNA — A Review,” *International Journal of Molecular Sciences*, 2015. doi:10.3390/ijms16022971.
- [2] W. Yan and D.J. Economou, “Gas flow rate dependence of the discharge characteristics of a helium atmospheric pressure plasma jet interacting with a substrate” *Journal of Physics D: Applied Physics*, 2017. doi:10.1088/1361-6463/aa8794.
- [3] J. Gay-Mimbrera, M.C. García, B. Isla-Tejera, A. Rodero-Serrano, A.V. García-Nieto, and J. Ruano, “Clinical and Biological Principles of Cold Atmospheric Plasma Application in Skin Cancer,” *Advances in Therapy*, 2016. doi:10.1007/s12325-016-0338-1.
- [4] D. Gümbel, S. Bekeschus, N. Gelbrich, M. Napp, A. Ekkernkamp, A. Kramer, and M. B. Stope, “Cold Atmospheric Plasma in the Treatment of Osteosarcoma,” *International Journal of Molecular Sciences*, 2017. doi: 10.3390/ijms18092004.
- [5] E.R. Adhikari, S. Ptasinska, “Correlation between helium atmospheric pressure plasma jet (APPJ) variables and plasma-induced DNA damage,” *European Physical Journal D*, 2016. doi:10.1140/epjd/e2016-70274-6.

Appendix

Appendix A: Gel Electrophoresis

Gel electrophoresis is a technique that separates biomolecules based on their polarity, which is partially determined by a given molecule’s size and shape. The more negatively electronegative a molecule is, the more likely it is to move across an agarose gel from the negative electrode to the positive electrode. However, if the molecule has a lot of mass, it may also move slower across the gel. Figure 3 shows what a typical gel looks like for this experiment.

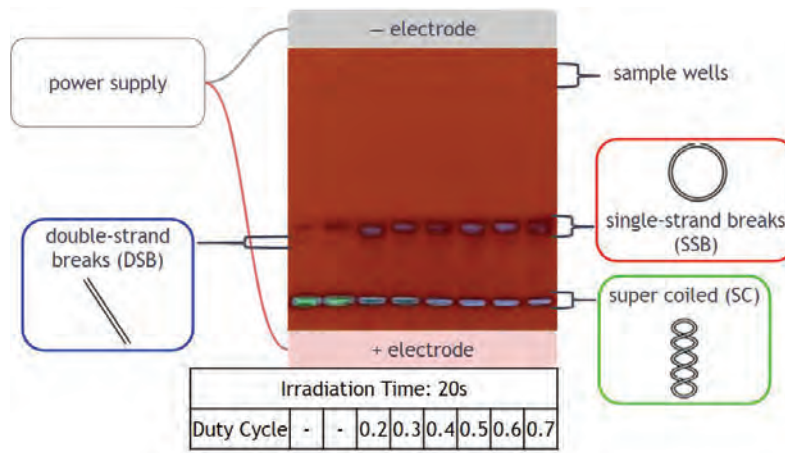


Figure 3. Schematic of a gel electrophoresis machine using an example piece of data from a 20 s trial.

Detecting PFAS in Water Samples

Using PIGE

Emily McGill

2019 NSF/REU Program

Physics Department, University of Notre Dame

Advisor: Dr. Graham Peaslee

Abstract

Perfluoroalkyl substances (PFAS) are man-made chemicals that have been linked to a variety of adverse health effects in humans. One of the primary means through which humans are exposed to these chemicals is through drinking PFAS-contaminated water. PFOA (perfluorooctanoic acid) and PFOS (perfluorooctanesulfonic acid) have been the most widely produced and studied of all PFAS, and the US Environmental Protection Agency (EPA) has issued a health advisory level for the combined concentration of PFOA and PFOS in drinking water of no more than 70 ng/L. In this study, particle-induced gamma-ray emission (PIGE) and weak-anion exchange (WAX) cartridges were used to analyze water samples containing varying amounts of PFOA. The accuracy, precision and limits of detection and quantification of PIGE as a total fluorine measurement technique were established. It was found that for fluorine masses on the order of μg s, the method could be used to accurately determine the amount of fluorine present in each sample. The short analysis times and accurate measurements could make PIGE a very valuable tool in screening water samples quickly and reliably for the presence of PFAS.

Introduction

PFAS are a group of man-made chemicals notable for their excellent hydrophobic and lipophobic properties, as well as their environmental persistence and toxicity. PFAS have been manufactured and used in industries globally since the 1940s, in products such as non-stick cooking appliances, FCMs (food contact materials), waterproof cosmetics and clothing, stain resistant carpets, paints and polishes, and aqueous film-forming foams (AFFFs) [1]. AFFFs, used widely to extinguish fires, contain especially high levels of PFAS. These substances are used by firefighters and members of the military when responding to fires, but were also used daily during practice drills, after which they would flow into and accumulate in surrounding soil and groundwater. Sending

PFAS-containing products to landfills also causes these chemicals to leach into groundwater sources [2]. Humans are exposed to PFAS by drinking contaminated water and consuming PFAS-containing products. Biomonitoring studies have suggested that ~95% of the US population have measurable amounts of PFAS in their bloodstream [1]. Because of their stability, they stay in the body for many years, meaning that the concentration of these chemicals in human blood gradually increases over time. Due to the bioaccumulation of PFAS, concentrations tend to be very high in breastmilk, which in turn can lead to high PFAS concentrations in young babies [3].

Worryingly, studies of PFAS and their effects on human health have indicated that they can contribute to increased cholesterol levels, low infant birth weights, immunodeficiencies, various cancers and thyroid hormone disruption. Perfluorooctanoic acid (PFOA) has been specifically linked to reproductive and developmental issues, liver and kidney problems and negative immunological effects in laboratory animals [4].

Most common methods of screening water samples for PFAS are time-consuming and expensive, and many only screen samples for a few specific perfluorinated compounds at a time. Particle-induced gamma-ray emission, or PIGE, is a rapid, quantitative and non-destructive technique that can be used to determine the presence of lighter elements (such as fluorine) quantitatively in an analyzed sample. The method has been used to establish the total fluorine concentration of solid samples, with sensitivities in the mg/kg range [5]. By passing water samples through weak anion-exchange (WAX) cartridges, fluorine from PFAS adheres to the sorbent beads in the cartridge, meaning that the fluorine is concentrated on the surface of a ~1 cm diameter solid target which can then be analyzed with PIGE.

In this study, samples containing varying amounts of PFOA were passed through WAX cartridges, which were subsequently irradiated with 3.9 MeV protons; the high energy of the protons meant

that the samples could be analyzed *ex vacuo*, reducing the complexity of analysis and increasing the efficiency of the method. The signals obtained were studied to determine the reproducibility, accuracy and limits of detection and quantification (LOD and LOQ, respectively) of PIGE as an analysis technique for measuring the total amount of fluorine present in a sample. The LOD and LOQ were used to examine the applicability of PIGE to scanning water samples with PFOA concentrations on the order of 70 ng/L, the health advisory level issued by the US EPA for the maximum concentration of PFOS and PFOA combined in drinking water [4].

Methods

Sample Preparation:

The prepared PFOA solutions had concentrations in the $\mu\text{g/L}$ range, with samples containing between 0 and 70 μg of fluorine. First, a 12000 mg/L (12000 ppm) fluorine solution was prepared by using a weight boat to measure out 8.672 g PFOA (the chemical formula for PFOA is $\text{C}_8\text{HF}_{15}\text{O}_2$; 8.672 g PFOA corresponds to 5.970 g fluorine) and adding it to 50 mL of methanol and 450 mL deionized (DI) water. This solution was then diluted by adding appropriate amounts of DI water. Since PFOA is a surfactant, the solution had to be shaken well to homogenize it between dilutions. An Oasis[®] WAX cartridge, as shown in Figure 1, was used to extract the fluorine from the water sample passed through it. This technique is known as solid-phase extraction, or SPE:

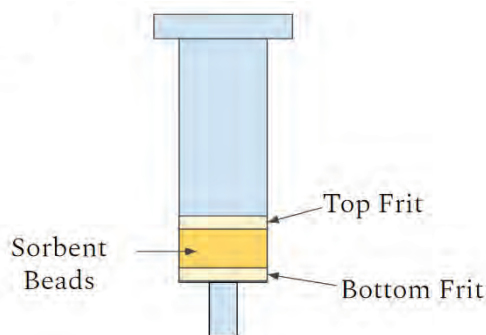


Figure 1: A diagram showing the layers of an Oasis[®] WAX cartridge.

Each cartridge was conditioned by applying 3 mL of 0.1% (v/v) ammonium hydroxide in methanol (for inorganic fluorine removal), 3 mL of methanol, 3 mL of deionized (DI) water, and varying volumes and concentrations of PFOA solutions. The solutions were inverted 10 times before being added to the cartridge to ensure homogeneity. Blanks were prepared for each batch of samples (typically one blank for every 6-10 PFOA samples) by passing 50 mL of DI water through the WAX cartridge.

The cartridges were dried by applying millitorr vacuum for 30 s. The sorbent beads were solidified by applying ~2.5 mL of shellac, a natural bioadhesive. Vacuum was re-applied for 1 min, and the cartridges were then allowed to dry (passively) for at least 1 h before analysis. The solidification process was necessary to prevent the surface layer of sorbent beads from dispersing when the cover frit was removed for ion beam analysis, which would have resulted in a lower PIGE signal.

Once dry, the solidified sorbent beads were cut from the plastic cartridges and the cover frit was removed. Each sample was mounted on a stainless steel target frame for PIGE analysis. The WAX cartridges each contained 60mg of 60 μ m sorbent beads, with each slice consisting of a ~3 mm thick section of the beads. There was a gap of ~1 mm left between the surface of the bead layer and where the plastic cartridge was cut.

The target frames were labeled and then mounted on a target wheel. The wheel was placed at the end of the beamline, with the targets perpendicular to the incoming proton beam. PIGE analysis of powdered inorganic fluorine standards (NaF in cellulose) of known concentrations was also carried out twice per day in order to normalize the total fluorine signals from the PFOA samples.

PIGE Analysis:

Particle-induced gamma-ray emission (PIGE) was achieved using the Alpha-Toss ion source (a modified version of the NEC Alphasource) and the 3 MV St. Andre accelerator at the

University of Notre Dame. The Alpha-Toss separated hydrogen atoms, which flowed into a quartz bottle through a thermomechanical leak, into their constituent H^+ ions (protons) and electrons using a radio frequency (RF) oscillator. The protons were then accelerated through gaseous rubidium, which transferred 2 electrons to some of the H^+ ions, forming negative H^- ions. These ions then accelerated towards the positive charge at the center of the accelerator tank, generated by a Van de Graaff generator. Upon reaching the center of the tank, they passed through a piece of carbon foil. This stripped them of their electrons, forming H^+ ions once more. These protons were then repelled by the positive charge in the center of the tank, resulting in further acceleration.

Having been accelerated through the tank, the protons passed through bending dipole magnets, which bent the beam by 90° to the end station, where the samples were located. They also passed through two sets of focusing quadrupole magnets on either side of the bending magnets.

Upon reaching the end station, the beam of protons passed through an $8\ \mu\text{m}$ Kapton[®] window and through ~ 30 mm of air to the target. The beam excited the target nuclei, which subsequently de-excited by emitting gamma rays of characteristic energies. Fluorine-19 nuclei emit characteristic gamma rays at 110, 197, 1236, 1349, 1357 and 1459 keV. The yields at 110 and 197 keV, however, are much higher than those at other energies; therefore, the areas of these two peaks were measured in this experiment. The gamma rays were detected, and their energies measured, using a high-purity germanium (HPGe) detector at the end station, at an angle of 45° to the incoming beam.

Each sample was irradiated for 180 s with a beam current of ~ 50 nA. This current was recorded before and after each of the NaF standards was analyzed. The average current during the 180 s run was assumed to be the mean of these two beam current readings.

As well as PIGE, PIXE (particle-induced x-ray emission) data were recorded during each run, to determine the relative amounts of heavier elements, such as argon (Ar), exposed to the ion beam.

Because both the concentration of argon in air and the amount of air in front of the targets remained constant, changes in the strength of the Ar PIXE signal between analyses were assumed to depend only on differences in the beam current. By comparing the Ar peaks corresponding to the NaF standards (for which the beam currents were recorded) to the Ar peaks for each water sample, the current incident on each sample could be determined. Thus, the fluorine signal (i.e. the sum of the number of counts in the 110 keV and 197 keV peaks) was expressed in Ar-normalized counts/ μC (the current was multiplied by 180 (seconds) to determine the total charge incident on each sample during irradiation). This normalization meant that differences in fluorine signals depended only on corresponding differences in the amount of fluorine present in each target.

Results, Discussions and Conclusions

The first test examined whether the Ar-normalized signal per μC depended only on the amount of fluorine (in μg) present. 16 samples containing 2.5 μg F (~ 3.6 μg PFOA) were prepared, with four duplicates each of four different concentration/volume combinations (100/25 (25 mL of 100 $\mu\text{g}/\text{L}$ F solution), 50/50, 25/100 and 10/250). One of the 50/50 samples became contaminated, so the data relating to it were discarded. The mean signal was 121.1 (Ar-normalized counts/ μC), with a standard deviation of 16.5 (13.6% relative standard deviation, or RSD) and a standard error of the mean (SE) of 4.3. Overall, the signals obtained from each sample were approximately equivalent. There was no dependence observed on the concentration or volume of PFOA solution used; so long as the amount of fluorine in each solution was kept constant, the corresponding PIGE signals also remained approximately constant.

A calibration curve was plotted to determine the accuracy of PIGE as a measuring tool for total fluorine in water, and to find the limits of detection and quantification of the technique. A total of 46 different solutions containing between 0 and 2.5 μg F were analyzed using PIGE. The mean

and standard deviation of the signals corresponding to each fluorine mass were calculated and used to plot the following linear trendline and the error bars on each of the data points, respectively:

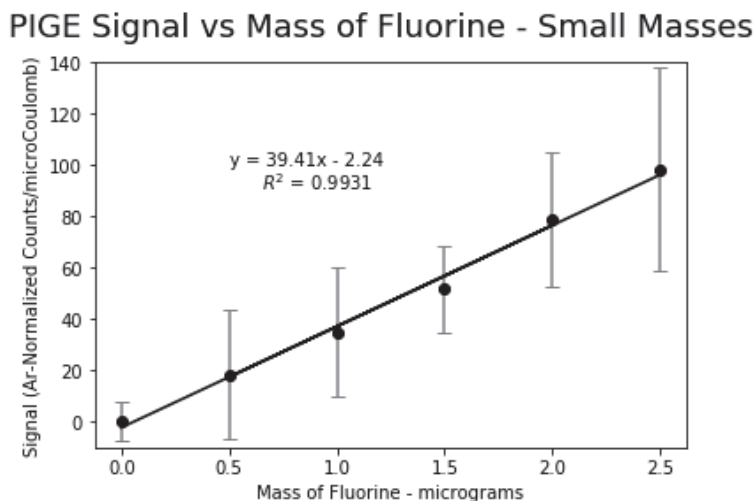


Figure 2: PIGE signal (background subtracted) vs fluorine mass in n = 46 PFOA solutions.

The trendline drawn was within the error bars of all data points. The large error bars resulted from the relatively high standard deviation of the PIGE signals corresponding to each fluorine mass. While the signal for each mass differed between samples, the high R^2 value (0.9931) of the trendline shows that the relationship between the mean signals was highly linear.

The LOD and LOQ for the PIGE method of analyzing water samples were calculated from the data shown in Figure 2. The LOD was defined as the mass of fluorine needed to produce a signal three times the standard error of the estimate using an ordinary least squares regression analysis. The LOQ was defined as three times the LOD. The LOD and LOQ were found to be 0.26 and 0.78 μg of fluorine respectively, corresponding to ~ 5.4 L and ~ 16.3 L of 70 ng/L PFOA. These limits could potentially be decreased by running more replicates of each sample, or by increasing the beam current and/or sample irradiation time. However, increasing the beam intensity could result in the samples being thermally damaged, while increasing analysis times would negatively

impact one of the main advantages of the PIGE method, namely the speed at which samples can be analyzed.

The relatively high LOD and LOQ for pure PFOA solutions are in stark contrast with other studies conducted in the lab on groundwater samples from a US Air Force base, which were also tested for fluorine presence using PIGE. Many 50 mL volumes of these groundwater samples returned signals above the LOD defined above. If the total fluorine in these samples was a result of PFOA contamination alone, their concentrations would be in the range of ~7600 ng/L PFOA; over 100 times the EPA advisory level. We hypothesize that there are likely multiple PFAS in any environmental solution, for which the EPA has not yet issued any health advisory levels. Detection of these “precursor” PFAS and other environmental PFAS without having to run multiple analyses is one of the main advantages of total fluorine analysis techniques such as PIGE.

Finally, 32 PFOA solutions containing fluorine masses ranging from 0 – 70 µg were analyzed to determine the upper limit of quantification of fluorine using the WAX cartridge and PIGE method.

The following plot displays the relationship between the signals and fluorine masses:

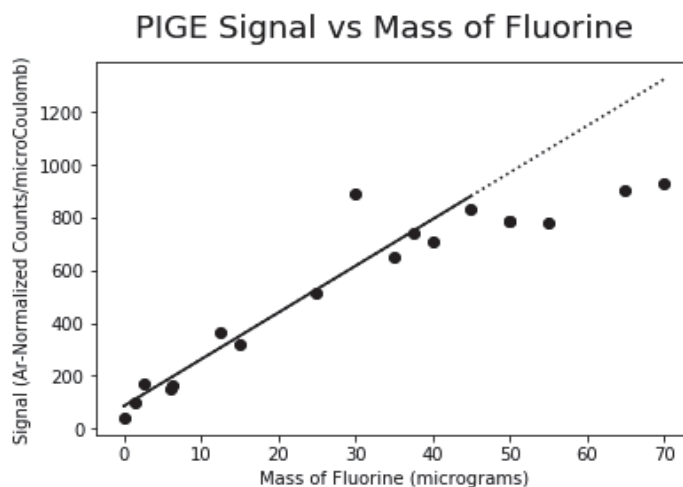


Figure 3: PIGE signal (background subtracted) vs fluorine mass over a range of 70 µg F.

From the data in Figure 3, the relationship between signals from lower fluorine masses appears relatively linear. However, once the fluorine mass per sample exceeded $\sim 45 \mu\text{g}$, this linearity began to disappear, and the amount of fluorine present could not be accurately quantified based on the PIGE signal from these samples. When larger amounts of fluorine were added, the surface of the sorbent bead layer of the WAX cartridges became saturated with F^- ions. Some of the fluorine captured by the WAX cartridge adhered to sorbent beads deeper within the cartridge, below the surface layer. As protons cannot penetrate through the entire cartridge, fluorine within the bead layer produced a smaller signal than fluorine bonded to the surface sorbent beads.

PIGE is an extremely valuable technique for detecting harmful PFAS in water. Results obtained from 3 min analyses allowed quantification of total fluorine in PFAS down to masses below $1 \mu\text{g}$. The comparison of the detection limits with signals from small volumes of groundwater highlighted the fact that PFOA made up a very small percentage of the total concentration of PFAS in the contaminated samples; this comparison could only be made because PIGE is a total fluorine technique.

References

- [1] NGWA Press, *Groundwater and PFAS: State of Knowledge and Practice*, 2018.
- [2] Hannah Hamid, Loretta Y. Li and John R. Grace, *Review of the Fate and Transformation of per- and polyfluoroalkyl substances (PFAS) in landfills*, 2018.
- [3] Grandjean, P. et al., *Estimated Exposures to Perfluorinated Compounds in Infancy Predict Attenuated Vaccine Antibody Concentrations at Age 5-Years*, 2017.
- [4] EPA, *PFOA and PFOS Drinking Water Health Advisories*, 2016.
- [5] Ritter E. et al., *PIGE as a screening tool for Per- and polyfluorinated substances in papers and textiles*, 2017.



AUSTIN MITCHELL

2019 NSF/REU Program

Physics Department, University of Notre Dame

ADVISORS: DANIEL BARDAYAN, PATRICK O'MALLEY

Abstract:

There is a vast catalogue of unexplored reactions which take place in stellar environments, and in this experiment we sought to characterize one of them. By using the Rhinoceros gas target system in conjunction with the 5U particle accelerator at the University of Notre Dame, we were able to circulate ^{20}Ne gas for our target and create a beam of alpha particles to simulate the reaction $^{20}\text{Ne}(\alpha, p)^{23}\text{Na}$. This reaction has been previously studied, but not at astrophysically relevant energies or in adequate detail. Our goal was to use beam charge integration data to normalize the reaction rates we measured, and thus explore a previously studied energy range with greater certainty. The 5U accelerator also allowed us to drop to lower energies than previous experiments had been able to reach, extending the range of data on this reaction.

Background:

In the study of Type 1A Supernovae, it is believed that this reaction is one of a handful that have a great influence on many other reaction rates. This reaction has been studied before with an alpha beam and a Ne target, but they were only able to indirectly detect the reaction by measuring gamma emissions from the decay of the first excited state of ^{23}Na (p1), and thus had no information on the p0 state. Another study used a ^{20}Ne beam on a He target, but at much higher energies than the stellar environment between 30 and 100 MeV.

Experimental Setup:

To model this reaction in the Notre Dame nuclear laboratory, we utilized the Rhino gas target system on the 5U accelerator beamline. Rhino is a pumping system

designed to circulate gases and create an extended gas target for the particle beam to collide with. Thus, we circulated ^{20}Ne gas through the target chamber and bombarded it with a beam of alpha particles from the 5U accelerator. As the particles come down the beamline, they will go through the multiple sections of Rhino's differential pumping. Because the main beamline is kept near vacuum, we do not want excess gas from Rhino leaking back upstream. Rhino is therefore designed with successive chambers that step up the pressure to ~ 10 Torr in the target chamber.

To measure the reaction, we have to know what the reaction products are. When the alpha particles collide with the ^{20}Ne gas, several reactions are possible. The one we are interested in happens when the alpha embeds itself in the ^{20}Ne nucleus and ejects a proton, leaving behind ^{23}Na . To pick up these protons, an array of Si detectors was installed around the target chamber. Of course, the detectors can also pick up scattering of alpha particles, and even some of the ^{20}Ne and ^{23}Na nuclei, thus we used the Catkin spreadsheet to calculate what energies these other particles as well as the protons will have when colliding with the detectors to identify their peaks.

In general, Si detectors are very sensitive. They work by conducting an electric current when a particle hits their detector face and bumps an electron up to the conduction band. Because they were critical to performing the experiment, we were tasked with testing the detectors we had at the university to make sure there were enough that work properly.

To test the roughly 30 Si detectors in the lab, we placed each one in a light-isolated vacuum chamber with an alpha particle emitting sample of Am-241. Each

detector was tested at an optimal voltage, determined by documentation or viewing the signal on an oscilloscope, as well as +/- 50% of the optimal voltage. The data we got from each test was a text file with each line containing the channel number of the detector corresponding to an energy level and the number of detections in each channel. For most of the detectors, the data appeared as a near-Gaussian peak. This peak shape would be crucial for determining the energy resolution of each detector, and so we went about writing code to fit a Gaussian peak to each data file.

In Python 3, we wrote a program to calculate a best fit Gaussian function of the form:

$$g(x) = Ae^{\frac{(x-c)^2}{2\sigma^2}}$$

Where A is the height of the peak, c is the x-coordinate of the peak, and sigma would normally be the standard deviation of some set of values. In a true Gaussian distribution, the standard deviation defines how wide the peak is, but for our purposes, we created a function to vary sigma and retain the value thereof which minimized the mean squared error of the fit and the actual data. After plotting each fit with its corresponding data to verify the quality of each fit, the energy resolution of each detector at each voltage was calculated. The energy resolution is calculated as the FWHM (full width at half maximum) of the Gaussian fit divided by the x-coordinate of its peak, and then multiplied by the energy of the alpha particles emitted by the Am-241 source. This comes out to

$$\text{Energy Resolution} = \frac{\sigma E}{c} \sqrt{\ln(2^8)}$$

where σ is the optimized gaussian parameter, c is the x-coordinate of the peak, E is the alpha energy of 5.486 MeV from the Am-241 source, and the square root coefficient comes from solving for the FWHM from the Gaussian parameters. The sharper the peak, the smaller the FWHM, and thus the smaller energy increment a detector is able to resolve.

After compiling a spreadsheet with the voltages and resolutions for each detector, we tested the detectors again without light isolation in the vacuum chamber. This is important for the experiment because we will be putting an electric current through Ne gas, and thus expect that it will fluoresce inside the target chamber. Because Si detectors are so sensitive, incident photons will trigger the detector and result in some amount of “dead time” where it is still processing the signal from a detection and cannot detect any new events. A majority of the tested detectors were not suitable for the job, having a dead time of 60% or higher, all except for the so called “ruggedized” detectors, which are treated to block out low energy ambient light particles. After the second round of testing, we had narrowed down our detector options to a group of about 9 with energy resolutions in the range of 30-40 keV.

The target chamber at the end of the beamline is in the shape of a disc standing on its side, roughly 20 cm in diameter and about 2.5 cm wide. There are mounting points for hardware at different angles around the disc, measured from 0° parallel to the beam, up to 90° perpendicular to the beam, and 180° anti-parallel to the beam. The top and bottom halves of the disc have mounting points at different intervals to allow for coverage of a greater amount of discrete angles. Because reaction products can

bounce in any direction after a collision, the geometry of detector placement is critical in interpreting any data collected.

At any point where a Si detector may be mounted, there are several pieces of hardware between the target chamber and the detector itself. A collimator roughly 5 cm in length fits into the side of the chamber, with a slit side that faces the inside of the chamber and a hole aperture that faces the detector. The orientation of the slit as well as its width determine what areas of the target-beam interaction a detector is exposed to, and were chosen so as to have every detector exposed to roughly the same length of target interaction to make comparing data from different detectors easier. On the outside of the chamber above the collimator a cylindrical mount is screwed into place, and a canister is clamped onto it with an O-ring in between them to hold vacuum. The detector itself is screwed into a feedthrough that is threaded through a disk, and the disk is fitted with an O-ring to hold a vacuum when clamped to the top of the canister.

The detectors at each angle were numbered 2 through 7 as follows:

Angle(deg rees)	45	60	90	105	120	135
Number	2	3	4	5	6	7

Each detector was wired to a combination preamp/amplifier, and the outputs for each from the amplifier were sent to their own analogue-to-digital converter (ADC) modules. Two bias suppliers were used to apply voltage to all six detectors, each with a meter to read the leakage current from the detectors. All ADCs were connected to a computer

system next to the target which can be remotely operated from the accelerator control room. The data from all detectors was recorded with MPANT on Windows XP.

Procedure:

To prepare Rhino for operation, the entire system must be pumped down with roughing pumps that are able to handle atmospheric pressures. Once they have achieved a decently low vacuum, roots blowers and then turbo pumps which are too fragile to operate in full atmospheric pressure can be activated to achieve a higher vacuum. Through an inlet in the system, the target gas can be released from a pressurized tank into the system in small amounts to begin circulating it through the target chamber. A single target chamber valve can redirect gas out of circulation leaving the chamber empty, or release it to be circulated through the target chamber again.

The 5U accelerator also required several hours of tuning at the start of the experiment to reach our desired starting energy and align the beam so that it makes it all the way to the target. The starting energy was 6 MeV per alpha particle to overlap with the energy range of the previous experiment, and with steps of a few hundred keV for each run we reached the endpoint of 3.5 MeV.

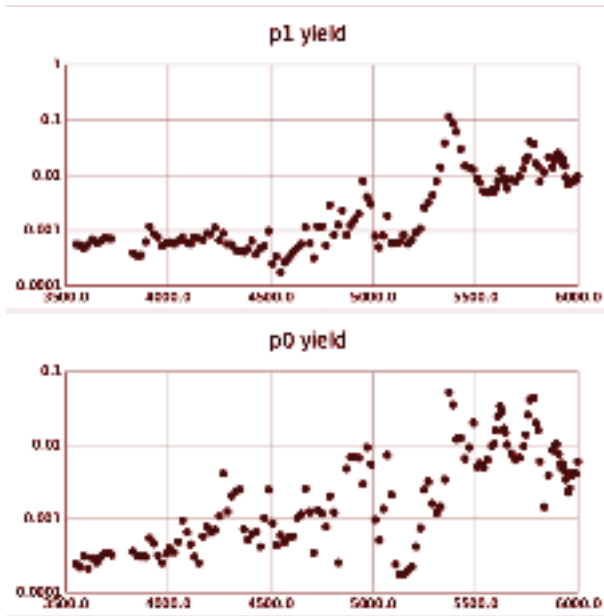
The experiment was very involved and required the experimenters to stay active in the data acquisition process. At each data run, the circulating gas had to be removed from the target chamber. With no gas in the target chamber, the beam charge was integrated for 2 minutes before taking data. Gas was then reintroduced to the chamber, and once the pressure stabilized around 9 Torr, it was recorded. The beam was then allowed into the target chamber and data acquisition began. After the data run was

stopped, the gas was evacuated from the chamber and the beam charge was integrated again before changing beam energies.

Integrating the beam charge before and after each run was important to normalize the data later, so we can account for how the amount of beam may have changed over the course of a single data run.

Results:

Throughout the experiment we witnessed many distinct resonances, or specific beam energies that induce a heightened reaction rate. There were different resonances for both the p0 and p1 ejected protons. The p0 is an ejected proton from a reaction which produced the ground state of ^{23}Na , and the p1 comes from a reaction producing the first excited state of ^{23}Na . Using numbers from the 90° and 120° detectors, we used a spreadsheet to calculate a rough estimate of the reaction yields by comparing the number of detected protons in each state to the number of alpha particles which



scattered off of the ^{20}Ne atoms. These yields are shown in the figure to the left. Much data analysis remains to be done to calculate the exact reaction cross section, and the reaction rate from there. We were able to take data to an energy range more analogous to the stellar environment than any prior studies.

Development of the Electrical Feedthroughs for the ND-cube Active-Target Detector

Adil Mubarak

2019 NSF/REU Program
Physics Department, University of Notre Dame

Advisor: Tan Ahn

Abstract

Studying the nucleus is a difficult task. This is because the nucleus has many variables that we must take into consideration if we are to explain what is going on. There have been models created to help understand the nucleus, but the problem is having these models validate experimental results. One of the ways to validate the model is by creating an active-target detector. The active target detector allows us to image the particles track as it travels through the detection medium, which we can use to infer the energy at which the reactions happen. Notre Dame is in the process of creating an active target detector, but the challenge was being able to have the electronic signal inside the cube to be sent to the data acquisition on the outside. The solution was to create a 1000 channel printed circuit board (PCB) board, that will have components on both sides so that the electron detector on the inside can send signals to the data acquisition. The reason behind using a PCB board was because it took up the less amount of space compared to having 1000 wires that is connected from inside the cube to the outside. To make sure that a PCB will hold up against the difference in pressure from inside the cube and outside, a prototype board was ordered. When testing with a roughing pump was done, the cube was about to pump down to 11 millitorr. This then proved that the PCB can now be manufactured. After both boards arrive the cube will be ready for testing.

Introduction

One of the models to describe the nucleus is the nuclear structure. These nuclear structures tell us how the nucleus is clustered which can help explain how the nucleus decays in a certain way. Studying nuclear structure can also help understand why the hoyle state exist, which is a key component in life. The hoyle state is an excited state of carbon that Fred Hoyle postulated that it must exist for there to be life. To get this carbon to create life we need a source

that produces these carbons. Which we rely on the sun for this. The sun can create carbon by first fusing hydrogen in the core to get helium. Then when the core shrinks, after it has burned through its fuel, the next stage of fusing occurs. The combination of two helium atoms is used to form beryllium-8. The thing is that beryllium is unstable and will decay in 8.19×10^{-17} s to two alpha particles, but sometimes a third alpha will combine with the first two to create the hoyle state. The problem is that hoyle state will decay to beryllium and an alpha particle most of the time. But one excited state of carbon in a 2,500, will give off a gamma ray and give us the stable atom that gave us life [2]. Basically, by studying nuclear structure we can understand how carbon came to exist which is a prerequisite for life.

A useful way to study nuclear structure is to use an active target detector. They are useful for two reasons. The first is that their usefulness for radioactive beams. A radioactive beam is a result of colliding a normal beam into a target and using a magnet to focus the product. For example, a boron-10 beam colliding with helium-3 will create carbon-10 and hydrogen-3. The carbon-10 beam is what we want, so the magnet is used to focus the beam. The problem is that the amount of beam at the start is significantly more, by a factor of million, than the beam that you would want to use. Since the reaction rate is proportional to beam intensity, this means you must wait for a very long time before you can get good enough data. For an active target, your taking into consideration that the reaction rate is proportional to the target area, so by having a larger area we can have more reactions occurring. This is done by filling a cube with gas, and allowing the beam particle to continuously collide with the gas particle until it deposits all of its energy. The other reason why active target detector is used is its usefulness of using a gas instead of a normal solid target. This means that the reactions will occur at a slower rate and more spread out thus allowing us to map out the collision path.

Here is how the cube uses the benefits of active target detector. To use the cube, we must choose a gas to fill the vacuum cube and choose the element that the beam is made of. Then shoot the beam inside the cube. When the beam collides with the atoms of the gas, it will have enough energy to ionize electrons. The ionized electrons are then pulled down by an electric field of 400V to the electron detector laid out at the bottom of the cube. The problem here is that detecting a single electron is a difficult task, but if there is more than one electron then we can detect them. This is where the micromegas come into play. The micromegas includes a micromesh plane that is 128 μ m above the anode PCB board. That spacing generates a 40,000V electric field gradient. So when one electron passes the micromesh it will speed up and ionize another gas which will lead to an avalanche effect. This avalanche effect can be easier to get the reading of electron than by having just one electron. One may ask, if we record many electrons how will we know the energy of the one at the start before the it entered the micromesh. This is where the gain comes into play. Before we record data, we need to know how many electrons are produced in the micromega for every one electron produced in the collision. In the end, by reconstructing the collision path, we can create a histogram of how many collisions occurred along the length of the cube as each beam enter the cube. By relating the collision occurring at each location and the energy deposits, we can look for peaks in the histogram that a reaction occurred at that location. Thereby relating this energy peak to the energy level of the atom, that will be created from the gas and beam particle, we help prove that clustering exists.

Objective

The goal of this summer is to create a bridge between the sensors inside the cube with the data analyzer on the outside. Also, another thing that must be done is for me to create a device

that will be used to filter out the low signal from the sensors inside the cube. Both of these tasks require the use of PCB boards. To create the PCB board, I needed to use a software called eagle.

Methods

Eagle

Eagle is a software that is useful for creating PCB boards. A PCB is a thin board that is made of laminate material and has conductive path etched in the material that is routed between components. For example, I can have a led light and battery soldered onto a PCB board and by creating the right conductive path, the led will light up from the supplied power of the battery. Most boards don't have simple routes, which is how eagle comes into play. Using eagle, we can have a multilayer board. This is really useful for when you want to use less board space or if you need to jump over routes. To access the other layers routes will be connected through vias which is similar to a drill hole but the thing is that once the route is connected to the via we can specify which layer we want the vias to be connected to each other and these will allow a route to be carried on. The only set back is that having more layers on a PCB board will cost extra, that is why we need to be aware of this and try to use the least number of layers. By getting some experience and understanding eagle, I was able to create two PCB boards that play a large role in my project.

The first board, which we called zap board A, is what will be used to connect the inside of the vacuum cube to the outside. Zap board A can be thought of as a lid to a glass jar. The board will be placed up against the back flange and the slots on the flange will allow us to connect to the board. To make sure the vacuum is actually sealed o-rings are utilized which are compressible plastic rings which will fill any area that may have a leak. Zap boards A has

components on both sides of the board with both these components being non right-angled female connectors. The inside will be connected to the micromega sensor, having a configuration of 3x3 while utilizing 112 out of the 120 pins female connector pins, through the use of ribbon cable. The outside will be connected to another PCB boards, having a configuration is 4x4 while 64 of the 80 pins are used. This other board will have right angle components which mean once the two board are connected, they will be perpendicular to each other. The reason why we could not use all the pins is because the data acquisition and micromega sensor made sure that I used a specified amount. The connections between the inside components and outside components were simple. The other PCB board, on the other hand, was more complex to route.

The other PCB board, which we called Zap board B, is a filtering device for the signals that will be received from the micromega to zap board b. The high frequency signal gets by while the lower signals are thrown out. The difference between the high and low signal, is that the low signal is the noise while the high is the actual data we want. What filters out the low frequency is the capacitor. The capacitor is able to filter out low signals because the path along the capacitor has less resistance, according to the capacitance reactance equation, compared to the path along the resistor. But if it was just a plane DC circuit then the signal would not get filtered at all, because the capacitor will be treated as an open circuit and no information can be sent back and forth. For this reason, the micromesh sends out a pulse of signal which gives us the information that electron was ionized at a certain position.

Zap board B has 4 male right angle connectors on one side and female connectors on the other. The zap board B is routed in such a way that a path is created from the male side of the connector then it splits off into two paths. One of these paths goes to the capacitor and then gets

to the female components on the other side. The other path leads to a resistor that is then grounded. This is where the lower signals are deposited

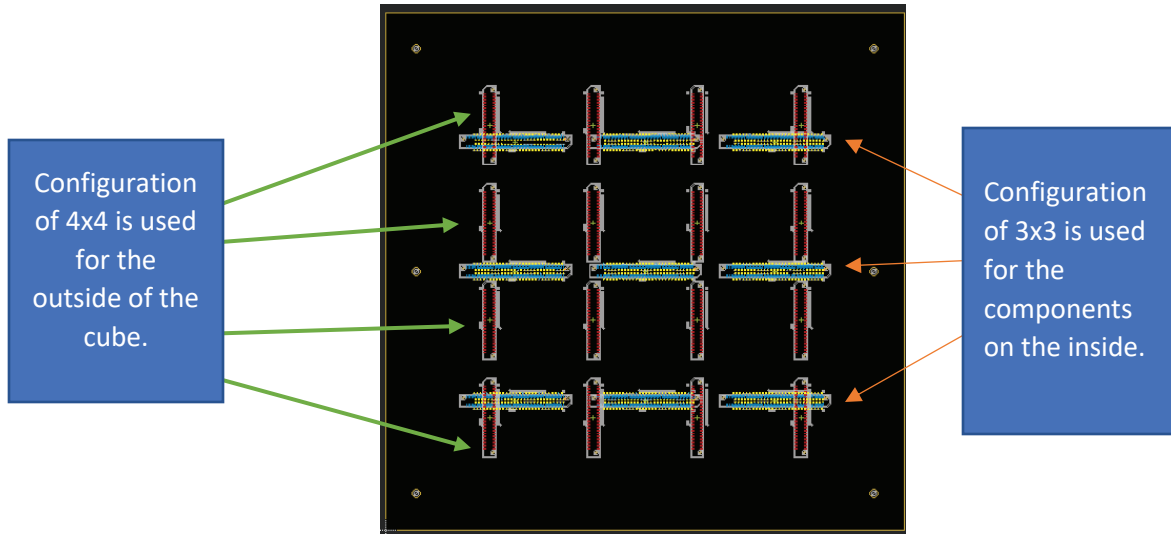


Figure 1. Visual representation of Zap board A without the route, just until the prototype has been tested and works.



Figure 2. Visual representation of zap board B.

Inventor

Besides using eagle to create PCB boards, I was also able to use inventor to create an aluminum plate for which zap board A will lay on. Supposedly, the aluminum plate will have

three slots through the plate. This is where the ribbon cable will be able to attach to the board from the anode plane. Since the board will be placed on the outside, we will need to make sure the vacuum stays sealed by using o-rings. These o-rings will compress and make sure that along the perimeter of the three slots, there is no leakage.

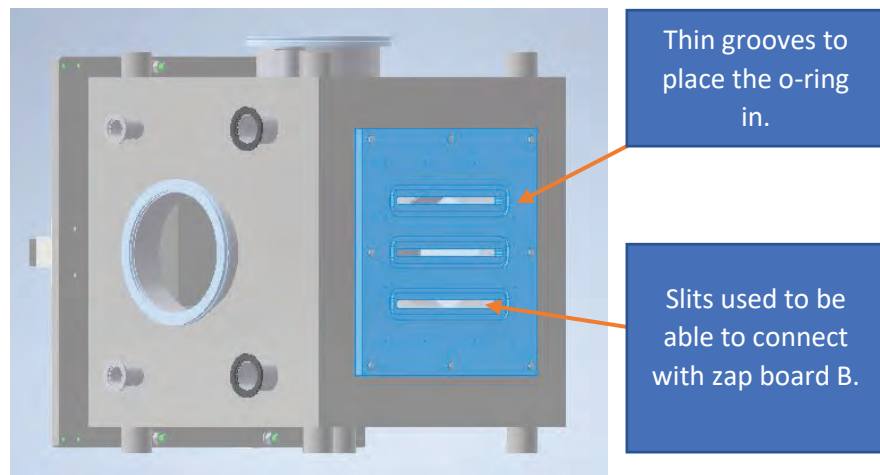


Figure 3. A screenshot was taken of inventor to visually show the inventor designed I made for the back plate to place zap board A on.

Results

One of the tests that was done with the vacuum cube was to see if zap board A will hold up against the difference in pressure from the inside of the cube compared to the outside as the air is sucked out from the inside. A prototype PCB board was ordered, which was a plain board with no routes on it, to see if zap board A will hold up in the vacuum cube. Testing was done with a ruffing pump, which connected the cube and a conveyer belt. The belt has teeth which create air pockets that will be used to pull air out of the cube and place it in the environment. What went well with the testing of the prototype board is that it held up really well in the vacuum, but what didn't go well is when the cube was left in vacuum there was a significant increase in atmospheric pressure inside the cube. It was concluded that there was a leak because

for a small volume that we were working with, the ruffing pump seemed to take a long time to pump out the air. Also, when alcohol was applied around the edges to check for leaks, we later saw that it bled through the o-ring which furthermore confirmed that there is a leak. One of the problem noticed for why there was a leak was that the o-ring was not deep enough in the grooves to allow it to squish. When the screws are tightened around the perimeter and the o-ring is not leveled with the aluminum plate, then this allows the board to be flexed and is bound to have some leakage going on. Currently one of the solution to fix the problem is to have a thinner o-ring that will fully fit in the grooves and be allowed to squish as the air is pumped. This option allows us to get the PCB flatter against the aluminum surface. Therefore, further testing needs to be done to see if having a different o-rings size will work and seal the vacuum cube and if not we need a new design to create a bridge between the sensors on the inside and the data analyzer on the outside.

Conclusion

This summer I was given the task of creating a feedthrough that will allow the electron detector on the inside of the cube to communicate with the data acquisition on the outside. I was also given the task creating a filtering device that will get rid of the low signal from the electron detector. Both of these designs have been completed with the use of eagle and inventor. Since the cube was able to pump down with the PCB board used as a door, this means that PCB board design should work in vacuum condition thus should be sent out to be manufactured. Once the board arrive, the ND-cube will ready to run its first round of tests.

Reference

D. Suzuki, et al. "Resonant α Scattering of ${}^6\text{He}$: Limits of Clustering in ${}^{10}\text{Be}$." *PHYSICAL REVIEW C*, vol. 87, no. 5, 2 May 2013.

Wolchover, Natalie. "The Hoyle State: A Primordial Nucleus behind the Elements of Life: Amazing Science." *Scoop.it*, 6 Dec. 2012, www.scoop.it/topic/amazing-science/p/4103322267/2018/11/13/the-hoyle-state-a-primordial-nucleus-behind-the-elements-of-life.

Synthesis of $(\text{BiSb})_2\text{Te}_3$ Thin Films on
Mica Through Chemical Vapor Deposition

Yohan Musle

2019 NSF/REU Program
Physics Department, University of Notre Dame

Advisor: Badih Assaf

Abstract: Topological insulators allow for interesting states of matter that can possibly make dissipationless electronic devices [1]. The states include the quantum hall effect [1] and the quantum anomalous hall effect, a quantum Hall effect that arises at zero magnetic field [1]. This work shows that chemical vapor deposition is cost effective, time efficient and a reliable method to synthesize topological insulator $(\text{BiSb})_2\text{Te}_3$. Once these films are synthesized, they are characterized through Raman Spectroscopy to verify the exact thin film composition. Most importantly electrical transport measurements are done and allow us to observe a p-type to n-type transition.

1. Introduction

Topological insulators are one of the current exciting fields in physics at the moment [5]. This is because they are insulating on the interior, conductors on the boundary, and exhibit a spin-momentum coupling effect when current is applied to the edges of the material [5]. They are most interesting because they can exhibit the quantum anomalous hall effect [1]. A phenomenon related to the quantum hall effect, yet there is zero magnetic field applied to the material. The objective is to manage to synthesize topological insulators to further study this phenomenon. The challenge is the fact that Bi_2Te_3 is usually n-type while Sb_2Te_3 is p-type. This means that they're conductors as opposed to insulators. The alloy of the two is insulating and has only been done by molecular beam epitaxy [6]. Using a CVD furnace can be a much more cost-effective and time-efficient manner.

We accomplished synthesis of $(\text{BiSb})_2\text{Te}_3$ thin films by CVD. The characterization of these films was performed through Raman spectroscopy. Electrical transport measurements observed successful tuning from p-type to n-type.

Results

A. Synthesis

The CVD furnace has three main zones left, center, and right shown in figure 1. The left zone is where the source alloys (Bi_2Te_3 and Sb_2Te_3) were placed in a quartz boat and heated to a maximum of 750°C . Mica, substrates are placed in the center zone at a temperature of 270°C , where the deposition rate is maximal. The right zone is kept at 270°C , the same temperature as the center zone. Bi_2Te_3 and Sb_2Te_3 compounds all have melting points above 320°C at 10^{-3} bar of pressure. This is important to note because the quartz tube is held at a constant pressure of 2.11×10^{-3} bar and a constant flow of inert Argon gas at 0.20 ccm to aid in the deposition of the film. The entire tube is initially heated up to 200°C and kept at that temperature for 30 minutes. Once that temperature is stable, the left zone will be elevated to 750°C , and the center and right zone will increase to 270°C in the course of 30 minutes. Those temperatures are held stable for 1 minute, then the entire tube is cooled down to 200°C in 80 minutes.

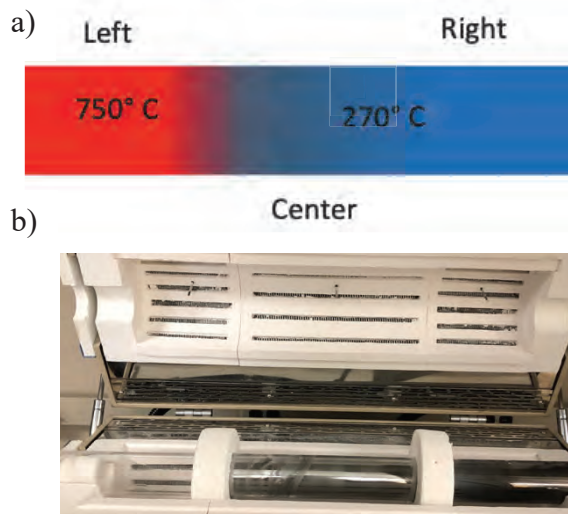


Figure 1. (a) Shows the temperature differential going from 750°C on the left zone where the alloys lie, to 270°C on the center and right zone where the substrate is placed. (b) A picture of a

An effective method of characterizing the thin films was through Raman Spectroscopy. Raman spectroscopy probes the crystal lattice vibrations to see a Raman spectrum as in figure 2 (b). The idea was to find Raman peak shifts in energy at $60\text{-}70\text{ cm}^{-1}$, $105\text{-}115\text{ cm}^{-1}$, and $135\text{-}165$

cm^{-1} . These peaks determine the crystal vibrations of $(\text{BiSb})_2\text{Te}_3$ structures, based on the W. Richter, H. Köhler, and C. R. Becker paper [3] on the investigations of the lattice vibrations of Bi_2Te_3 and Sb_2Te_3 . Along with the peaks stated, additional peaks were found at 125 cm^{-1} and 145 cm^{-1} .

Figure. 2 (a) depicts the Raman excitation modes of the $(\text{BiSb})_2\text{Te}_3$ thin film lattice. The three excitation modes are assigned to be A_{1g} or E_g . The peaks ranging from $60\text{-}70 \text{ cm}^{-1}$ and $135\text{-}165 \text{ cm}^{-1}$ are defined to be the out-of-plane A_{1g} modes. While the peaks ranging from $105\text{-}115 \text{ cm}^{-1}$ are the in-plane E_g modes [3]. Furthermore, figure. 2 (b) depicts the Raman spectra of different compositions. The excitation modes on the $135\text{-}165 \text{ cm}^{-1}$ range allow us to deduce the exact composition of the thin film according to [3]. Figure. 2 (c) shows a plot with Raman modes vs. composition extracted by comparing the data to [3]. The composition is on the scale of 0% Bismuth- 100% Antimony composition to 70% Bismuth- 30% Antimony composition. The 125 cm^{-1} and 145 cm^{-1} peaks seen in the lower compositions are not displayed in figure. 2 (c) because they are lattice vibrations of tellurium aggregates that develop on the surface of the film.

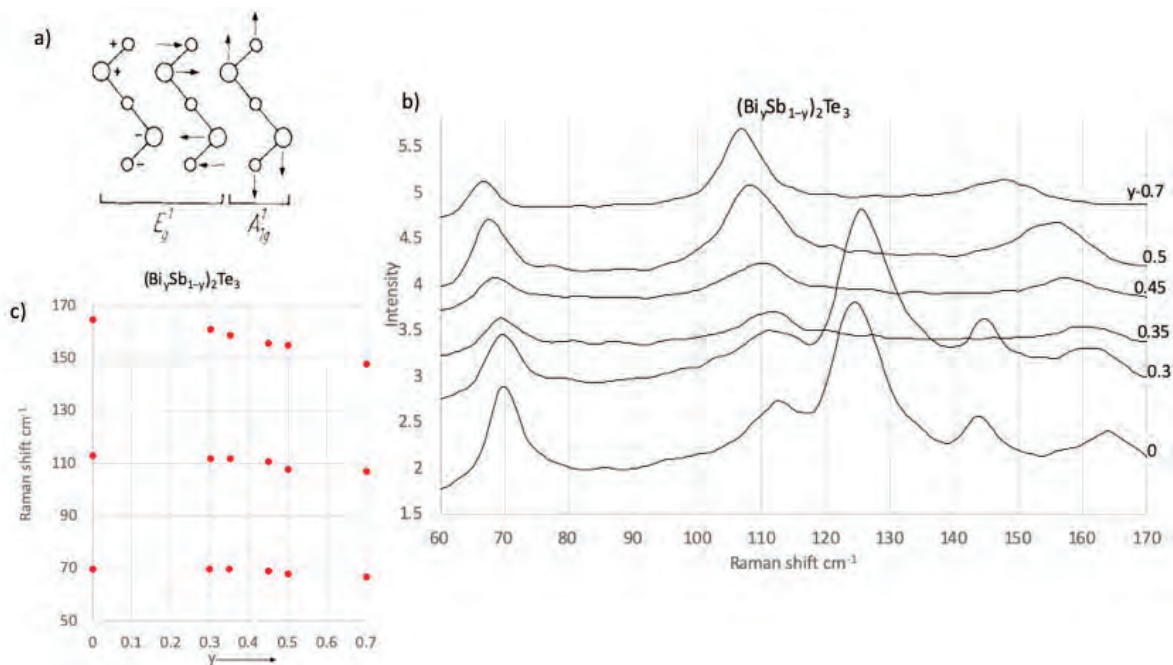


Figure 2. (a) Raman excitation modes, (b) Experimental data for $(\text{Bi}_y\text{Sb}_{1-y})_2\text{Te}_3$ mixed crystals ($0 \leq y \leq 1$). Raman spectra; (c) phonon frequencies plotted versus the composition parameter y [3].

The melting point of tellurium is 318°C , therefore annealing the samples who have peaks at 125 cm^{-1} and 145 cm^{-1} at 350°C might eliminate the Te aggregates. Therefore, two samples synthesized at 220°C 300°C respectively, were annealed for 2.5 hours at 350°C . After annealing, Raman spectroscopy was performed on them to record the changes. The surprising fact is that the peaks either completely vanished or were dramatically suppressed as shown in figure 3(a,b). From this, we can deduce that the origin of these peaks is due to an excess in tellurium. Along with this experimental effort, a paper on thermal co-evaporation of Sb_2Te_3 thin films by L. M. Goncalves, P. Alpuim, A. G. Rolo, and J. H. Correia [4] also attributed peaks in the same range to be due to of tellurium aggregates. shown in figure 3 (a) and (b).

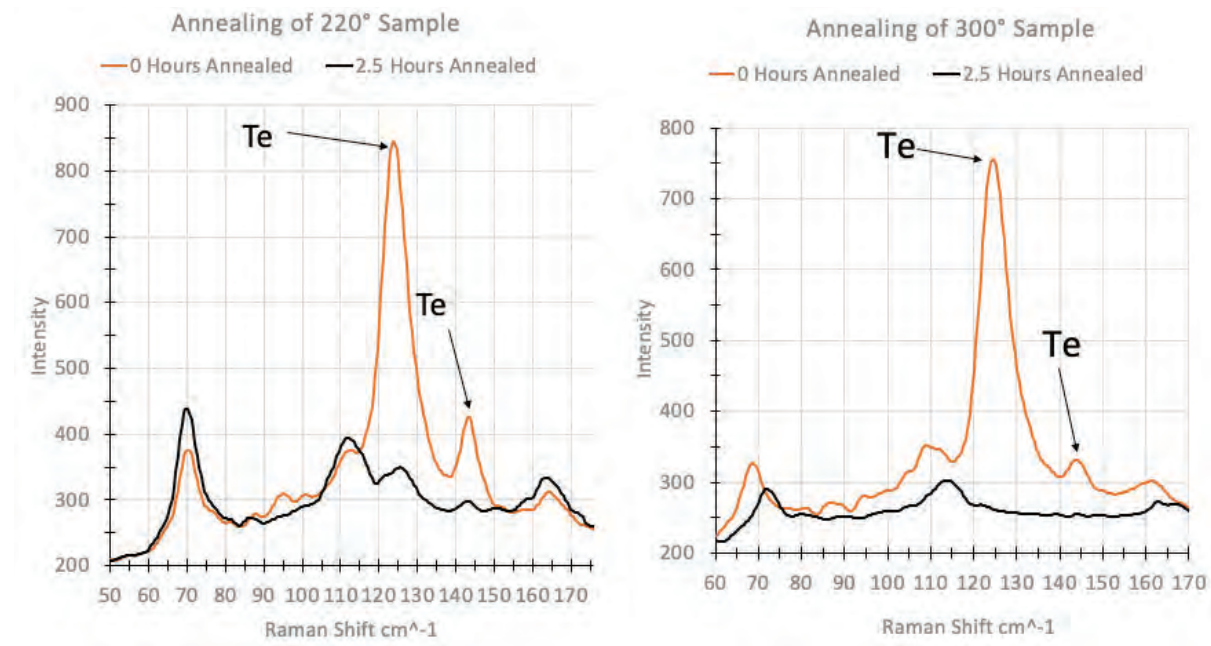


Figure. 3 (a) and (b) shows a grown sample before (orange spectra) and after annealing (black spectra). The same Raman modes we expect to see are shown on the graph, but the important

peaks to notice are the peaks marked by an arrow. As discussed before, these peaks are likely to be telluride lattice vibrations. Therefore, annealing the particular sample to 350° C shortens or removes the peaks entirely.

C. Electrical Transport

We next perform electrical transport measurements on 6 samples. At first, indium contacts are soldered onto the surface of the thin film. Then the indium contacts are connected to a holder through gold wires. Where the holder is placed on a cryocooler that is placed inside a magnetic field of maximum 0.6 T and cooled down to $T= 10.9$ K. To begin the measurement, an excitation current of 1 mA was used. We then measure the Hall resistance (R_{xy}) with respect to magnetic field and extract the carrier density from that. Figure 4 below has 6 curves extracted from electrical measurements done on the same samples discussed in figure 2 spanning $y=0$ to $y=0.7$. From each of these curves we can extract the two-dimensional carrier concentration and mobility of electrons within the thin film. This is because the carrier concentration is inversely proportional to the slope of the curve in figure 4. From the Hall effect, we obtain the carrier concentration:

$$n_{2d} = \frac{1}{ek}$$

Where e is electron charge and k represents the slope of the curve. From the carrier concentration, the measured resistance (R_{xx}), the width of sample (w), and its length (L) we can find the mobility.

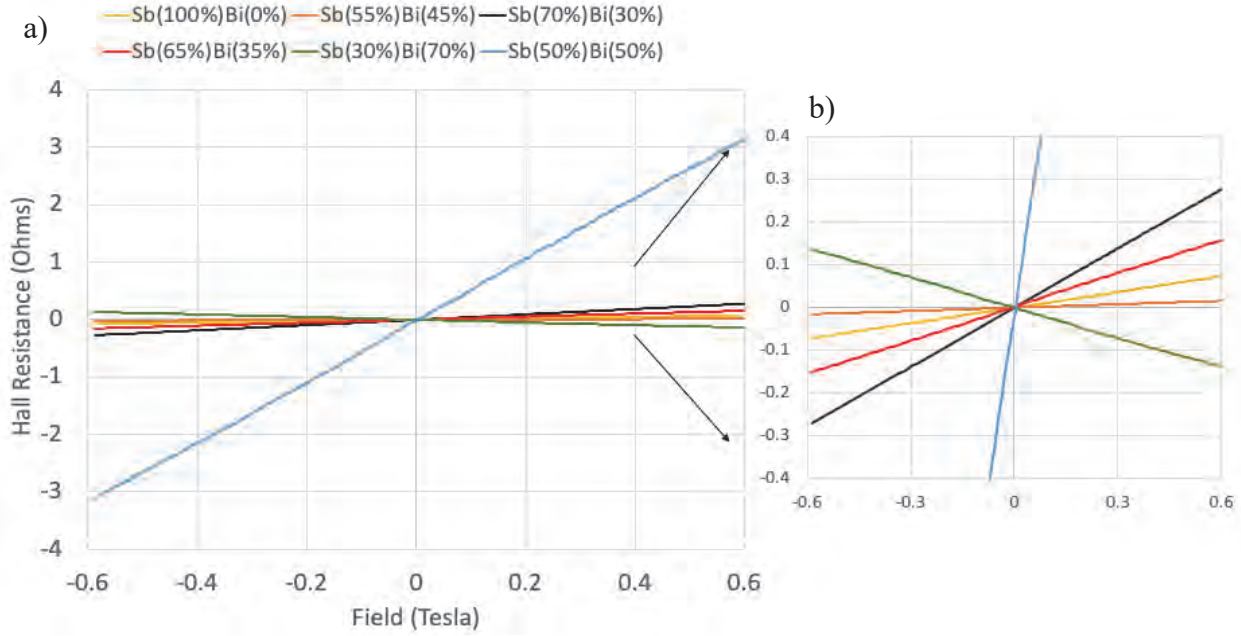


Figure 4. Hall resistance with respect to field to depict the type of semiconductor. Curves with positive slope are p-type semiconductors and negative slopes are n-type semiconductors.

$$\mu = \frac{L}{w e n_{2d} R_{xx}} \quad (2)$$

In Figure 5 (a) and (b), we plot the mobility and carrier concentration with respect to composition y . The data resulted in (i) the carrier type going from a positive to negative in the range of 5.92×10^{19} to $-2.53 \times 10^{19} \frac{1}{m^2}$, and reaching a minimum of $1.11 \times 10^{18} \frac{1}{m^2}$, which describes a better insulator. (ii) Additionally, the mobility changes by a whole order of magnitude in the range of 520 to $25 \frac{cm^2}{Vs}$. Although there are a few outliers for each figure, the trend is to a lower mobility and carrier concentration as the content of Bismuth increases. The reason for these outliers is not understood, but the figures still show a clear downward trend.

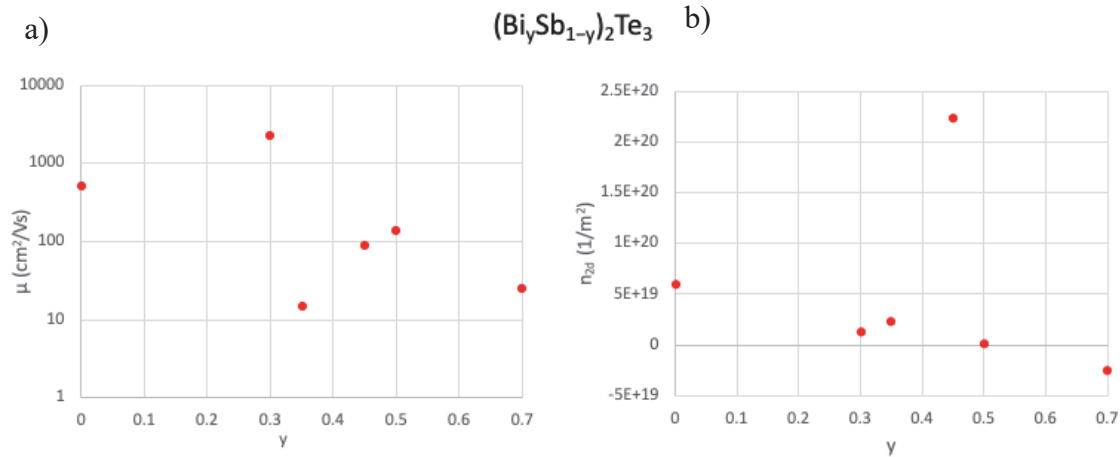


Figure 5. (a) Hall mobility versus composition. (b) Carrier concentration versus composition.

2. Conclusion

In conclusion, the CVD furnace made it possible for successful $(\text{BiSb})_2\text{Te}_3$ synthesis on the surface of mica. Raman spectroscopy allowed for proper characterization to determine the exact molar percentages of Bismuth to Antimony ratios. Once characterized, electrical transport measurements measure the Hall effect, which defines the type of film. The films are either p-type or n-type. By tuning the sample compositions, we see a clear p-type to n-type transition. This work allows future experiments on these newly created thin films in a cost-efficient and time saving way. Along with the assurance that $(\text{BiSb})_2\text{Te}_3$ thin films can exhibit topological insulator properties.

References:

[1] Chang, C., Zhao, W., Kim, D. Y., Zhang, H., Assaf, B. A., Heiman, D., . . . Moodera, J. S. (2015). High-precision realization of robust quantum anomalous Hall state in a hard-ferromagnetic topological insulator. *Nature Materials*, 14(5), 473-477. doi:10.1038/nmat4204

[2] Tu, N. H., Tanabe, Y., Satake, Y., Huynh, K. K., Le, P. H., Matsushita, S. Y., & Tanigaki, K. (2017). Large-Area and Transferred High-Quality Three-Dimensional Topological Insulator $\text{Bi}_{2-x}\text{Sb}_x\text{Te}_{3-y}\text{Se}_y$ Ultrathin Film by Catalyst-Free Physical Vapor Deposition. *Nano Letters*, 17(4), 2354-2360. doi: 10.1021/acs.nanolett.6b05260

[3] Richter, W., Becker, C. R., & Köhler, H. (1977). A Raman and far-infrared investigation of phonons in the rhombohedral $\text{V}_2\text{--VI}_3$ compounds Bi_2Te_3 , Bi_2Se_3 , Sb_2Te_3 and $\text{Bi}_2(\text{Te}_{1-x}\text{Se}_x)_3$ (*0. Physica Status Solidi (b)*, 84(2), 619-628. doi:10.1002/pssb.2220840226

[4] Goncalves, L., Alpuim, P., Rolo, A., & Correia, J. (2011). Thermal co-evaporation of Sb_2Te_3 thin-films optimized for thermoelectric applications. *Thin Solid Films*, 519(13), 4152-4157. doi: 10.1016/j.tsf.2011.01.395

[5] Inhofer, A., Duffy, J., Boukhicha, M., Bocquillon, E., Palomo, J., Watanabe, K., . . . Assaf, B. (2018). Rf Quantum Capacitance of the Topological Insulator Bi_2Se_3 in the Bulk Depleted Regime for Field-Effect Transistors. *Physical Review Applied*, 9(2). doi:10.1103/physrevapplied.9.024022

[6] Liu, W., Endicott, L., Stoica, V. A., Chi, H., Clarke, R., & Uher, C. (2015). High-quality ultra-flat BiSbTe_3 films grown by MBE. *Journal of Crystal Growth*, 410, 23-29. doi: 10.1016/j.jcrysgro.2014.10.011

A model for marine species distribution in advective-diffusive ecosystems

HA CONG NGUYEN

2019 NSF/REU Program

Physics Department, University of Notre Dame

ADVISOR(Dervis Can Vural)

Abstract

In this work, we will study the reaction-diffusion-advection models to describe population dynamics of aquatic species subject to a constant drift. We are interested in the vertical distribution profile of marine organisms at lowest trophic level by analyzing spatiotemporal pattern formation. We make use of Lotka-Volterra competition model and couple it with diffusive turbulence and advective downward drift current. We do numerical experiment to present the competition outcome, the non-trivial steady state and its dependence of the parameters that characterize the environment under certain conditions. Our models are built up step by step from single species to multispecies.

Introduction

The population dynamics and distribution of living organism in oceans has been intriguing scientists, mathematician, naturalists for a long time. Due to the highly complexity of the ecosystems, it is really challenging to have a firm understanding of the dynamics of the species. From Physics's point of view, we make assumption that the living things is shaped by the present of non-living things and physical environment. Our research philosophy is: "In biology and ecology, there are lots qualitative observations, but there are not many mathematical models underneath". In other words, we try to mathematically model the ecosystem in physical sense in order to interpret the qualitative characteristics of the ecosystem. In this work, we are interested in the problem of spatial spread of population of marine species and resources in time. We start with the simplest picture and gradually make the picture more complicated and realistic by studying different cases: single species and multi-

ple species with different physical effects. We build up the models by combine the effect of interaction ,advection and diffusion in different systems of partial derivative equations. We numerically study the nonlinear reaction-advection-diffusion equations to find its non-trivial steady state and its dependence of the parameters that characterize the ecosystem.

Background

Diffusion is the movement of a substance from an area of higher concentration to an area of lower concentration, which results in the more uniform distribution. Convection refers to the movement of a substance within a medium (e.g., water, air). Reaction between individuals refers to the process that results in the interaction and conversion of individuals. The Advection-Diffusion-Reaction (ADR) model is a mathematical model that describe how the concentration of the substance distributed in the medium changes under the influence of these three processes. In ocean environment, the turbulence of the water play the role of diffusion process. Downward currents is the advection process. The grazing and reproducing of living organisms is accounted for the reaction process. In our model, we use the Lotka-Volterra predator-prey equations for describing the of growth an interactions among species. The general form of ADR equation for two speices in 1D is[1]:

$$\frac{\partial N_1}{\partial t} = f_1(N_1, N_2) - a \frac{\partial N_1}{\partial x} + D_1 \frac{\partial^2 N_1}{\partial x^2}$$

$$\frac{\partial N_2}{\partial t} = f_2(N_1, N_2) - a \frac{\partial N_2}{\partial x} + D_2 \frac{\partial^2 N_2}{\partial x^2}$$

The Model

Single Species

Phytoplankton need sunlight for photosynthesis to turn it into chemical energy. Most phytoplankton have higher mass density than that of water, therefore they sink downward.

Despite of that paradox, the sufficient amount of random movement can balance that biased movement and lead to population persistence. We use Huisman's[2] modified equation to

illustrate this situation: $\frac{\partial u}{\partial t} = growth + death + selfcompetition + advective + diffusive$
 $= p(I_{in}exp[-K_{gb}z])u - lu - ku^2 - v\frac{\partial u}{\partial z} + D\frac{\partial^2 u}{\partial z^2}$

where $u(z,t)$ is density of the phytoplankton at depth z and time t , $p(I) = \frac{p_{max}I}{H+I}$ where p_{max} is the maximal specific production rate and H is a half-saturation constant. The light gradient is assumed to follow Lambert-Beer's law:

$$I_z = I_{in}exp[-\int_0^z ku(\sigma)d(\sigma) - K_{gb}z] \quad (1)$$

The amount of light block due to phytoplankton is negligibly small, therefore we have

$$\int_0^z ku(\sigma)d(\sigma) \ll K_{gb}z$$

The bottom and the top of the lake are reflecting boundaries, therefore we assume zero-flux

boundary conditions: $vu(z,t) - D\frac{\partial u(z,t)}{\partial z} = 0$ at $z = 0$ and $z = z_m$ The phytoplankton is

not able to manage limited light condition, therefore we set initial condition to be $u(z, 0) =$

$$exp(-\frac{vz}{D})$$

Consider explicitly the dynamics of nutrient

The phytoplankton profile in vertical axis is determined by two factors: the reduction of the light intensity near the top and nutrient in the deep layer. We assume the growth rate as follows: $\mu(N, I) = \mu_{max} \min(\frac{N}{H_N+N}, \frac{I}{H_I+N})$ We use modified ADR equations in Ryabov et al paper[3]:

$$\frac{\partial P}{\partial t} = \mu(N, I)P - mP - nP^2 - v_p \frac{\partial P}{\partial z} + D_p \frac{\partial^2 P}{\partial z^2}$$

$$\frac{\partial N}{\partial t} = -\alpha\mu(N, I)P + \varepsilon\alpha mP - \lambda N - v_n \frac{\partial N}{\partial z} + D_n \frac{\partial^2 N}{\partial z^2}$$

We simulate the model up to a depth of z_m and with the impenetrable boundaries assumption at the top and at the bottom for the phytoplankton. $vP(z, t) - D\frac{\partial P(z,t)}{\partial z} = 0$ at $z = 0$ and $z = z_m$, and $v_n N(z, t) - D_n \frac{\partial N(z,t)}{\partial z} = 0$ at $z = 0$ and N equals constant number N_B at $z = z_B$ at the bottom

Two species

We now add a higher trophic level species that graze on the plankton. The nutrient is included as resources. The PDEs turn to:

$$\frac{\partial P}{\partial t} = \mu(N, I)P - mP - qP^2 - \gamma PF - v_p \frac{\partial P}{\partial z} + D_p \frac{\partial^2 P}{\partial z^2}$$

$$\frac{\partial N}{\partial t} = -\alpha\mu(N, I)(P + F) + \varepsilon\alpha mP - \lambda N - v_n \frac{\partial N}{\partial z} + D_n \frac{\partial^2 N}{\partial z^2}$$

$$\frac{\partial F}{\partial t} = \beta\gamma PF - \delta F - v_f \frac{\partial F}{\partial z} + D_f \frac{\partial^2 F}{\partial z^2}$$

The nonlinear terms PF refers to interaction between plankton the the next upper trophic level filter feeders. The filter feeders are assumed not to have self competition. The boundary condition is similar to the single model case. We have zero flux boundary conditions.

Multiple species: A discretization generalized case

The idea of add up more species is that we build up from the 2 species case before by considering more plankton and more filter feeders. The equations becomes:

$$\frac{\partial P_i}{\partial t} = \mu(N, I)P_i - mP - qP_i^2 - P_i \sum_{j=1}^n M_{ij}F_j - v_p \frac{\partial P_i}{\partial z} + D_P \frac{\partial^2 P_i}{\partial z^2}$$

$$\frac{\partial N}{\partial t} = -\alpha\mu(N, I) \sum_{i=1}^n P_i + \varepsilon\alpha m \sum_{j=1}^n (P_i + F_i) - \lambda N - v_n \frac{\partial N}{\partial z} + D_n \frac{\partial^2 N}{\partial z^2}$$

$$\frac{\partial F_i}{\partial t} = F_i \sum_{j=1}^n M_{ji}P_j - \delta F_i - v_f \frac{\partial F_i}{\partial z} + D_f \frac{\partial^2 F_i}{\partial z^2}$$

Now we have the interaction term characterized by the matrix M. This Lotka Volterra-like terms determines how the feeders consume the plankton. Moreover, the sinking speeds are not necessary the same for the different plankton. The peak of plankton bloom is determined by the $\mu(I)$ function . The nutrient becomes at steady state as we see in our code running.

Therefore, we change the variable I in the $p(I) = \frac{p_{max}I}{H+I}$ function so that different plankton have different light preference. In our simulation, firstly, we try the case that plankton have the same light preference and the same sinking speed first. Secondly, we try to vary the light preference the try with different sinking speeds. We want to control the effect of plankton consuming by making an assumption that a certain filter feeder can only eat some certain kind of plankton. It can be done by the interaction matrix M. We choose it be upper triangle matrix satisfies $M[i,i] = 1$, $M[i,j] = 0$ when $i < j$, $M[i,j] = \exp[-(i-j)^2]$ when $i > j$. Theoretically, our model expect that i^{th} plankton has less light requirement as well as sinking rate than the $(i+1)^{th}$ plankton. The upper triangle matrix expects the i^{th} feeder can only eat i plankton from 1 to i. This topology for matrix M came from an idea the we want the indexing is based on the size of the plankton and filter feeder. The boundary conditions are again no flux at the top and bottom for plankton and filter feeders, and nutrient is static

at the bottom with no flux on the top. The initial conditions are chosen to be Gaussian distribution centering at varying depth.

Method

We use the Wolfram Language function `NDSolve` with automatically numerical methods to give the solution for our coupling nonlinear PDEs. The automatic algorithm selection worked quite well since it showed no errors and gave the reasonable and consistent results. We simulate the system long time enough for the system to reach the steady state. The parameters data is based on Ryabov's et al paper with some critical changes for experiment purpose when build up multispecies model from the original case of the author.

Results and Discussion

Single Species

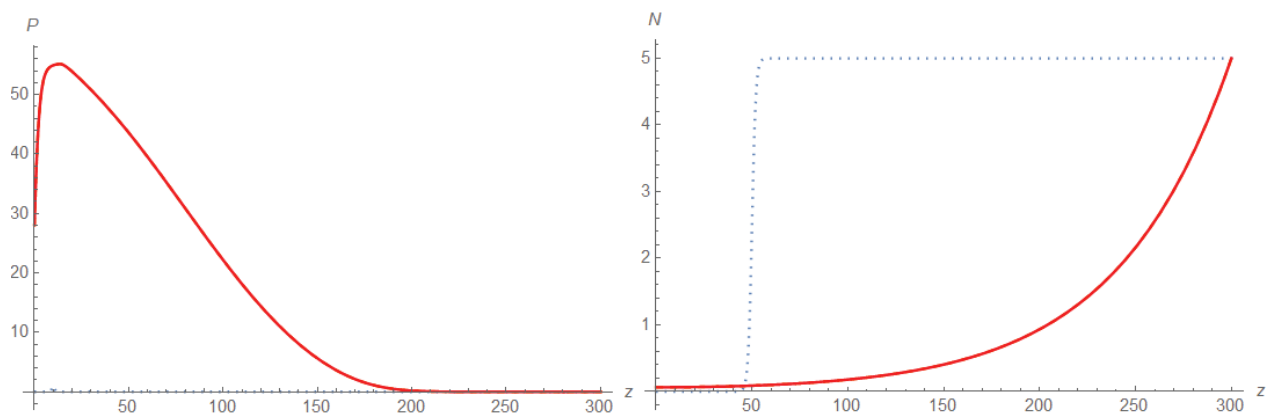


Figure 1: Plankton (left),Nutrient (right) profile at reach steady states

The results in this case in which the single plankton limited by both light and nutrient shows that the peak shifts to right. This means we can find plankton more likely at well-lit water. The results is consistent with our expectation.

No Light Preference in Multispecies Case

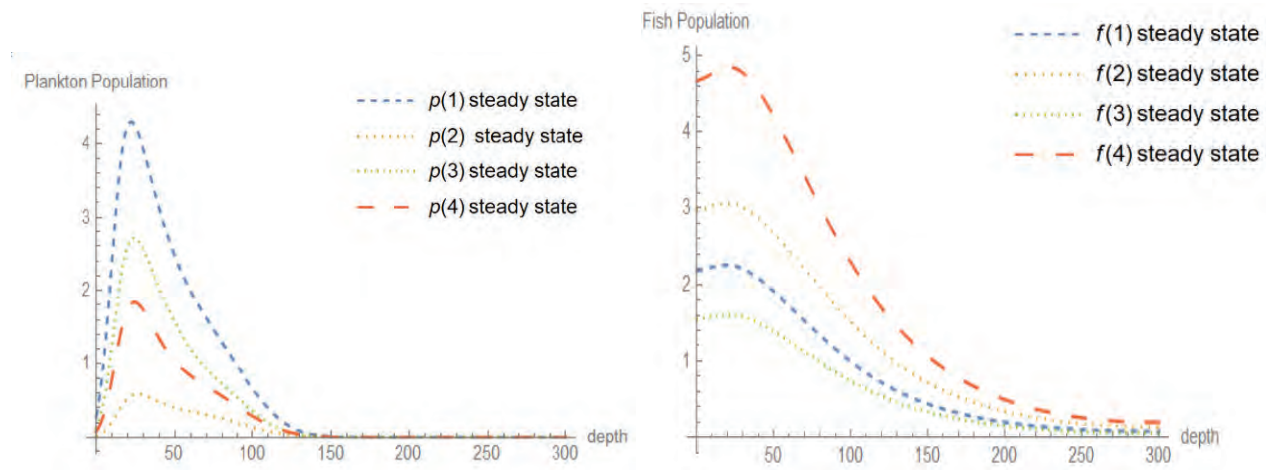


Figure 2: Plankton (left), Filter feeders (right) profiles at reach steady states

Figure 2 show the profile of plankton and filter feeders in no light preference case. We have the Gaussian distribution for plankton and feeders centering at different depth. However, the distribution of different plankton bloom at nearly the same depth. Moreover the pattern of the predators follows the prey with nearly the same location.

Light Preference in multispecies case

The plankton light requirement in this case is inversely proportional to the sinking depth. The predators has the same sinking speed, and their prefer foods is still decided by the upper

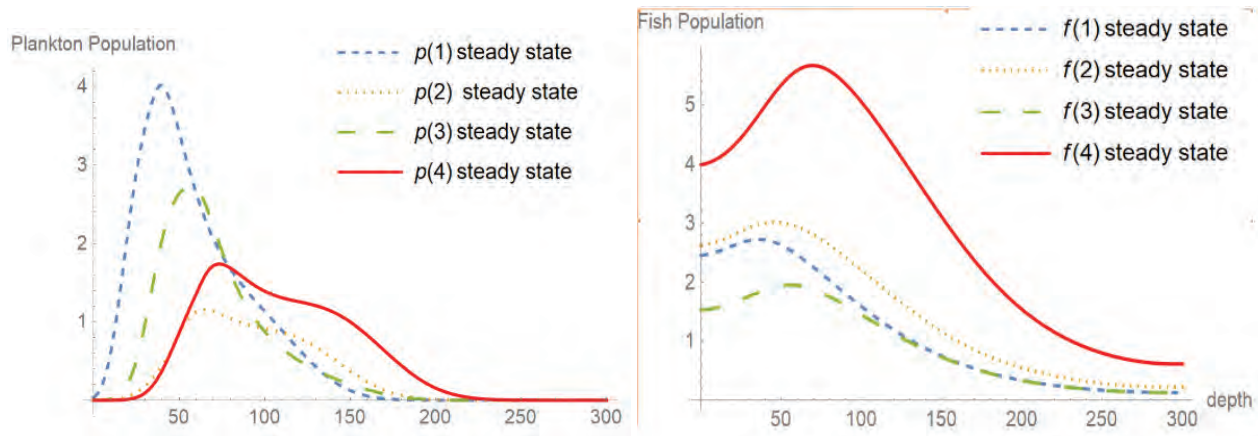


Figure 3: Plankton with different light preference and different sinking rate (left), Filter feeders (right) profiles at reach steady states

matrix as same as the previous case. Figure 3 show the distribution of predators follows the distribution of their prefer prey, which is agree with our model prediction. Figure 4 show that the peak of plankton growth rate $\mu(I, N)$ is very close to the peak of corresponding plankton and filter feeder and then it determines the spatial profile.

Conclusion and Future Work

In this work, we use the numerical experiments to verify the our theoretical prediction. The results from numerical simulation is well agree with our model. In fact, the pattern of distribution we observe is consistent regardless of the number of species we vary. In order to generalize our model, there are several way to improve our model. Fist, we have to find a better algorithm to solve to PDEs .More importantly, we need to improve our model by vectorizing the species and try the more general continuous model.

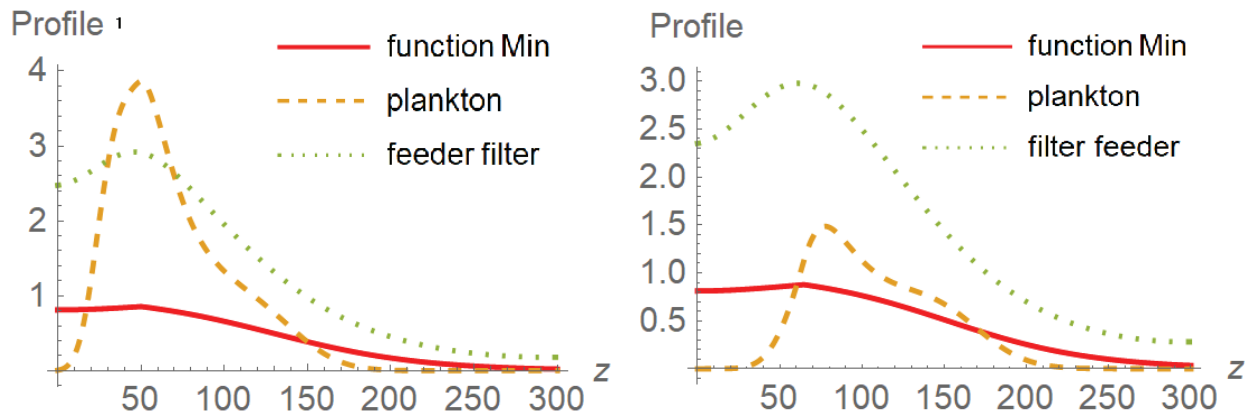


Figure 4: In another simulation, we broaden the light preference as well as the sinking speed. We see the peak of that the growth rate $\mu(I, N)$ function is very close to the peak of the plankton and filter feeders. The left is the profile of plankton 1 and feeder 1, the left is the profile of plankton 2 and feeder 2.

Reference

1. Turing, A. M. (1952). "The Chemical Basis of Morphogenesis" (PDF). Philosophical Transactions of the Royal Society of London B. doi:10.1098/rstb.1952.00122.
2. Jef Huisman, et al, "How Do Sinking Phytoplankton Species Manage to Persist?", The American naturalist March 2002.
3. Alexei B. Ryabov et al, "Vertical distribution and composition of phytoplankton under the influence of an upper mixed layer", Journal of Theoretical Biology Volume 263, Issue 1, 7 March 2010, Pages 120-133

Investigating CMS Binary Chip Data Losses in the Phase II High
Luminosity Upgrade to the CMS

Mary-Ellen Phillips

2019 NSF/REU Program

Physics Department, University of Notre Dame

Advisors:

Kevin Lannon, Michael Hildreth

Abstract

The Large Hadron Collider (LHC) is set to reach a stage of high luminosity by 2026. In order to keep up with the resulting increase in pileup conditions, the Compact Muon Solenoid (CMS) will also be getting an upgrade. With this upgrade, it is important to understand the full capabilities and limitations of the tracker & trigger to read and store data about particles of interest. The following study details the losses of data due to limitations on the CMS Binary Chip (CBC). CMSSW 10.4.0 was used to simulate and analyze a sample of 500 events for stub losses in the barrel of the CMS due to CBC limitations. It was found that stubs from secondary reactions were consistently the highest volume of stubs that were lost due to a CBC failure in each of the layers and that layers 4, 5, & 6 had higher losses in comparison to losses in layers 1, 2, & 3.

1. Background

1.1 The Compact Muon Solenoid

The Compact Muon Solenoid (CMS) is one of seven experiments found at the LHC. The CMS is designed to detect and store data about the products of a high-energy collision. This is achieved using a solenoid with a magnetic field greater than 100,000 times than the earth's [2].

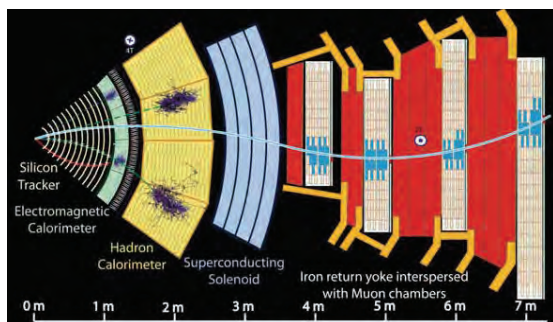


Figure 1: Layers of the CMS detector [1]

Figure 1 illustrates the many layers of the CMS

detector. Each layer takes precise measurements of different types of particles. The following study is concerned with the tracker of the detector, which tracks and stores data about the path of particles as they go through the layer.

The tracker is the innermost layer of the CMS which allows it to catch all of the particle spray that occurs from an event. The tracker can be divided into four subsections: Tracker Inner Barrel (TIB), Tracker Outer Barrel (TOB), Tracker Inner Disk (TID), and Tracker End Caps (TEC). Each subsection's location can be described by the radial distance from the center of the CMS detector (r), the linear distance down the center of the CMS detector (z), and pseudorapidity (η). The following study examines the TOB. Figure 2 shows a cross section of the tracker labeled with each of the subsections described. TOB is located where $r > 550$ and $z < 1200$

TOB has six layers of detector modules which are represented by lines in Figure 2. Each detector module is made up of two parallel silicon sensors. The first three layers use PS modules which use a strip sensor and a pixel sensor. The last three layers contain 2S modules which are simply made of two identical strip sensors. In comparison, PS modules have a higher granularity and provide higher precision hits which helps with the high levels of occupancy in the inner three layers [3].

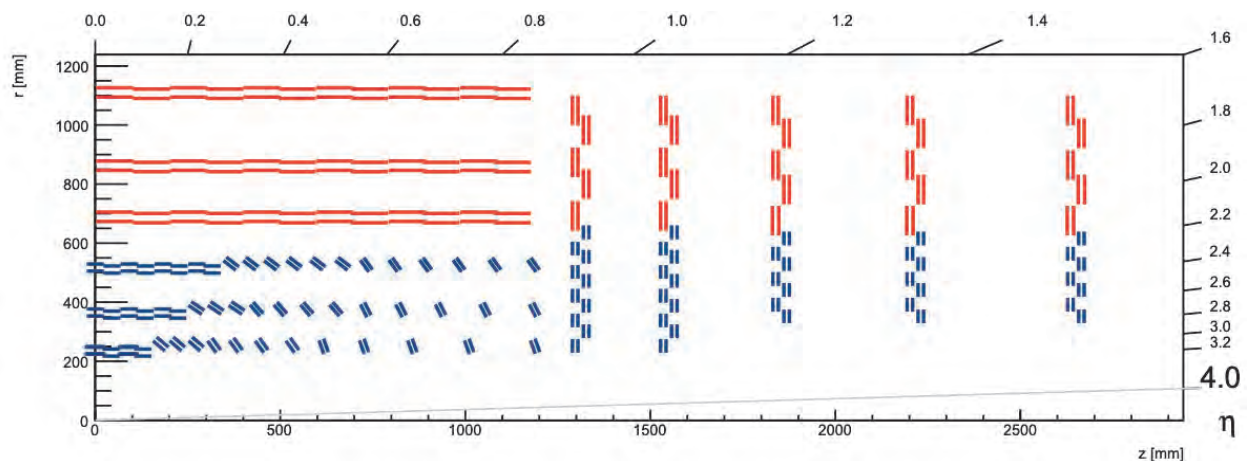


Figure 2: Schematic cross section through the CMS []

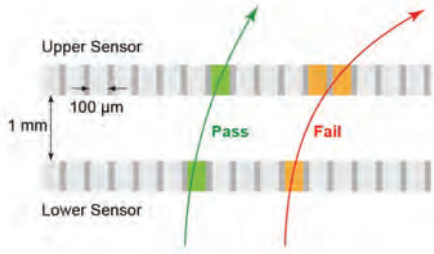


Figure 3: Stub schematic [3].

When a collision occurs, an electric signal is produced as a particle passes through pixels or strips creating a cluster. Correlated clusters in the parallel detectors within a module become reconstructed by CMS Binary chips (CBC) or Macro Pixel ASIC (MPA) chips to

create stubs; CBC are used with 2S modules while MPA chips are used for PS modules.

Figure 3 shows the concept of a stub and explains how stubs can be used to significantly reduce the enormous inflow of data. The transverse momentum (p_T) of a particle is directly related to the width of the stub that it creates. A cut-off p_T can easily be applied by examining the deviation of the second cluster and the implied momentum. As figure 3 suggests, a high p_T cut-off will cause certain particle paths to fail rejecting those stubs. Since CBC/MPA chips only readout stubs, this rejection of stubs helps reduce the flow of data coming in significantly.

Though stubs can reduce the amount of data coming in, there are still losses due to failures in the CBC readout chip. The CBC has a buffer that can be filled up when there is too much data which causes the data that does not make it into the buffer to be lost. Figure 4 shown below offers a diagram showing the full front-end data extraction and the rates at which data is produced in each step. The following study focuses on the truncation of data done by the CBC.



Figure 4: Front-end data extraction [4].

1.2 Past Studies

In a study performed in 2018, Christopher E. McGrady set out to understand how high data rates and limits on bandwidth readout affected losses of data in the tracker of the CMS. McGrady used CMSSW 9.3.7 to analyze data that were lost and understand what conditions caused the data to be lost. It was found that TOB encountered the highest percentage of losses ranging from 1.51% to 5.58% depending on pile-up conditions [1]. Table 1 demonstrates the high percentage of data lost in TOB (barrel layers 4, 5, & 6) due to CBC limitations. The full limit of data losses were based on a sample in which there was a pile-up of 300 collisions. With the conclusions found in McGrady’s study, it was suggested that more studies should be done in order to understand why such high losses were occurring due to CBC/MPA losses.

Table 1: Stub loss from different limitations [1]

Location Loss	Full Limits	CIC Losses	CBC/MPA Losses
Layer 1 Barrel	1.36%	0.72%	0.19%
Layer 2 Barrel	1.02%	0.90%	0.04%
Layer 3 Barrel	0.17%	0.05%	0.04%
Layer 4 Barrel	3.13%	0.30%	1.39%
Layer 5 Barrel	4.34%	0.24%	2.20%
Layer 6 Barrel	5.58%	0.15%	2.95%
Layer 1 End Cap	0.94%	0.66%	0.08%
Layer 2 End Cap	1.88%	1.57%	0.11%
Layer 3 End Cap	1.67%	1.56%	0.01%
Layer 4 End Cap	1.74%	1.70%	0.01%
Layer 5 End Cap	1.39%	1.31%	0.01%

2. Methods

CMS SoftWare (CMSSW) creates samples of events and shows how the CMS detects those events. In this study, CMSSW 10.4.0 was used. Events are simulated using the Monte Carlo technique, which estimates the value of an unknown quantity through inferential statistics [6]. A sample was created where the max events was set to 500 using the

L1TrackNtupleMaker_cfg.py file which can be found in the CMSSW_10_4_0/src/L1Trigger/TrackFindingTracklet/test directory. This sample was then used to make plots using stubRate.C located in the CMSSW_10_4_0/src/L1Trigger/TrackFindingTracklet/test/code2 directory. Losses due to CBC limitations were broken up into categories of stub types in order to understand what kind of stubs were being lost.

Three types of stubs were considered in this study: genuine, combinatoric, and unknown. A genuine stub contains two hits from the same Monte Carlo truth track, while a combinatoric stub contains one Monte Carlo hit and another hit with a different ID. An unknown stub contains hits that are not differentiable.

Four-dimensional arrays were created to account for stub volumes while also keeping track of the particular stubs' location. the parameters for the arrays created were barrel, layer, ladder, and module. Table 2 provides a comprehensive list of arrays created and descriptions.

Table 2: Arrays created

Array	Description
GenuineStubs	Count of all genuine stubs in each module
GenuineStubsCBCfail	Count of genuine stubs that failed CBC in each module
CombinatoricStubs	Count of all combinatoric stubs in each module
CombinatoricStubsCBCfail	Count of combinatoric stubs that failed CBC in each module
UnknownStubs	Count of all unknown stubs in each module
UnknownStubsCBCfail	Count of unknown stubs that failed CBC in each module

The arrays shown were then used to create one-dimensional plots so that they could be analyzed visually. The plots were made using ROOT. One-dimensional plots of each type of stub were made in each layer for a stub count. The plots were then superimposed into stacked histograms so that the full population of stubs could be seen while also knowing how many stubs belonged in each category.

3. Results

Figures 5, 7, & 9 show a count of stubs per module in each layer of TIB on a logarithmic scale. The different colors represent the stub type; Red represents unknown stubs, green shows combinatoric stubs, and blue is for genuine stubs. Similarly, Figures 6, 8, & 10 show the count of stubs that were lost due to a CBC failure broken up in colors again by stub types in layers of TIB. TOB is represented by Figures 11-16.

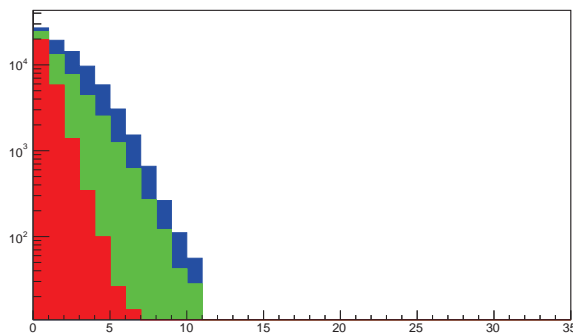


Figure 5: All stubs layer 1

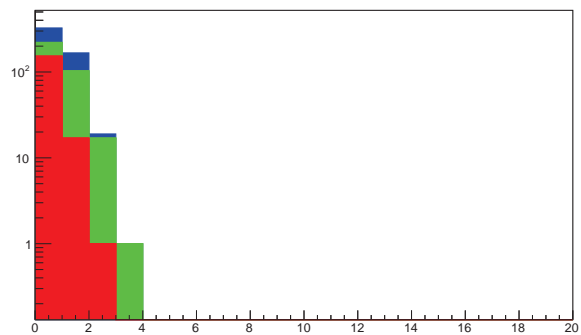


Figure 6: CBC failed stubs layer 1

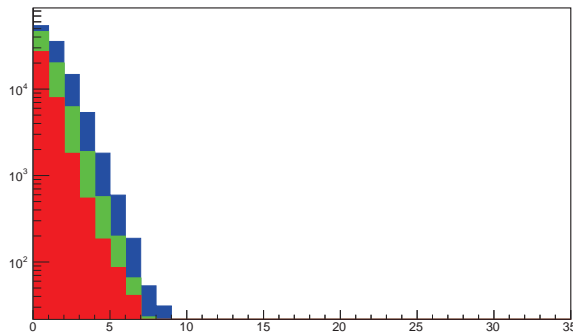


Figure 7: All stubs layer 2

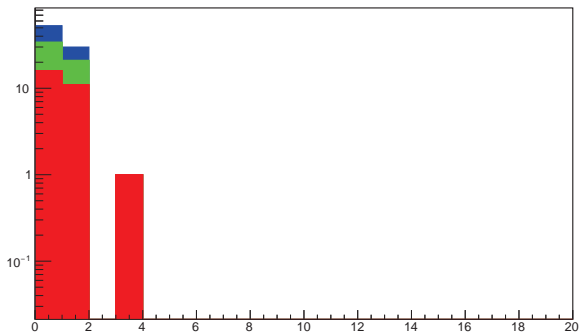


Figure 8: CBC failed stubs layer 2

Legend:

- Genuine
- Combinatoric
- Unknown

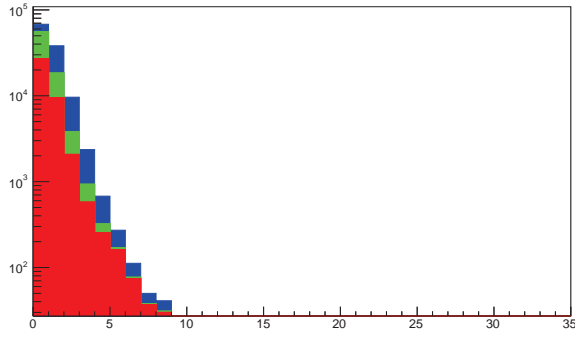


Figure 9: All stubs layer 3

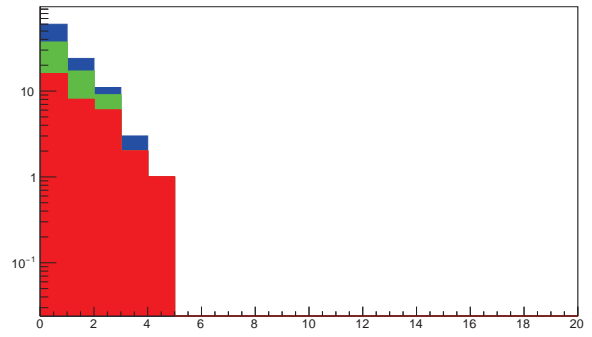


Figure 10: CBC failed stubs layer 3

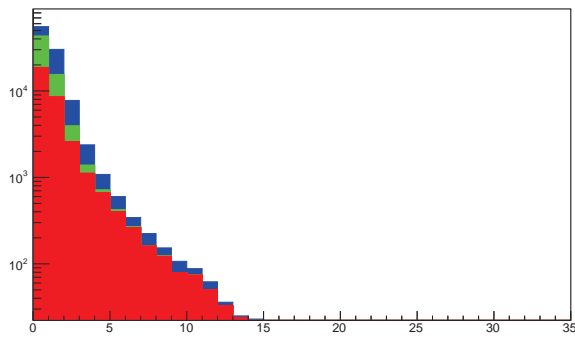


Figure 11: All stubs layer 4

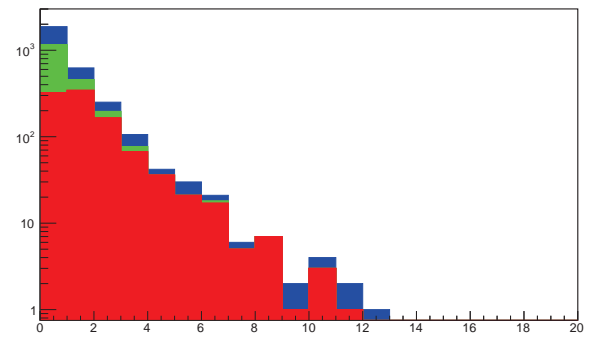


Figure 12: CBC failed stubs layer 4

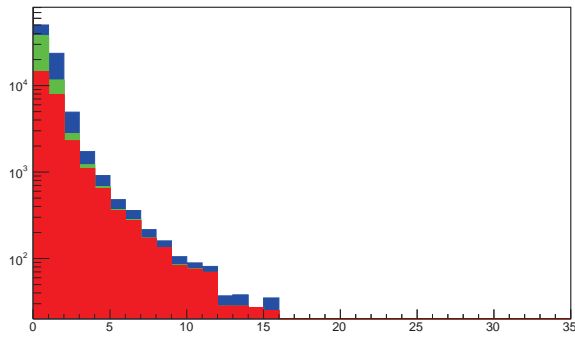


Figure 13: All stubs layer 5

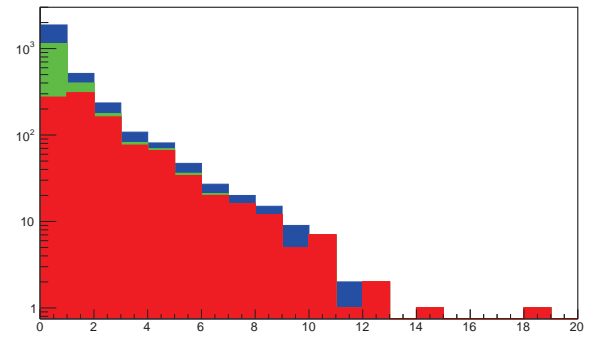


Figure 14: CBC failed stubs layer 5

Legend:

- Genuine
- Combinatoric
- Unknown

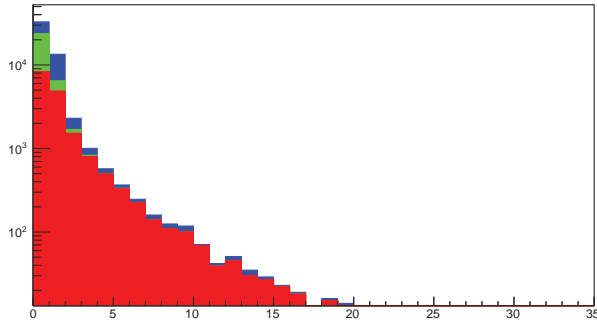


Figure 15: All stubs layer 6

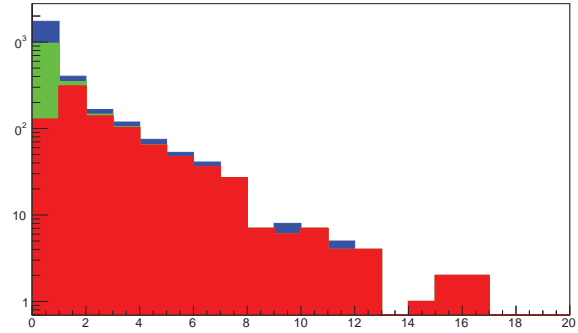


Figure 16: CBC failed stubs layer 6

Table 3 seen below shows the total amount of stubs and stub losses due to a CBC failure.

Table 3: Count of total stubs and stub layers

	Total Stubs	Losses due to CBC failure
Layer 1	27262	171
Layer 2	37536	28
Layer 3	39853	33
Layer 4	32888	991
Layer 5	27731	982
Layer 6	17158	887

4. Discussion

The population of unknown stubs grew to be the majority of all stubs when progressing through the layers. Unknown stubs were also the majority for stubs that were lost due to CBC failures in each of the layers. However, there is a distinct increase in the sheer amount of CBC losses when comparing TOB to TIB.

The amount of CBC failures in the first three layers decrease when moving outwards (from layer 1 to layer 3) from the collision point. Although the CBC failures decrease from layers 1 to 3, the amount of total stubs increases by nearly a factor of 1.46. This is shown in Figures 5-10 and in Table 3. Moving from layer 3 to 4, the amount of total stubs decreases a little

bit but the population of stubs that are lost from a CBC failure increases drastically. In layer 3, there are only 33 stubs lost to a CBC failure. In layer 4 there are 991 stubs lost from a CBC failure which is an increase of a factor of about 30. This is shown in Table 3 and in Figures 9-12.

The low amount of CBC failures in layers 1-3 can be attributed to the fact that these layers use an MPA chip to reconstruct stubs while layers 4-6 use CBC chips to reconstruct stubs. The CBC failures in each of these cases were mostly unknown stubs which can account for why the track efficiency in layers 4-6 are high despite the high loss of stubs.

In further studies, The performance of the MPA chip should be looked at and compared to the performance of the CBC chip. Ways to improve losses in TOB should also be researched by looking into other data compression methods.

References

- (1) McGrady, C. E. (2018). *Using particle interaction simulations to understand tracker efficiency for the phase II high luminosity upgrade on the cms experiment* (National Science Foundation). Indiana, United States: Notre Dame University, Physics.
- (2) Taylor, L. (2011, November 23). *What is cms?* Retrieved from <http://cms.web.cern.ch>
- (3) Viret, S. (2018). *Stubs*.
- (4) Viret, S. (2017). *Data transmission efficiency of the phase II tracker front-end system for the tilted geometry*.
- (5) The CMS Collaboration *et al* 2008 *JINST* **3** S08004
- (6) Guttag, J. [MIT OpenCourseWare]. (2017, May 19). *Monte Carlo Simulation*. Retrieved from <https://www.youtube.com/watch?v=OgO1gpXSUzU>

**Improving the Notre Dame MR-TOF and using Photodiode Detectors for
Beam Analysis**

Jason Prochaska

2019 NSF/REU Program

Physics Department, University of Notre Dame

Advisor: Maxime Brodeur

Abstract

This report first discusses the use of Multiple Reflection Time-of-Flight Mass Spectrometry in analyzing Radioactive Ion Beams. Particularly, the optimal beam pulse width to maximize the Mass Resolving power of said Mass Spectrometer. The successful use of Multiple Reflection Time-of-Flight Mass Spectrometry will aid in the study of many rare nuclei that have an extremely low natural abundance here on Earth. Additionally, we discuss the use of a particle detector called Ackbar in analyzing beam contents. The Ackbar detector utilizes a small gas chamber coupled to a silicon surface barrier to identify the beam contents. This paper presents a potential replacement for the silicon detector, by a photo-diode detector, as well as a mount for said photo-diode.

Introduction

There are two major processes that create elements heavier than iron. The discussion of this paper is focused on the r-process, or rapid neutron capture process, which generally synthesizes the most neutron-rich isotopes of the heavy elements. The r-process produces approximately half of all elements beyond iron in the universe [7]. To better understand the rapid neutron capture process it is necessary to study nuclei near neutron number $N=126$. This is because nuclei around the closed neutron shells of $N=82$ and $N=126$ have a large influence on the final abundances of nuclei that are produced by the r-process [7]. However, nuclei near $N=126$ are rare given their radioactivity, and production of these radioactive nuclei presents many challenges. Multi-nucleon transfer reactions are a viable method for reaching the $N=126$ region [8]. At Argonne National Laboratory, a facility is being created

to produce these rare nuclei allowing for their study [9]. However, production of these nuclei yields contaminant isobars. In order to filter out the contaminants, a Multiple Reflection Time-of-Flight Mass Spectrometer (MR-TOF-MS) [1, 2] will be utilized in the facility at Argonne National Laboratory.

The University of Notre Dame has developed an MR-TOF-MS that has been tested and commissioned off-line. One of the main goals of this endeavor was to optimize the resolving power of the mass spectrometer.

The off-line testing of MR-TOF-MS at Notre dame utilized a Bradbury-Nielsen Gate (BNG) to chop the beam into pulses, allowing only a specified width to go on to the Mass Spectrometer. The size of the pulse can have an influence on the resolving power of the beam. In order to determine the ideal size for the width of the beam, characteristics of the detected peak were analyzed.

Implications and Advantages of the MR-TOF-MS

Argonne National Laboratory is creating a facility in which radioactive beams of high purity are required. These beams will provide insight into the astrophysical processes under which r-process neutron capture can occur. However, many experiments like specifically a mass measurement requires isobarically pure beams. Hence, a MR-TOF-MS is required to filter out isobaric contaminants (isobars are isotopes having the same atomic mass) [3]. Even isobars have slight variations in their mass. Therefore, if the ions are produced at a constant energy, isobars will travel at a slightly different velocity. Thus, the time of flight will vary

between isobars.

One of the major advantages presented by TOF-MS is the extremely short time scale on which it can separate isobars. This is of particular importance in the Argonne National Laboratory setup, as the beams produced will be radioactive in nature. Another significant advantages of the Multi-Reflection TOF-MS is the length of the device [2]. An ordinary time of flight mass spectrometer would require a significant distance for the beam to travel to achieve a sufficient resolving power. Multiple-Reflection TOF-MS traps ions within a potential well, allowing them to oscillate along the length of the chamber. This allows for a far shorter beam line as mentioned, and has the added benefit of allowing for the Time-of-Flight to be modified and optimized. The MR-TOF-MS at the University of Notre Dame utilizes two sets of 5 electrodes forming mirrors and two Einzel lenses in order to create a modifiable reflecting potential.

MR-TOF-MS Optimization

When optimizing the MR-TOF-MS we seek to maximize the resolving power, which is given by the following equation:

$$R = \frac{t}{2\Delta t} \quad (1)$$

In equation (1), Δt is the width of the peak at half the height of the peak, and t is the total time of flight of the ions. At Argonne National Laboratory the Radioactive Ion Beam will be bunched by a component prior to the MR-TOF-MS. However, we decided to analyze the optimal pulse length for the MR-TOF-MS. On the offline setup, the BNG can be opened

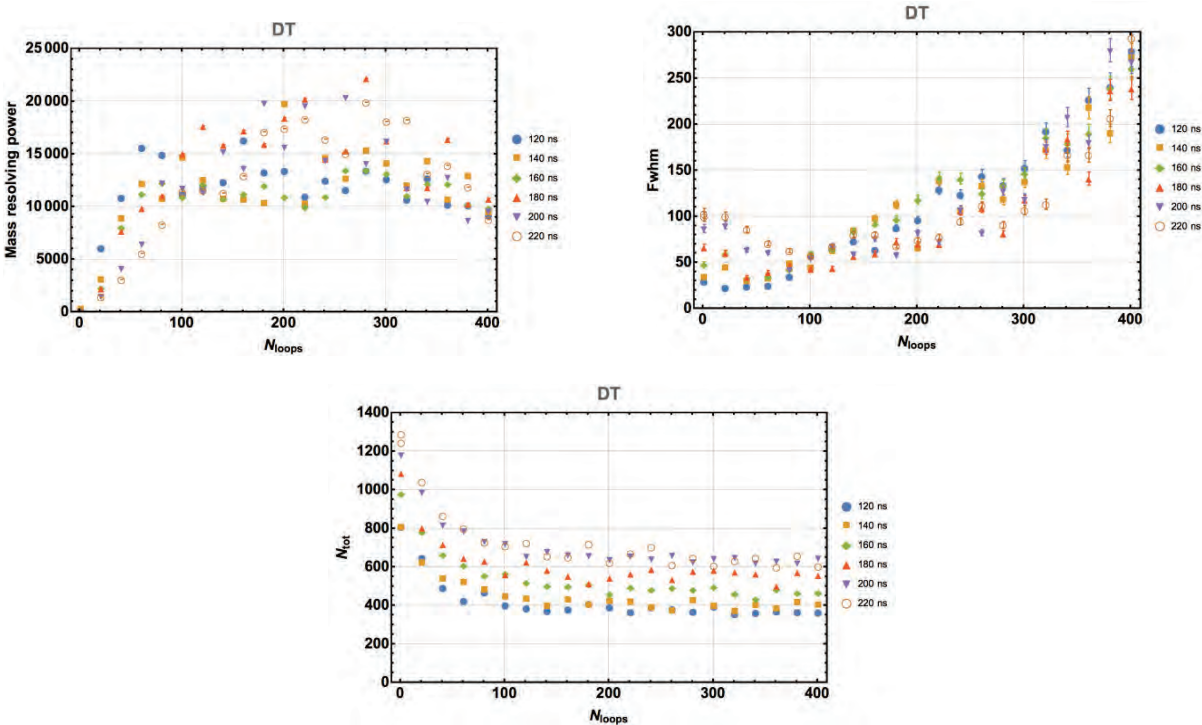


Figure 1: The above plots display the total counts, full width half maximum, and resolving power vs. the number of loops the ions are reflected. Each plot displays various pulse widths.

for a set amount of time [2]. However, it is a delicate balance between peak height and width. Too short of a pulse and less ions will get through. Also, a greater proportion of the beam will suffer from a transverse kick that will adversely affect the efficiency and resolving power. Too long of a pulse the width of the peak will be too large. The number of loops that the ions undergo determines the total distance they will travel. For all widths studied the mass resolving power and total number of ions gets affected the same way with the increased number of loops. Also the total number of ions increases with the pulse width as expected. The large drop in FWHM in the first 100 loops is due to ions entering the MR-TOF with large angles no longer being detected. The ideal resolving power is reached after 200 loops for 180 ns.

Issues Addressed and Potential Causes

Throughout measurement using the MR-TOF-MS a few issues were encountered. The first of which is that the influence of the steerer potential drifts. One possible cause for this is the varying temperature in the detector development lab. The facility at Argonne National Laboratory will be better temperature controlled, nullifying this issue. Another issue that was faced was the loss of vacuum in the system. The turbo-vacuums require a back pressure that was provided by a pure nitrogen supply. This supply ran out during the summer, and caused the system to lose vacuum briefly. Finally, the ion source seemed to die out, yielding progressively less counts and thus causing mass resolving power to plummet for high loop counts.

Testing TwinSol Contents with Ackbar

A particle identification detector, called Ackbar is used to analyze the contents of the TwinSol beams. Often these beams contain the primary beam from the FN that has scattered, the radioactive species of interest, as well as an array of isotopes that were not the intention of production. The Ackbar particle identification system allows operators to tune the beam to minimize contaminants. The Ackbar system is similar to a $\Delta E - E$ telescope detector that is built in two parts to classify the particles within the beam (see Figure 2). Particular isotopes can be identified according to their energy loss through the ionization chamber, and the final energy they deposit on the second detector. Usually for a telescope, the first of these detectors is ordinarily a thin silicone detector, which allows the incoming

particles to pass through. The first detector measures the energy loss of the particle. Within the Ackbar system the first detector is instead a gas detector, which provides three main advantages over the normal silicone detector. The first of which is it allows for detection of ions with a higher number of protons (Z). The second major advantage is the flexibility presented by varying the pressure and composition of the gas in the chamber. The most common gas utilized is P-10 gas which is comprised of 90% argon gas and 10% methane gas. The final advantage that gas detectors present is the ability to detect lower energy particles with higher accuracy. Gas detectors utilize a container with conducting walls, and is often filled with an inert gas [7]. When the ions enter the chamber they lose energy via excitation and ionization through the creation of a free electron and ion [7]. The cross-section for the latter to occur is one order of magnitude higher [7]. However, excitation reactions are generally more observed as they have a lower energy threshold than ionization processes [4]. The gaseous region of Ackbar is held under a constant applied voltage. These freed electrons then drift to the anode plate, and are detected as a current on the circuit. The second detector of the system will measure the remaining energy of the particle. The next section will discuss the two options for the final detector.

Photodiode Detector compared to Silicone Detector

Silicone detectors utilize a P-N junction diode that is put under reverse-bias [4]. This P-N junction has a depletion layer (which becomes larger in the presence of a reverse-bias) in which external particles that enter the region will deposit energy. This deposited energy

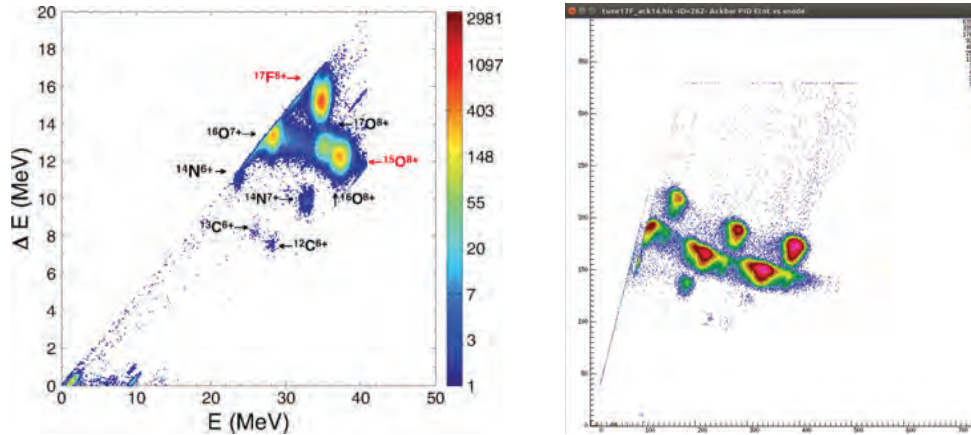


Figure 2: The lefthand particle identification plot that was created using Ackbar in it's previous telescopic form. The righthand utilizes a gaseous ionization detector to measure ΔE . The beam was produced by accelerating Oxygen-16 on a deuterium target with the goal of producing Flourine-17 for both plots. The righthand plot clearly displays a higher resolution than the previous arrangement.

creates electron-hole pairs. The N-type semiconductor collects the electrons, and visa versa for the P-type semiconductor [7]. Both of these enter the external circuit in which they can be detected. Silicone has a crystal lattice structure that vibrates when excited [8]. Photodiode detectors also utilize a p-n junction. Photodiodes utilize light as their external input. Photodiodes, however, utilize Gallium Arsenide instead of silicone, which has the benefit of bypassing the crystal lattice structure of silicone. Gallium Arsenide produces electron-hole pairs without the need for slow crystal lattice vibrations, making photodiodes more sensitive [8]. Photodiodes provide a better resolution of total energy. The main benefit of photodiode detectors is their reduced cost in comparison to silicone detectors. Photodiode detectors can be purchased for nearly a tenth of the cost of silicone detectors, and especially important given that the detectors will have a finite lifespan when exposed to accelerated beam. In the case of the Ackbar system, the ion beam will first strike a scintillation material which emits photons that will be detected in the photodiode.

Proposed Detector Mount

The following detector mount is designed such that the aluminum fixture can still support the previously used silicone detectors, but can also house the photodiode detector. The photodiode will be housed in the designed mount which will connect to the output wire (see Figure 3). The center of the photodiode will be exposed to the center of the beam. An aluminum mounting plate will be placed on top, and is designed to collimate the beam (reducing fringe effects). The righthand mount is to be fabricated out of plastic or ceramic.

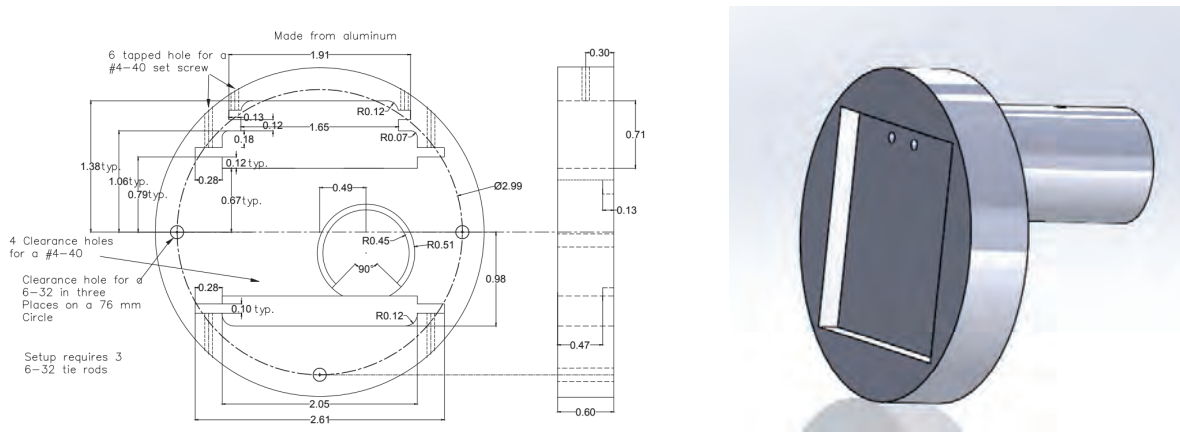


Figure 3: The lefthand plate has been designed to house a photodiode detector. The detector itself will be raised off the surface, with the back cylinder on the righthand side resting on the ridge inside the plate.

Conclusion

In this report the importance of optimizing the MR-TOF has been emphasized. The optimal pulse width was determined to be 180 ns, with a time of flight corresponding to 200 reflections. Further research into the effects of temperature on the steering potentials could

provide insight into the root cause of potential drift. However, this will likely be unnecessary for the setup at Argonne National Laboratory.

Photodiode detectors present clear advantages over silicone detectors. The cost advantage of the photodiode is significant. Further, the photodiode allows for faster data collection and will reduce detector dead-time. The manufacture of the above mounting system is still required, and then the mount must be tested with a well known beam like Oxygen-16 accelerated on a deuterium target.

References

- [1] J.M. Kelly, et al., First off-line tests and performance of the Notre Dame multi-reflection time-of flight mass spectrometer. Nuclear Inst. and Methods in Physics Research B
- [2] B.E. Schultz et al., Construction and simulation of a multi-reflection time of-flight mass spectrometer at University of Notre Dame, Nuclear Inst. and Methods in Physics Research B
- [3] Wolfgang R. Pla, Timo Dickel, and Christoph Scheidenberger. Multiple-reflection time-of-flight mass spectrometry. International Journal of Mass Spectrometry, 100 years of Mass Spectrometry.
- [4] Knoll, G.F., 2000, Radiation Detection and Measurement, Wiley.
- [5] Leo, W.R., 1987, Techniques for nuclear and particle physics experiments: a how-to approach, Springer-Verlag.
- [6] Braley, J., 2008, Photo Detectors. University of Rhode Island.
- [7] Mumpower M.R., Surman R., McLaughlin G.C., Aprahamian A. Prog. Part. Nucl. Phys., 86 (2016), pp. 86-126
- [8] Yutaka X, et al., 2015, Pathway for the Production of Neutron-Rich Isotopes around the N=126 Shell Closure., Physical Review Letters
- [9] G. Savard, M. Brodeur, J.A. Clark, R. Knaack, A.A. Valverde., 2019, Nucl. Instr. Meth. Phys. Res. B

Energy Reconstruction of Low Energy Supernova Neutrinos

Rachel Procter-Murphy
2019 REU Program
Physics Department, University of Notre Dame

Advisor: Dr. John LoSecco

Abstract

The Deep Underground Neutrino Experiment is an international experiment through the Fermi National Accelerator Laboratory that will study neutrinos. In this study, we examined at the detector effects on low energy supernova neutrinos in order to improve energy reconstruction at energies less than 40 MeV. In order to do this we looked at supernova neutrino events in a LarSoft detector simulator with and without background. We looked at the ratios between the true data and reconstructed data to identify the deficiencies of the detector, which we found to be low energies and high drift times. We also improved the ratio between the true and reconstructed data by applying the physical limits of the detector. The efficiency of the improved ratio of the clean data was 93.2% and the efficiency of the improved ratio with the data with background was 82.6%. We concluded that a second photon detector at the far wall of the detector would help improve the resolutions at high drift times and low energies.

Introduction

The Deep Underground Neutrino Experiment (DUNE) is an experiment that will study neutrinos and proton decays. Two detectors are currently being built and will be installed at the Fermi National Accelerator Laboratory and the Sanford Underground Research Laboratory. This experiment will aim to answer fundamental questions about matter, neutrinos, and the universe [4].

The DUNE detector will be installed almost 1,500 meters underground to reduce cosmic ray background. The detector consists of 17 kilotons of liquid argon each in a time projection chamber. The argon is viewed electronically with a cathode plane across from the wire collection

plane. The wire plane consists of three layers of wires in different orientations. The combination of ‘hits’ from each of these planes of wires allows researchers to reconstruct a three dimensional picture of what happens within the detector. The process of reconstruction ideally allows scientists to get an accurate representation of what happened in the detector from the digital information collected [5].

In this experiment we will study the detector effects on the data in order to improve the energy reconstruction, particularly at low energies. We specifically looked at the electron drift times which are important for energy correction and determining the coordinates of the neutrino interaction. The charge collected depends on the energy deposition so by learning about the charge and correcting for any lost charge helps us reconstruct the energy.

Neutrinos account for about 99% of the energy released from supernovae due to a process called neutrino cooling. The study of these neutrinos will allow a unique view into what is happening inside a star during its collapse.

There is a difference in the energy spectrum of actual supernova neutrinos as opposed to simulated neutrino energy spectrum is one of the main differences between the simulation [3] and what we expect from actual data.

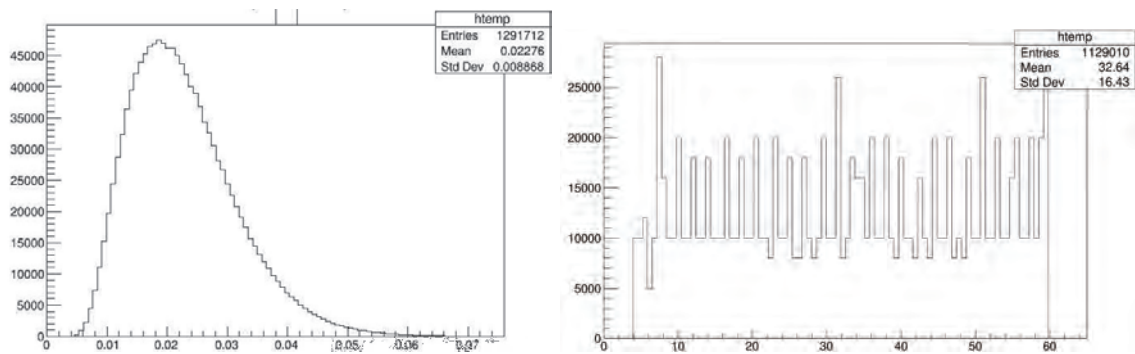


Figure 1: (Left to right) The spectrum created by the neutrino flux multiplied by the cross section in the detector in GeV; The simulation neutrino energy spectrum in (MeV).

The observed supernova neutrino energy spectrum peaks around 20 MeV, whereas in the simulation we are using, the neutrino energies are flat with the discrepancies due to binning effects.

Data

For this study we used a simulation created by Erin Conley [3] and the data without background [1] and data with background [2] that resulted from said simulation. One of the main focuses of this study was of the electron drift time (μs). The electron drift time was calculated by dividing the vertex position by the known drift velocity. The following plots show a comparison of the reconstructed drift times to the true drift times.

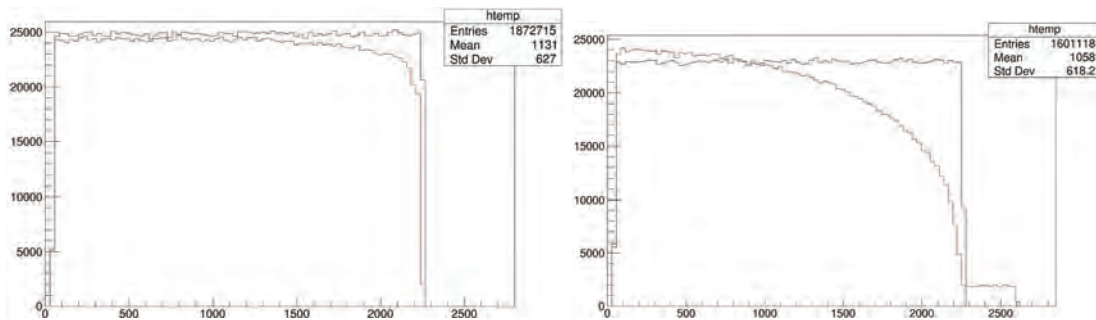


Figure 1:(Left to right) Comparing the reconstructed drift times (red) to the true drift times (blue) for clean data and data with background.

The detector seemed to have deficiencies at higher drift times that was worsened when background was added. Next, we created three dimensional histograms to compare the drift times to the true neutrino energies (MeV).

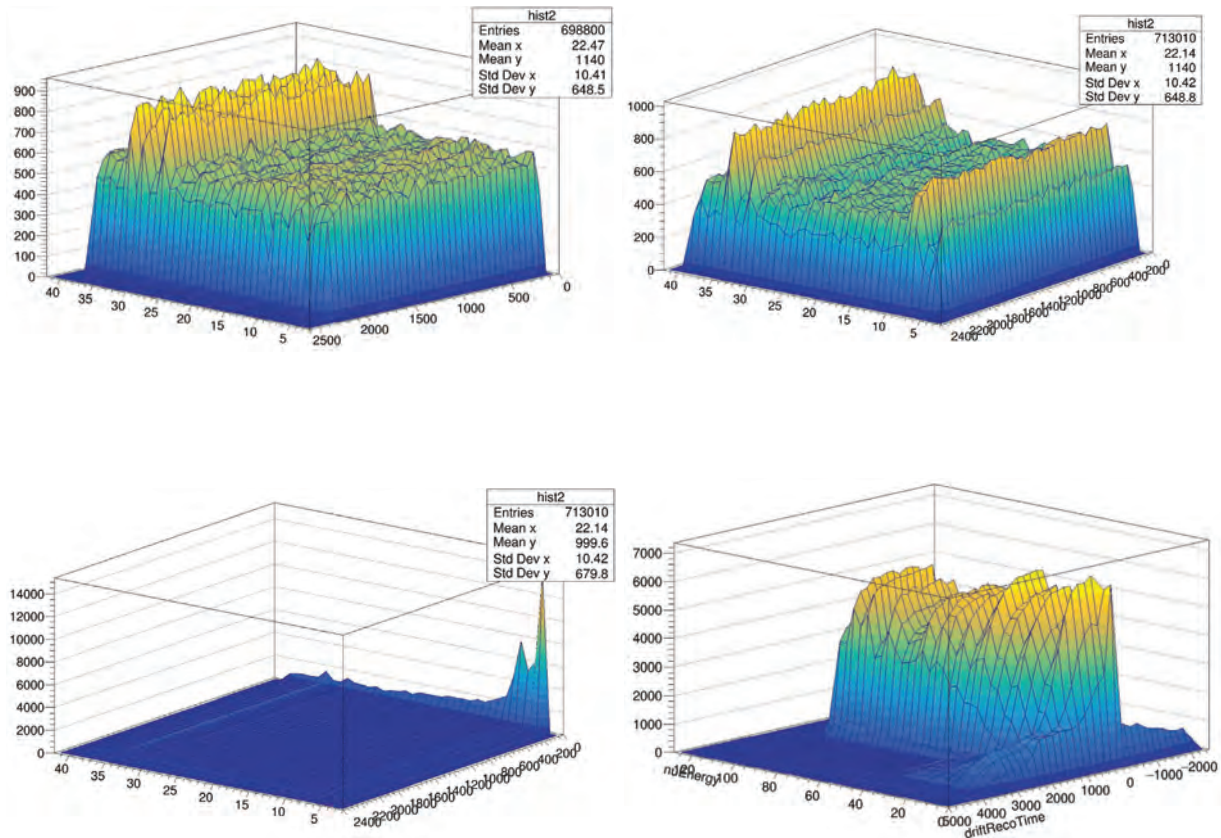


Figure 2: (Clockwise from top left) The true neutrino energies vs. the true drift time (clean); The true neutrino energies vs. the true drift time (with background); The true neutrino energies vs. the reconstructed drift times (with background); The true neutrino energies vs. the reconstructed drift times (clean).

Next we created ratios of the histograms of the true drift times divided by the reconstructed drift times. Different cuts were used to try to improve the ratio and to create histograms that are easier to read. The following plot shows the clean data with the true or reconstructed drift times (μs) compared to the true neutrino energies (MeV).

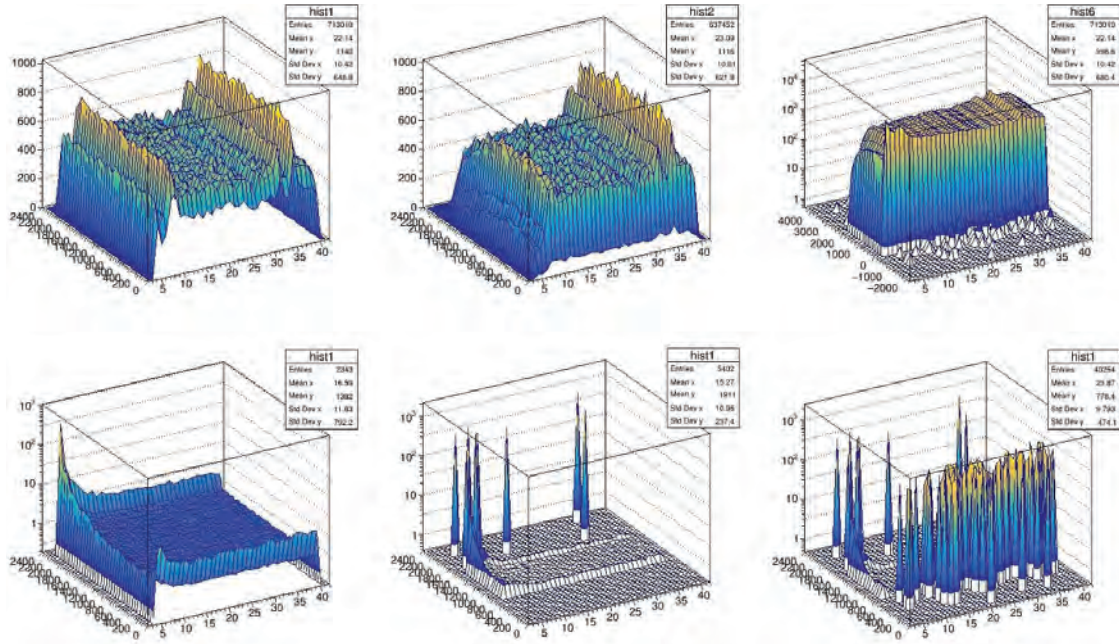


Figure 3: (Clockwise from upper left) The true neutrino energies vs. the true drift times; The true neutrino energies vs. the reconstructed drift times cut at physical bounds; The true neutrino energies vs. true drift times uncut; The ratio between the first histogram and the third histogram (uncut); The ratio between the first histogram and third histogram (cut at $0 \mu\text{s}$ to improve visibility); The ratio between the first and second histogram (cut at physical bounds).

The following shows similar plots but with background included.

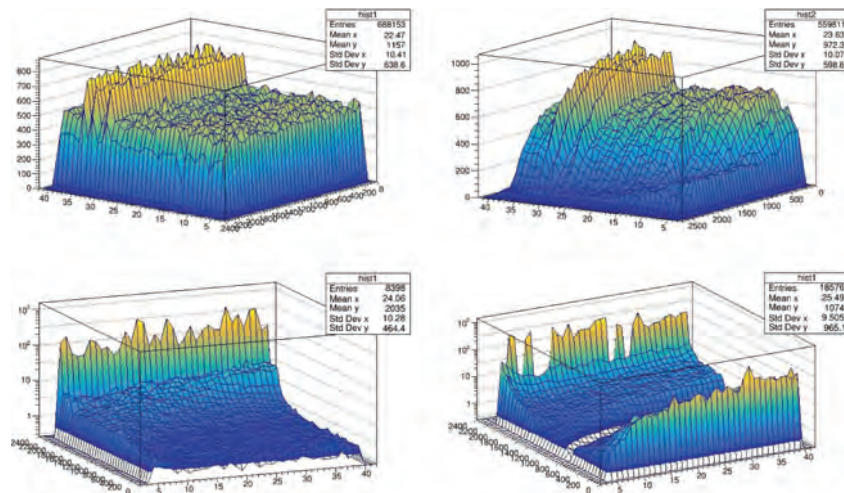


Figure 4: (Clockwise from top left) The true neutrino energies vs. the true drift times; The true neutrino energies vs. reconstructed drift times (with physical bounds); The first histogram

divided by the true neutrino energies vs. the reconstructed drift times (no bounds); The first histogram divided by the second histogram (physical bounds).

Methods

Many of the drift times for the reconstructed data (both with and without background) was outside of physical limits of the detector. To fix these inconsistencies, we added cuts to drift times that were too large to be found in the detector and cut drift times below $1 \mu\text{s}$. We also added cuts on the energy. We cut all of the data above 40 MeV and below 5 MeV. Finally we scaled the reconstructed data to account for the data that was lost in making these cuts.

Results

When these improvements were implemented some of the reconstructed data was lost. There was an efficiency of 93.2% with the clean data and an efficiency of 82.6% with the data with background. The following histograms show the improved ratios for the clean data.

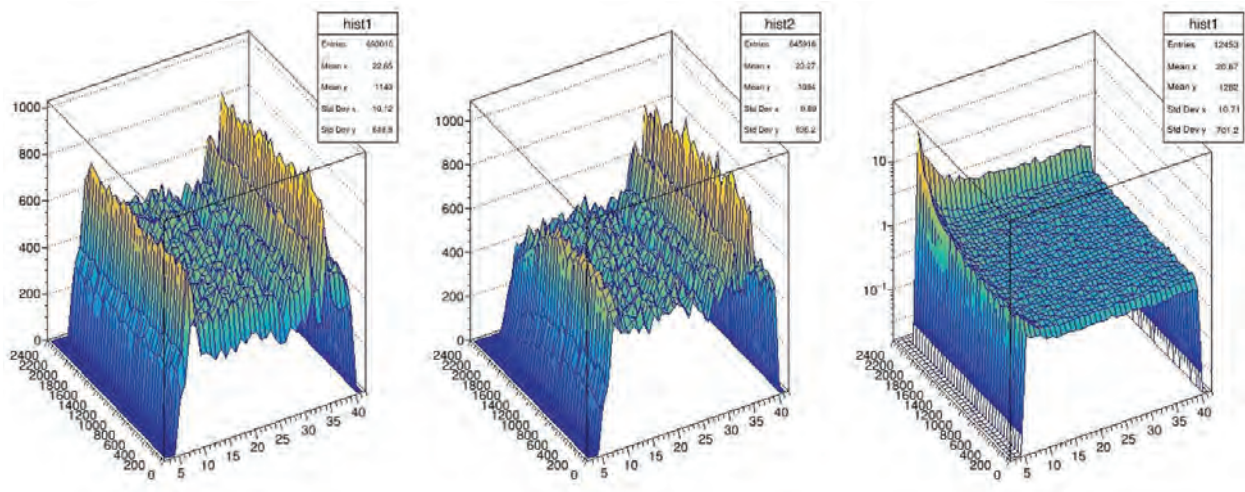


Figure 5: (Left to right) True neutrino energy vs. true drift time; Improved true neutrino energy vs. reconstructed drift time; Improved ratio between the first and second histograms.

These next set of plots show the improvements on data with background.

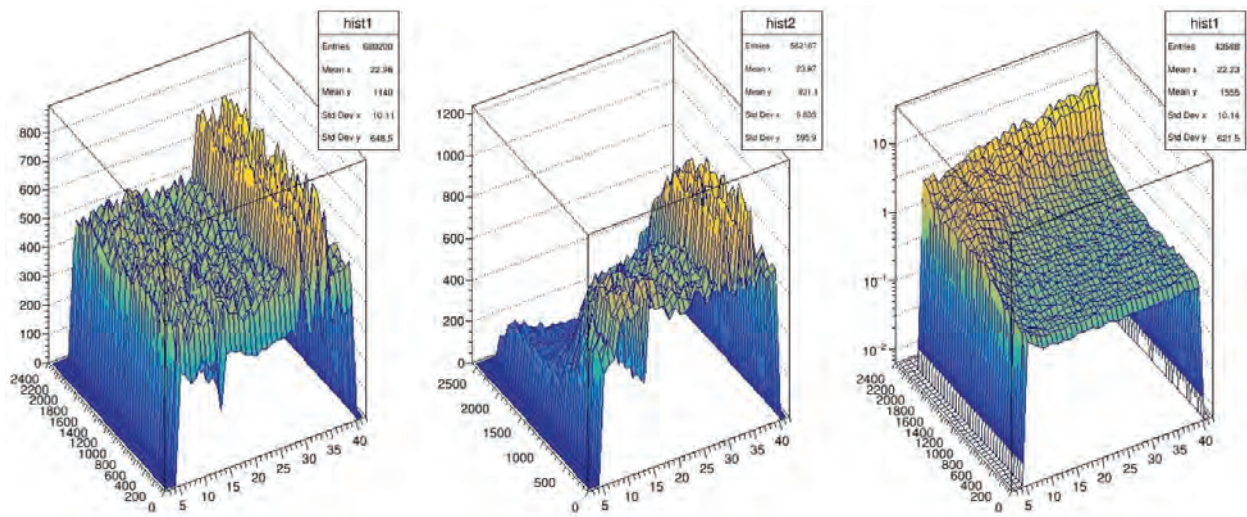


Figure 6: (Left to right) True neutrino energy vs. true drift time; Improved true neutrino energy vs. reconstructed drift time; Improved ratio between first and second histograms.

Discussion

When improving the ratio of the clean data set, the efficiency is quite good and we only lose a small fraction of the reconstructed data. However, almost 20% of the reconstructed data was lost when improving the ratio with background.

It is important to note when interpreting the previous histograms that the true drift time was divided by the reconstructed drift time so the peaks in the previous histograms highlight a deficiency in the detector as opposed to the detector over measuring a particular part of the dataset. In the clean data set, there are deficiencies at low energies and high drift times, with the greatest deficiency at the cross section of both. In the simulation with background, there is also a deficiency at low energies and high drift times. However, the deficiency at high drift times increases as the neutrino energy increases.

It would be possible to reduce the deficiencies of the detector at the high drift times if the

size of the detector was reduced to less than 2000 μs or if there was an added detector at the far wall of the detector. With a second detector the electron would never have a drift time greater than 2000 μs from either one of the detectors. Adding a second detector, while more expensive, would greatly improve the relationship between true and reconstructed drift times at high drift times without sacrificing the amount of data collected.

Conclusion

In this study, we looked at the relationship between the true and reconstructed drift times as a function of the true neutrino energy in order to further understand the detector effects on the energy resolution. The efficiency of these improvements for the reconstructed clean data was 93.2% and for the data with background was 82.6%. We created new histograms of the ratio between the true and reconstructed drift times against the true neutrino energy which reveal that there were deficiencies in the detector at low energies and high drift times. However, in the simulation with background, the deficiencies at high drift times increased at higher energies. Due to the large deficiencies in the detector at high drift distances for both the clean data and data with background, we believe that a second photon detector on the far wall would be best to improve the energy resolution.

Further Research

Unfortunately, there was more research that we did this summer than can be fit in ten pages. If you wish to read the full paper please check the dune science documents [6] or email me at rprocter@asu.edu.

References

- [1] Erin Conley. "ChargeDistEveryone_OpResim.root". June 12, 2019. Dunevgpm10.fnal.gov.
[/dune/data/users/econley](#).
- [2] Erin Conley. "ChargeDist_wbkg.root". June 12, 2019. Dunevgpm10.fnal.gov.
[/dune/data/user/econley](#).
- [3] Erin Conley. "ChargeDist_module.cc". June 12, 2019. Dunevgpm10.fnal.gov.
[/dune/app/users/econley/larsoftv082100/srcs/dunetpc/dune/ChargeDist/](#)
- [4] Erica Snider. "Introduction to LArSoft". August, 2015. Retrieved from
<https://indico.fnal.gov/event/9928/session/8/material/2/0>
- [5] An International Experiment for Neutrino Science. 2015. Retrieved from
<https://www.dunescience.org/>
- [6] Rachel Procter-Murphy. *Energy Reconstruction of Low Energy Supernova Neutrinos*.
<https://docs.dunescience.org>.

**Measurements on Magnetic Properties and Transport
Properties of Spintronic Materials**

BINGCHENG QING

Xi'an Jiaotong University

2019 NSF/REU Program

Physics Department,

University of Notre Dame

Advisor: Prof. Jacek K. Furdyna and Prof. Xinyu Liu

Abstract

This report explores the magnetic properties and transport properties of spintronic materials, including GaMnAsP and PbEuSe:PbSnSe:PbEuSe trilayer, using superconducting quantum interference device and Hall effect measurement. Moreover, the improvements to prevent the thermal noise in transport property measurements by using Delta mode, Pulse Delta mode and Conductance Differential mode are introduced and tested. As the result, the GaMnAsP samples show a strong ferromagnetic signal with the Curie temperature of 75K after annealing at 270°C, comparing the weak ferromagnetic signal with the Curie temperature of 38K before annealing; and the PbEuSe:PbSnSe:PbEuSe trilayer has the P-type carrier density of $2.486 \times 10^{18} \text{cm}^{-3}$ and the carrier mobility of $2319 \text{cm}^2 \text{V}^{-1} \text{s}^{-1}$.

Keywords: Spintronic, Magnetic semiconductor, Topological insulator, superconducting quantum interference device (SQUID), Hall effect, Curie temperature, Hall effect, Carrier mobility;

1 Introduction

The exploration of magnetic semiconductors and topological insulators (TI) has been continuing to gain great interest due to their potential in computer science, spintronic science and so on. The magnetic semiconductors, which are combined with the storage functional ferromagnetism and control functional semiconductivity in computer science together, can provide a new method of the computer system. As for the TI, the direction of electron flow on the surface is coupled with the spin, which can also be applied in spintronic science. There have been some experimental and theoretical researches reported,

including the spin control using GaMnAs based on spin injection [1] and the quantum anomalous Hall effects (QAHE) in magnetic doped TI. [2]. However, the application of magnetic semiconductors and TI is facing great challenges. For example, most magnetic semiconductors have a very low Curie temperature, and most QAHE is only observed at mK temperature range.

2 Method

2.1 Sample Growth through Molecular Beam Epitaxy (MBE)

Our samples are grown through MBE equipment which is a technique based on ultra-high vacuum to produce epitaxial structures with atomic monolayer control. The MBE method is firstly developed in the later 1960s at Bell Telephone Laboratories by J. R. Arthur and Alfred Y. Cho [3]. The structure of MBE is illustrated in Fig. 1. The substrate is located in a chamber with an ultra-high vacuum generated by the Turbo pump. When growing samples, the shutter of the target element cell is opened and the element is grown on the substrate. The substrate can rotate by the magnetic manipulator to ensure the uniformity of growth. A reflection high-energy electron diffraction (RHEED) system is applied to monitor the growth of samples. When a complete layer is grown successfully, the RHEED screen will perform the electron diffraction pattern, which is generally periodic bright lines. On the contrary, the RHEED screen will show a chaotic pattern when the layer is grown incompletely [4].

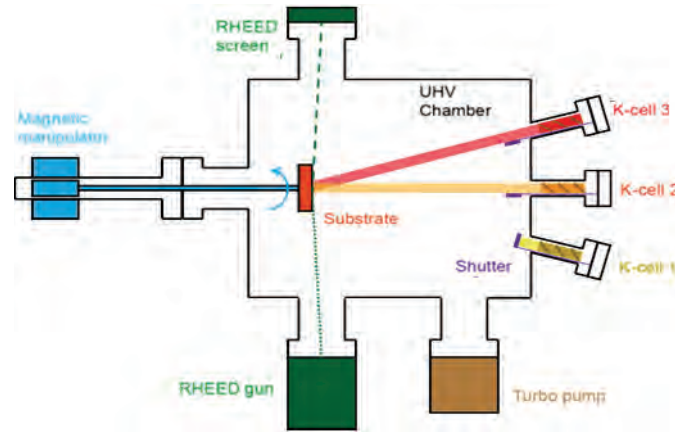


Fig. 1 MBE structure

By carefully controlling the flux of cells and the time of growth, the epitaxy structures of layers with specific thickness in nanoscale can be generated with high quality.

2.2 Magnetic Property Measurement through Superconducting Quantum Interference Device (SQUID)

Due to the tiny volume (thickness $\sim 10\text{nm}$, area $\sim 10\text{mm}^2$) of samples, the magnetic signals are very small. Thus, SQUID, a very sensitive magnetometer based on the Josephson effect, is used to measure the magnetization of samples. The SQUID structure is shown on the left of Fig. 2, and the core part of SQUID is a superconducting ring containing two Josephson junctions shown on the right of Fig. 2. Each Josephson junction consists of two superconductors separated by a very thin insulator.

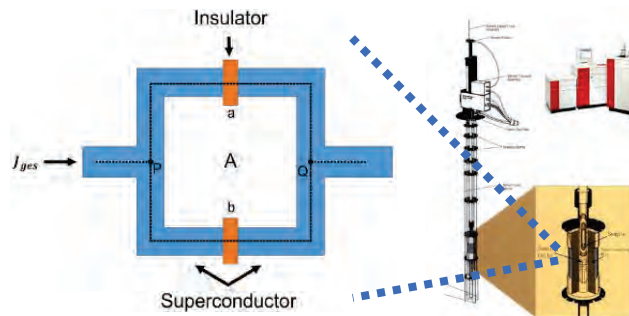


Fig. 2 SQUID structure and superconducting ring.

When applying current to the superconducting ring, the current flow through the ring is related to the magnetic flux Φ by equation 1, where q_e is the charge of an electron [5].

$$I_{ges} = I_{\max} \cos\left(\frac{2\pi q_e}{\hbar} \Phi\right) \quad (1)$$

Therefore, the magnetic flux has an interference-like relationship with current flow, which is very similar to double-slit interference in optics. When the magnetic flux changed continuously, the constructive and destructive interference of the current flow will happen in succession. Because of the large factor $\frac{2\pi q_e}{\hbar}$ in front of magnetic flux Φ , the change of current is so sensitive to the change of magnetic flux that even the change in $\frac{\hbar}{2\pi q_e}$ scale ($\sim 10^{-15} \text{Tm}^2$) can be detected.

The SQUID used in our measurement is a commercial system manufactured by Quantum Design, Inc., named Magnetic Property Measurement System (MPMS) Model XL, which is sensitive enough to measure magnetic moments of the sample as low as 10^{-9} emu [6].

2.3 Transport Measurement

The transport measurement is based on Hall bar geometry shown in Fig.3. Six contractors are applied to the sample. When the current flowing through the sample, the voltage U_{xy} and U_{xx} will be measured.

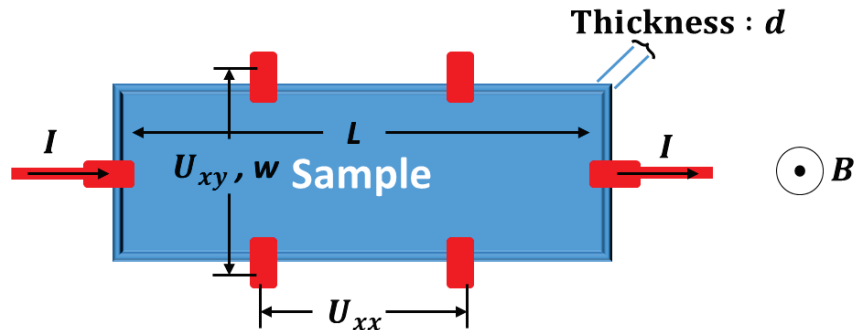


Fig. 3 Hall bar geometry

The voltage U_{xy} reveal the property of Hall resistance, which shows the carrier density.

With non-ferromagnetic materials, the normal Hall resistance is proportional to the out-of-plane magnetic field with equation 2, where n is the carrier density, B is the field applied, I is the current applied and e is the elementary charge.

$$U_{xy} = \frac{I}{ned} B \quad (2)$$

The voltage U_{xx} reveals the property of Longitudinal resistance, which is related to the carrier mobility μ with equation 3.

$$U_{xx} = \frac{IL}{wnde\mu} \quad (3)$$

3 Samples and Results

Our magnetic semiconductor GaMnAsP samples have the thickness of 62.5nm and are separated into two pieces, one is measured directly and the other is annealed at 270°C before the measurement.

By subtracting the magnetic signal of GaAs substrate, the out-of-plane and magnetizations of two GaMnAsP samples under 5K measured by SQUID are shown in Fig. 4. Before annealing, the sample shows a weak out-of-plane ferromagnetic signal, while after annealing, the sample shows a strong signal of out-of-plane ferromagnetism.

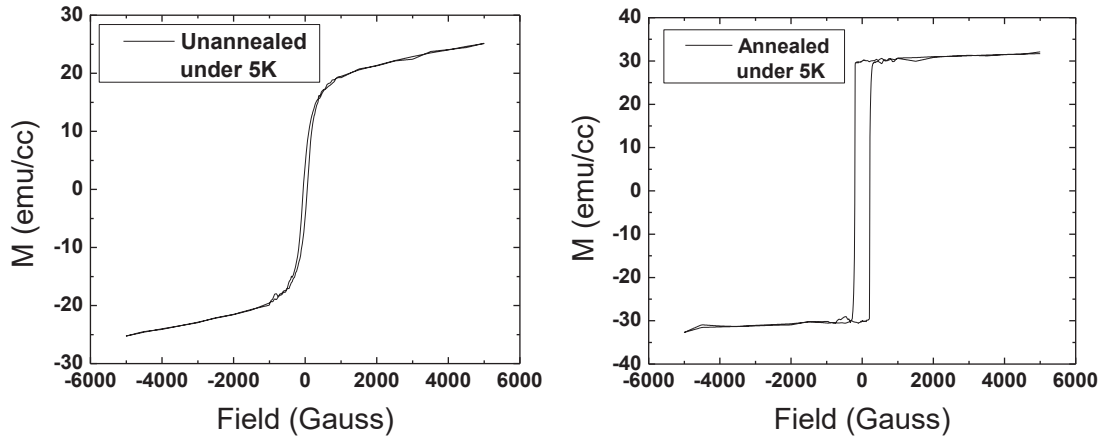


Fig. 4 Magnetizations of GaMnAsP samples

The magnetizations under the field of 25 Gauss with different temperature are measured as well and shown in Fig. 5. After annealing, the Curie temperature rises from 38K to 75K.

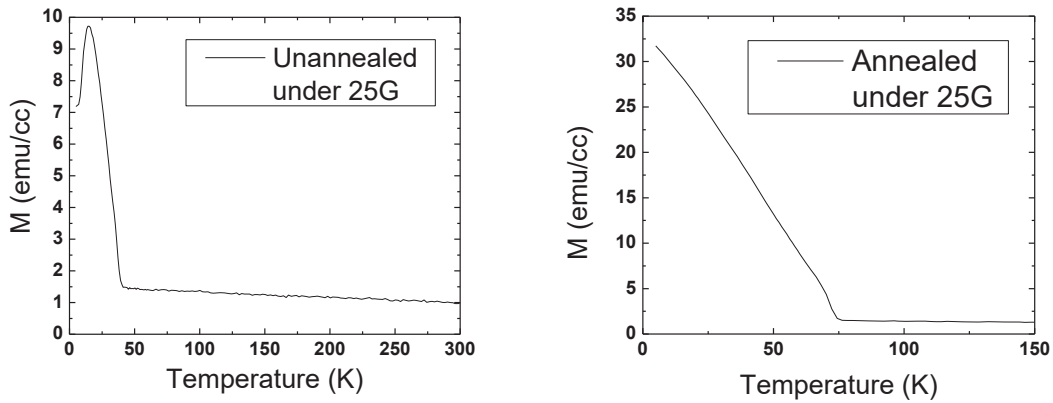


Fig. 5 Magnetization with different temperature

The transport properties of the topological insulator PbEuSe:PbSnSe:PbEuSe trilayer samples are measured. The relationship between field and Hall voltage of PbEuSe:PbSnSe:PbEuSe trilayer is shown on the left of Fig. 6. A linear relationship is observed because the ferromagnetism of the trilayer disappeared at 300K. By linear fitting, it is obtained that the carrier density is $n = 2.486 \times 10^{18} \text{cm}^{-3}$ and the trilayer is a p-type

semiconductor. The longitudinal voltage under 10K is shown on the right of Fig. 6, which shows that the longitudinal resistance increases when magnetic field goes beyond zero. The carrier mobility is $2319\text{cm}^2\text{V}^{-1}\text{s}^{-1}$.

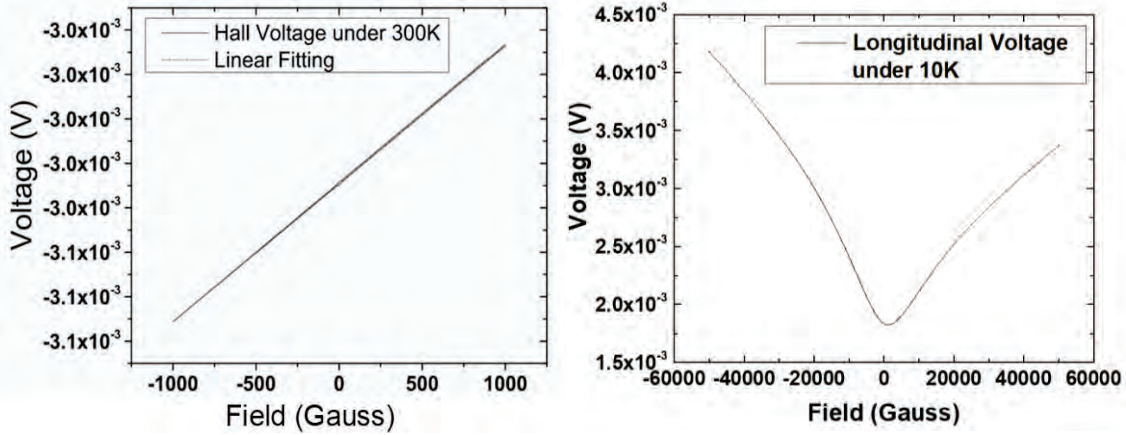


Fig. 6 Transport measurement

4 Discussion

It is observed that the ferromagnetism is enhanced by annealing for GaMnAsP. It can be explained by the dramatic change of carrier density after annealing. Such dramatic change strongly strengthens the out-of-plane anisotropy magnetic of GaMnAsP, thus the ferromagnetism and Curie temperature will be both enhanced by annealing.

When measuring the Hall voltage, the signal is on the scale of several millivolts. With such a small scale, the thermal noise is not neglectable. Considering the thermal noise in a short time, it is reasonable to approximately use a timely linear equation to describe the thermal noise. With such approximation, three methods are used to prevent the influence of thermal noise in transport measurement, including Delta mode, Pulse Delta mode and Conductance Differential mode [7].

After measuring the same sample under the same condition 100 time with each of the three

modes and traditional DC mode, the averages and standard deviations of the 100 measurements are shown in Fig. 7. It can be seen that the averages and standard deviations of those three modes is smaller than that of DC mode, which means the averagely positive thermal noise is subtracted in those three modes.

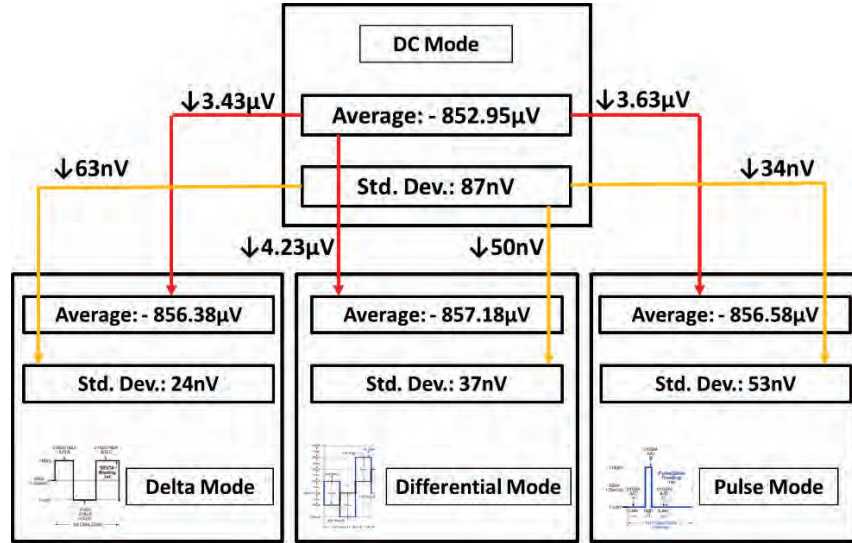


Fig. 7 Comparison between different modes

5 Conclusion

The study explored the magnetic property of magnetic semiconductor GaMnAsP and transport properties of the topological insulator PbEuSe:PbSnSe:PbEuSe trilayer sample. According to the data obtained by SQUID, the GaMnAsP sample shows weak ferromagnetic signal with Curie temperature of 38K before annealing but strong ferromagnetic signal with the Curie temperature of 75K after annealing. Moreover, with the data obtained by Hall effect measurement, PbEuSe:PbSnSe:PbEuSe trilayer is a P-type semiconductor with the carrier density of $2.486 \times 10^{18} \text{cm}^{-3}$, and has the carrier mobility of $2319 \text{cm}^2 \text{V}^{-1} \text{s}^{-1}$.

6 Acknowledgement

I would like to thank Prof. Jacek K. Furdyna for receiving me as his REU student and his generous help, and Prof. Xinyu Liu for his careful guidance on my REU project. Moreover, Prof. Seul-Ki Bac, Prof. Sanghoon Lee and Jiashu Wang are also strongly thanked for helping me. I should also thank Prof. Umesh Garg and Lori Fuson, as well as the University of Notre Dame and Xi'an Jiaotong University for providing me such a chance to experience research. Finally, I would thank my family, friends and girlfriend for their supporting.

Reference:

[1] Ohno, Y. et al. Electrical spin injection in a ferromagnetic semiconductor heterostructure. *Nature* 402, 790–792 (1999).

[2] Kou, X., Guo, S. T., Fan, Y., Pan, L., Lang, M., Jiang, Y., ... & Wang, Y. (2014). Scale-invariant quantum anomalous Hall effect in magnetic topological insulators beyond the two-dimensional limit. *Physical review letters*, 113(13), 137201.

[3] A. Cho, J. Arthur, *Prog. Solid-State Chem.*, 10, 157 (1975).

[4] Herman, M. A., & Sitter, H. (2012). *Molecular beam epitaxy: fundamentals and current status* (Vol. 7). Springer Science & Business Media.

[5] Leiner, J. et al. (2012). Exchange coupling in the ferromagnetic semiconductor GaMnAs. *Dissertations & Theses - Gradworks*, 8(2), 1120-1120.

[6] Quantum Design. (2011). *Magnetic Property Measurement System – MPMS®-XL* [Brochure].

[7] Model 6220 DC current source, model 6221 AC and DC current source user's manual (2005)

Low-energy electron interactions with triatomic molecules: CO₂ and H₂O

Melissa Quevedo Lopez

2019 REU Program

Department of Physics, University of Notre Dame

Advisor: Prof. Sylwia Ptasinska

Abstract

Low energy electron interactions with triatomic molecules: CO₂ and H₂O were studied using a crossed electron/neutral beams technique in combination with a quadrupole mass spectrometer (QMS). The QMS can be used for compound analysis by measuring mass spectra. In addition, energy and time dependencies can be measured for a specific ionic fragment and presented as ion yield curves as a function of electron energy or time. In this project mass spectra were determined for each molecule, for carbon dioxide an energy of 70 eV was used and for water 50 eV. The appearance energies (AE) were also obtained for positive ions and dissociative electron attachment resonances for negative ions formed due to electron impact on both molecules.

Introduction

When high-energy radiation (photons, ions, electrons) interacts with the matter, a high flux of secondary low energy electrons (LEE) is produced. These electrons can then efficiently trigger various dissociative processes and chemical reactions [1]. When an electron is incident on a generic molecule AB, it may lead to molecular dissociation in one of three reaction pathways: electron impact excitation (occurs at energies above ~ 3 eV), electron impact ionization (above 10 eV) and electron attachment (typically occurs at energies below 15 eV). In the last reaction pathway, i.e., electron attachment, a temporary negative ion (TNI) is formed. This reaction channel is perhaps the most important, as it is exclusive to electron induced fragmentation. Dissociative electron attachment (DEA) processes are applied to cross-disciplinary research areas: atmospheric and planetary atmosphere physics, astrochemistry (formation of molecules

in space) [3], semiconductor plasmas for manufacture of computer chips [4], radiation damage of DNA and cellular material [5], nanotechnology and surface engineering. Studies on near-threshold single and dissociative ionization of polyatomic molecules help to uncover the role of initial energy dissipation during electron–molecule interaction.

Experimental Set-up

For this project a high vacuum chamber was used (base pressure of $\sim 1 \times 10^{-7}$ mbar) with a quadrupole mass spectrometer (QMS) from Hiden Analytical. The QMS is the essential component of the whole setup which can be used for compound analysis by measuring a mass spectrum (up to 500 amu), as well as energy and time dependencies for a specific ionic fragment by measuring the ion yield curves as a function of electron energy or time. Correspondingly, the QMS can be operated in Secondary Ion Mass Spectrometer (SIMS) mode and Residual Gas Analysis (RGA) mode. In SIMS mode, a proper voltage is applied on the extractor equipped on the front end the QMS to attract ions generated outside the QMS. In RGA mode a current runs through the filament in the ion source part to emit electrons and the ions are generated through the electron molecule collision in this region. Mass spectrum measurements and the ion yield were recorded by means of MASsoft. The vapor of the liquid sample or gas-phase sample is introduced into the chamber through a gassing line connecting the sample container and a stainless steel leak valve affixed to the vacuum chamber wall. Inside the vacuum chamber, the gas sample is emitted from a thin metal tube attached to the outlet of the leak valve. The molecular beam is aimed at the small aperture in the front end of the mass spectrometer. There are two electron sources in this setup. An electron gun

affixed on the side wall of the chamber can generate a well collimated electron beam crossing the molecular beam right in front the QMS or built-in ion source part situated in the front end where two oxide iridium filaments are installed. [6]

Results and discussion

Electron impact to CO₂

Mass spectrum

Fig. 1 shows the mass spectrum of carbon dioxide (CO₂) measured at an electron energy of 70 eV. The peak 16 amu can be identified as O⁺, 32 amu as CO⁺, 44 amu is CO₂⁺ and the peak 45 amu is an isotope of CO₂⁺. There is good agreement between the measured spectrum showing a several fragment ions with that reported in the NIST database [8] and also in previous studies [9].

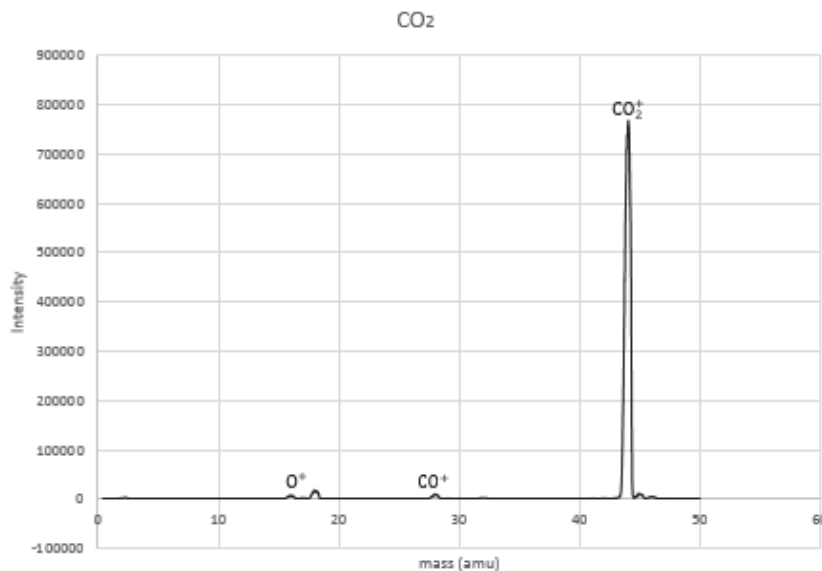


Fig.1 Mass spectrum of CO₂ obtained by 70 eV electron impact on neutral CO₂

Appearance Energies Resonances for Cations

The Fig. 2 shows the ionization efficiency curves for the parent ion, an isotope of the parent ion and two fragment ions of CO_2 . The parent ion CO_2^+ exhibits AE at 13.4 eV being the most abundant cation, the isotope of parent ion exhibits AE at 12.3 eV. The AE value of 15.5 eV corresponds to formation of CO^+ and finally the value of 18.5 eV corresponds to O^+ .

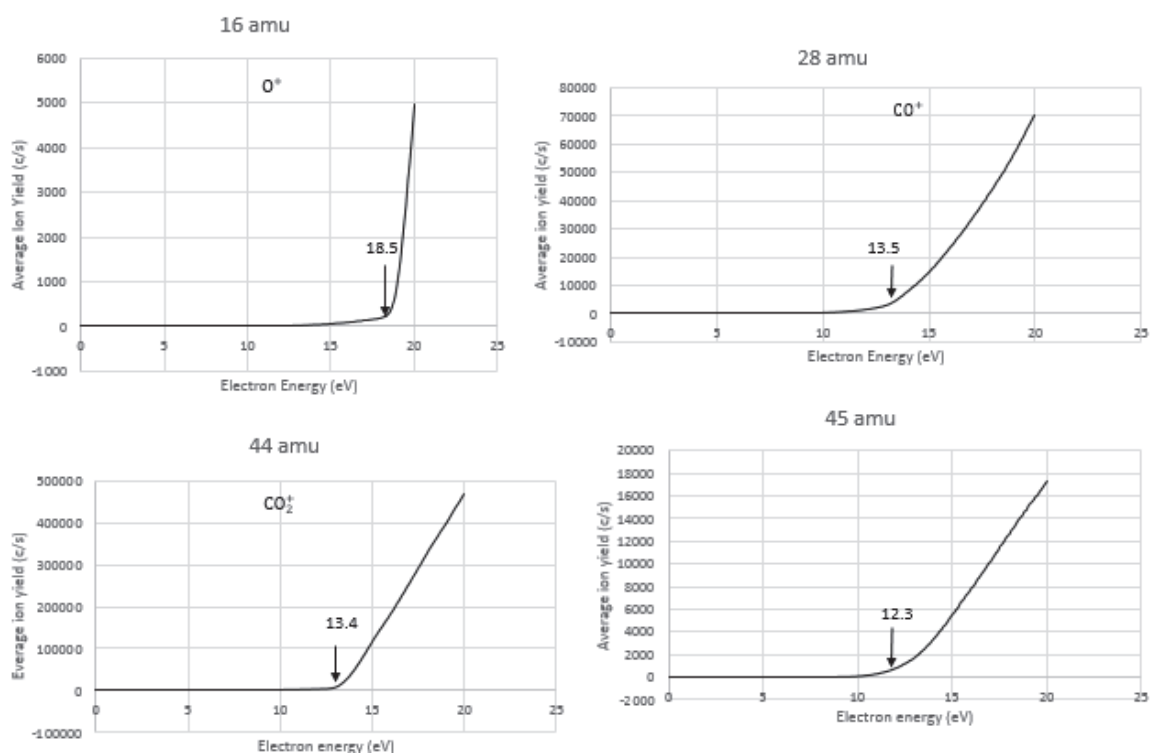


Fig.2 Fig. 2 Ionization efficiency curves for the formation of cations from neutral CO_2 by electron impact.

Table 1: Comparison of the present AEs of cations from CO₂ obtained experimentally with AEs reported previously in [11] and [7]

Cation	Mass (amu)	Present AE (eV)	Previous AE (eV)
O ⁺	16	18.5 ± 0.1	19.05 ± 0.05
CO ⁺	28	13.5 ± 0.1	14.014 ± 0.0003
CO ₂ ⁺	44	13.4 ± 0.1	13.79 ± 0.25
CO ₂ ⁺ isotope	45	12.3 ± 0.1	-

DEA Resonances for Anions

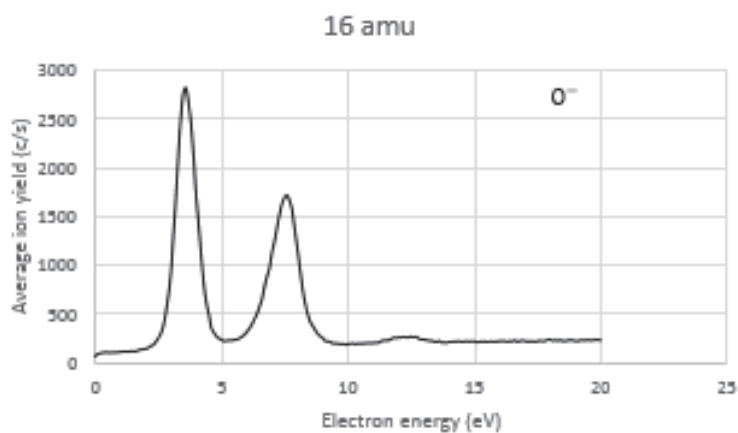


Fig. 3 Ion yield curve as a function of electron energy for the formation of O⁻ from DEA to CO₂

Fig. 3 shows the ion yield curve as a function of electron energy for the formation of O⁻ from DEA to a CO₂ molecule. The ion yield curve to O⁻ shows two significant resonances at 3.5 eV and 7.8 eV which are at similar energies and similar relative intensities as those reported previously [10].

Electron Impact to H₂O

Mass Spectrum

Fig. 4 shows the mass spectrum of water (H₂O) measured at an electron energy of 50 eV. The peak 16 amu can be identified as O⁺, the peak 17 amu correspondent to OH⁺, the peak 18 amu as H₂O⁺ and peak 19 amu corresponds to an isotope of H₂O⁺. There is agreement between the measured spectrum concerning the formation of fragment ions in this study with the mass spectrum reported in the NIST standard atomic and molecular constant database. [7]

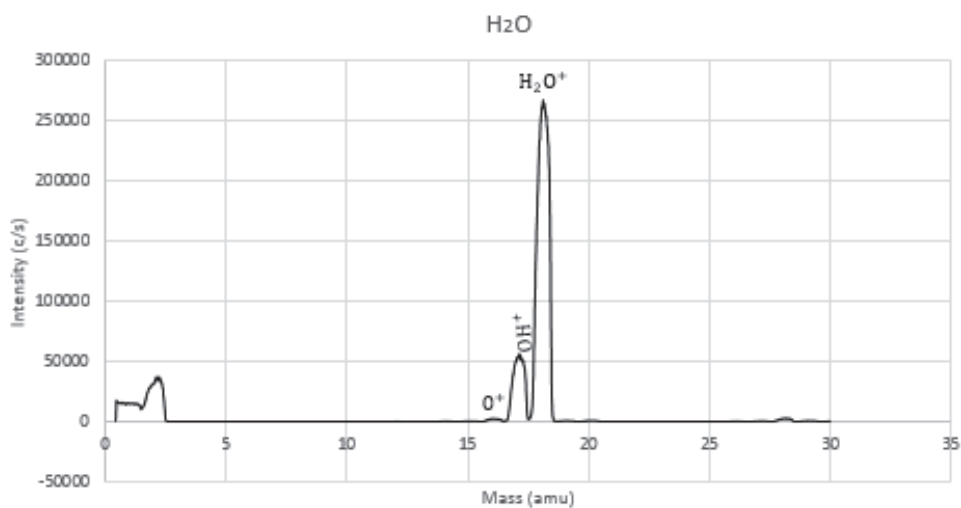


Fig.4 Mass spectrum of H₂O obtained by 50 eV electron impact on neutral H₂O

Appearance Energies Resonances for Cations

Fig.5 shows the ionization efficiency curves for the parent ion, an isotope of the parent ion and two fragment ions formed from H₂O. The parent ion H₂O⁺ exhibits AE at 12.2 eV, the lowest threshold of all

measured ionization efficiency curves, however the most abundant. The higher AE has the cation OH^+ formed at 17.9 eV. Whereas the AE 13.3 eV corresponds to O^+ formation.

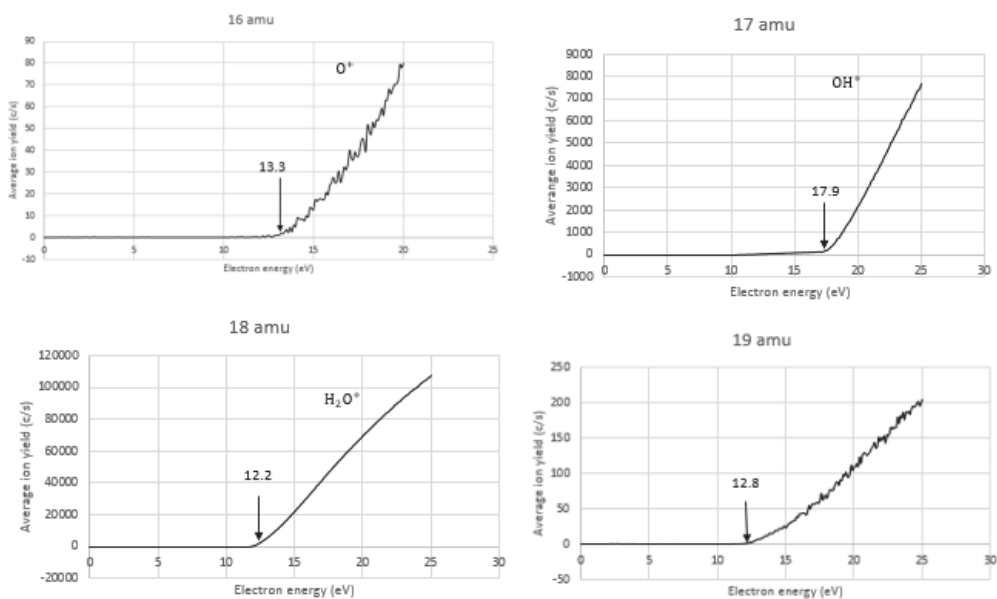


Fig.5 Ionization efficiency curves for the formation of cations from neutral H_2O by electron impact.

Table 2: Comparison of the present AEs of cations H_2O obtained experimentally with AEs reported previously [11]

<i>Cation</i>	<i>Mass (amu)</i>	<i>Present AE (eV)</i>	<i>Previous AE (eV)</i>
O^+	16	13.3 ± 0.1	13.618
OH^+	17	17.9 ± 0.1	18.115
H_2O^+	18	12.2 ± 0.1	12.58
H_2O^+ isotope	19	12.8 ± 0.1	-

Fig. 6 shows the ion yield curve as a function of electron energy for the formation of O^- from DEA to a H_2O molecule. The ion yield curve to O^- shows three resonances at 6.3 eV, 8.3 eV, and 10.3 eV, which are in good agreement with an earlier report [8].

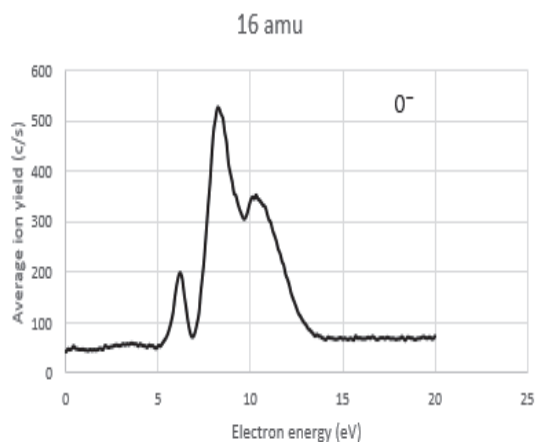


Fig. 6 ion yield curve as a function of electron energy for the formation of O^- from DEA to H_2O

Conclusions

The results obtained in this project show that for the mass spectra of both molecules, there is agreement between the measured spectrum concerning the formation of fragment ions with the NIST standard atomic and molecular constant database and different papers. The AEs and DEA resonances obtained for both molecules occur at very similar energies to those reported in the literature.

References

- [1] L. A. Sala, Low-Energy Electron Induced Chemistry in Supported Molecular Systems, Ph.D Thesis, University of Paris-Saclay, 1 (2018)

- [2] Zhu, Jane, The Dynamics of Electron-Induced Formation of N⁻² and N⁻³ Species from Condensed Ammonia, Honors Thesis Collection, 5-6 (2016).
- [3] M.C. Boyer et al. J. Phys. Chem. C, 2014, 118, 22592.
- [4] F.H. Ommarson et al. Angew. Chem. Int. Ed, 2014, 53, 12051.
- [5] E. Alizadeh & L. Sanche, Chem. Rev. 2012, 112, 5578
- [6] Zhou L Kasttner, Dissocitive electron Attachment to gas phase biomolecules, University of Notre Dame, 41, (2017).
- [7] NIST chemistry web book, available at: <http://webook.nist.gov>.
- [8] Prashant Rawat et al 2007 J. Phys. B: At. Mol. Opt. Phys. 40 4625.
- [9] Kaur, Parminder and Peter B. O'Connor. "Comparison of charge state determination methods for high resolution mass spectra." 2006 IEEE International Conference on Granular Computing (2006): 550-553.
- [10] S. K. Srivastava and O. J. Orient. "Double e-beam technique for collision studies from excited states: Application to vibrationally excited CO₂", (1983).
- [11] A. N. Zavilopulo, F. F. Chipev, and O. B. Shpenik. "Ionization of Nitrogen, Oxygen, Water, and Carbon Dioxide Molecules by Near-Threshold Electron Impact" (2004).

Characterization of Clover Detectors for use in fIREBall Detectors

Zarif Rahman

2019 NSF/REU Program

Physics Department, University of Notre Dame

Advisors:

Prof. Ani Aprahamian

Prof. Wanpeng Tan

Prof. Shelly Leshner

Abstract: Measurement of conversion electrons is an important aspect of nuclear structure studies. A new fIREBall (fInternal conveRision Electron Ball Array) array is being constructed by building on the existing “ICEBall” mini-orange array of SiLi detectors. fIREBall will come into existence from the replacement of the current array of six mini-orange Si(Li) detectors of ICEBall with twelve Si(Li) detectors to broaden the energy range of the detected electrons. fIREBall will be used in conjunction with two Compton suppressed Ge detectors. Compton suppression shields of Bizmuth Germanate (BGO) will be used on two clover detectors for coincidence measurements of gamma-rays and conversion electrons. I have studied the clover detectors in order to characterize their efficiencies and resolutions. They were calibrated using ^{60}Co and ^{252}Eu sources and a digital DAQ system. Each of the four crystals for each clover detector were evaluated separately and in summing of all four quadrants. This work is based on the full characterization of the energy resolution and the detection efficiency of the two clover detectors envisioned for use with fIREBall.

Introduction:

Measurement of conversion electrons is important in nuclear structure physics with importance in low-lying levels and various degrees of freedom in deformed nuclei and nuclear astrophysics. Knowing how to measure conversion electrons will be crucial in the understanding of the structure of 0^+ states in deformed nuclei, exploring the role of cluster states in light nuclei for stellar evolution, and testing the ab-initio theoretical model predictions. The Pittsburgh Internal Conversion Electron Spectrometer Array or “ICEBall” was constructed in 1993 with six mini-orange spectrometers and was a multiple element array for in-beam internal conversion electron spectroscopy. Since then, new designs have been made to increase the efficiency of mini-orange spectrometers and the acceptance window of electrons. fIREBall (Internal conversion Electron

Ball Array) will be constructed to upgrade the ICEBall system replacing the array of six mini-orange spectrometer with twelve Si(Li) detectors and two Bizmuth Germanate (BGO) anti-Compton suppression shields for use with two Germanium clover detectors at the University of Notre Dame. The new design will result in improved measurements of electrons in coincidence with gamma rays. The clover detectors will be essential in detecting the gamma rays.

A clover detector consists of 4 coaxial N-type high purity germanium crystals. A gamma ray may interact with one or more crystals in the clover detector. When it interacts with one crystal, it may deposit its full energy to the crystal. On the other hand, it can interact with multiple crystals through the process of Compton scattering and share its energy. This is why it is important to study the interaction of gamma rays with individual crystals and any possible combination of crystals.

The serial no., position, and the bias voltage of each of the crystal in the clovers are in the following tables.

Table 1. Serial No., Position, and Bias Voltage for Clover 1.

Crystal Position	Serial No.	Bias Voltage (in V)
1	40-N11538A	3500
2	40-N21518A	3000
3	40-N21456A	3000
4	40-N11539A	3200

Table 2. Serial No., Position, and Bias Voltage for Clover 2.

Crystal Position	Serial No.	Bias Voltage (in V)
1	41-N11542A	4000
2	41-N21573A	4000
3	41-N11534A	3000
4	41-N11672A	4000

Experiment:

Clover 1 was connected to a digital DAQ system following the bias voltage for each crystal from Table 1. A ^{60}Co source was used on the clover and ten minute runs were conducted using mesytec with different settings on the DAQ system. All the crystals were connected for the run. The process was repeated for clover 1 with a ^{152}Eu source and clover 2 with the same ^{60}Co source. The setting on the DAQ system that would give the best efficiency and resolution were determined. The raw data was in the zip.file format and the horizontal axis was in terms of channel numbers and not energy. The system was calibrated to convert the horizontal axis from channels to energy using linear fits.

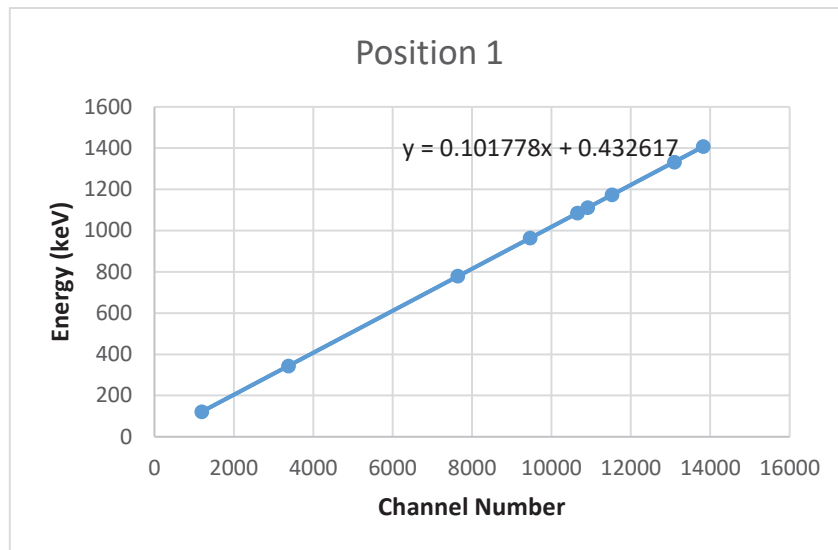


Figure 1. Linear Fit for calibration of Crystal 1 in Clover 1.

Table 3: Calibration parameters of all four crystals of clover 1 & clover 2 from linear fits where x is the corresponding channel number.

	Energies in Clover 1	Energies in Clover 2
Crystal 1	$0.101778x + 0.432617$	$0.108093x + 1.663683$
Crystal 2	$0.102023x + 0.032335$	$0.110993x + 0.907773$
Crystal 3	$0.102377x + 0.520720$	$0.109302x + 0.701314$
Crystal 4	$0.102331x + 0.191605$	$0.112284x + 0.800629$

Histograms were created for the peaks of each of the crystal and any possible combination between them. A threshold of each individual crystal is measured to be around 30 keV.

Normalized Gaussian was used to fit the peaks. Linear fit was also used to account for the background noise. The two parameters that we were interested on were area and standard deviation.

Results:

The following results were obtained from clover 1 and 2 with Normalized Gaussian:

Table 4: Characterization of Clover 1 crystals.

Combination of Summed Peaks	Peak 1			Peak 2		
	Gaussian Area	Sigma (keV)	FWHM (keV)	Gaussian Area	Sigma (keV)	FWHM (keV)
Crystal 1	2738.05	0.93	2.19	2511.9	0.96	2.25
Crystal 2	2878.51	1	2.34	2577.85	1.04	2.45
Crystal 3	3274.5	0.94	2.2	2968.25	0.98	2.32
Crystal 4	3135.31	0.94	2.21	2821.84	0.98	2.31
Crystal (1+2)	1005	1.22	2.86	945.283	1.26	2.96
Crystal (1+3)	309.397	1.23	2.89	288.288	1.26	2.97
Crystal (1+4)	1127.05	1.19	2.79	1030.75	1.25	2.95
Crystal (2+3)	1091.42	1.23	2.89	1055.09	1.28	3
Crystal (2+4)	310.01	1.24	2.92	292.26	1.3	3.07
Crystal (3+4)	1133.7	1.21	2.85	1050.77	1.22	2.88
Crystal (1+2+3)	89.3898	1.35	3.18	78.0488	1.36	3.2
Crystal (1+2+4)	85.0683	1.42	3.33	84.3758	1.33	3.13
Crystal (1+3+4)	92.1652	1.43	3.37	86.973	1.51	3.56
Crystal (2+3+4)	76.9839	1.27	2.98	77.0115	1.45	3.42
Sum (All combinations)	17352.6	1.11	2.62	15919.5	1.19	2.8
Sum (Individual Peaks)	12057.8	1.03	2.43	10907.4	1.11	2.62

Table 5: Characterization of Clover 2 crystals.

Combination of Summed Peaks	Peak 1			Peak 2		
	Gaussian Area	Sigma (keV)	FWHM (keV)	Gaussian Area	Sigma (keV)	FWHM (keV)
Crystal 1	2647.16	1.08	2.54	2282.06	1.11	2.6
Crystal 2	2492.39	0.86	2.03	2263.66	0.91	2.13
Crystal 3	2152.24	0.89	2.1	1953.84	0.92	2.18
Crystal 4	3159.72	1.43	3.37	2866.97	1.46	3.43
Crystal (1+2)	877.989	1.33	3.14	833.74	1.43	3.36
Crystal (1+3)	215.734	1.32	3.12	199.374	1.36	3.21
Crystal (1+4)	1053.54	1.79	4.22	960.956	1.82	4.28
Crystal (2+3)	791.415	1.12	2.64	767.456	1.18	2.78
Crystal (2+4)	279.308	1.59	3.74	249.727	1.58	3.72
Crystal (3+4)	906.165	1.61	3.78	855.549	1.6	3.77
Crystal (1+2+3)	65.4239	1.6	3.76	53.6534	1.51	3.56
Crystal (1+2+4)	71.1582	1.78	4.19	68.3341	1.85	4.35
Crystal (1+3+4)	56.8253	1.63	3.83	60.442	1.67	3.94
Crystal (2+3+4)	72.3703	1.48	3.5	70.2454	1.58	3.72
Sum (All combinations)	14543.1	1.2	2.82	13402.8	1.25	2.95
Sum (Individual Peaks)	10318.1	1.08	2.54	9232.45	1.11	2.61

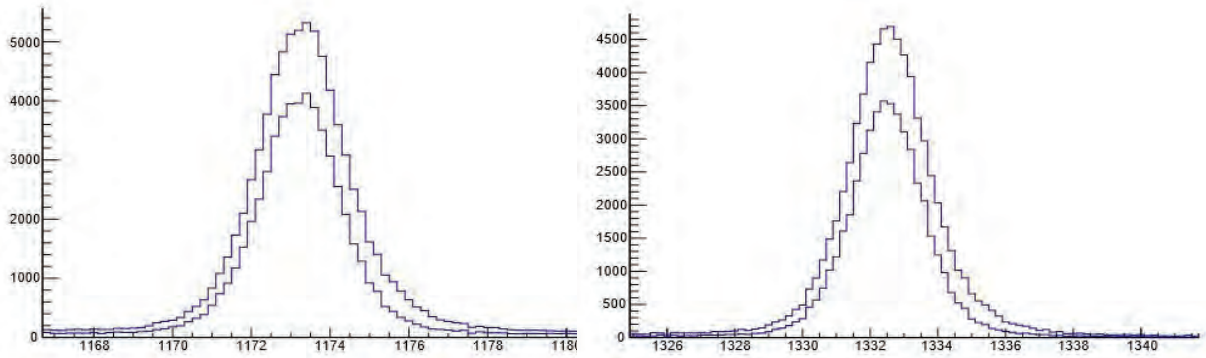


Figure 2. Normalized Gaussian fit of sum of all the combinations vs. the sum of all the individual crystals for Peak 1 & 2 of Clover 1.

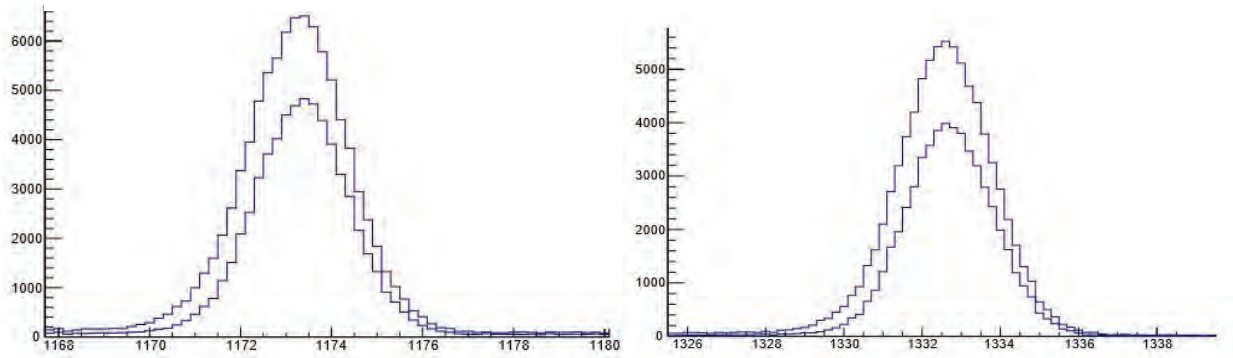


Figure 3. Normalized Gaussian fit of sum of all the combinations vs. the sum of all the individual crystals for Peak 1 & 2 of Clover 2.

When gamma rays were made to go through two crystals, less counts were attained than they were for one crystal. Similarly, when they were made to go through three or four crystals, there were even lower. At four crystals, the count was extremely small and so making a proper Normalized Gaussian fit was not practical. Thus it was not included in the table, but it was included in the sum of all the combinations. As seen from the calculation and the graphs, the sum of all the possible combinations gave a higher efficiency when compared to the sum of all the

individual crystals. However, the resolution was higher for the sum of the individual peaks than for the sum of all the possible combinations as expected.

Conclusion:

The two clover detectors at the University of Notre Dame were studied and characterized for fIREBA11 using a ^{60}Co and ^{152}Eu source. The first clover gave a Gaussian Area of 17352.6 and a resolution of 2.62 approximately for the first peak and a Gaussian Area of 15919.5 and a resolution of 2.8 approximately for the second peak for the sum of all the combination possible among the crystals. The second clover gave a Gaussian Area of 14543.1 and a resolution of 2.817 approximately for the first peak and a Gaussian Area of 13402.8 and a resolution of 2.954 approximately for the second peak for the sum of all the combination possible among the crystals. It was also observed that the sum individual modes had a better resolution, but the summing of all the possible combination had resulted in improved efficiency.

References:

- [1] M.P. Metlay, J.X. Saladin, I.Y. Lee, O. Dietzsch. 1993. The ICEBall: a multiple element array for in-beam internal conversion electron spectroscopy. 0168-9002
- [2] S.R. Leshner, A. Aprahamian, W. Tan. 2019. Proposal to purchase 12 Si(Li) detectors & 2 BGO anti-Compton shields to develop the FIREBALL spectrometer.
- [3] G. Duchene, F.A. Beck, P.J. Twin, G. de France, D. Curien, L. Hau, C.W. Beausang, M.A. Bentley, P.J. Nolan, J. Simpson. 1999. The Clover: a new generation of composite Ge detectors. *Elsevier Preprint*.

**EXTRACTION OF OPTICAL MODEL PARAMETERS FOR $^{90}\text{Zr}(^6\text{Li}, ^6\text{Li})$ AT
60 MEV/U USING A MARKOV CHAIN MONTE CARLO ALGORITHM**

AUSTIN SMITH

2019 NSF/REU Program

Physics Department, University of Notre Dame

DR. UMESH GARG

Abstract

The nuclear incompressibility is a fundamental property of nuclear matter which is critical for modeling astrophysical processes. Measurements of the isoscalar giant monopole resonance (ISGMR) is the most direct means to extract the incompressibility from finite nuclei. ${}^6\text{Li}$ can be used in studies of the ISGMR with radioactive ion beams. However, before measurements with radioactive ion beams may begin, the optical model parameters for ${}^6\text{Li}$ scattering need to be determined. To determine the optical model parameters, the elastic angular distributions of the ${}^{90}\text{Zr}({}^6\text{Li}, {}^6\text{Li})$ reaction were measured using the Grand Raiden spectrometer at the Research Center for Nuclear Physics at Osaka University. Experimental density distributions were used for the projectile and target nuclei to generate realistic volume potentials for the DWBA calculations. The optical model code, ECIS, and a Markov Chain Monte Carlo (MCMC) algorithm were employed to constrain the remaining optical model parameters for the reaction. The MCMC algorithm sampled from the 11-dimensional parameter space to visualize parameter probability distributions, from which the ideal optical model parameters were extracted.

Introduction

Nuclear Incompressibility

The nuclear incompressibility is a fundamental property of nuclear matter that can help provide insight into the dense internal environment of neutron stars [1]. It would provide information that could help determine the equation of state for these stars. K_∞ is the

most important incompressibility term for astrophysics, incompressibility of infinite nuclear matter, currently measured to be 240 ± 20 MeV [2].

$$K_A \approx K_\infty + K_{surf}A^{-1/3} + K_\tau \left(\frac{N-Z}{A} \right)^2 + K_{Coul}Z^2A^{-1/3} \quad (1)$$

Another important value is that of K_τ , the asymmetry term, and it was found to be -555 ± 75 MeV from analysis of Cd isotopes [3]. Both these values are in Eq. (1) that describes finite nuclear incompressibility K_A . As for the other terms in Eq. (1), K_{Coul} is the best known, but least important, with a value found to be 5.2 ± 0.7 MeV, and K_{surf} has no firm value [2].

$$E_{ISGMR} = \hbar \sqrt{\frac{K_A}{m \langle r_0^2 \rangle}} \quad (2)$$

The relationships in Eq. (2) and Eq. (1) allow us to measure the value of K_∞ by studying the energy of isoscalar giant monopole resonance (ISGMR) of nuclei. The strength of the ISGMR is determined experimentally with inelastic scattering; in the past, this has typically been done with ^{208}Pb and ^{90}Zr , due to their stature of doubly-magic nuclei. In measuring tin isotopes though, the strength of the ISGMR was significantly lower than predicted by theory. This tendency has been labeled as “fluffy” nuclei. In order to understand the fluffiness of nuclei, more nuclei need to be studied, including radioactive nuclei. Measuring ^{132}Sn , one of the prototypical radioactive nuclei for ISGMR studies, would be a particularly important experiment where ^6Li would be used, since it has a large proton-neutron imbalance as well as having a doubly-closed shell structure. Owing to their radioactive decay, it is difficult to prepare a target from radioactive isotopes to be used in a traditional scattering experiment. When used in inverse kinematics, the beam intensities available at modern-day radioactive isotope beam facilities are typically low, but sufficient to measure the ISGMR when the

radioisotopes are scattered off the stable targets. ${}^6\text{Li}$ is an isoscalar nucleus that can be made into a target for radioactive beams.

Optical Model

Before ${}^6\text{Li}$ can be used for radioactive beams, the optical model of ${}^6\text{Li}$ must be studied. The optical model offers a phenomenological way to model the angular distributions resulting from reactions, which then are used to extract the strength distributions of giant resonances using Distorted-Wave Born Approximation calculations and a multipole decomposition analysis [3]. The functional form of the optical model is,

$$V = V_{Coul} + V_{VOL} + V_{SURF} + i[W_{VOL} + W_{SURF}] + V_{LS} \quad (3)$$

where,

$$V_{VOL} = -V_{vol}f_v(r, R_v, a_v), \quad (4)$$

$$W_{VOL} = -W_{vol}f_{wv}(r, R_{wv}, a_{wv}), \quad (5)$$

$$W_{SURF} = 4a_{ws}W_{surf}\frac{d}{dr}f_{ws}(r, R_{ws}, a_{ws}), \quad (6)$$

$$V_{SURF} = 4a_sV_{surf}\frac{d}{dr}f_s(r, R_s, a_s), \quad (7)$$

$$V_{LS} = V_{ls}\left(\frac{\hbar}{m_\pi c}\right)^2\frac{1}{r}(\vec{L} \cdot \vec{S})\frac{d}{dr}f_{ls}(r, R_{ls}, a_{ls}), \quad (8)$$

ECIS is a optical model calculating code which is used to create a fit to angular distribution data. The code DFPD5 was used to calculate values for the real and imaginary volume potentials in ECIS at angles and the folded Coulomb part of the optical potential. The

functional form of “f”, Eq.(7) is of the Woods-Saxon form, where for ^{90}Zr $a = 0.523$ and $c = 4.911$ fm.

$$f(r, c, a) = \frac{1}{1 + e^{\frac{(r-c)}{a}}} \quad (9)$$

Markov Chain Monte Carlo Method

The principle of Markov Chain Monte Carlo (MCMC) methods is that the posterior distribution is estimated by taking simulated samples from the prior distribution. There are many types of MCMC algorithms, but the one used in this research is known as the Metropolis algorithm (see Algorithm 1). This algorithm draws samples from a probability distribution by using the full joint density function and independent proposal distributions for every parameter [4]. In Algorithm 1, $\pi(\cdot)$ represents the prior distributions, which in our case is the bounds of the parameters based on physical requirements and $q(\cdot)$ represents the likelihood based on the calculated weighted χ^2 value. The acceptance probability for a sample that increases the likelihood of matching the posterior distribution, which in our case reduces χ^2 , will be 1, so the sample will be accepted. Otherwise, a sample has a chance, based on the ratio α and a uniform distribution, to be accepted even if it increases the value of χ^2 . This allows the program, with a sufficient amount of samples, to escape local minima and find the absolute minimum within the bounded parameter space. An important part of the algorithm is the size of the steps for each parameter. These are tuned by hand to get an appropriate acceptance fraction, somewhere between 30% and 70%. This, along with a burn in phase, where the first portion of results the algorithm produces is ignored, allows the program to

reach a higher probability region of the sample distribution and provides a more reasonable posterior distribution from the accepted samples.

```

initialize  $x^{(0)} \sim q(x)$ ;

for iteration  $i=1,2,\dots$  do
    Propose:  $x^{prop} \sim q(x^{(i)}|x^{(i-1)})$ ;
    Acceptance Probability:;
     $\alpha(x^{prop}|x^{(i-1)}) = \min\{1, \frac{q(x^{(i-1)}|x^{(prop)})\pi(x^{prop})}{q(x^{prop}|x^{(i-1)})\pi(x^{(i-1)})}\}$ ;
     $u \sim \text{Uniform}(u; 0, 1)$ ;

    if  $u < \alpha$  then
        | Accept the proposal:  $x^{(i)} \leftarrow x^{prop}$ ;
    else
        | Reject the proposal:  $x^{(i)} \leftarrow x^{(i-1)}$ ;
    end
end

```

Algorithm 1: Metropolis Algorithm

Methods

Grand Raiden Spectrometer

The data collection for the $^{90}\text{Zr}(^6\text{Li}, ^6\text{Li})$ reaction, with the incident ^6Li at 340 MeV, took place at the Research Center for Nuclear Physics (RCNP), Osaka University, Japan. The Grand Raiden spectrometer is a high-resolution spectrometer that can measure forward angles up to 0° . This is especially useful since the cross section of the giant monopole

resonance is maximum at 0° . The data collected from the reaction is the cross section at a specific angles, ranging from 2.90° to 26.30° in 0.40° increments. For further specifications about the Grand Raiden spectrometer, see [3].

Parameter	Step Size Scale
Real Volume Normalization	0.0001
Imaginary Volume Normalization	0.0001
Real Surface Depth	0.005
Real Surface Radius	0.0001
Real Surface Diffuseness	0.0001
Imaginary Surface Depth	0.005
Imaginary Surface Radius	0.0002
Imaginary Surface Diffuseness	0.0002
Real Spin-Orbit Depth	0.005
Real Spin-Orbit Radius	0.0001
Real Spin-Orbit Diffuseness	0.0001

Table 1: The step size scale for the random walk steps for each parameter.

Metropolis Program

The Metropolis program that was developed in python can handle large ($> 10^9$) χ^2 values by rearranging the exponentials and logarithms preventing overflow errors. The program reads in an ECIS input file, inputs the parameters the program will search over, runs ECIS, then

recovers the χ^2 value from the ECIS output and that value is compared to the previous value. At the end, the program will generate a plot based on the best optical model parameters found. It also generates distribution plots of the tested parameters to provide a visual to determine if there are any correlations between parameters. The tuned step size scaled parameters are seen in Table 1, and the burn in size is set at 10% of the total number of samples. The parameters that were searched for were the normalizations for real and imaginary volume potentials, and the depth, radius, and diffuseness terms for the imaginary surface, real surface, and real spin-orbit potentials.

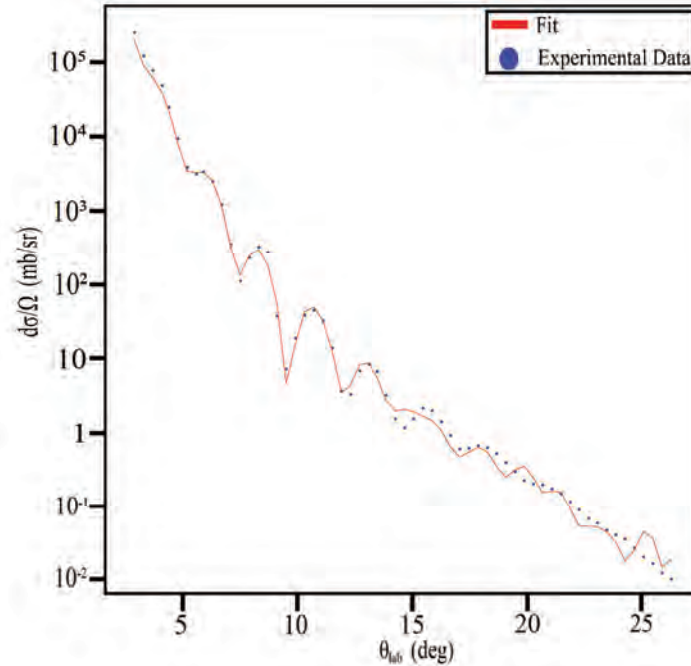


Figure 1: The fit of the data from the extracted optical model parameters.

Results

The values extracted by the Metropolis program that produced the best fit can be seen in Table 2. Figure 1 shows the fit based on these parameters with the experimental data. The χ^2 value of this fit is 27381.5, and the Metropolis program took about 7 hours to run for a hundred-thousand samples. The acceptance fraction was acceptable at 42.12%

Parameter	Extracted Value
Real Volume Normalization	-0.633
Imaginary Volume Normalization	-0.598
Real Surface Depth	-19.456
Real Surface Radius	0.785
Real Surface Diffuseness	1.566
Imaginary Surface Depth	31.098
Imaginary Surface Radius	1.072
Imaginary Surface Diffuseness	0.864
Real Spin-Orbit Depth	1.512
Real Spin-Orbit Radius	1.243
Real Spin-Orbit Diffuseness	0.744

Table 2: The final set of optical model parameters extracted by the program.

Discussion

A longer run time would also produce a better fit, since the Metropolis algorithm, given enough time, will find the best fit even if the parameters are correlated. The next step is to run this code for one or two million samples, since it is likely the program had not yet reached the stationary distribution. Additionally, the value of χ^2 seems disturbingly high, but this is due to the high precision of the measurements, which raises the χ^2 . The extracted parameters in this paper were just for the inelastic part of the $^{90}\text{Zr}(^6\text{Li},^6\text{Li})$ reaction. The next step of this research would be to expand this to also find the parameters for the inelastic optical model. Making this program more efficient would be important for the future, or exploring other algorithms to see if, in this correlated parameter space, a faster and better algorithm exists.

References

- [1] J. Piekarewicz, “Emergence of low-energy monopole strength in the neutron-rich calcium isotopes,” *Phys. Rev. C*, vol. 96, p. 044314, Oct 2017.
- [2] G. Umesh and G. Colò, “The compression-mode giant resonances and nuclear incompressibility,” *Progress in Particle and Nuclear Physics*, vol. 101, pp. 55–95, 2018.
- [3] D. Patel, “A study of the isoscalar giant monopole resonance: The role of symmetry energy in nuclear incompressibility in the open-shell nuclei,” *Springer Theses*, 2016.
- [4] I. Yildirim, “Bayesian inference: Metropolis-hastings sampling,” 2012.

**Adaptive Optics Instrumentation:
Building a Better Wave Front Sensor**

Nicholas Tusay

2019 NSF/REU Program

Physics Department, University of Notre Dame

Advisor: Justin Crepp

Abstract

Instrumentation development is a key component of observational astronomy. Since the mid-90's ground based telescopes have been using adaptive optics to improve their resolution capabilities. Adaptive optics uses real time computing to identify distortions in an incoming wave front, correct for them with a deformable mirror and then repeat the process. The industry standard is the Shack-Hartmann Wave Front Sensor (SHWFS). Technological advances in instrumentation have led to recent developments in more accurate ways of identifying the aberrations in incoming light. Combining expertise in computer science, theoretical modeling and optical systems assembly, our team is working on creating a new wave front sensor that can surpass the resolution power of the current industry standard. The non-linear Curvature Wave Front Sensor (nlCWFS) being developed will greatly enhance the capability of adaptive optics systems.

Introduction

The science of astronomy is conducted primarily by collecting light from distant sources in the universe and analyzing that data. Even close objects are very far in physical space and a high degree of precision is required to obtain usable data. Naturally, improving the resolution of the images provides better data. In some cases this can mean the difference between indiscernible noise and a verifiable signal.

Increasing resolution presents certain technological challenges. The obvious answer is to build bigger telescopes, with bigger mirrors to collect more light. The scientific community

has been doing just that, but at a certain point this becomes logistically and financially prohibitive. And because of financial and logistical issues only a limited number of the biggest telescopes can be built, which introduces supply and demand considerations for time usage.

Building bigger telescopes, however, is not the only way to increase resolution capability. Space based telescopes have the advantage of being able to resolve better images with smaller mirrors simply by collecting light before the Earth's atmosphere interferes with it. Turbulence in the atmosphere distorts and scatters incident rays of light. But space based telescopes are also prohibitively expensive and few and far between.

By being able to account for atmospheric distortions with relatively inexpensive hardware it is possible to significantly increase the resolving power of all ground based telescopes. Optical systems for this purpose have already been put into effect since the 1990s. The current industry standard employed at most major telescopes is the Shack-Hartmann Wave Front Sensor (SHWFS). It uses a lenslet array, a detector, a real time computer and a deformable mirror to analyze the atmospheric distortions, calculate how to counteract them and deform the mirror accordingly. Since it was first implemented, advances in optics, computing and the actuator hardware that deforms the mirror accordingly, have all improved the system to make this a robust method of increasing the resolution of ground based telescopes.

Since the advent of adaptive optics, advances in theory have led to a new kind of wave front sensor called a non-linear curvature wave front sensor. While the theory is more complicated and less intuitive than the Shack-Hartmann, this new sensor offers distinct advantages over its predecessor. The non-linear Curvature Wave Front Sensor (nlCWFS) uses four defocused

planes straddling the pupil to reconstruct an image at the pupil plane. This requires the use of Fourier transforms and iterative numerical analysis. Technological advances in computing power have made it possible to perform these calculations in real time, making a closed loop system feasible to construct. The nICWFS is theoretically capable of more than ten times the sensitivity of the SHWFS. [2]

Method

Adaptive Optics

The most effective adaptive optics systems work in a closed loop by splitting some of the incoming light to a wave front sensor to detect distortions in the light wave, calculate how to correct for that distortion, signal a deformable mirror to make the corrections and repeating the process as the distortions change with time. Figure 1 shows how this process flows through the system. The wave front sensor depicted is the SHWFS, though any wave front sensor can be applied in its place. The key feature is to have a closed loop system that can iterate and correct for the constantly changing aberrations in real time. This process needs to cycle on the order of microseconds in order to keep up with the rapidly changing perturbations caused by atmospheric interference. Current technology allows arrays of thousands of actuators to deform a mirror at $50\mu s$ with nanometer precision. [2] Naturally, the real time computer needs to work faster than this to calculate the wave front and communicate the correction to the actuators.

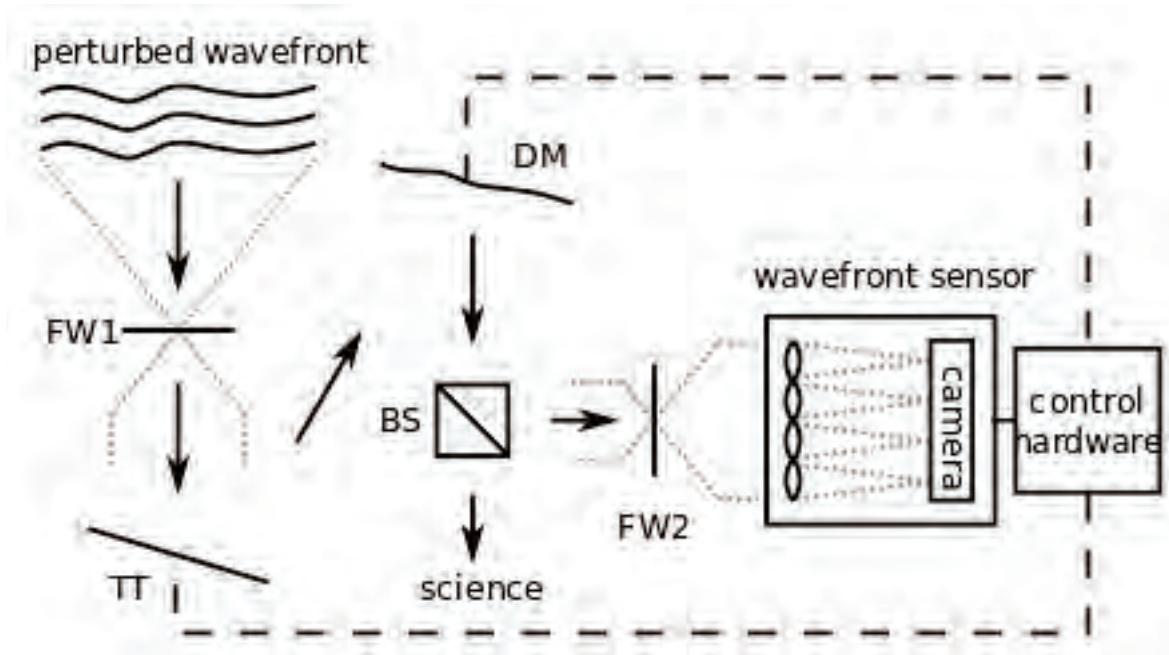


Figure 1: A typical closed loop adaptive optics system uses a beam splitter (BS) to send some of the incident light to a wave front sensor to be analyzed.

Industry Standard

The Shack-Hartmann wave front sensor is currently the industry standard in adaptive optics. It utilizes a simple lenslet array to identify how the wave front is distorted. Knowing that a plane wave front should create a perfectly focused image at the center of each lenslet array, it is easy to reconstruct how a wave has been distorted by analyzing how the image in each cell has been shifted. By increasing the number of lenslets in the array, higher order measurements can be made. However, that also decreases the amount of light per cell and the SHWFS cannot detect aberrations in the absence of light. [2] While adaptive optics using the SHWFS have proven incredibly successful, there is a technological limit to the device that is well below the theoretical diffraction limit that could be achieved with better instrumentation.

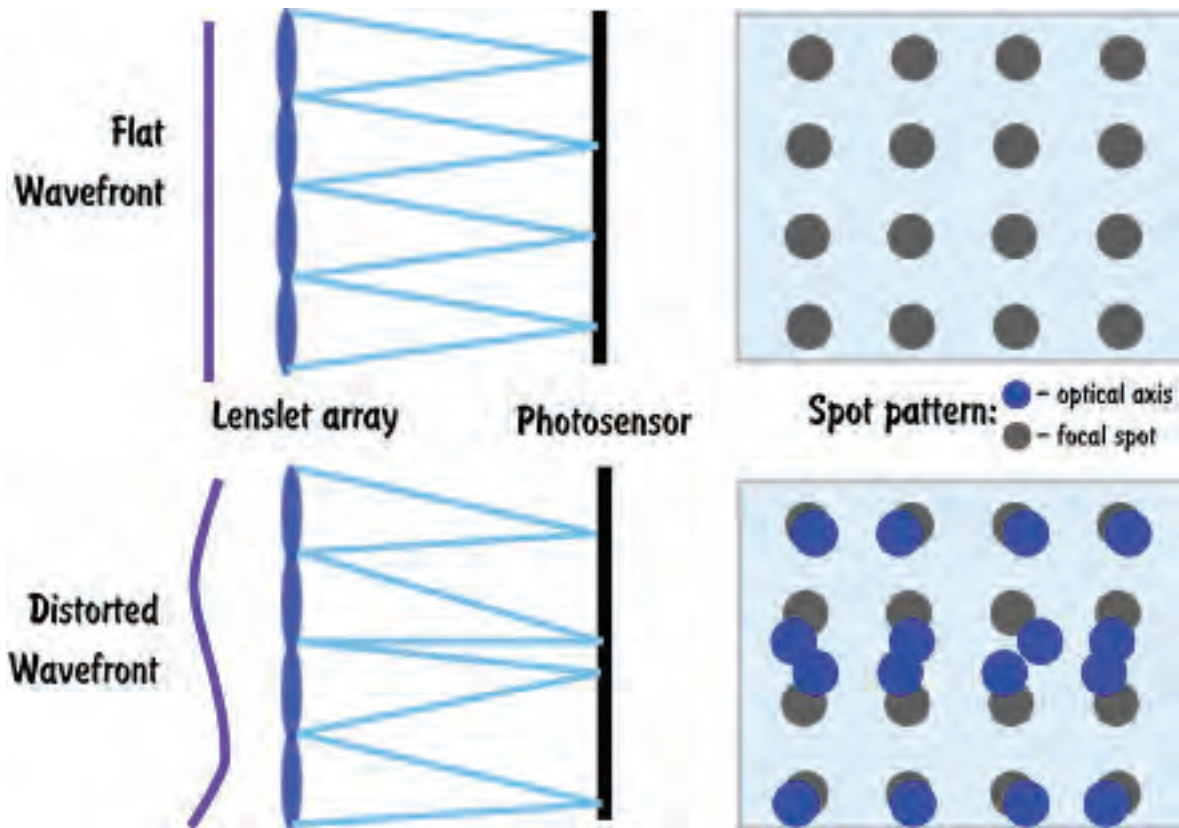


Figure 2: The Shack-Hartmann Wave Front Sensor uses a lenslet array to detect how a wavefront is distorted from what a flat wave front should look like.

The New Wave Front Sensor

The non-linear Curvature Wave Front Sensor (nlCWFS) or Fresnel WFS is capable of improved resolution over the SHWFS. It utilizes four defocused images on either side of the pupil to reconstruct an image at the pupil plane. Figure 3 shows the basic idea behind a conventional Curvature Wave Front Sensor, which utilizes the same physics but only two planes. By comparing phase information between defocused planes on either side of a pupil it is possible to reconstruct an image at the pupil plane. Utilizing four planes instead of two greatly enhances the sensitivity of the wave front sensor. [1] In order to reconstruct the

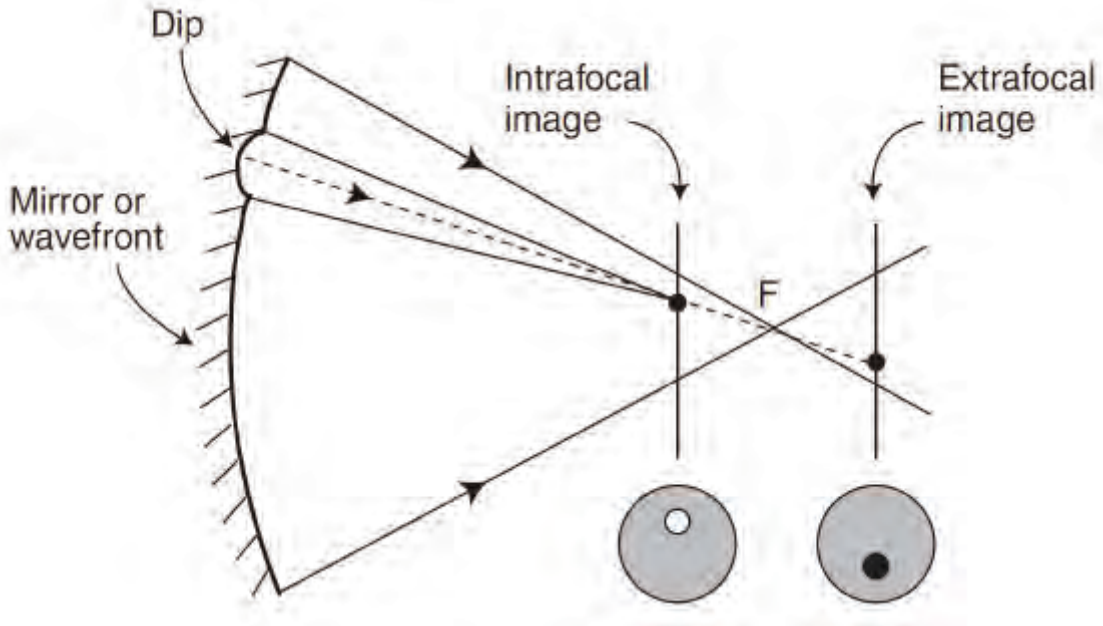


Figure 3: non-linear Curvature Sensors use defocused planes on either side of the pupil to compare the relative curvature in the wave front and reconstruct an image at the pupil plane between them. [2]

image at the pupil plane, the Fresnel diffraction integral must be used: [4]

$$U(x_2, y_2) = \frac{e^{ik\Delta z}}{i\lambda\Delta z} \int_{-\infty}^{\infty} \int_{-\infty}^{\infty} U(x_1, y_1) e^{i\frac{k}{2\Delta z} [(x_1-x_2)^2 + (y_1-y_2)^2]} dx_1 dy_1. \quad (1)$$

This integral must be solved numerically through an iterative process using Fourier Transforms. The solution method has been easily doable for some time, however only recently have advances in computing power made it possible to converge on a solution and reconstruct a wave front in real time.

Conclusion

This project is still ongoing and will culminate with the successful completion of a self-contained nCWFS optical system for use at a major telescope. It will replace the Shack-Hartmann wave front sensor as the industry standard and provide superior resolution by at least a factor of ten. This will allow ground based telescopes to obtain images much closer to the theoretical diffraction limit than is currently possible.

Current progress is proceeding apace with many milestones met and many more feasible on the horizon. Using Object Oriented Matlab Adaptive Optics (OOMAO) the team has demonstrated the theoretical capability for the new wave front sensor. A real time computer (RTC) has been built with a wave front error budget within acceptable processing time using simulated data. The instrumentation has been setup and aligned to provide real data using both the SHWFS and the nCWFS. Artificial aberrators have been constructed and put in place to demonstrate the resolving power of the system. More work needs to be done to the RTC system to improve its performance and ensure proper treatment of any wave front distortion. Once a reasonable comparison between the SHWFS and the nCWFS can be made using real data, proof of concept will help draw the necessary funds to upgrade the equipment to improve all aspects of the design and increase resolution and processing speed.

References

- [1] Guyon, O. (2009). High sensitivity wavefront sensing with a nonlinear curvature wavefront sensor. *Publications of the Astronomical Society of the Pacific*, 122(887), 49.
- [2] Crass, J. (2014). *The Adaptive Optics Lucky Imager: combining adaptive optics and lucky imaging* (Doctoral dissertation, University of Cambridge).
- [3] Mateen, M. (2015). *Development and verification of the non-linear curvature wavefront sensor*.
- [4] Schmidt, J. D. (2010, July). *Numerical simulation of optical wave propagation with examples in MATLAB*. Bellingham, Washington, USA: SPIE.

Study of Stub Momentum Resolution and Hardware Benchmarking for CMS Track Trigger

Author: Tianyi Wang

2019 NSF REU Program

Physics Department, University of Notre Dame

July 22, 2019

Advisors: Kevin Lannon, Michael Hildreth

millimeters away from each other, where two hits from a particle constructs a stub. Another quantity named bend is introduced to describe the amount of horizontal shift in a stub [2].

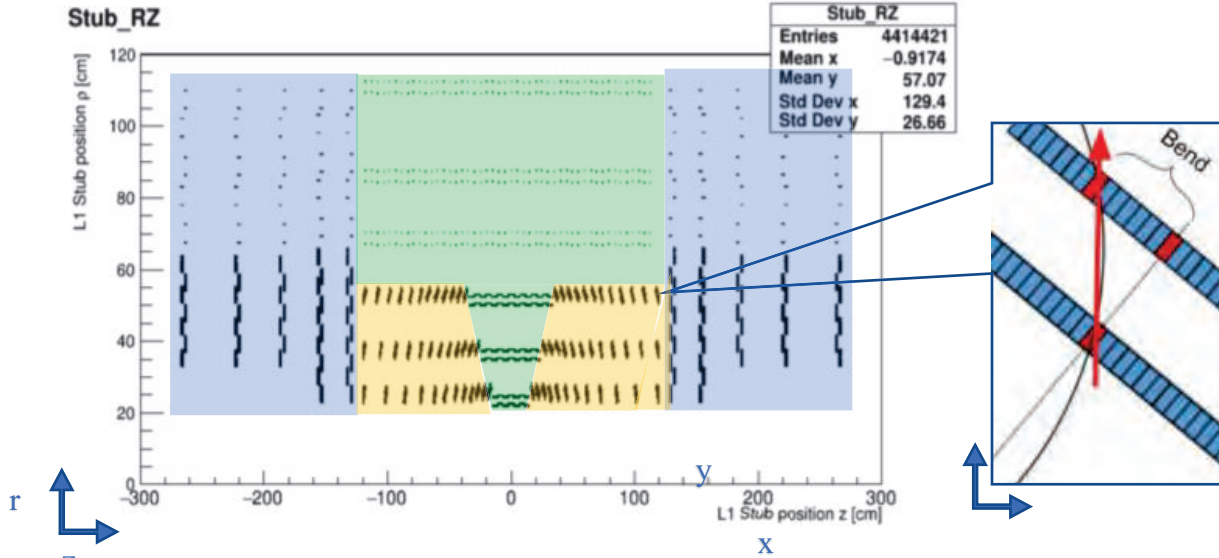


Figure 2: Cross section of silicon trackers, with barrel colored green, tilted barrel colored yellow, and endcap colored blue. On the right it shows the detail of a pair of stubs and an example of bend

With the assumption that the collision comes from the original point (0, 0) in the x-y coordinate, the bend can be calculated from the position of stub and the transverse momentum of particle creating the track. The analytic formula for bend prediction includes extensive trigonometric and angular components that the FPGA are inefficient to calculate and lead to large uncertainty in many situations involving small angles. Previous researchers have proposed a simplified formula with correction factor to calculate the bend:

$$bend = \frac{-r \cdot dr \cdot B \cdot c}{pitch \cdot p_T \cdot correction \cdot 2 \cdot 10^{11}} \quad [4]$$

- For the tilted barrel: correction = 0.886454*(|stub_zl/stub_r) + 0.504148
- For the ECs: correction = (|stub_zl/stub_r)
- For the barrel: correction = 1

Where *pitch* is the width of an individual strip of sensor, *dr* is the spacing between layers in a stub,

and p_T is the transverse momentum. The factor $2 \cdot 10^{11}$ at the denominator is to compensate for unit conversions. Inserting numerical values for the constants, the formula becomes:

$$bend = \frac{-0.5 \cdot dr \cdot r \cdot r_{inv}}{pitch \cdot correction}$$

Where r_{inv} is the inverse of the particle trajectory's radius. This value is inversely proportional to the momentum of the particle as it travels in a magnetic field. The correction factor [4] is applied to account for the error cause by direction difference of tilted barrel and endcap. It is an approximation to the full geometrical correction for the module tilts and has been shown to be totally adequate for the purposes of the algorithm.

The Track Trigger is developed to reconstruct trajectories of charged particles by linking together stubs. To reject fake combinations of stubs caused by different particles, it requires the momentum of the stub to comply with the momentum of the track that it's being used to reconstruct. The stub momentum is calculated from the measured bend of the stub, while track momentum is measured from the radius of curvature of the particle trajectory in the magnetic field created by CMS. Given momentum of the track and position of the stub, its stub bend can be calculated by bend predicting algorithm. Then the bend consistency cut algorithm checks whether the measured bend matches this predicted bend, and thus decide whether the stub belongs to the track. However, the measured bend of the stub would always deviate a little from the predicted one due to two major reasons. First, the accuracy of measured stub bends is about 0.4 to 0.5 strip width due to limited sensor precision [5]. Second, the algorithm that predicts stub bends from p_T relies on information that aren't known perfectly in real experiment. The primary goal of this research is to test the stub momentum resolution of the bend prediction algorithm, which determines if the

geometric corrections applied to the bend prediction algorithm are accurate enough for use.

The track reconstruction algorithm will be implemented into FPGA firmware, which are processors simpler than CPUs but specializing in performing certain command at very high frequency. There will also be processors configuring and controlling the FPGAs serving as part of the track trigger control system. In addition to studying bend resolution, I also worked on competent processor options to see whether they are suitable for the track trigger control system.

Method

The research utilizes a simulation of the upgraded CMS detector [6]. It is used to simulate two classes of collision: One in which a pair of muons with same momentum and opposite charge and direction is produced with randomly selected transverse momentum between 2 and 100 GeV. The other resembles real LHC collisions in which a top quark pair is produced, but with additional 200 additional overlapping collisions to represent the situation after the HL-LHC upgrade.

The bend prediction algorithm takes the value of stub coordinate (r, z) and the true value of the transverse momentum for the particle the produced the stub in the simulation . In this way, its prediction results are free of measurement errors and only contain deviations from the approximated geometric correction factors. Then the program reads in measured bends generated by simulator for the same stub, which have been processed to simulate data output from actual LHC runs. Measured bends are therefore disturbed by device uncertainty. They in a stored accuracy slightly less than 0.5 pitch, or half the width of an individual sensor due to limited sensor precision and storage assigned to each stub bend (4 bits for outer barrel and 3 bits for other regions).

The performance of bend prediction algorithm is measured by two ways. First is the range of deviation distribution. The second is sign of systematic biases, especially if deviation between predicted and measured bend is not random and evenly distributed, but instead suggesting an inclination to underestimate or overestimate the bend or performing much worse in certain regions.

The hardware benchmarking project consists of three different benchmarks: sbc bench, Zeromq performance tests, and CoreMark. The sbc bench [7] tests the processors' capability to compress and decompress files via 7-zip and conduct AES encryptions with different sizes of data being encrypted. The Zeromq performance test [8] transmits and receives data via local Ethernet to test the network and interthread latency of processors. CoreMark [9] tests their capability of solving simple functions, as well as assigning value for arrays of empty memory space.

Results

The most general and representative indicator of how well the bend prediction algorithm functions is statistics of deviation between predicted and measured bend. Because error assigned to measured bends are random, the deviation distribution should be a Gaussian curve. The smallest possible width of the Gaussian curve would be at around 0.4 based on the intrinsic bend measurement precision and would be larger if other sources of error exist.

Figure 3 contains distribution of deviation between predicted and measured bends for 100 top pair production events with 0.5 bend as single bin width. The bend prediction curve has a mean value at 0.0026 ± 0.0015 bend and sigma of 0.533 ± 0.001 . With average value very close to 0 and sigma close to theoretical limit of 0.4, it shows that there's no significant, systematic flaw in

the bend predicting algorithm and there's no visible error in detecting charge of particles. In distribution of bend deviation for 10000 muon pair events, the fitted Gaussian curve has a mean value at $5.316 \cdot 10^{-5}$ bend and sigma at 0.492 ± 0.001 . The Gaussian width in top pair production events is bigger than in muons because it includes stubs from many other types of particles, including electrons which lose a lot of energy moving through the detector and pions which have a similar mass to muons but also experience nuclear interactions. These particles experience significant impact when they pass through the detectors, and thus have a worse p_T resolution in prediction

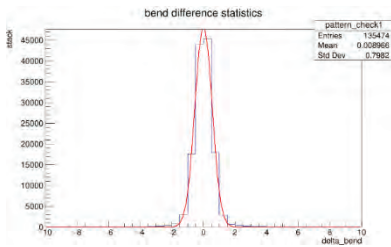


Figure 3: bend deviation statistic for top pair production events with Gaussian curve fitting

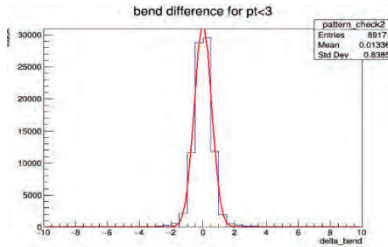


Figure 4: bend deviation for pt smaller than 3 GeV in top pair production events (0.5 step)

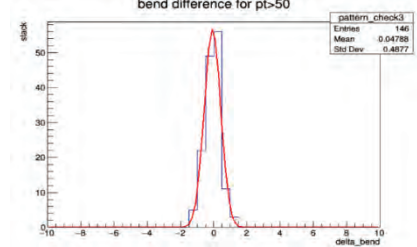


Figure 5: bend deviation for pt larger than 50 GeV in top pair production events (0.5 step)

Pt (GeV)	2-3	3-10	10-20	20-30	30-40	40-50	50+	General
Muon	0.499	0.491	0.478	0.482	0.472	0.486	0.501	0.493
Top pair	0.538	0.526	0.490	0.460	0.491	0.496	0.499	0.533

Table 1: sigma value (width) of Gaussian curve for different pt in muon and top pair production events

Table 1 shows that the width of Gaussian curve is largest when p_T is less than 3 GeV and larger than 50 GeV, while being smallest in between. The larger Gaussian curve width at smaller p_T is at least partially contributed by the excessively large number of entries that fall under this region, so the p_T resolution in general drops as its value rises at a minimal rate. No other tendency

or bias is observed relating to energy level, as shown in Figure 4 and 5.

Region	Inner barrel	Outer barrel	Tilted barrel	Endcaps
Muon	0.494	0.419	0.516	0.509
Top pair	0.527	0.507	0.539	0.544

Table 2: sigma value (width) of Gaussian curve for different region in muon and top pair production events

Table 2 shows that in both muon and top pair production events the bend prediction algorithm is most accurate in outer barrel region, while being less accurate in inner barrel region and deviate the most in tilted barrel and endcaps. In general, the Gaussian curve width is smaller than 0.55 in all cases. This implies that the geometric corrections compensate for most of the deviations caused by stub position difference and avoid major systematic errors. However, its resolution in the tilted modules and the endcap is worse than ideal. This is not completely unexpected especially for stubs in tilted barrel region because the geometric corrections don't take specific angle of individual stubs into account. However, these regions should be studied more carefully in the future to see if additional corrections can improve the resolution.

In hardware benchmark, comparisons were drawn between COM Express, a competent SoC for

local latency	raspi					raspi 3 b+							
latency/ms	100	1000	10000	100000	1000000	exe time/ite	100	1000	10000	100000	1000000		
100Byte	/	69.19	77.9	81.77	82.08		100byte	-0.3	-0.4		1.9	16.7	
1K	/	71.58	80.85	83.57	83.69		1K	-0.4	-0.4	-1.9		16.9	
10K	112.74	125.48	139.16	140.01	139.89		10K	-0.2	-0.2	-0.5		3	28.2
100K	330.79				/		100K	-0.3				/	
1M				/	/		1M				/	/	
local latency	COM Express					COM Express							
latency/ms	100	1000	10000	100000	1000000	exe time/ite	100	1000	10000	100000	1000000		
100Byte	536.58	932.02	762.17	625.63			100Byte	1.148	2.902	16.288	126.165		
1K	518.62	907.84	837.48	575.48			1K	1.144	2.856	16.574	116.136		
10K	795.17(unstable)	768.76	746.5	600.78			10K	1.199	2.576	15.969	121.193		
100K	597.32	857.48	642.24	569.53			100K	1.16	2.754	13.885	114.946		
1M	1755.77	1633.7	1522	1602.87			1M	1.391	4.308	31.479	321.615		

Table 3: Latency and execution time of Zeromq local latency test for COM Express and raspi3 b+

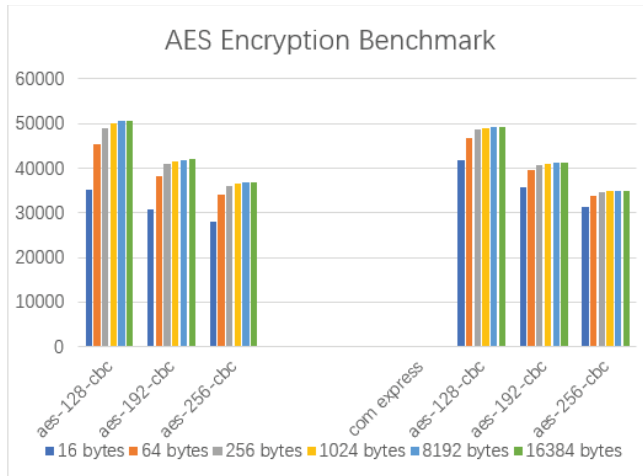


Figure 6: AES encryption test results of Raspi 3b+ and COM Express

Track Trigger equipped with a quad-core Intel Celeron J1900 processor and Raspi 3b+, a popular SoC model in the market with a quad-core Broadcom Cortex A53 processor. The encryption test from sbc bench shows that while they provide similar processing power

in dealing with larger data chunks, the efficiency of Raspi 3b+ drops significantly when processing small chunks of data, especially in the 16 bytes category as shown in Figure 6. This might be due to the lower clock speed of its processor, which is at 1.4GHz compared to 2.42GHz in COM Express. In average of 10 successive runs of Zeromq local latency test via bash script, COM Express shows a much larger and unstable latency compared to Raspi 3b+. This might be caused by its lack of hardware network control component or because it is booted on an older version kernel. Its detail awaits for further investigation in the future.

Further Studies

The next step for the simulation project is to figure out whether and how much influence to deviation is caused by resolution of p_T measurement, binning of results, or insufficiencies in the geometric correction respectively. This would be helpful in finding out whether the width of the bend deviation curve could be cut down further, and thus increase the resolution of the bend prediction algorithm. Special attention will be given in exploring the necessity and influence of additional geometric corrections applied on the tilted modules and the endcaps to improve the

algorithm's performance in these regions.

For benchmarking project, the Zynq will be built and configured with the same environment as COM Express. Comparisons will be then made according to their hardware parameters and performance in benchmarks. The goal is to measure their comparative strength in performing various types of tasks and help determine which one is a better choice for the Track Trigger.

Reference

- [1] The HL-LHC Project | High Luminosity Large Hadron Collider. CERN. <http://hilumilhc.web.cern.ch/>
- [2] Detector | CMS Experiment. CERN. <https://cms.cern/detector>
- [3] CERN, High-Luminosity Large Hadron Collider (HL-LHC) Technical Design Report V. 0.1., <http://dx.doi.org/10.23731/CYRM-2017-004>
- [4] Bend prediction formula and Correction Factors developed by Emyr Clement (Private communication)
- [5] Kevin Greif, "Bend Consistency Cut Performance in the CMS Detector L1-Trigger Upgrade", 2018
- [6] L1TrackNtupleMaker, program from CMSSW10_1_4 software environment
- [7] Thomas Kaiser, sbc-bench, <https://github.com/ThomasKaiser/sbc-bench>
- [8] Zeromq Performance Tests, 2011, <http://zeromq.org/area:results>
- [9] Embedded Microprocessor Benchmark Consortium (EEMBC), CoreMark®, <https://github.com/eembc/coremark>

The Effect of Finite Organism Size and Contact Forces in Population Dynamics

Hiroka Warren

2019 REU/NSF Program
Physics Department, University of Notre Dame

Adviser: Professor Dervis Can Vural

Abstract

We study the Lotka-Volterra model with intraspecific competition. The Lotka-Volterra equation describes the population dynamics of interactions between predators and preys. The intensity of the interactions depends on the size of species as well as area density. We show numerically and analytically that properties of this model changes depending on the size of species.

Introduction

The Lotka-Volterra equations (also known as predator-prey equations) give the population model of interactions between predators and preys. In the Lotka-Volterra model with two species, the predators feed on the preys [1], which in turn feed on some natural resource. There are several assumptions in this model. One of the assumptions is that the prey population always has an unlimited food supply. In other words, this model is applied only in some ideal conditions [2]. Multi-species Lotka-Volterra models have been studied by many researchers. However, not much known for the competitive model statistically. A research shows that the position of species can affect the intensity of competitive interactions. Typically, species can experience a stronger competition in areas of high density. As a result, a species can only survive if it can maintain some distance with the other species [3].

The aim of this research is to include finite size effects to the Lotka-Volterra model with intraspecific competition by using a simulation. We also show how to correct the mean-field model when size of the species is included.

Methods

Simulation Methods

We built a simulation which contains two species: namely, green balls (as prey) and red balls (as predator). Here is the scenario.

1. If a green ball hits another green ball, one of them disappears (because they compete for the same resources) with probability $P1$. With probability $1 - P1$, nothing happens.
2. If a green ball hits a red ball, the green ball turns a red ball (because the predator ate the prey and reproduced another predator) with probability $P2$. With probability $1 - P2$, nothing happens.
3. If no one collides or nothing happened in the scenario 1 and 2, a green ball reproduces another green ball with probability $P3$. With probability $1 - P3$, nothing happens.
4. A red ball dies with probability $P4$. With probability $1 - P4$, nothing happens.
5. The both green balls and red balls have finite size and perform a random walk in 2D.

Green balls have a step size of g , and red balls have a step size of r .

The simulation was compared with the theoretical model. The interaction matrix of the system in the simulation is

$$\begin{array}{cc} & \begin{array}{cc} G & R \end{array} \\ \begin{array}{c} G \\ R \end{array} & \begin{bmatrix} -P1 & -P2 \\ P2 & 0 \end{bmatrix} \end{array} \quad (1)$$

From this matrix, we obtain the Lotka-Volterra equations for the simulation.

$$\dot{G} \sim G [P3 - P1G - P2R] \quad (2 - a)$$

$$\dot{R} \sim R [-P4 + P2G] \quad (2 - b)$$

At steady state,

$$\dot{G} = 0 = P3 - P1G^* - P2R^* \quad (3 - a)$$

$$\dot{R} = 0 = -P4 + P2G^* \quad (3 - b)$$

From equation (3 – a) and (3 – b), we obtain population ratio of green balls and red balls.

$$\frac{G^*}{R^*} = \frac{P2P4}{P2P3 - P1P4} \quad (4)$$

We varied the radius $R = (0.1, 0.3, 0.5, 1.0, 1.5, 2.0)$, of each ball across multiple simulations making all balls the same radius. Since the results varied depending on the size of balls, we assumed that there must be other probabilities that we should include in the equation. In order to include “size” in the equation, we assume a modified set of equations

$$\dot{G} \sim G [P3 - P1\rho_{hit}^{GG}G - P2\rho_{hit}^{GR}R] \quad (5 - a)$$

$$\dot{R} \sim R[-P4 + P2\rho_{hit}^{GR}G] \quad (5 - b)$$

where ρ_{hit}^{GG} is the probability that a green ball hits another green ball, and ρ_{hit}^{GR} is the probability that a green ball hits a red ball. At steady state, we get population ratio of green balls and red balls from the equation (5 – a) and (5 – b).

$$\frac{G^*}{R^*} = \frac{P2P4\rho_{hit}^{GR}}{P2P3\rho_{hit}^{GR} - P1P4\rho_{hit}^{GG}} \quad (6)$$

In order to calculate ρ_{hit}^{GG} and ρ_{hit}^{GR} , we made simulations for each size of balls with each population ratio and area density by using the numerical steady-state results in the simulation. When a green ball hits a red ball and turns into a red ball, the probability of this event is $P(P2 \cap \rho_{hit}^{GR}) = P2\rho_{hit}^{GR}$. $P2\rho_{hit}^{GR}$ can be measured in the simulation by setting other probabilities $P1 = P3 = P4 = 0$ and counting how many green balls survived after one simulation time-step (tick).

$$P2\rho_{hit}^{GR} = 1 - \frac{\text{number of ball after one tick}}{\text{initial number of ball}} \quad (7)$$

We set $P2 = 1$ to simplify the calculation to obtain ρ_{hit}^{GR} . ρ_{hit}^{GG} can be obtained with the same procedure as ρ_{hit}^{GR} . However, since it was difficult to measure ρ_{hit}^{GG} unlike ρ_{hit}^{GR} (Figure 1), we calculated ρ_{hit}^{GG} by setting equation (6) equals to numerical number of population ratio.

$$\rho_{hit}^{GG} = \frac{(\text{numerical}_{\frac{G}{R}})P2P3\rho_{hit}^{GR} - P2P4\rho_{hit}^{GR}}{(\text{numerical}_{\frac{G}{R}})P1P4} \quad (8)$$

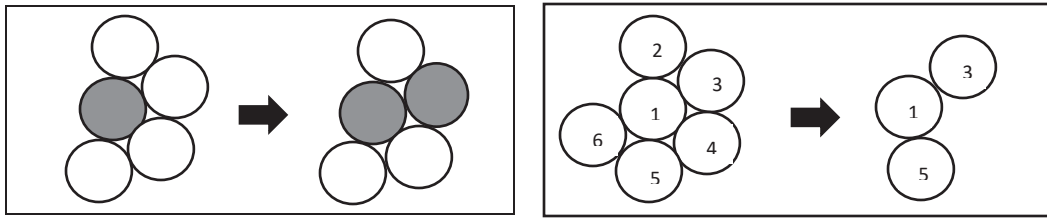


Figure 1: a) When a red ball hits multiple green balls at the same time, only one of them becomes a red ball. b) When a green ball hits multiple other green balls at the same time, multiple green balls can disappear at a time (Green 1 kills Green 2, Green 3 kills Green 4, and Green 5 kills Green 6.).

Calculation Methods

In order to get the same population ratio of green balls and red balls as the numerical result, we modify the population ratio as

$$f(\bar{\epsilon}) = \frac{(P2 + \epsilon_2)(P4 + \epsilon_4)}{(P2 + \epsilon_2)(P3 + \epsilon_3) - (P1 + \epsilon_1)(P4 + \epsilon_4)} \quad (9)$$

We want to find $\bar{\epsilon}$ such that $|\bar{\epsilon}|$ is minimum. Therefore, we define Lagrangian,

$$L = (n - f(\epsilon))^2 + \sum_i \epsilon_i^2 \quad (10)$$

where n is the numerical number of population ratio. Minimizing the Lagrangian attempts to get a better prediction of the ratio while also regularizing the amount of change we introduce into the model. L can be minimized by taking derivative of equation (10) and set it to 0.

$$\frac{\partial L}{\partial \epsilon_1} = 0 = 2(n - f(\epsilon)) \frac{\partial f}{\partial \epsilon_1} + 2\epsilon_1 \quad (11 - a)$$

$$\frac{\partial L}{\partial \varepsilon_2} = 0 = 2(n - f(\varepsilon)) \frac{\partial f}{\partial \varepsilon_2} + 2\varepsilon_2 \quad (11 - b)$$

$$\frac{\partial L}{\partial \varepsilon_3} = 0 = 2(n - f(\varepsilon)) \frac{\partial f}{\partial \varepsilon_3} + 2\varepsilon_3 \quad (11 - c)$$

$$\frac{\partial L}{\partial \varepsilon_4} = 0 = 2(n - f(\varepsilon)) \frac{\partial f}{\partial \varepsilon_4} + 2\varepsilon_4 \quad (11 - d)$$

We assume the corrections are small in comparison to the initial probability values ($\frac{\varepsilon_1}{P_1} \ll 1, \frac{\varepsilon_2}{P_2} \ll 1, \frac{\varepsilon_3}{P_3} \ll 1, \frac{\varepsilon_4}{P_4} \ll 1$). The resulting system of the equation can be linearized around $0 \approx \bar{a} + B\bar{\varepsilon}$.

Therefore, we can approximate the optimal solution by solving the linear set of equations to get

$$\bar{\varepsilon} \approx -\bar{B}^{-1}\bar{a}. \quad (12)$$

Results

Simulation results

Figure 2 shows the difference between the theory and the numerical results in the simulation, where radius $R = 0.5$, $P_1 = 0.5$, $P_2 = 0.3$, $P_3 = 0.3$, $P_4 = 0.1$, step-size $g = r = 1$, and the initial

number of both balls = 20. While the

theory suggests that $\frac{G^*}{R^*} = 0.75$, the result

in the simulation is $\langle \frac{G}{R} \rangle = 0.749$, which

results in $error = \left| \frac{\langle \frac{G}{R} \rangle - \frac{G^*}{R^*}}{\frac{G^*}{R^*}} \right| = 0.011$.

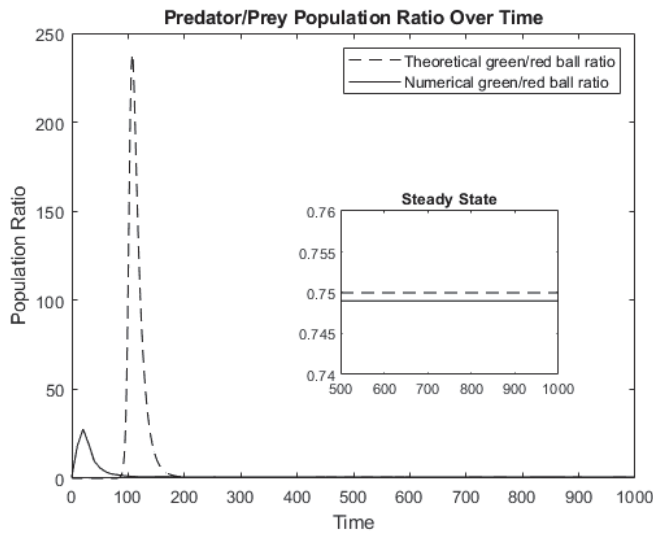


Figure 2: Theoretical and numerical population ratio of green balls and red balls.

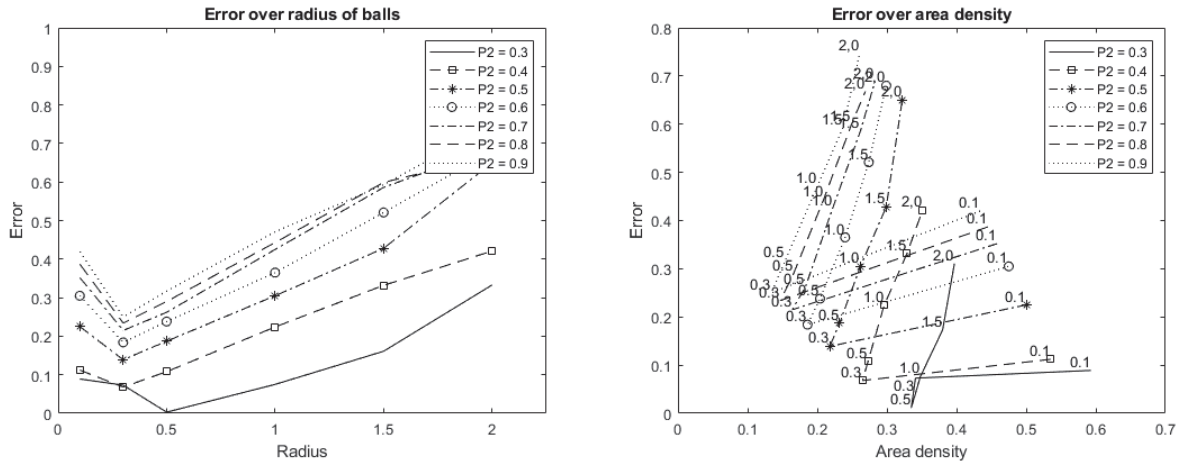


Figure 3: a) Error over radius of balls with different probability P2. b) Error over area density with different probability P2.

Figure 3 (a) shows a relation between error and the size of balls with the same step-size, initial number of balls, and probabilities with different P2. Figure 3 (b) shows a relation between error and $area\ density = \frac{total\ number\ of\ balls}{total\ area\ in\ the\ space}$. We expected that as we increase the radius of ball, error would be larger, and as we decrease the radius, error would be even smaller. However, the simulation for P2 = 0.3 shows larger error for smaller radius than R = 0.5 while error for larger radius becomes larger as we expected. Figure 3 (b) tells us the large error for the smaller size of balls is related to area density. Because there are more balls when the size of balls is very small, its area density becomes higher (Figure 4). The interesting fact in the graphs is that

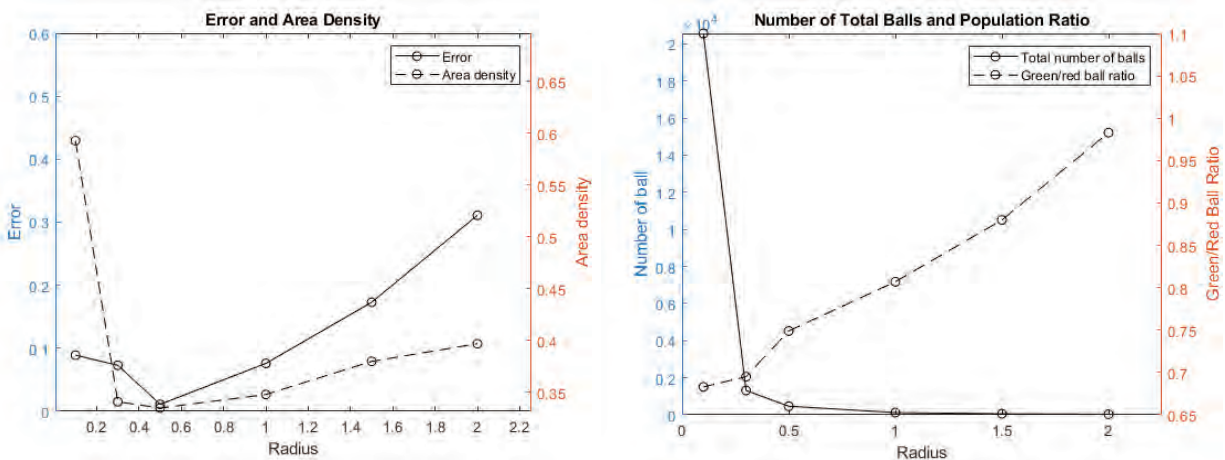


Figure 4: a) Error and area density. b) Number of total balls and population ratio of green balls and red balls.

the size is not the only factor that affects the results in error. The minimum error for $P_2 = 0.3$ is $R = 0.5$ while for other P_2 probabilities, $R = 0.3$ results in the smallest error. It implies that not only the size of balls but also probability combinations can affect total number of species in the space.

Figure 5 shows a relation between error and area density with the same step-size, initial number of balls, and probabilities with different P_1 (a), P_2 (b), P_3 (c), and P_4 (d). Not every probability is included in the graphs because with some probability combinations we got negative theoretical number, or in the simulation either green balls or red balls did not survive.

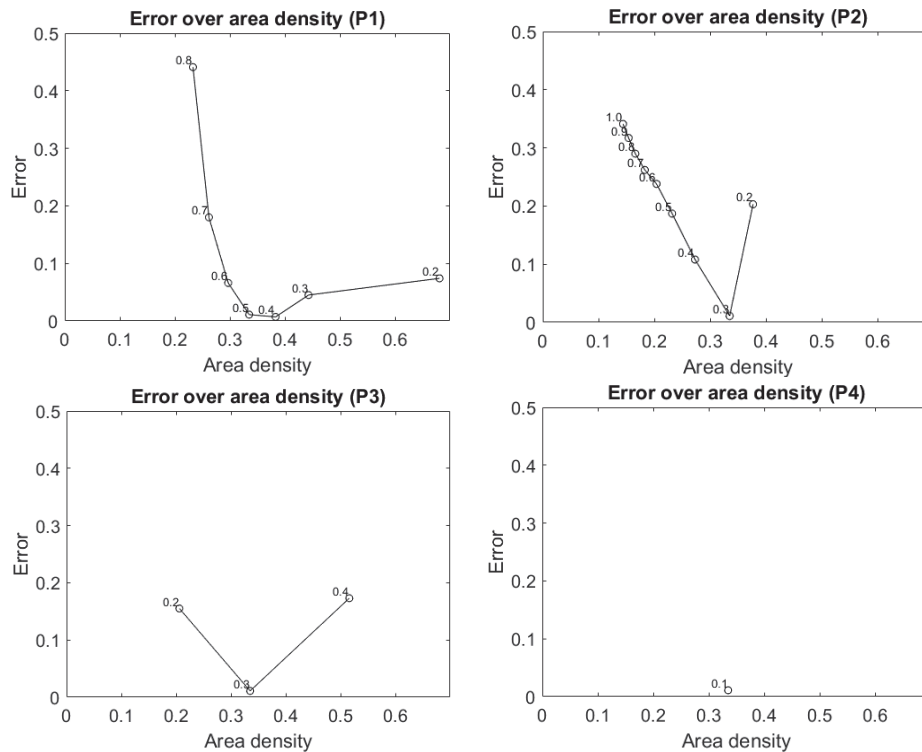


Figure 5: Error over area density for a) different P_1 with $P_2 = P_3 = 0.3$ and $P_4 = 0.1$, b) different P_2 with $P_1 = 0.5$, $P_3 = 0.3$, and $P_4 = 0.1$, c) different P_3 with $P_1 = 0.5$, $P_2 = 0.3$, $P_4 = 0.1$, and d) different P_4 with $P_1 = 0.5$, $P_2 = P_3 = 0.3$.

Figure 6 shows the result of ρ_{hit}^{GR} and ρ_{hit}^{GG} , where $P_1 = 0.5$, $P_2 = 0.3$, $P_3 = 0.3$, $P_4 = 0.1$, step-size $g = r = 1$, and the initial number of both balls = 20. Since the minimum error as well as area density in the situation is $R = 0.5$ as shown in Figure 3, we can expect at larger and smaller radius than $R = 0.5$, there would be more interactions among species because of high area density. This